International Journal of Acoustics and Vibration

A quarterly publication of the International Institute of Acoustics and Vibration

Volume 20, Number 4, December 2015

EDITORIAL

ARTICLES

INFORMATION

Editor's Space

The Fourier Transform in Sound and Vibration Analysis

During my years as a researcher and lecturer, I have frequently encountered the Fourier Transform, particularly in terms of the Discrete Fourier Transform (DFT), which is defined for sampled signals and is generally computed using the computationally efficient FFT (Fast Fourier Transform). The Fourier Transform is a fundamental tool in numerous signal processing applications, and it is extensively used in sound and vibration analysis where it concerns rotating machinery analysis, condition monitoring, experimental modal analysis, noise source identification, transfer path analysis, etc.

My experiences in the sound and vibration areas concerning the application of the DFT emphasizes the importance of producing relevant and accurate spectrum estimates - **power spectrum** (Unit of signal^2), **power spectral density** (Unit of signal^2/Hz) and **energy spectral density** (Unit of signal^2/Hz*s).

Generally, when measuring physical quantities in practice, equipment like the sensors, amplifiers, A/D converters, etc. all introduce noise to the acquired signal. In other words, the acquired signals usually display random properties. This suggests that the production of spectrum estimates for sound and vibration signals has to be based on a **statistical approach** to enable spectrum estimates having sufficiently low **bias errors** and **variance** as well as accessible **statistical confidence**.

From this point of view, I think it is appropriate to post a warning that a frequency spectrum produced as the direct output from the DFT of a time series of a measured sound or vibration will, in general, not be useful, relevant, or accurate.

In general, the **spectrum estimator**, used for producing an estimate of a spectrum, is related to the signal content of interest, such as periodic, random, or transient. Periodic signals are characterised by showing a discrete power distribution in the frequency domain, while random signals have a continuous power distribution in the frequency domain, and transient signals have a continuous energy distribution in the frequency domain. Estimates of their spectra are generally based on so-called **Periodograms**. A Periodogram for a signal time series is basically produced by the squared magnitude of the DFT of the signal or a signal segment. This makes sense since we are discussing power and energy distributions in the frequency domain.

In the "early days," spectrum analyses of signals were carried out by using an analogue bandpass-filter with adjustable centre frequency, for example. A spectrum was produced by successively adjusting the centre frequency of the filter and, for each selected centre frequency, the power of the filter's output signal was measured via a time average (integration) of the squared output signal of the filter.

In fact, this is related to the modern DFT, which can be understood in terms of a filter bank consisting of N bandpass-filters whose centre frequencies are defined by the discrete frequencies of the DFT. The output of the filter bank will be the N complex values of the DFT for each signal segments of N samples of the input signal. Each of the N bandpass-filters will consequently produce an output signal with complex valued samples. Observe that when sampled sound or vibration signals display random properties the output signals from the DFT filter bank of such signals will also have random properties! Thus, a frequency spectrum produced as the direct output from the DFT or FFT of a time series will, in general, **not make any sense!**

But if time averaging is applied on the squared magnitude of respective bandpass-filters output signal samples, it will yield an average of the Periodogram at each discrete frequency of the DFT. If the input signal to the DFT fulfil sufficient ergodicity conditions, the variance of the average of the Periodogram will decrease with an increasing number of averages!

The number of averages required to obtain sufficiently low variance depends on the degree of randomness of a signal, and this is inversely proportional to its correlation length, which, in turn, is approximately inversely proportional to the signal's bandwidth.

For periodic and random input signals to the DFT, signal segments of N samples are generally **cut out** or **windowed** and used for the production of each output sample of the DFT filters. On the other hand, if the input signal to the DFT is transient, N is selected to include the complete transient, a signal segment is **not cut out**, and **no windowing** is carried out. The DFT length N and selected window type will usually have a direct influence on the bias errors introduced in a spectrum estimate. On the other hand, if the complete signal fits within the N samples, no windowing is used and the filter bandwidth may be considered infinitely narrow and no bias errors will be introduced.

The proper spectrum estimator for a periodic signal is the **power spectrum** estimator; for a random signal, it is the **power spectral density** estimator; and for a transient signal, it is the **energy spectral density** estimator.

Lars Håkansson
Director, IIAV

New IIAV Officers and Directors

New IIAV Vice-President for Communications

Mark Asselineau

Marc Asselineau has been a consulting engineer with Peutz & Associates acoustical consultants in France for the past 27 years. He is currently a senior engineer in the firm, which is active in the fields of building and room acoustics, as well as occupational noise assessment and control. He is a member of the French Acoustical Society and the Canadian Acoustical Association. Previously, he served for three years as an assistant at Laval University in Quebec, Canada. He graduated in 1987 with a PhD in applied acoustics, and he speaks English, and some Dutch and Russian. Dr. Asselineau has undertaken engineering projects in several countries and has also been involved in international standardization in the fields of occupational noise and building acoustics in various working groups (ISO, EU). He has also written papers (some of them invited) and presented them at a number of conferences around the world. He was in charge of the building acoustics part of the French Congress of Acoustics held in 2010 in Lyon, and is an associate editor of the journal Advances in Acoustics and Vibrations. He was awarded the Canac prize by the French Society of Acoustics in 2004.

New IIAV Directors

Bela Buna

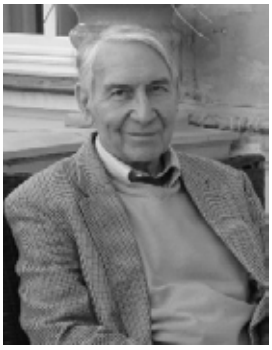

Bela Buna has served as head and main owner of a company concerned with environmental protection since 1994. His main focus is in acoustics, noise, and vibration control. He is a member of the Acoustical Committee of the Hungarian Academy of Science, a member of the German and French Acoustical Societies, and a fellow of the UK Institute of Acoustics. Previously, he worked for 27 years at the Institute of Transport Sciences, Budapest. He received a MS in traffic engineering and later in electrical engineering (instruments and process control). He speaks English, German, and some French. His PhD thesis was concerned with the prediction of road transport noise. Dr. Buna has been involved in international studies and study tours, and has represented Hungary in various working groups (ISO, ECE, EU, and the EU WG6 Railway Noise). He has published more than 55 articles in various journals (e.g., ATA, Applied Acoustics, Noise Control Engineering, Vehicle Design) and presented papers at international conferences. He has written four books and book chapters (in Verminderung des Verkerslärms of Springer Verlag and the Transportation Noise Reference Book of Butterworths. Dr. Buna recently organised a workshop in Hungary on the application of numerical methods in acoustical planning under the Hungarian Academy of Science. He has also taken part in different European common projects and regularly writes book reviews for the IJAV.

Maria de Diego

Maria de Diego received her degree in telecommunications engineering from the Universitat Politecnica de Valencia in Valencia, Spain, in 1994 and her PhD from the same university in 2003. Her dissertation was on active noise conformation of enclosed acoustic fields. She is currently serving as an associate professor in digital signal processing and communications. Dr. de Diego has been involved in different research projects including active noise control, fast adaptive filtering algorithms, sound quality evaluation, and sound reproduction, in the Audio and Communications Signal Processing (GTAC) group of the Institute of Telecommunications and Multimedia Applications (iTEAM) of Valencia. She has published more than 70 papers in journals and conferences about signal processing and applied acoustics. Her current research interests include signal processing of arrays, multichannel adaptive signal processing, and distributed signal processing. She is also conducting research on non-linear adaptive filtering, and its parallel implementation as well as applications to active noise control and listening-room compensation systems. She organized a special session at the 19th European Signal Processing Conference in 2011 in Barcelona and is a member of the Institute of Electrical and Electronics Engineers (IEEE) and the IIAV.

Mohammed Hussein

Dr. Mohammed Hussein is an associate professor in the College of Engineering at Qatar University. His main area of expertise is structural dynamics, and he has a particular interest in the topics of railway dynamics, soil-structure interaction, and human-structure interaction. He has been a member of the IIAV since 2003 and a fellow of the Higher Education Academy since 2013. He joined Qatar University in September 2014 after the Institute of Sound and Vibration Research (ISVR) at the University of Southampton where he served as a senior lecturer from July 2013 to August 2014. Previously, he worked at the University of Nottingham as a lecturer and at the University of Cambridge as a postdoctoral research associate. Dr. Hussein completed his PhD at the University of Cambridge in July 2005. His work has resulted in more than 80 publications (including 30 journal papers). He is a co-developer of the PiP software ¡www.pipmodel.com¿ for calculating vibration from underground railways. Dr. Hussein has supervised six PhD students and more than 40 MS students. He is a recipient of major grants, a member of a number of professional committees, and a reviewer for more than ten major journals in the field of dynamics and vibration.

Giuseppe Miccoli

Giuseppe Miccoli graduated with a degree in physics from the University of Ferrara in Italy in 1979. Since 1985, he has been a senior researcher of the National Research Council's (C.N.R.) Institute for Agricultural and Earthmoving Machines (IMAMOTER) where he is the scientific manager of research activities including active and passive noise & vibration control; system/structure computational and experimental dynamic analysis; and system/machine component vibroacoustic numerical simulation, experimental validation, and optimization; and fluid/structure interaction by CAD-FEM/BEM integrated computation methods. He is a member of the Italian Acoustics Association (AIA) and has served as the scientific director of the Analisi e Calcolo (A&C) Review from 2003-2008. He was also a member of the Technology Network Alliance (TechNet), a service and distribution network for high technology products, from 2004-2006 and served on the Board of Directors of IIAV from 2004-2008. He is also a member of the Board of Directors of NAFEMS (the International Association for the Engineering Analysis Community) since 2003, and he is the Manager of the NAFEMS Italia Association. He is the author of more than 200 papers and technical reports.

Konstantinos E. Vogiatzis

Konstantinos Vogiatzis is an associate professor of public transportation, environmental engineering & environmental acoustics, environmental impact assessment, and environmental management for transportation networks at the University of Thessaly. He graduated with an MS degree in rural and surveying engineering from the National Technical University of Athens (UNTA) in 1977. He also obtained an MS in civil engineering (transportation planning) from UNTA in 1980. In addition, he obtained a post-graduate diploma in urban and rural planning from the Centre of Research in Paris in 1980 and a PhD from the Doctorat University of Paris 1 Pantheon-Sorbonne in January 1981. His professional and scientific memberships include enterprise directorate (general) of a working group on road traffic noise WG 8, European Commission; former General Secretary of the Acoustical Society of Greece; Hellenic Institute of Transportation Engineers; and Consultant in Ministry of Environment in France - Programs GEUS I & II (Gestion d' Environnement Urbain Sonore). He has served as a member of the International Scientific Committees for ICSV 12, ICSV 13, ICSV 14, ICSV 16, and ICSV 17 and of the Management Committee of the European projects QCity and City Hush. His most important research interests focus on the protection of the urban acoustical environment and transportation noise with an emphasis on airborne and groundborne noise and vibration. He is also interested in the mass urban transportation networks as well as airport operation, urban and semi-urban road transportation infrastructure with a focus on the integrated environmental, and land use planning management. He received an award for Academic and Scientific Excellence from the Greek Ministry of Education in 2012.

Student Award Winners

Giulio Dolcetti

Giulio Dolcetti received his MS in mechanical engineering from the University of Ferrara, Italy. He is currently working towards his PhD at the Department of Mechanical Engineering at the University of Sheffield, UK. His research is focused on the scattering of airborne acoustic waves by composite dynamic rough surfaces, characterisation of the air-water interface in shallow water flows, and non-contact measurement devices in open-channel flow and pipe flow.

Daipei Liu

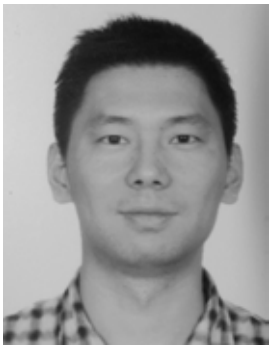

Daipei Liu is a PhD candidate at the School of Mechanical and Manufacturing Engineering at University of New South Wales Australia, Sydney, Australia. After completing his BS in 2006, Daipei worked as a project manager for five years in China. Daipei received his MS at UNSW Australia in 2013. He joined UNSW's vibration and acoustics group and started his PhD study in 2014. His current research focuses on the numerical prediction of surface contributions to far field radiated and scattered sound.

Dario Vignali

Dario Vignali graduated from the University of Southampton in 2011 with his MS in acoustical engineering. While working toward his degree, he took a year out to work as an acoustic consultant undertaking a number of projects dealing with building acoustics. His final thesis focused on signal processing methods with particular attention to biological signals. Currently, he is undertaking a PhD project on modelling cochlear mechanics in the Signal Processing and Controls Group (SPCG) of the Institute of Sound and Vibration Research (ISVR), University of Southampton.

Stanislaw Wrona

Stanislaw Wrona was born in Katowice, Poland, in 1988. He obtained his MS in automatic control and robotics in 2012 from the Silesian University of Technology, Poland, where he is currently a PhD student. He also gained professional experience at universities in the Czech Republic, Spain, and the Netherlands. He is involved in teaching students subjects related to modelling and signal processing, including acoustic signal processing, and bioacoustics. He is a co-author of over a dozen journal and proceeding papers and of three patent applications. He has received awards for his research from the Acoustical Society of the Netherlands, from the Programme Committee of an international conference on control (MMAR), and from a domestic institution for technological development (Technopark). The research he conducts for his PhD dissertation is focused on the reduction of device and machinery noise by controlling the vibration of their casings through mathematical modelling, acoustic signal processing, synthesis, and analysis of active control systems.

Obituary Notice of Geoffrey Lilley, 1919–2015

Geoffrey Lilley who died on 20 September 2015 was born in Isleworth, England, on 16 November 1919. He was the youngest of four children. His father, Micholl Morland Dessau, made his fortune as an American inventor and rubber magnate, but lost it during the Great Depression. Later, his father deserted the family and Lilley took his mother's maiden name as his own.

Lilley attended Isleworth Grammar School, but left in 1934 at the age of 15 hoping to join the Royal Air Force and become a pilot; however, he failed the vision test and instead became an apprentice engineer with Kodak in 1936.

In 1940 Lilley joined Vickers-Armstrongs Limited at Weybridge and Supermarine Aviation, where he worked briefly with Sir Barnes Wallace, inventor of the "bouncing bomb." Lilley continued this work on aircraft design during World War II, in addition serving in the Home Guard in London. He also took evening classes to work toward his bachelor's degree. He subsequently earned his MS from Imperial College, London in 1945. After the war, he worked on the design of wind tunnels, one of which remains in use by British Aerospace.

Lilley became known as one of the founders of aeroacoustics and helped establish the College of Aeronautics at Cranfield in 1946, where he was appointed Professor of Experimental Fluid Mechanics in 1961 because of his work on aircraft. He and Bob Westley carried out the first experiments on jet noise that provided early confirmation of the "eighth power law" of Sir James Lighthill, which states that the acoustic power of a jet engine is proportional to the eighth power of the jet exhaust velocity. Lilley made a crucial extension to Lighthill's theory by improving the description of the separation of sound and its sources inside a flow: the equation known as Lilley's equation considers propagation expressed by linear terms in the turbulent flow fluctuations. The approach is widely used.

In 1963 Lilley was appointed Professor of Aerodynamics and Astronautics at Southampton University the same year that Malcolm Crocker began his master's degree studies at the Institute of Sound and Vibration also at Southampton.

Perhaps Lilley's greatest contribution to aviation was made as leader of the Concorde technical team. When in 1971 the United States cancelled orders for the American supersonic Boeing 2707, and when five years later the US Congress banned Concorde landings because of concern over sonic booms, Lilley and his team worked to counter US technical objections line-by-line and succeeded in persuading the Port Authority of New York that the new Anglo-French supersonic aircraft would meet strict US noise regulations. Had they failed, Concorde would have been discontinued at that time.

Lilley is one of the very few who have flown the Gossamer Condor human-powered aircraft operated solely by pedal power. In his later years he became interested in how owls can fly so silently and how light propagates through the cosmos.

Lilley was awarded an OBE (Order of the British Empire) in 1981 for services to the British government. In 1983 he was awarded the Gold Medal of the Royal Aeronautical Society and the Aeroacoustic Medal of the American Institute of Aeronautics and Astronautics.

After his retirement in 1983, Lilley was appointed to several visiting professorships, and worked for NASA at the institute for Computer Applications in Science and Engineering. He was named an honorary fellow of the International Institute of Acoustics and Vibration in 2009. We shall always remember Lilley's remarkable contributions to aeroacoustics, and in particular jet noise theory.

Active Control Experiment Study of a Flexible Beam with Multiple Time Delays

Chen Long-Xiang and Cai Guo-Ping

Department of Engineering Mechanics, Shanghai Jiaotong University, Shanghai 200240, P.R. China

(Received 25 April 2013; accepted 3 March 2014)

In this paper, active control for vibration of a flexible beam with multiple time delays is studied numerically and experimentally. Piezoelectric (PZT) patches are used as actuators, and foil gauges were used as sensors. Firstly the motion equation of a flexible beam with multiple time delays and Piezoelectric patches is presented and written into a state space form. Then the state equation is discretized and transformed into a standard form without any explicit time delay by a particular augmentation for state variables. So time-delay controller could be designed based on the standard state equation using the discrete active control method. Finally, numerical and experimental studies are presented to verify the validity of the time-delay processing method using the discrete optimal control method and the discrete variable structure control method, respectively. An experimental setup is constructed using DSP TMS320F2812. The numerical and experimental results show that the proposed time-delay controller is effective in suppressing the beam vibration. It is also applicable to both short- and long- time delays.

1. INTRODUCTION

Time delay exists inevitably in active control systems. It may make the actuator input energy into the controlled systems when energy is not needed. This may cause the degradation of control efficiency or even the instability of control systems.[1] Therefore, the research on time delay is of important theoretical significance and practical value.

Generally, the investigations on time delay may be divided into two classes: elimination and utilization technologies. At first, time delay was regarded as a "bad" factor that had only negative side effect on control systems. In order to eliminate or weaken the effect of time delay, some methods were subsequently proposed, including Taylor series expansion, phase shift technique and state pre-estimation.[2–4] These methods can deal effectively with some short time delay problems in control systems, but awkwardly with long ones. Cai and Huang have proposed a new time-delay controller.[5,6] This controller is designed directly from time-delay differential equation without any hypothesis in whole process of controller design, applicable for both short and long time delays. Chen proposed a theoretical method for a flexible beam with multiple time delays using the discrete optimal control.[7] Sun has recently proposed a continuous time approximation method for linear and nonlinear dynamical systems with time delay.[8] The key point of the methods mentioned above to eliminate the negative effect of time delay is so-called time-delay elimination technology or time-delay compensation technology. Its main function is to eliminate or weaken the negative effect of time delay on control efficiency. On the other hands, recent investigations have shown that voluntary introduction of delay into control systems can also benefit the control. For example, in nonlinear dynamics area, achievement is remarkable using time delay to control chaos motion.[9] Daqaq, Alhazza and Arafat studied the effect of feedback delays on the non-linear vibration of a cantilever beam.[10] In structural control area, Hosek and Olgac developed a time-delay resonator that may be used for vibration control of structures.[11] Cavdaroglu and Olgac considered the cart-and-pendulum system as research object, this study shows that systems with multiple delays may exhibit better performance by increasing the delays to more desirable levels.[12] Liu, Haraguchi, and Hu presents a reduction-based linear quadratic control for the dynamic system with a constant or a slowly time-varying input delay.[13] In robotics area, Cai and Lim designed a time-delay controller for a flexible manipulator and their results show that delayed feedback control design may possibly achieve much better control efficiency than the no-delay control design.[14] In control system of pipeline transport, time delay may be utilized to enhance steady critical speed of flowing liquid.[15] Time delay may be also used to improve system stability.[16,17] Those researches above involving the active utilization of time delay is so-called time-delay utilization technology, which assumes time delay as a design parameter to obtain good control performance. Although up to now researches have been done much on the elimination and utilization of time delay, most of work is theoretical one but few on experiment.

In this paper, Piezoelectric (PZT) patches are used as actuators, foil gauges as sensors, active control for vibration of a flexible beam with multiple time delays is studied numerically and experimentally. The controller with time delays is designed using the discrete optimal control method and the discrete variable structure control method, respectively. The feasibility and efficiency of the time-delay controller are verified theoretically and experimentally. This paper is organized

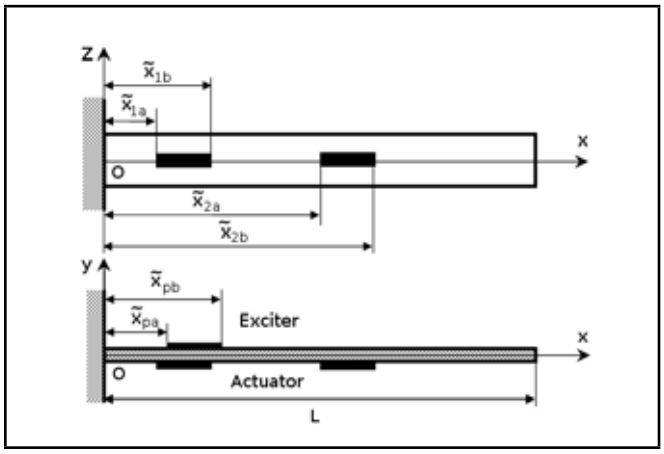

Figure 1. Cantilever beam model and the locations of PZT patches.

as follows. Section 2 presents the motion equation of flexible cantilever beam with time delays. The design of time-delay controller is described in Section 3. Section 4 gives the experimental scheme. The numerical and experimental results are shown in Section 5 in the consideration of the time-delay controller in this paper. Finally, concluding remarks are given in Section 6.

2. MOTION EQUATION

The transverse vibration of a flexible cantilever beam is considered, as shown in Fig. 1. The beam has a constant cross-section area with every center inertia axis being in the same plane, xoy. One PZT patch is used as exciter to initiate beam-forced vibration, and two PZT patches were used for controlling the vibration. The control forces produced by the two PZT actuators have different delays λ_1 and λ_2. Based on the Euler-Bernoulli hypothesis and using modal orthogonality, the i-th modal equation may be deduced as

$$\ddot{\varphi}_i(t) + 2\zeta_i\omega_i\dot{\varphi}_i(t) + \omega_i^2\varphi_i(t) = \sum_{j=1}^{2} K_z[Y'_i(\tilde{x}_{ja}) - Y'_i(\tilde{x}_{jb})]V_j(t-\lambda_j) + K_z[Y'_i(\tilde{x}_{pa}) - Y'_i(\tilde{x}_{pb})]V_p(t); \quad (1)$$

$i = 1, 2, \cdots, \infty$ where $\varphi_i(t)$ is the i-th modal coordinate; ω_i is the natural frequency of the i-th mode; ζ_i is the i-th modal damping ratio; $Y_i(x)$ is the normalized modal shape corresponding to the i-th mode; $\tilde{x}_{ja}$ and $\tilde{x}_{kb}$ are the locations of the j-th PZT actuator on the beam, j = 1, 2; V_j is the applied voltage on the j-th PZT actuator; $\tilde{x}_{pa}$ and $\tilde{x}_{pb}$ are the locations of the PZT exciter; V_p is the applied voltage on the PZT exciter; and K_z is the constant value related to the physics and geometry characteristics of PZT material, may be found in.[7,18]

3. DESIGN OF MULTIPLE TIME-DELAY CONTROLLER

The first two vibration modes are considered to be controlled using the two PZT actuators in this paper. So, the modal equation can be written as

$$\ddot{\mathbf{\Phi}}(t)+\mathbf{C}\dot{\mathbf{\Phi}}(t)+\mathbf{K}\mathbf{\Phi}(t) = \sum_{j=1}^{2}\mathbf{H}_j V_j(t-\lambda_j)+\mathbf{H}_p V_p(t); \quad (2)$$

where $\mathbf{\Phi}(t) = [\varphi_1(t), \varphi_2(t)]^{\mathrm{T}}$,
$\mathbf{C} = diag(2\zeta_1\omega_1, 2\zeta_2\omega_2)$,
$\mathbf{K} = diag(\omega_1^2, \omega_2^2)$,
$\mathbf{H}_j = K_z[Y'_1(\tilde{x}_{ja}) - Y'_1(\tilde{x}_{jb}), Y'_2(\tilde{x}_{ja}) - Y'_2(\tilde{x}_{jb})]^{\mathrm{T}}$, and
$\mathbf{H}_p = K_z[Y'_1(\tilde{x}_{pa}) - Y'_1(\tilde{x}_{pb}), Y'_2(\tilde{x}_{pa}) - Y'_2(\tilde{x}_{pb})]^{\mathrm{T}}$.

In the state-space representation, Eq. (2) becomes

$$\dot{\mathbf{Z}}(t) = \mathbf{A}\mathbf{Z}(t) + \sum_{j=1}^{2}\mathbf{B}_j V_j(t-\lambda_j) + \mathbf{B}_p V_p(t); \quad (3)$$

where $\mathbf{Z}(t) = \begin{bmatrix} \mathbf{\Phi}(t) \\ \dot{\mathbf{\Phi}}(t) \end{bmatrix}$, $\mathbf{A} = \begin{bmatrix} 0 & I \\ -\mathbf{K} & -\mathbf{C} \end{bmatrix}$,
$\mathbf{B}_j = \begin{bmatrix} 0 \\ \mathbf{H}_j \end{bmatrix}$, $\mathbf{B}_p = \begin{bmatrix} 0 \\ \mathbf{H}_p \end{bmatrix}$.

3.1. Discretization and Standard of Multiple Time-Delay Control Equation

Equation (3) is a time-delay differential equation that is inconvenient for control design. Here we consider the discretization and standard of this equation. The time delay λ_j can be written as

$$\lambda_j = l_j\bar{T}; \quad (4)$$

where $\bar{T}$ is data sampling period and $l_j > 1$ is a positive integral number.

Zero-order holder is used in the structure, i.e.

$$V_j(t) = V_j(k), k\bar{T} \leqslant t < (k+1)\bar{T}; \quad (5)$$

where k represents the k-th step of control and $V_j(k)$ denotes $V_j(kT)$. Equation (5) represents that the actuators exert constant control forces on the beam during two adjoining sampling points. This is feasible because data sampling period is usually very small.

Using Eq. (5), Eq. (3) becomes[7,19]

$$\mathbf{Z}(k+1) = \mathbf{F}\mathbf{Z}(k) + \sum_{j=1}^{2}\mathbf{G}_j V_j(k-l_j) + \mathbf{G}_p V_p(k); \quad (6)$$

where $\mathbf{F} = e^{\mathbf{A}\bar{T}}$, $\mathbf{G}_j = \int_0^{\bar{T}} e^{\mathbf{A}\eta}\mathrm{d}\eta\mathbf{B}_j$, $\mathbf{G}_p = \int_0^{\bar{T}} e^{\mathbf{A}\eta}\mathrm{d}\eta\mathbf{B}_p$, and $\mathbf{G}_{11} = \int_0^{\bar{T}} e^{\mathbf{A}\eta}\mathrm{d}\eta$.

Augmenting the state variables in Eq. (6) as

$$\begin{cases} Z_{4+1}(k) = V_1(k-l_1) \\ \vdots \\ Z_{4+l_1}(k) = V_1(k-1) \\ Z_{4+l_1+1}(k) = V_2(k-l_2) \\ \vdots \\ Z_{4+l_1+l_2}(k) = V_2(k-1) \end{cases}; \tag{7}$$

and defining a new state vector as

$$\bar{\mathbf{Z}}(k) = [\ \mathbf{Z}(k), \quad Z_{4+1}(k), \quad \cdots, \quad Z_{4+l_1+l_2}(k)\ ]^{\mathrm{T}}; \tag{8}$$

Thus Eq. (6) can be changed into the following standard discrete form without any explicit time delay:

$$\bar{\mathbf{Z}}(k+1) = \bar{\mathbf{F}}\,\bar{\mathbf{Z}}(k) + \bar{\mathbf{G}}\,\mathbf{V}(k) + \bar{\mathbf{G}}_p V_p(k); \tag{9}$$

where $\mathbf{V}(k) = [V_1(k),\ V_2(k)]^{\mathrm{T}}$,

$$\bar{\mathbf{F}} = \begin{bmatrix} \mathbf{F} & \mathbf{G}_1 & 0 & \cdots & 0 & \mathbf{G}_2 & 0 & \cdots & 0 \\ 0 & 0 & 1 & \cdots & 0 & 0 & 0 & \cdots & 0 \\ \vdots & \vdots & \vdots & \ddots & \vdots & \vdots & \vdots & \cdots & \vdots \\ 0 & 0 & 0 & \cdots & 1 & 0 & 0 & \cdots & 0 \\ 0 & 0 & 0 & \cdots & 0 & 0 & 0 & \cdots & 0 \\ 0 & 0 & 0 & \cdots & 0 & 0 & 1 & \cdots & 0 \\ \vdots & \vdots & \vdots & \cdots & \vdots & \vdots & \vdots & \ddots & \vdots \\ 0 & 0 & 0 & \cdots & 0 & 0 & 0 & \cdots & 1 \\ 0 & 0 & 0 & \cdots & 0 & 0 & 0 & \cdots & 0 \end{bmatrix},$$

$$\bar{\mathbf{G}} = \begin{bmatrix} 0 & 0 \\ 0 & 0 \\ \vdots & \vdots \\ 0 & 0 \\ 1 & 0 \\ 0 & 0 \\ \vdots & \vdots \\ 0 & 0 \\ 0 & 1 \end{bmatrix}, \bar{\mathbf{G}}_p = \begin{bmatrix} \mathbf{G}_p \\ 0 \\ \vdots \\ 0 \\ 0 \\ 0 \\ \vdots \\ 0 \\ 0 \end{bmatrix}.$$

Equation (9) is a standard discrete state equation that contains no time delay. The sufficient condition for stability of Eq. (9) is that all the eigenvalues of $\bar{\mathbf{F}}$ is within a unit circle. The system (9) is controllable provided that the matrix $[\bar{\mathbf{F}}, \bar{\mathbf{G}}]$ is controllable. When the system is controllable, the controllers can be designed. Next, the optimal control method and the variable structure control method will be used to design the controllers. Compared to other controller method, these two controllers can be simply designed. In addition, the optimal control can guarantee optimal control efficiency of systems, and the variable structure control method has strong robustness, and is insensitive for system parameters and external disturbances, and this method has good stability.

3.2. Controller Design using Optimal Control Method

Here we consider the controller design using the classical optimal control strategy. In the optimal controller design, external excitation term is neglected. The following performance index is used:

$$J = \int_0^{\infty} [\mathbf{Z}^{\mathrm{T}}(t)\bar{\mathbf{Q}}_1\mathbf{Z}(t) + \mathbf{V}^{\mathrm{T}}(t)\bar{\mathbf{Q}}_2\mathbf{V}(t)]\,\mathrm{d}t; \tag{10}$$

where $\bar{\mathbf{Q}}_1$ is non-negative definite symmetric matrix and $\bar{\mathbf{Q}}_2$ is positive definite symmetric matrix. The performance index is a continuous form so as to guarantee good response efficiency of systems not only on every sampling point but also between any two adjacent sampling points. However, the discrete performance index can only guarantee good efficiency on every sampling point and surge behavior may possibly exist between sampling points. So the continuous performance index is used as the objective function in this paper. Now the task of control design is to design controller for the system Eq. (3) such that the performance index in Eq. (10) attains minimum. In the above, Eq. (3) has been discretized and changed into the standard discrete form without any explicit time delay. Below the performance index will be discretized and changed to be the function of the augmented state.

Equation (10) may be written as the following discrete form

$$J = \sum_{k=1}^{\infty} J_k, J_k = \int_{k\bar{T}}^{(k+1)\bar{T}} [\mathbf{Z}^{\mathrm{T}}(t)\bar{\mathbf{Q}}_1\mathbf{Z}(t) + \mathbf{V}^{\mathrm{T}}(t)\bar{\mathbf{Q}}_2\mathbf{V}(t)]\,\mathrm{d}t; \tag{11}$$

The performance index in (11) may be rearranged as the following form:[7,19]

$$J = \sum_{k=0}^{\infty} [\bar{\mathbf{Z}}^{\mathrm{T}}(k)\hat{\mathbf{Q}}_1\bar{\mathbf{Z}}(k) + \mathbf{V}^{\mathrm{T}}(k)\hat{\mathbf{Q}}_2\mathbf{V}(k)]; \tag{12}$$

where $\hat{\mathbf{Q}}_1$ and $\hat{\mathbf{Q}}_2$ are given by

$$\hat{\mathbf{Q}}_1 = \begin{bmatrix} \mathbf{Q}_1 & \mathbf{Q}_{01} & 0 & \mathbf{Q}_{02} & 0 \\ \mathbf{Q}_{01}^{\mathrm{T}} & Q_{11} & 0 & Q_{12} & 0 \\ 0 & 0 & 0 & 0 & 0 \\ \mathbf{Q}_{02}^{\mathrm{T}} & Q_{21} & 0 & Q_{22} & 0 \\ 0 & 0 & 0 & 0 & 0 \end{bmatrix}, \hat{\mathbf{Q}}_2 = \mathbf{Q}_2; \tag{13}$$

where

$$\begin{cases} \mathbf{Q}_1 = \int_0^{\bar{T}} \mathbf{F}^{\mathrm{T}}(t)\bar{\mathbf{Q}}_1\mathbf{F}(t)\,\mathrm{d}t, \quad \mathbf{Q}_2 = \bar{\mathbf{Q}}_2\bar{T} \\ \mathbf{Q}_{0i} = [\int_0^{\bar{T}} \mathbf{F}^{\mathrm{T}}(t)\bar{\mathbf{Q}}_1\mathbf{G}_{11}(t)\,\mathrm{d}t]\mathbf{B}_i, \quad i = 1,2 \\ Q_{ij} = \mathbf{B}_i^{\mathrm{T}}[\int_0^{\bar{T}} \mathbf{G}_{11}^{\mathrm{T}}(t)\bar{\mathbf{Q}}_1\mathbf{G}_{11}(t)\,\mathrm{d}t]\mathbf{B}_j, \quad i,j = 1,2 \end{cases}; \tag{14}$$

and where $\mathbf{F}(t) = e^{At}$ and $\mathbf{G}_{11}(t) = \int_0^t e^{A\tau}d\tau$.

Equation (12) is a standard discrete form of performance index. So the next work is to design an optimal controller for the system in (9) by minimizing the objective function given by Eq. (12). This controller may be designed using the discrete optimal control method, given by

$$\begin{aligned}\mathbf{V}(k) &= -\mathbf{L}\bar{\mathbf{Z}}(k)\\ &= -\mathbf{L}_1\mathbf{Z}(k) - \mathbf{L}_2 V_1(k-l_1) - \cdots - \mathbf{L}_{l_1+1}V_1(k-1);\\ &- \mathbf{L}_{l_1+2}V_2(k-l_2)\cdots - \mathbf{L}_{l_1+l_2+1}V_2(k-1)\end{aligned} \tag{15}$$

where $\mathbf{L}_1(i=1,\cdots,l_1+l_2+1)$ are the component matrices of $\mathbf{L}$. We can observe from Eq. (15) that the controller contains not only the current step of state feedback term, but also the linear combination of some former steps of controls. Since the time-delay controller is designed directly from the time-delay differential equation and no approximation or hypothesis involved, it tends to guarantee the stability of control systems, and is suitable for both small time delay and large time delay.

3.3. Controller Design using Variable Structure Method

The variable structure control method is known as the sliding mode control method, where sliding mode is the remarkable characteristics of this control method. The controller can be obtained by using the discrete reaching condition. The phase trajectory of the system will move toward the switching surface in finite time, and then reaching the origin point or the equilibrium position until the system reaches stabilization.

In the variable structure control method, a linear switching function is considered

$$\mathbf{S}(\bar{\mathbf{Z}}) = \mathbf{C}\bar{\mathbf{Z}}; \tag{16}$$

where $\mathbf{C}$ is undetermined coefficient vector of the switching function. $\mathbf{S}(\mathbf{Z}) = \mathbf{C}\mathbf{Z} = \mathbf{0}$ is the linear switching surface.

The discrete approach law is given by[20]

$$\mathbf{S}(k+1) - \mathbf{S}(k) = -\varepsilon\bar{T}\,\mathrm{sgn}[\mathbf{S}(k)] - q\bar{T}\,\mathbf{S}(k); \tag{17}$$

where $\bar{T}$ is the sampling period, $\epsilon > 0$, $q > 0$ and $q\bar{T} < 1$.

From Eqs. (9) and (16), the left-hand term of Eq. (17) can be further written as

$$\mathbf{S}(k+1)-\mathbf{S}(k) = \mathbf{C}[\bar{\mathbf{F}}\,\bar{\mathbf{Z}}(k)+\bar{\mathbf{G}}\,\mathbf{V}(k)+\bar{\mathbf{G}}_p\,\mathbf{V}_p(k)]-\mathbf{C}\bar{\mathbf{Z}}(k); \tag{18}$$

Hence the controller can be obtained from Eqs. (17) and (18) and written as

$$\begin{aligned}\mathbf{V}(k) = [\mathbf{C}\bar{\mathbf{G}}]^{-1}\{&\mathbf{C}(I-\bar{\mathbf{F}}-q\bar{T}\mathbf{I})\bar{\mathbf{Z}}(k)\\ &-\mathbf{C}\,\bar{\mathbf{G}}_p\,\mathbf{V}_p(k) - \varepsilon\bar{T}\,\mathrm{sgn}[\mathbf{C}\bar{\mathbf{Z}}(k)]\}.\end{aligned} \tag{19}$$

The vector $\mathbf{C}$ of the switching surface can be obtained using the pole assignment method or the optimal control method. When the optimal control method is used, the task is to design $\mathbf{C}$ by minimizing the objective function $\mathbf{J} = \sum_{k=0}^{\infty}[\bar{\mathbf{Z}}^{\mathrm{T}}(k)\tilde{\mathbf{Q}}\bar{\mathbf{Z}}(k)]$, where $\tilde{\mathbf{Q}}$ is a non-negative definite symmetric matrix. Similarly, the time-delay controller is designed directly from the time-delay differential equation and no approximation or hypothesis is involved, it tends to guarantee the stability of control systems, and is suitable for both small time delay and large time delay.

4. EXPERIMENT AND DATA PROCESSING

The feasibility and effectiveness of the proposed time-delay controller had been proven by simulation results.[9] In this paper, PZT patches are used as actuators, foil gauges were used as sensors, experiments are presented based on a digital signal processing (DSP) board. Firstly, an experimental setup using the DSP board is introduced. Subsequently, the measurement methods for signal and signal difference are presented.

4.1. Experiment System

In the experiment, two PZT patches are used as actuators, one PZT patch as a vibration exciter, and two foil gauges as sensors. The control mechanism of free and forced beam vibration are considered. For free vibration, the free end of beam has an initial displacement 0.04 m while the initial velocity is zero. For forced vibration, the PZT vibration exciter initiates beam vibration.

An experimental setup is constructed using DSP board (TMS320F2812). DSP deals with online computation of controllers in terms of the feedback signal from the foil gauge to obtain PZT voltage. Fig. 2 shows an experimental flow chart for forced vibration. For free vibration, the signal generator and PZT exciter in Fig. 2 are not in use. The details of signal flow and process are described as follows:

1. Excitation Loop: the signal generator generates an external excitation that is amplified by the PZT power amplifier and then goes into the PZT exciter. The flow chart of excitation loop is shown by the dashed line in Fig. 2.

2. Feedback Signal Loop: the signal collected from the foil gauge is amplified by a strain signal amplifier and then enters the analog digital converter (ADC) module in DSP.

3. Control Signal Loop: the voltage signal goes through the two channels of digital analog converter DAC module into the PZT power amplifier where it is amplified, and then channels into the two PZT actuators.

4. The DSP communicates with a computer via the serial communication interface (SCI) module which transfers the experimental data to the computer for storage and for post-processing.

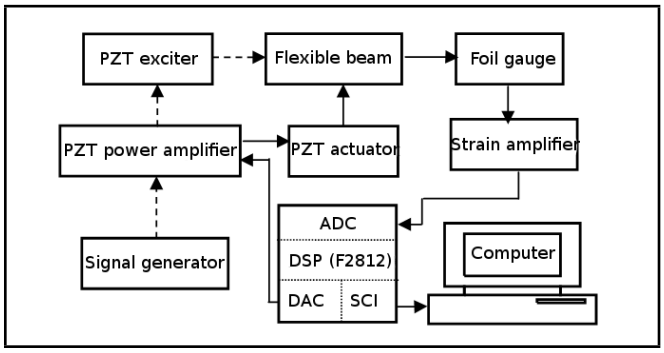

Figure 2. Flow chart of experiment system.

4.2. Signal Measurement

The controller described in Section 3 depends on the beam modal coordinate. Hence, a method to extract modal coordinate from the physical sensor measurements of foil gauges needs to be developed. In addition, the beam tip responses from foil gauge measurements with and without control will be compared to determine the efficiency. The methods required are introduced as follows.

The beam strain-curvature relationship can be expressed as

$$\varepsilon(x,t) = \frac{t_b}{2} y''(x,t); \tag{20}$$

where ϵ, t_b and y are the bending strain, thickness and beam transverse displacement, respectively. As mentioned, two foil gauges are used as sensors in the experiment. Since the first vibration mode has maximum strain at its fixed end while that of the second mode near the middle of beam, the two foil gauges are placed at these two positions at $x_1 = 37$ mm and $x_2 = 476$ mm , respectively. To extract the modal coordinate, the assumed mode method is applied where the beam response can be represented as $y(x,t) = \sum_{i=1}^{\infty} Y_i(x)\varphi_i(t)$ Because the beam response is dominated by its lower-order vibration modes, $y(x,t) \approx \sum_{i=1}^{2} Y_i(x)\varphi_i(t)$ is adopted in this paper. We can obtain the dominant modes by the modal cost analysis method to other geometries.[21] Using Eq. (20), the estimated modal displacement can be deduced as in Eq. (21)

After obtaining the modal displacement, the modal velocity can be determined using the tracking-differentiator given in Section 4.3. From modal coordinate thus obtained, the controlling system can be calculated.

Subsequently, the strain measurements from the two foil gauges can be transformed into the transverse displacement of the beam by Eq. (22) Taking $x = L$ in Eq. (22), where L is the length, the beam tip response can be approximately from Eq. (21).

4.3. Signal Difference

The states for an active controller system, i.e. displacement and velocity, are required in the feedback control. Because the velocity signal (also called the differential signal) cannot be measured directly from sensors in practice, it should be estimated from the physical measurements, and then be used to calculate the control forces. In an early attempt, it was found that the foil gauge signal may contain high-frequency noise due to mechanism and electricity disturbances; hence, the differential signal derived from the classical interpolation method is disorganized. As a result, the tracking differentiator is adopted and it is able quickly tracking the input signal and giving out high-quality differential signal. The tracking differentiator in discrete form is[22]

$$\begin{cases} \bar{x}_1(k+1) = \bar{x}_1(k) + \bar{T}\bar{x}_2(k) \\ \bar{x}_2(k+1) = \bar{x}_2(k) + \bar{T} fst(\bar{x}_1(k), \bar{x}_2(k), u(k), \bar{r}, \bar{h}) \end{cases}; \tag{23}$$

where $u(k)$ is the input signal at the moment k, $\bar{x}_1$ is the tracking signal of $u(k)$, $\bar{x}_2$ is the estimated differential signal of $\bar{x}_1$, $\bar{T}$ is the sampling period, $\bar{r}$ is a parameter determining the tracking speed, and $\bar{h}$ is a parameter determining the filter effect when the input signal is polluted by noise. The variable fst is given in Reference.[22]

5. NUMERICAL SIMULATIONS AND EXPERIMENTAL STUDIES

A beam made of aluminum alloy is used in the experiment shown in Fig. 3. The length, width and thickness are 900 mm, 35 mm, and 1.50 mm, respectively. Material properties of the beam are as follows: Young's elastic modulus $E_p = 69$ GPa, Poisson's ratio $v_p = 0.3$ and density $\rho_p = 2.7 \times 10^3$ kg/m^3. The first two natural frequencies of the beam determined from the experiment are 1.4947 Hz and 9.3679 Hz, respectively, and the corresponding modal damping ratios are 0.012 and 0.0055.

In the experiment, one PZT patch is used as an exciter to initiate beam vibration and the other two PZT patches are used as actuators to control vibration. The PZT patches have identical sizes, 60 mm × 15 mm × 0.5 mm. The PZT exciter is placed near the root of beam at $\tilde{x}_{pa} = 77$ mm and $\tilde{x}_{pb} = 137$ mm. One PZT actuator (denoted as Actuator I) was attached to the other side of the beam at $\tilde{x}_{1a} = 82$ mm and $\tilde{x}_{1b} = 142$ mm. The time delay of Actuator I is denoted by λ_1 . Another PZT actuator (denoted as Actuator II) was attached near the beam midpoint at $\tilde{x}_{2a} = 375$ mm and $\tilde{x}_{2b} = 435$ mm, and the time delay is denoted by λ_2 (see Fig. 1). The PZT material parameters are: Young's modulus 63 GPa, Poisson's ratio 0.35 and piezoelectric strain constants 1.75×10^{-10} m/V. For the differentiator, $\bar{r} = 1000$ and $\bar{h} = 0.008$ are taken.

The inherent delays in the system may have small effect on control efficiency and can be ignored in control design. From Fig. 4, we can see that the beam vibration can be effectively suppressed when the inherent delays in the system are not considered. So, the experiment system used in this paper may be regarded as a non-time-delay control system. We think that just under this condition, the effect of time delay on control systems and the effectiveness of delayed feedback control method may possibly be studied. The time delay used in the experimental studies of this paper is voluntarily introduced in the

$$\begin{bmatrix} \varphi_1(t) \\ \varphi_2(t) \end{bmatrix} = \frac{2}{t_b} \begin{bmatrix} Y''_1(x_1) & Y''_2(x_1) \\ Y''_1(x_2) & Y''_2(x_2) \end{bmatrix}^{-1} \begin{bmatrix} \varepsilon(x_1,t) \\ \varepsilon(x_2,t) \end{bmatrix}; \tag{21}$$

$$y(x,t) = \frac{2}{t_b} \begin{bmatrix} Y_1(x) & Y_2(x) \end{bmatrix} \begin{bmatrix} Y''_1(x_1) & Y''_2(x_1) \\ Y''_1(x_2) & Y''_2(x_2) \end{bmatrix}^{-1} \begin{bmatrix} \varepsilon(x_1,t) \\ \varepsilon(x_2,t) \end{bmatrix}; \tag{22}$$

Figure 3. Photo of experiment beam.

control system by means of adding arbitrary delayed times to control input.

5.1. Results of Forced Vibration Case

The forced vibration control is investigated in this section. In the experiment, the signal generator generates a sine voltage signal with frequency 1.524 Hz and amplitude 5 V. The sine signal is amplified fifteen times by the PZT power amplifier and it then goes into the PZT exciter in order to introduce beam forced vibration. The two PZT actuators are used for controlling the vibration. The optimal control strategy is applied as control. From Eq. (10), large $\bar{\mathbf{Q}}_1$ means that the corresponding state will be quickly suppressed and large $\bar{\mathbf{Q}}_2$ will penalize the control inputs. So increasing $\bar{\mathbf{Q}}_1$ or decreasing $\bar{\mathbf{Q}}_2$ within the capacity of the actuator, the better control effect will be obtained. In the controller design, the weighting matrices in Eq. (10) are chosen as $\bar{\mathbf{Q}}_1 = diag[100, 100, 1, 1]$ and $\bar{\mathbf{Q}}_2 = diag[4 \times 10^{-6}, 4 \times 10^{-6}]$ because the electrical field intensity keeps linear relationship with the strain of PZT only when external electrical field intensity does not exceed 150 V.

The no-delay controller design is applied to control the system without time delay. The beam tip responses and the PZT applied voltage are shown in Fig. 4. The dotted line refers to the results with no control while the solid line refers to the results with control. Fig. 4a are the simulation results, and Fig. 4b are the experimental ones. As observed in Fig. 4b1, the maximum amplitude without control is 0.0262 m and that with control is 0.0108 m. The beam vibration could be effectively suppressed.

The time-delay controller is subsequently investigated here. Two cases are considered: one with a short time delay ($\lambda_1 = 0.05$s, $\lambda_2 = 0.04$s), and another with a long time delay ($\lambda_1 = 0.2$s, $\lambda_2 = 0.1$s). A time-delay controller can be designed with reference to the method described in Section 3.2. The results using a time-delay controller for controlling beam vibration are shown in Figs. 5 and 6, where the dotted line donates the results without control, and the solid line donates the results with control. Figs. 5b1 and 6b1 show that the amplitudes with control are 0.0112 m, 0.013 m, respectively. We can observe that the beam vibration can be suppressed effectively by the time-delay controller, and the proposed time-delay controller is also applicable to short and long time delays.

5.2. Results of Free Vibration Case

Further examples for the control of beam free vibration are presented here to demonstrate the effectiveness of the proposed time-delay controller. An external force is applied to create an initial displacement 0.04 m with zero initial velocity at the free end of the beam. With such conditions, Actuators I and II are used to control the free vibration. A control strategy based on the variable structure control method is used. In the controller design, $\epsilon = 0.01$ and $q = 10$ are chosen in Eq. (19). $\tilde{\mathbf{Q}}$ is chosen as $\tilde{\mathbf{Q}}(1,1) = 100$, $\tilde{\mathbf{Q}}(2,2) = 100$, $\tilde{\mathbf{Q}}(4+l_1, 4+l_1) = 5 \times 10^{-7}$, $\tilde{\mathbf{Q}}(4+l_1+l_2, 4+l_1+l_2) = 5 \times 10^{-7}$ with other elements being zero.

A short time delay ($\lambda_1 = 0.05$s, $\lambda_2 = 0.08$s) and a long time delay ($\lambda_1 = 0.2$s, $\lambda_2 = 0.3$s) are considered. A time-delay controller is designed using the method described in Section 3.3. Numerical and experimental results are shown in Figs. 7 and 8 where the dotted line donates the results without control, and the solid line donates the result with control. From Figs. 7b1 and 8b1, the logarithmic decay ratios of the first period are 0.0179 and 0.0145, respectively. As observed in Figs. 7 and 8, the time-delay controller is able to control the beam vibration effectively and the experiment results agree better with respect to simulation.

6. CONCLUSION

In this paper, delayed feedback control for vibration of a flexible beam is studied numerically and experimentally. Time-delay controllers are proposed to suppress the beam vibration. The discrete optimal control method and the discrete variable structure control method are used for designing the controllers. An experiment system based on a DSP board is introduced. The numerical and experimental results show that the proposed time-delay processing method is effective in suppressing beam vibration. It is applicable to any time delays.

ACKNOWLEDGEMENTS

This work was supported by the Natural Science Foundation of China (11002087, 11272202), the Specialized Research Fund for the Doctoral Program of Higher Education of China (20110073110008), and the Key Scientific Project of Shanghai Municipal Education Commission (14ZZ021). should be revised to This work was supported by the Natural Science Foundation of China (11132001, 11272202 and 11472171), the Specialized Research Fund for the Doctoral Program of Higher Education of China (20110073110008), the Key Scientific Project of Shanghai Municipal Education Commission (14ZZ021), and the Natural Science Foundation of Shanghai (14ZR1421000).

REFERENCES

[1] Hu, H. Y. and Wang, Z. H. Dynamics of Controlled Mechanical Systems with Delayed Feedback, Springer-Verlag, Berlin, (2002).

[2] Abdel-Rohman, M. Time-delay effects on active damped structures, *J. Eng. Mech.*, **113**(11), 1709–1719, (1987).

[3] Chung, L. L., Reinhorn, A. M., and Soong, T. T. Experiments on active control of seismic structures, *J. Eng. Mech.*, **114**(2), 241–256, (1988).

[4] McGreery, S., Soong, T. T., and Reinhorn, A. M. An experiments study of time delay compensation in active structural control, *Proc. Sixth International Modal Analysis Conference, SEM*, 1733–1739, (1988).

[5] Cai, G. P. and Huang, J. Z. Optimal control method for seismically excited building structures with time-delay in control, J. Eng. Mech., 128 (6), 602612, (2002).

[6] Cai, G. P., Huang, J. Z., and Yang, S. X. An optimal control method for linear systems with time delay, *Comput. Struct.*, **81**(15), 1539–1546, (2003).

[7] Chen, L. X. and Cai, G. P. Optimal control of a flexible beam with multiple time delays, *J. Vib. Control.*, **15**(10), 1493–1512, (2009).

[8] Sun, J. Q. A method of continuous time approximation of delayed dynamical systems, *Commun. Nonlinear. Sci.*, **14**(4), 998–1007, (2009).

[9] Xu, J. and Chung, K. W. Effects of time delayed position feedback on a van der Pol-Duffing oscillator, *Phys. D*, **180**(1), 17–39, (2003).

[10] Daqaq, M., Alhazza, K., and Arafat, H. Non-linear vibrations of cantilever beams with feedback delays, *Int. J. Nonlin. Mech.*, **43**(9), 962–978, (2008)

[11] Hosek, M. and Olgac, N. A single-step automatic tuning algorithm for the delayed resonator vibration absorber, *IEEE/ASME Trans. Mechatron*, **7**(2), 245–255, (2002).

[12] Cavdaroglu, M. E. and Olgac, N. Full-state feedback controller design with delay scheduling for cart-and-pendulum dynamics, *Mechatronics*, **21**(1), 38–47, (2011).

[13] Liu, B., Haraguchi, M., and Hu, H. Y. A new reduction-based LQ control for dynamic systems with a slowly time-varying delay, *Acta Mech. Sin.*, **25**(4), 529–537, (2009).

[14] Cai, G. P. and Lim, C. W. Optimal tracking control of flexible hub-beam system with time delay, *Multibody Syst. Dyn.*, **16**(4), 331–350, (2006).

[15] Yuan, F. Effects of delayed feedback control on stability in the cantilever pipe conveying fluid, *Master Thesis*, Tongji University, China, (2008). (in Chinese)

[16] Wang, Z. H. and Hu, H. Y. Stabilization of vibration systems via delayed state difference feedback, *J. Sound Vib.*, **296**(1–2), 117–129, (2006).

[17] Xu, J., Chung, K. W., and Chan, C. L. An efficient method for studying weak resonant double Hopf bifurcation in nonlinear systems with delayed feedbacks, *SIAM J. Appl. Dyn. Syst.*, **6**(1), 29–60, (2007).

[18] Crawley, E. F. and Anderson, E. H. Detailed models of piezoceramic actuation of beams, *J. Intel. Mat. Syst. Str.*, **1**(1), 4–25, (1990).

[19] Sun, Z. Q. *Theory and Application of Computer Control*, Tsinghua University Press, Beijing, (1989). (in Chinese)

[20] Gao, W. B. *Theory and Design Method of the Variable Structure Control*, Science Press, Beijing, (1996). (in Chinese)

[21] Zhang, M. and Cai, G. P. Modal cost reduction and active control of a flexible plate. *J. Dyn. Control*, **6**(4), 348–352, (2008). (in Chinese)

[22] Han, J. Q. and Yuan, L. L. The discrete form of tracking-differentiator, *J. Syst. Sci. Math. Sci.*, **19**(3), 268–273, (1999). (in Chinese)

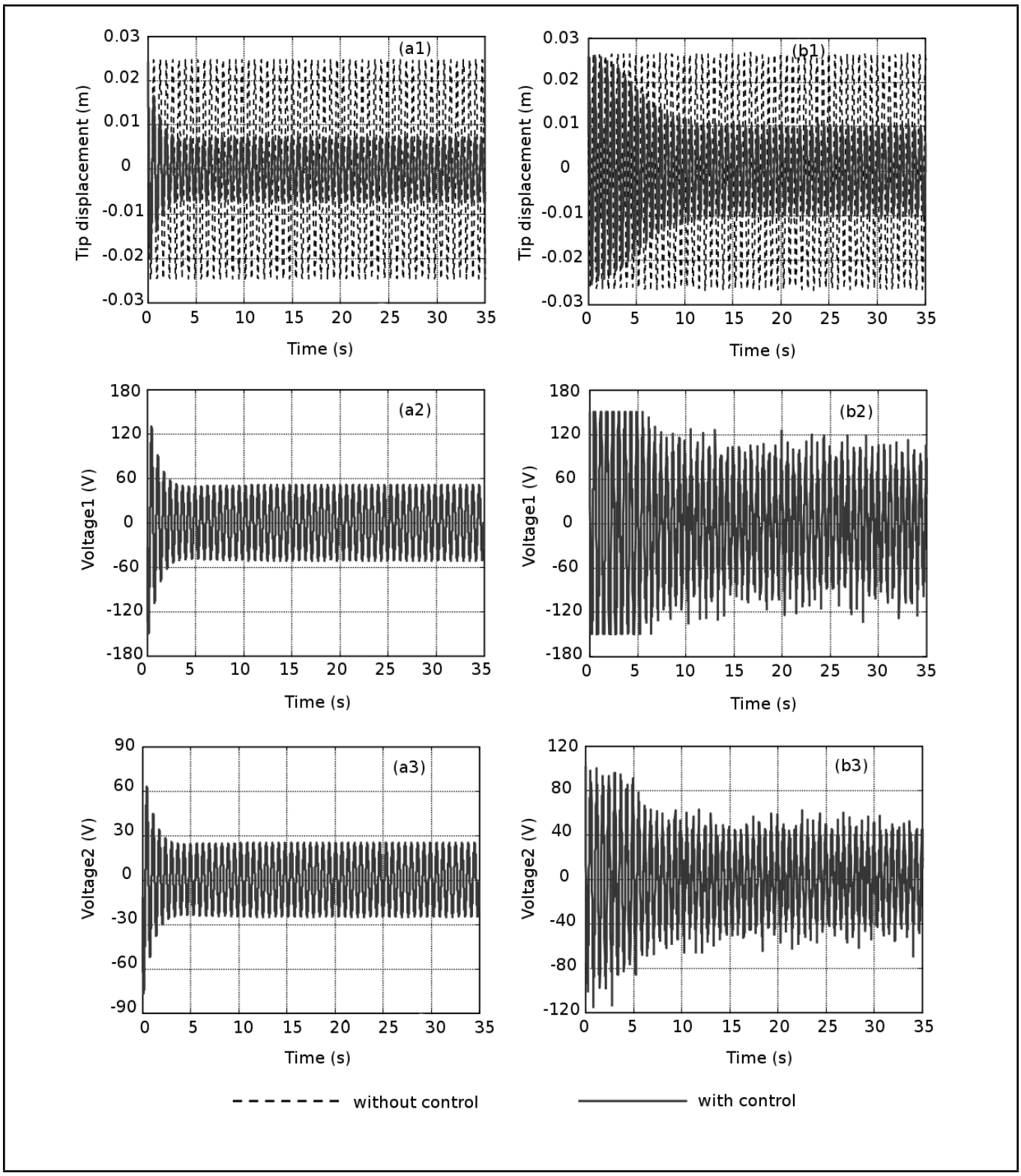

Figure 4. Tip response of the beam and applied voltages on the two actuators (without time delay; optimal controller): (a) simulation result, (b) experimental result.

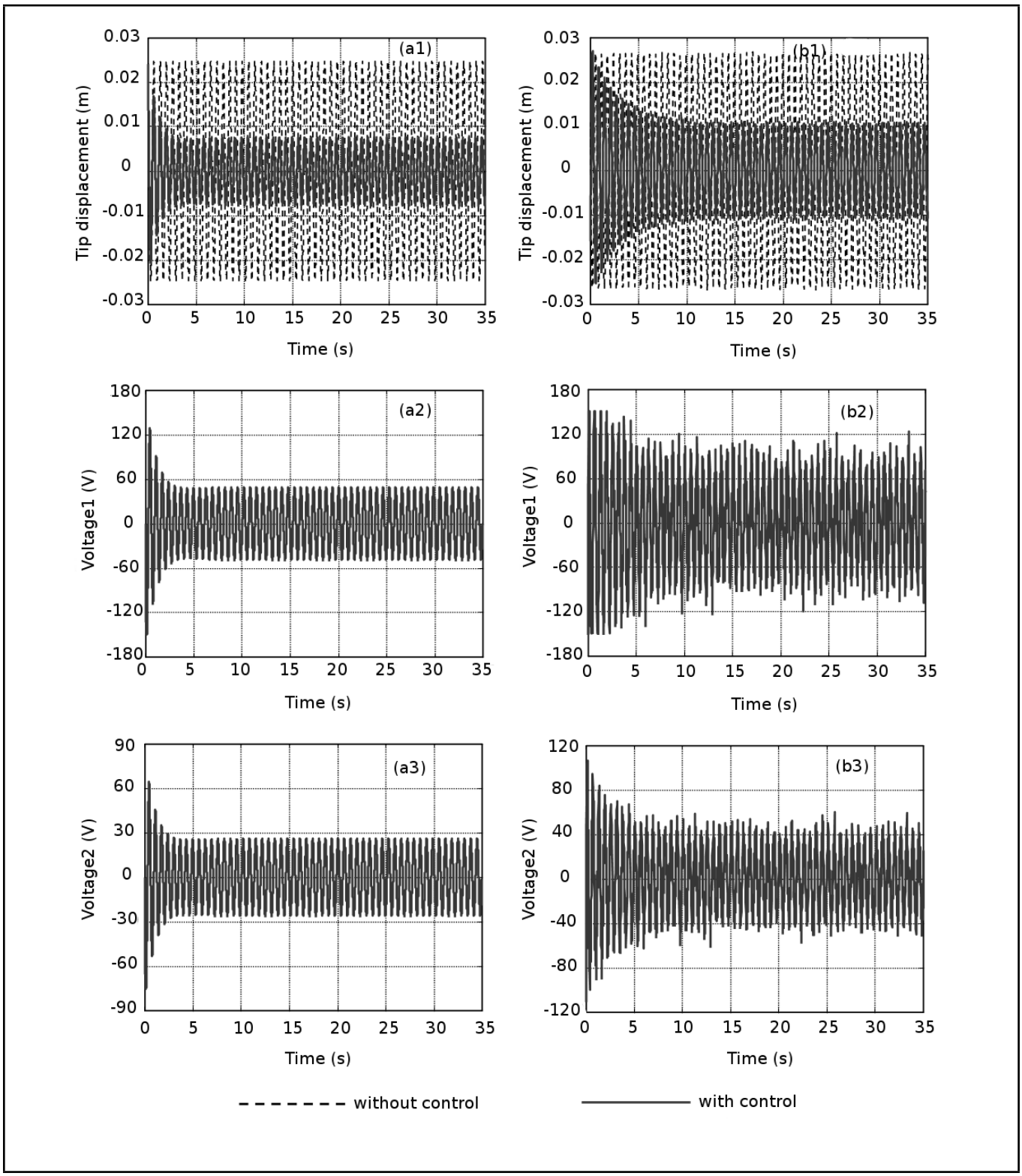

Figure 5. Tip response of the beam and applied voltages on the two actuators ($\lambda_1 = 0.05$ s, $\lambda_2 = 0.04$ s; time-delay optimal controller): (a) simulation result, (b) experimental result.

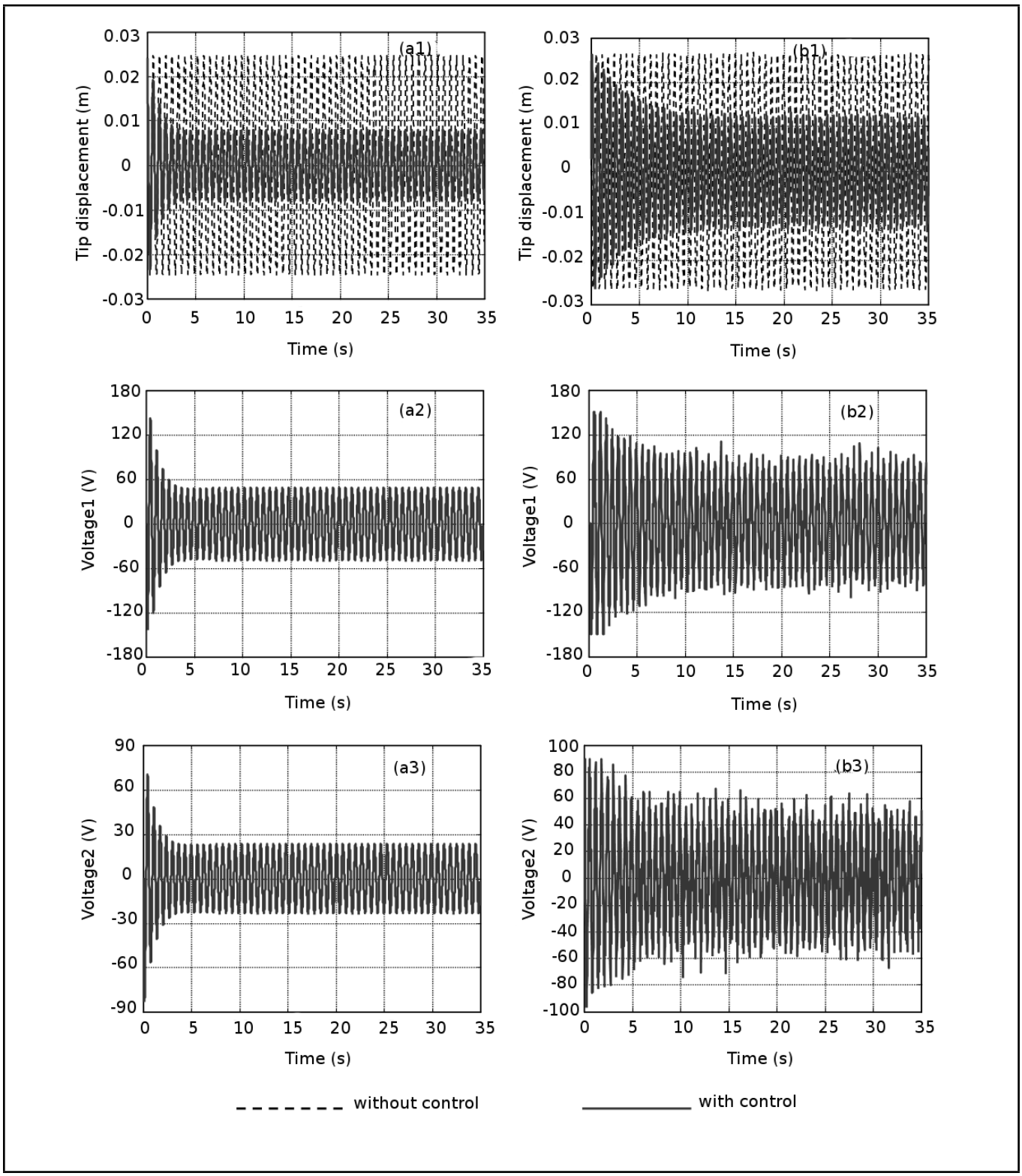

Figure 6. Tip response of the beam and applied voltages on the two actuators ($\lambda_1 = 0.2$ s, $\lambda_2 = 0.1$ s; time-delay optimal controller): (a) simulation result, (b) experimental result.

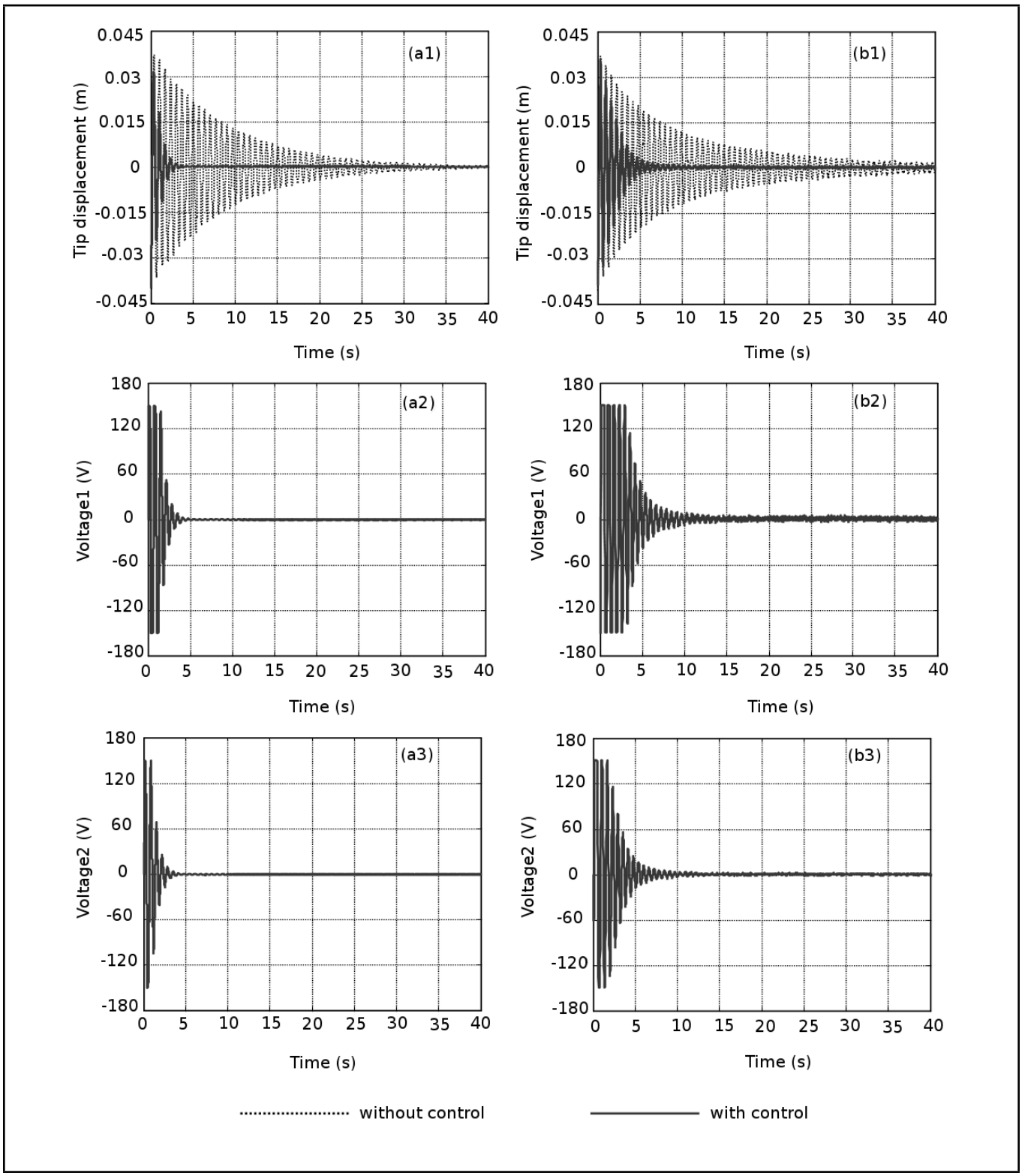

Figure 7. Tip response of the beam and applied voltages on the two actuators ($\lambda_1 = 0.05$ s, $\lambda_2 = 0.08$ s; time-delay variable structure controller): (a) simulation result, (b) experimental result.

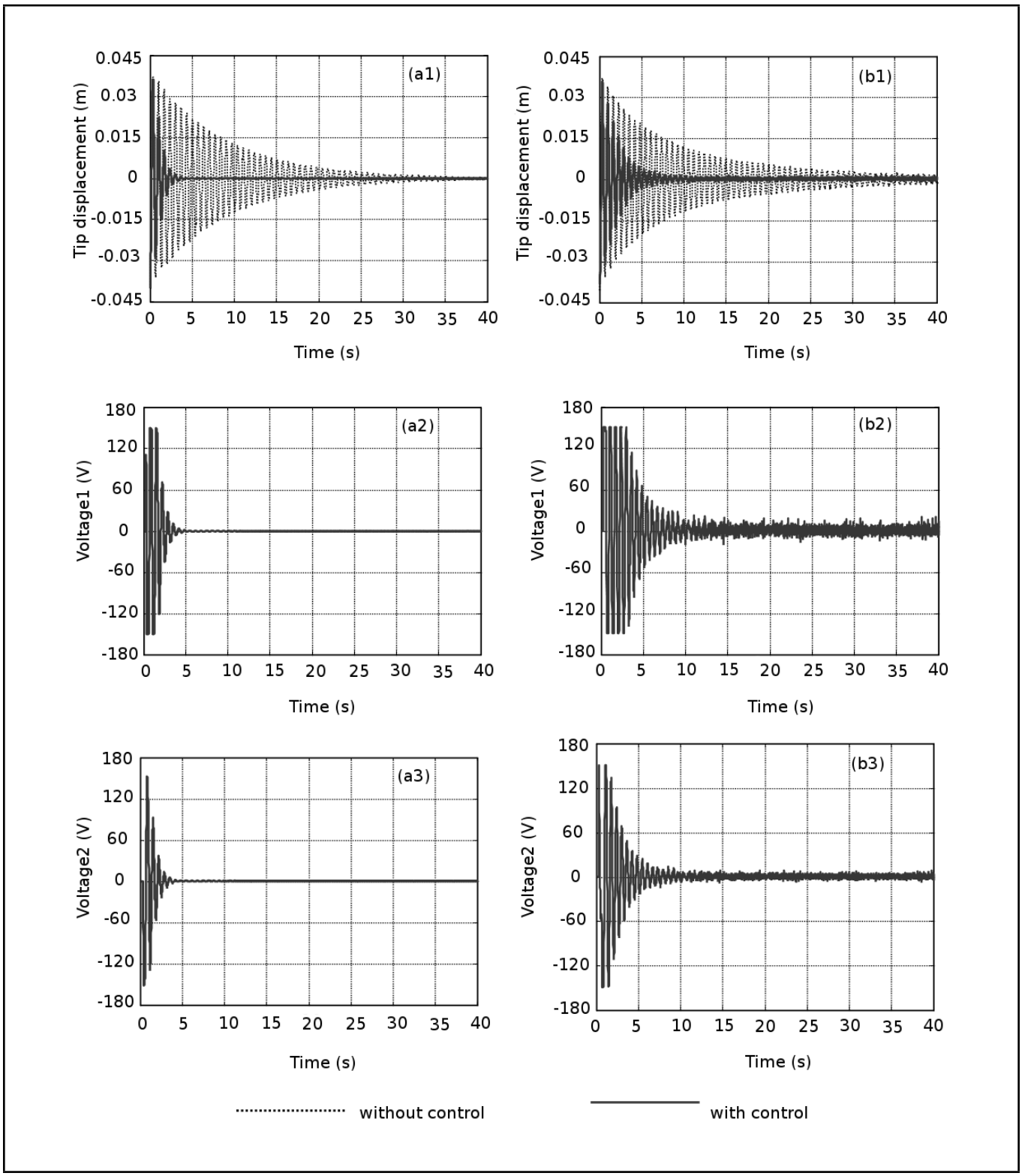

Figure 8. Tip response of the beam and applied voltages on the two actuators ($\lambda_1 = 0.2$ s, $\lambda_2 = 0.3$ s; time-delay variable structure controller): (a) simulation result, (b) experimental result.

Simulation of the Hysteresis Model for the MR Fluid Damper Using a Hybrid Evolutionary Algorithm

Xue Xiaomin

Department of Civil Engineering, Xi'an Jiaotong University, Xi'an, China

Wu Xiaohong

School of Aerospace, Xi'an Jiaotong University, Xi'an, China

Sun Qing

Department of Civil Engineering, Xi'an Jiaotong University, Xi'an, China

Zhang Ling

School of Aerospace, Xi'an Jiaotong University, Xi'an, China

(Received 18 July 2013; accepted 14 May 2014)

The developed MF dampers can be used for diverse applications, including structural vibration mitigation, shock absorption, and vibration control in various systems. This paper has firstly investigated the mechanical characteristics of the self-made MR damper through experimentation. Based on the test data, the damper is found to possess nonlinear hysteresis. Usually, various models, especially the Bouc-Wen model, are proposed to interpret the complex characteristics which have the capability to capture behavior of a wide class of hysteretic systems. However, the Bouc-Wen model consists of a set of multi-unknown parameters that need to be estimated simultaneously. It is a burdensome task to effectively identify the exact values of the parameters. In view of this, this paper proposes a novel hybrid evolutionary algorithm combining Genetic Algorithm with Particle Swarm Optimization (GA-PSO). By using the GA-PSO, the optimized result would be more effective and accurate than the traditional one, because it overcomes the drawbacks of low-speed convergence in GA and local optimization in PSO. Finally it is verified through a large amount of experimental data, which can estimate the multi parameters in the Bouc-Wen model efficiently and precisely. Also suggested are the implications of the present study on other nonlinear hysteretic models or other complex mathematical models.

1. INTRODUCTION

Hysteresis is a memory-dependent, non-linear behavior in which the system output is not only dependent on the instantaneous input, but also on the past history of the input.[1,2] This type of inelastic behavior is encountered in many engineering fields, such as biology, electronics, ferroelectricity, mechanics, magnetism, etc. For efficient description of such inelastic systems, over the past years many mathematical models have been proposed for use in practical applications involving characterization of systems, identification or control.[3] The Bouc-Wen model[4] is widely used to describe systems with hysteresis and non-linear behavior, especially in civil and mechanical engineering. In this model, restoring force is related to the system viscous deformation through a first-order differential equation, which has a series of undefined parameters. By assigning proper values to these parameters, the response of the model will be in keeping with the actual behavior of hysteretic systems. Thus, it is pivotal to select an appropriate optimization algorithm to perform the task of parameter identification.

Recently, optimization techniques have been most widely applied to estimate the parameters of the Bouc-Wen model that characterize hysteretic behavior, such as Gauss-Newton and modified Gauss-Newton,[5] Levenberg-Marquardt,[6,7] Genetic Algorithms,[4,8] Particle Swarm Optimization,[9,10] etc. Traditional techniques (Gauss-Newton and Levenberg-Marquardt, etc.) are adequate to identify favorable parameters in the case of simple problems, since a good initial value can be easily obtained based on previous information. With regard to complex problems, favorable parameters cannot be identified with ease by local search algorithms due to the difficulties of setting the initial value.[8] As a result, parameter identification techniques based on intelligent algorithms are arousing more interest in modeling and parameter identification. For example, Genetic Algorithm (GA) and Particle Swarm Optimization (PSO) have robust features and are suitable for solving multi-objective problems. However, these methods also have their limitations. GA generally requires a large number of function evaluations whose convergence speed is quite slow because the evolution of solutions depends on evolutionary operators.[11] According to this situation, Liu focuses on the problem of premature convergence in GA, and proposes an adaptive GA based on population diversity.[10] Chang proposes an improved real-coded GA for parameter estimation of nonlinear systems to directly implement the programming operations.[12] Aine states that parameters of evolutionary algorithms should be appropriately

controlled for implementing an effective search, and a concept of dominance among control parameter vectors should be developed to show how it can be effectively used to reduce the storage.[13] In contrast to GA, PSO was reported to show better results in terms of computational time and cost,[12] but the problem of premature convergence is serious due to the lack of diversity where multiple objective function is concerned.[14] It is also sensitive to control parameter choices, especially the inertia weight, acceleration coefficients and velocity clamping. Incorrect initialization of these parameters may easily lead to divergence of cyclic behavior.[15]

In order to perfect the performance of intelligent algorithms, there have been some new ideas focusing on the hybrid PSO algorithm by adding GAs.[11,14,16] Simulations for a series of benchmark test functions show that the proposed method possesses better ability to find the global optimum with a relative high efficiency.[17] In this paper, a hybrid evolutionary algorithm combining the GA with PSO is proposed, called GA-PSO. In the GA-PSO, the part GA is improved by using an elitism strategy, and the part PSO is executed by an adaptive inertia weighting factor. At the same time, the GA-PSO is designed with an adaptive termination criteria. After these improvements are made, the proposed algorithm will achieve more accurate solutions with higher computational efficiency than traditional ones. In order to testify that the method is superior, we applied it to one classic multi-variate and multi-extremum function (*Shubert function*) to search for the minimum solution. Through comparing the results of the novel method with the Standard GA, it is found that the proposed approach is capable of much more accuracy and efficiency. In addition, parameter estimation of the Bouc-Wen model with noisy data is also considered, and its results are used to verify that the proposed approach is prominently robust and reliable. Finally, a large amount of experimental data of real MR damper is utilized to further validate the GA-PSO with satisfactory parameter estimation results and highly efficient computational capability.

This paper proposes a new promising identification method for highly nonlinear hysteretic systems described by using the Bouc-Wen model through adapting a novel hybrid evolutionary algorithm (GA-PSO). The paper is organized as follows: Section 2 introduces the self-made MR fluid damper and investigates its hysteretic behavior through experiment. Next, the Bouc-Wen model of the MR fluid damper and its parameter identification is introduced in section 3. In order to implement parameter identification effectively, a novel hybrid evolutionary algorithm is designed and proposed in Section 4. Section 5 discusses the efficiency and accuracy of the proposed approach. Finally, concluding remarks are given in Section 6.

2. MR FLUID DAMPER

The MR fluid damper is an ideal candidate in semi-active control for civil engineering structures. As is revealed by the introduction, the MR fluid damper has complex and dynamic mechanical characteristics. In this section, an experimental prototype of the MR fluid damper is designed and performed to obtain the necessary data for further study on modeling the hysteretic behavior using an appropriate algorithm.

(a) Cross section of MR damper.

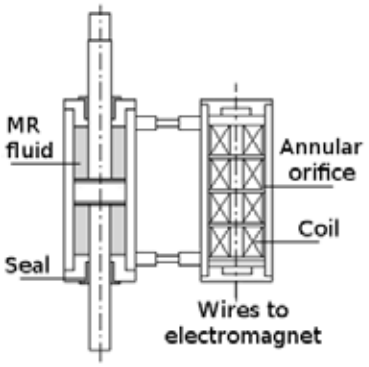

(b) Experimental setup of MR damper performed by MTS.

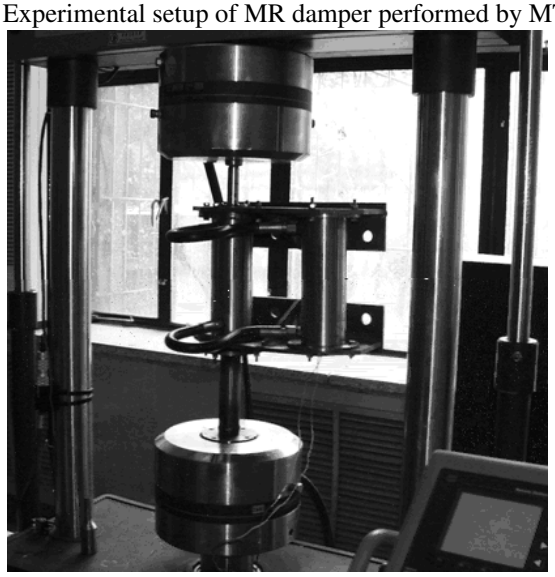

Figure 1. MR damper test setup.

2.1. Design of the MR Fluid Damper

As is shown in Fig. 1, a self-made MR fluid damper is performed by the Material Test System (MTS) at *State Key Laboratory for Strength and Vibration of Mechanical Structures in China*. We can see the schematic representation of the cylindrical type of MR damper in Fig. 1a. The MR fluid is housed within two cylinders: one is installed within the piston device, and the other is installed within electromagnets and coils. Within the piston device cylinder, the piston of the MR damper is driven by a two-way pusher-pull bar. When the magnetic field changes, the mechanical behavior of MR damper can be changed. As is exhibited in Fig. 1b, the actual damper is driven by a mechanical driver, and the generated force is measured by a force sensor.

2.2. Hysteresis Behavior of the MR Fluid Damper

By using the setup in Fig. 1, a series of preliminary tests are conducted to measure the response of the damper under various loading conditions. Fig. 2a displays partial cases of the damper's responses under 0.5 Hz and 2.0 Hz sinusoid excitation with the amplitude range fluctuating gradually from zero to ± 10 mm, and the magnetic field varies as measured by the currents of 2.0 A.

It should be noted that the displacement-force curves are basically akin to ellipticals, suggesting that the relationship be-

(a) Case of 2.0 A Current intensity and 0.5 Hz Frequency with 10 mm displacement amplitude.

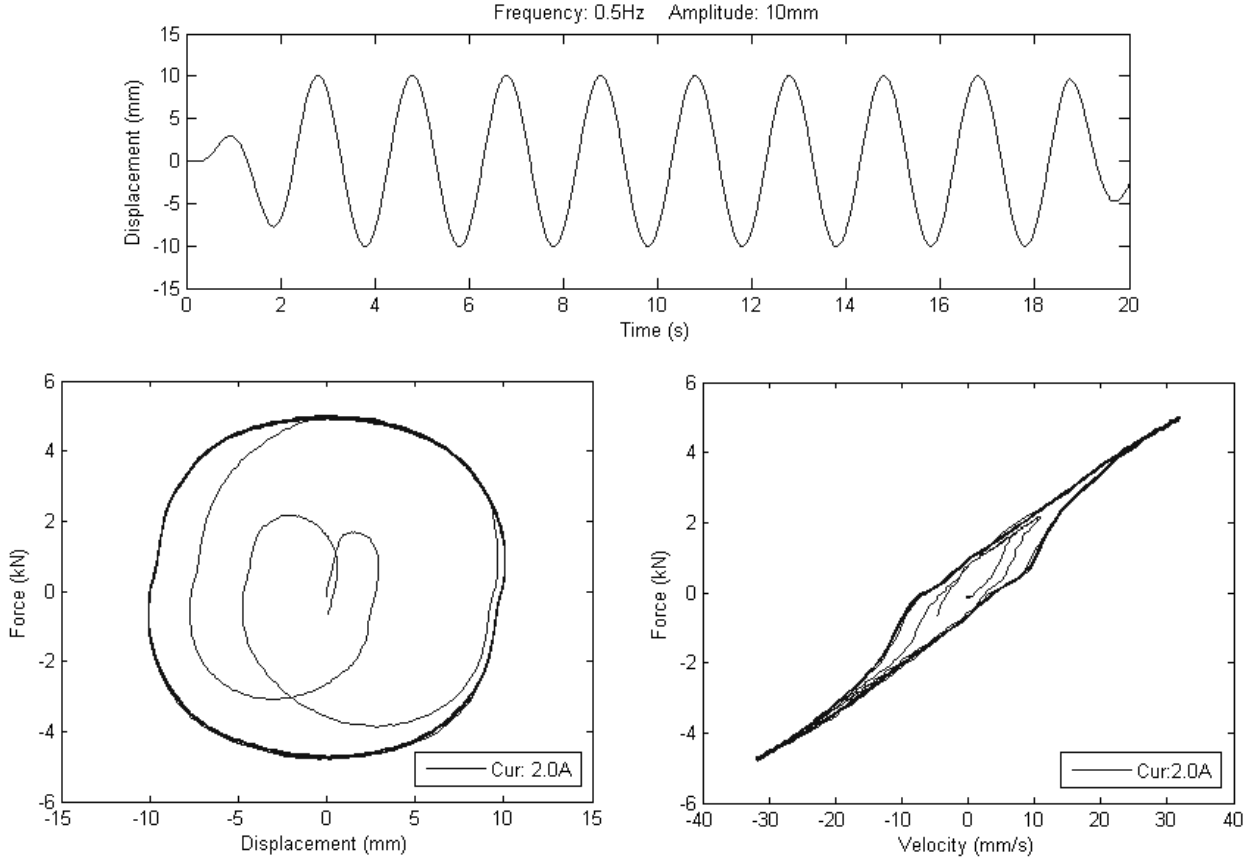

(b) Case of 2.0 A Current intensity and 2.0 Hz Frequency with 10 mm displacement amplitude.

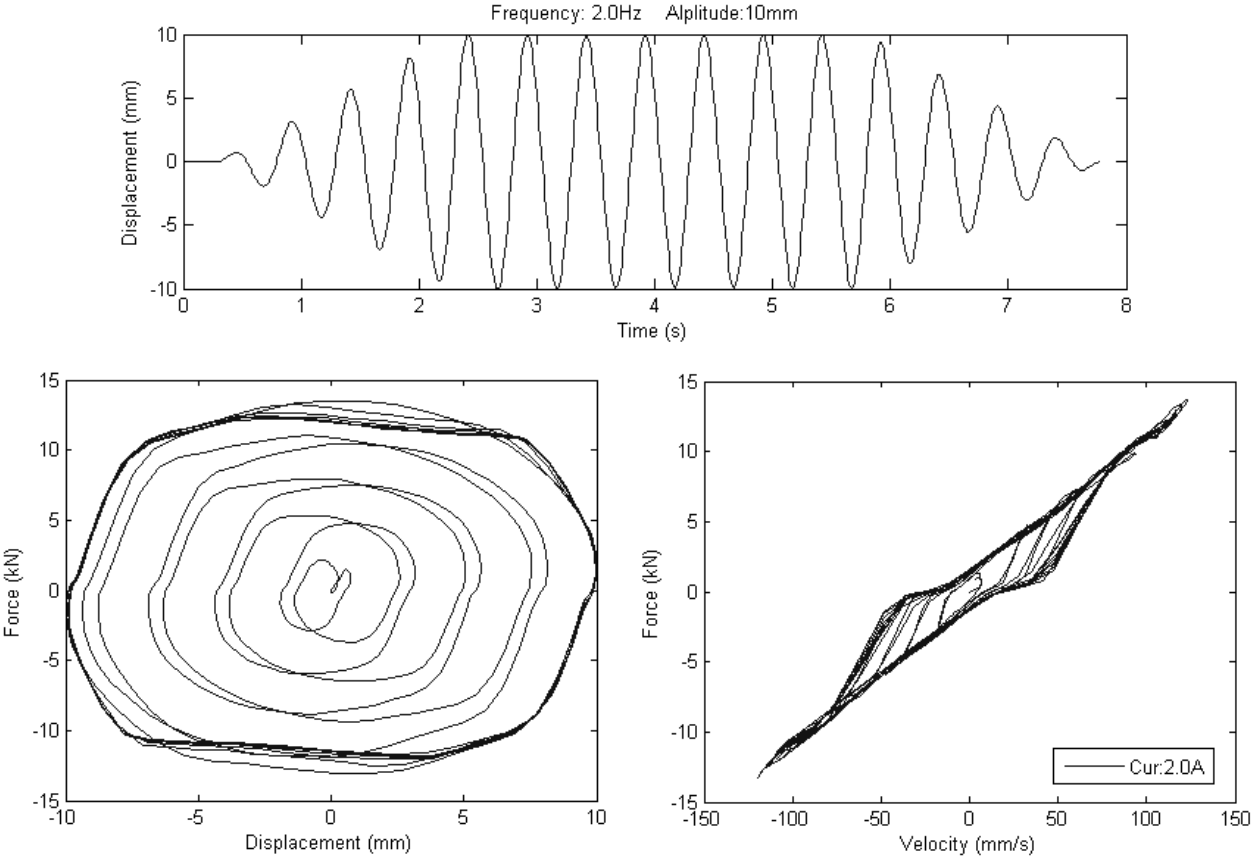

Figure 2. Hysteresis characteristic of the MR fluid damper.

tween displacement and force is nonlinear. Meanwhile as illustrated by the velocity-force curves in Fig. 2, their relationship is linear in high-velocity regions, but not in low-velocity regions centered at zero, appearing to be obvious hysteresis. As a result, the force-velocity relationship is characterized with obviously nonlinear hysteresis that should be much more paid attention. The above complex nonlinear hysteresis should be described accurately by an advanced model.

3. MECHANICAL MODEL OF THE MR FLUID DAMPER

The Bouc-Wen model is one of the important models used extensively for modeling various kinds of hysteretic systems. It has an important merit of being extremely versatile and can exhibit a wide variety of hysteretic behavior. In this paper, we mainly discuss how to make the Bouc-Wen model applicable to simulate the dynamic characteristic of the MR fluid damper.

3.1. Bouc-Wen Model

The normalized version of the Bouc-Wen model introduced in [4] relating the output $F(t)$ to the input $x(t)$ is given by

$$F(t) = c\dot{x}(t) + kx(t) + \alpha z(t) + f; \quad (1)$$

where evolutionary variable z is governed by

$$\dot{z}(t) = Ax(t) - \beta\dot{x}(t)|z(t)|^n - \gamma\,|\dot{x}(t)|\,z(t)|z(t)|^{n-1}; \quad (2)$$

where c is the viscous coefficient contributing to the scaling relationship of the proportion by force and velocity, k is the stiffness contributing to the scaling relationship of the proportion by force and displacement, α is a scaling factor, and f is the initial damper displacement. As seen from the expressions, the characteristic parameters $c, k, \alpha, f, A, \beta, \gamma$ and n are undetermined in advance that should be identified by an optimization algorithm.

3.2. Parameter Analysis

Considering the nonlinear system governed by Eqs. (1) and (2), most of the parameters do not have clear physical meanings for damper's dynamic property.[8] When we employ one parallel algorithm to search for the optimal values of these parameters, initial settings such as searching ranges. for every parameter have an important effect upon the convergence rate and training speed of the algorithm. Moreover, these settings are generally designed based on their physical meanings to a large degree. For this reason, it is very imperative to discuss the contribution of every parameter to the Bouc-Wen model's output.

In order to explore the undetermined parameters playing what part of physical meaning or contribution for the hysteretic curves, different hysteretic curves are plotted in Fig. 3. The results are derived from numerical simulation of the Bouc-Wen model by a 4$^{\text{th}}$ order Runge-Kutta method with a time step $\Delta t = 0.01$ s. Herein, assume input x is harmonic displacement $x = Bsin(\omega t)$ where $\omega = \pi$ rad/s[1] and $B = 10$. The variables $x, \dot{x}, z$ and F and parameters $c, k, \alpha, f, A, \beta, \gamma$ and n in the Bouc-Wen model are temporarily supposed to be dimensionless. Various hysteretic curves are drawn in Fig. 3 by changing the values of every parameter. Based on their varying pattern, the parameters are analyzed below:

Table 1. Parameter description in Bouc-Wen model.

Parameters	Description
c	viscous factor
k	stiffness factor
α	Hysteretic factor
f	offset
A, β, γ	Shape control factor
n	Yield slope factor

- ***Parameter*** c: Fig. 3a shows that the original values of parameters $k, f, \alpha, A, \beta, \gamma$ and n are assumed to be fixed at 0.1, 0, 20, 0.1, 2, 2 and 1 respectively. Then, observe the curves' transformation along with the change of the parameter c. When the value of c is increased, we found that the displacement-force ($x - F$) curves become more distinctly full maintaining a certain slope. On the contrary, the average slope of the velocity-force ($\dot{x} - F$) curve, depicted by Fig. 3a, becomes larger when c does. Parameter c is susceptible to the relationship of velocity and force, and therefore it can be named "viscous coefficient".

- ***Parameter*** k: $c, f, \alpha, A, \beta, \gamma$ and n are assumed to be fixed at 0.1, 0, 20, 0.1, 2, 2 and 1 respectively. The value of k is susceptible to the relationship of displacement and generated force, and the average slope of the curve depicted by Fig. 3b becomes larger when k does. For this reason, k is always to represent the average slope of $x-F$ loops, which can be regarded as stiffness factor.

- ***Parameter*** f: The variety of the curves in Fig. 3c seems obviously simple. The force f is an offset that accounts for the nonzero mean value observed in the measured force.

- ***Parameter*** α: Its value is dependent on the hysteresis variable z which is a solution of the hysteresis differential z. Thus, it is very difficult to obtain an explicit value of α. The variety of the curves in Fig. 3d shows that α represents the ratio of linear to nonlinear responses, which is responsible for hysteretic characteristics.

- ***Parameters*** A, β and γ: The deformation of the curves seems analogous when A, β and γ vary severally (see Fig. 3e). They do not have a very clear physical meaning in general, which is the main reason that they match a wide class of hysteretic curves. Hence, we can call them shape control factors.

- ***Parameter*** n: As shown in Fig. 3f, it represents the sharpness of yield which controls the fullness of the hysteresis loops. In general, its value range is usually from 1 to 3.

Based on the above analysis, it is concluded that the common definition of these parameters in the Bouc-Wen model is suitable for the MR fluid damper in Table 1.

3.3. Parameter Identification

The Bouc-Wen model comprises two equations, one of which is a differential equation concerning the intermediate variable z . Since the expressions are obviously complex, for convenience, Bouc-Wen mathematic equations can be described by a discrete form, such as

$$F_{sim}(k) = f(x(k),\, \dot{x}(k),\, z(k),\, \Theta); \quad (3)$$

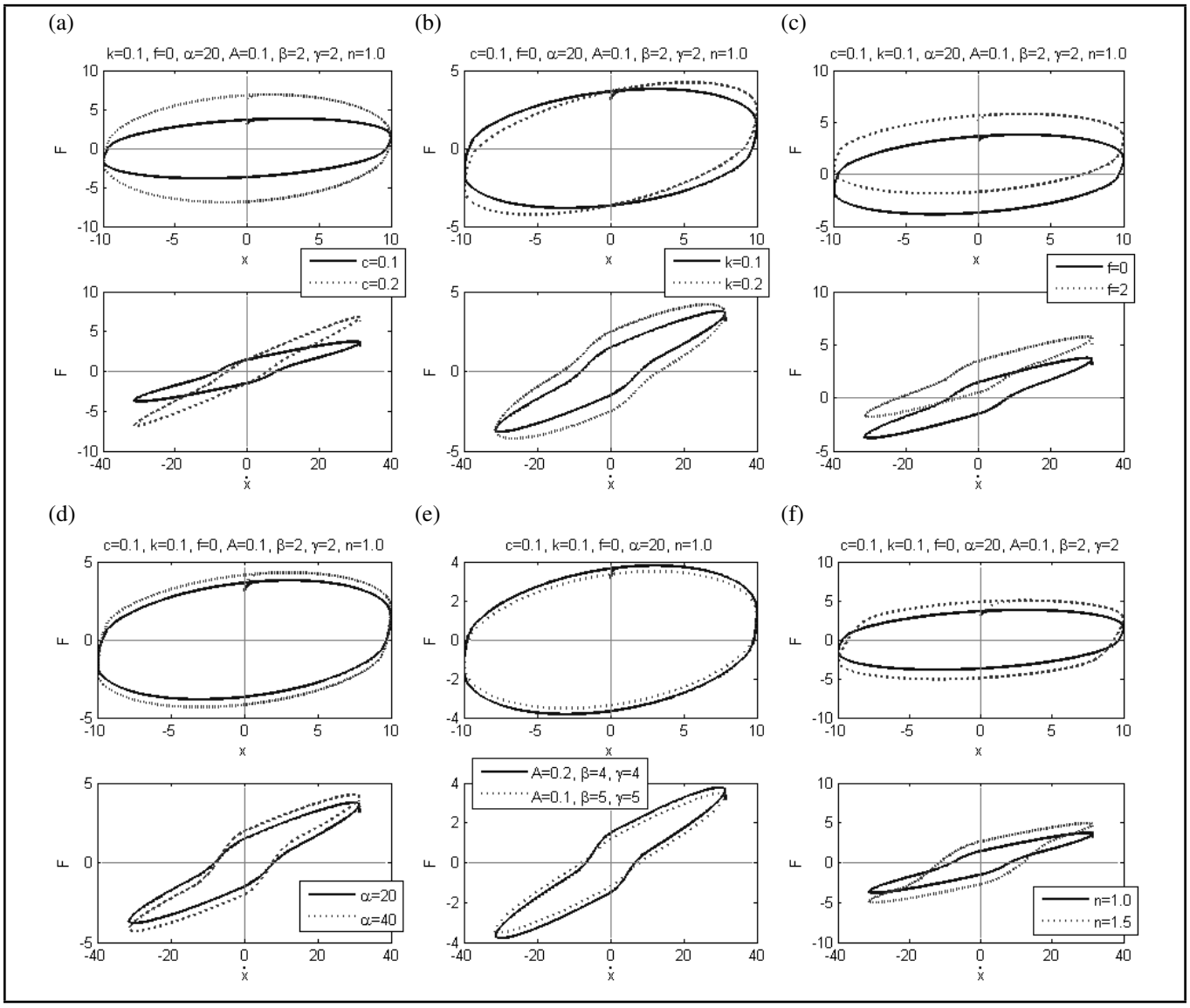

Figure 3. Examples of hysteresis curves generated by the Bouc-Wen model with different parameters.

where F_{sim} is simulated force and $\Theta = [c, k, f, \alpha, A, \beta, \gamma, n]$ is a set of identified parameters of the Bouc-Wen model, and $x/\dot{x}$ is the damper displacement/velocity derived from experimental data.

We also assume the responses of one hysteretic system or device to be a Bouc-Wen model. Then the system can be expressed by

$$F_{\exp}(k) = f(x(k),\, \dot{x}(k),\, z(k),\, \Theta_0); \tag{4}$$

where F_{exp} is damper force derived from experimental data, and Θ_0 is a set of original parameters representing the inherent characteristics of the hysteretic systems, which must be found out by an advanced parallel algorithm.

A flow chart on the parallel algorithm for parameter estimation of the Bouc-Wen model is depicted in Fig. 4. Its process is introduced as follows: At first, experimental data, including damper displacement x and velocity $\bar{x}$, were collected and incorporated into the Bouc-Wen model formulation expressed in Eqs. (1) and (2). Accordingly, the simulated MR damper force F_{sim} was figured out. During this phase of the parallel algorithm, the objective function was defined as the sum of differences between the MR damper force of experimental results

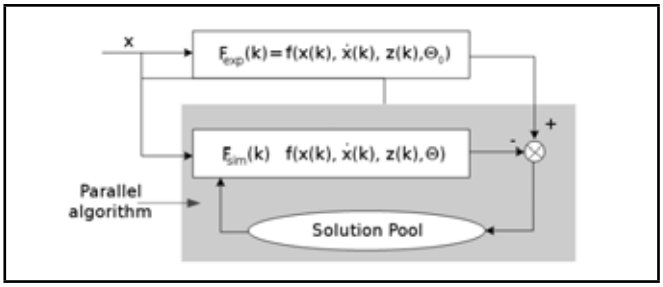

Figure 4. The procedure of parameter estimation by Parallel Algorithm.

and those of the simulated results. It can thus be concluded that, the lower the objective function value, the better the estimated parameters. Through appropriate iterative circulation, the best results will eventually be picked out.

4. HYBRID EVOLUTIONARY ALGORITHM

4.1. Modified GA

As a powerful computational search and optimization tool, the GAs have been applied successfully to problems in many fields such as optimization design, fuzzy logic control, neural

networks, expert systems, scheduling and many others.[4,8,18] Generally, GA procedure consists of three basic factors: chromosome structure, fitness function, and some control parameters (select operator, crossover operator, etc.). The standard GA implementation was generally in its standard form, using a fixed number of generations for iteration and with predetermined crossover and mutation rates. However, the algorithm efficiency was not adequately considered in the GA. With the development of GA, variations to the traditional procedures were proposed in a large amount of literature. By setting appropriate control-parameters, they will conspire to make optimization results more accurate and effective. In this paper, a computationally-efficient GA is proposed firstly.

4.1.1. Chromosome Structure

Chromosome structure mainly depends on the nature of the problem to be solved. In the case of the solution structure of parameter estimation of the Bouc-Wen model, there are altogether eight undetermined parameters ($c, k, f, \alpha, A, \beta, \gamma$ and n) in Eqs. (1) and (2). Therefore, the chromosome can be

$$\Theta_i = \{c_i, k_i, f_i, \alpha_i, A_i, \beta_i, \gamma_i, n_i\}, i = 1, ..., N; \quad (5)$$

where N is the maximum of chromosomes and i is the i^{th} individual in chromosome.

4.1.2. Elitism Strategy

The lowest fitness obtained in the chromosome during the GA iteration is stored so as to ensure the offspring of the best chromosome in subsequent generations.[19] Generally, standard GA uses the roulette wheel strategy to reserve the relative "good" individuals for next circle based upon the values of individual fitness function. However, this method easily arouses some vital problems such as "low efficiency" and "local optimization," because of its random search property.[20] Drawing on this, we can reserve the fittest individual in each generation without undergoing crossover and mutation progress, which can converge to the global optimum. When the generation evolves, the minimum error (elite individual) will directly approach the global optimum. That is

$$e_{min}^{i+1} \leq e_{min}^{i}; \quad (6)$$

where e_{min}^{i} is the minimum error (elite individual) at the i th generation. "e" can be designed by the distance between the simulation and experiment results of damper forces. In this paper, we choose the fitness function as the error "e" (see Eq. (10)). As a result of the elitism strategy, the value of the error function is descending to zero directly. The stored minimum errors cannot increase over iterations.

Unlike the standard GA implementation where the best individual (chromosome) might be lost due to encountered stochastic effects, the iterative process in improved GA is always searching for the universal best solution at the minimum error rate since the strategy can remove the destructive effect of the crossover and mutation. Consequently, the tendency of descending errors is successfully maintained and the efficiency of the algorithm is greatly enhanced.

4.2. Modified PSO

Swarm intelligence is an exciting new research field still in its infancy compared to other paradigms in artificial intelligence. A number of computational swarm-based systems have been developed in the past decade, where the approach is to model the very simple local interactions among individuals, from which complex problem-solving behaviors emerge.[21]

Suppose that the searching space is D-dimensional and n particles form the colony. The i th particle represents a D-dimensional vector $X_i (i = 1, 2, \ldots, n)$ that stands for the i th particle location $X_i = (x_{i1}, x_{i2}, ..., x_{iD}) (i = 1, 2, ..., n)$ in the searching space. In the PSOs, the location vector $x^{(t+1)_{id}}$ at the next time step is given by

$$x_{id}^{(t+1)} = x_{id}^{(t)} + v_{id}^{(t+1)}; \quad (7)$$

where $x_{id}^{(t)}$, $v_{id}^{(t+1)}$ are the location at the current time step and the velocity at the next time step for the i th particle and d th dimensional vector.

We should calculate the particle's fitness value by putting its location into a designated objective function that is analogous to the process of GA. When the value of the fitness is higher, the corresponding X_i is more "excellent". The velocity vectors are adjusted to move toward the previous best position of each particle and that of a swarm, defined as

$$v_{id}^{(t+1)} = \omega v_{id}^{(t)} + c_1 r_1 (P_{id} - x_{id}^{(t)}) + c_2 r_2 (P_{gd} - x_{gd}^{(t)}); \quad (8)$$

where $i = 1, 2, \ldots, n$, $d = 1, 2, \ldots, D$, r_1 and r_2 are uniformly distributed random numbers ($r_1, r_2 \in [0, 1]$), and c_1 and c_2 are learning rates controlling the effects of the personal and global guides, respectively, while ω is the inertia weight controlling the balance between exploration and exploitation, and it is the following decreasing linear function:

$$\omega(t) = \omega_{\max} - (\omega_{\max} - \omega_{\min}) \frac{t}{t_{\max}}; \quad (9)$$

where ω_{max} and ω_{min} are the final weight and initial weight respectively. The equation is meant to decrease the diversification characteristic of particles within a certain velocity, which guarantees the searching point gradually approximate to P_{id} and P_{gd}. In this paper we set the values of ω_{max} and ω_{min} equal to 0.9 at the beginning of the search and 0.4 at the end of the search respectively, according to the empirical study.[5] By using a linearly-decreasing inertia weight, the PSO will be ameliorated greatly in contrast to the cases where the inertia weight is a positive constant. Like the improved GA, the fitness function fit is equal to the objective function RMSE as in Eq. (10).

4.3. Hybrid Evolutionary Algorithm

GA and PSO are basically similar in their inherent parallel characteristics, whereas experiments display that they have their respective advantages and disadvantages. This paper is set out to present a hybrid evolutionary algorithm, by combining the advantages of GA and PSO. This algorithm can highlight the excellent features of GA and PSO while avoiding the weaknesses, such as low calculation efficiency in GAs and premature convergence in PSOs.

In hybrid evolutionary algorithm, the appropriate objective function and termination rule should be designed as are introduced as below.

4.3.1. Fitness Function

A fitness function is a measuring mechanism that is used to evaluate the status of every individual or particle. Each goes through the same evaluating exercise. The key to directly influencing the final identified results is in designing an appropriate identified function. This paper employs the Root-Mean-Square Error (RMSE), herein to be taken as the fitness function, which is governed by

$$fit = \frac{1}{n}\sqrt{\sum_{i=1}^{n}\left(F_{sim,i} - F_{\exp,i}\right)^2}; \tag{10}$$

where n is the number of data points, and each simulation/experimental data point is indexed by subscript $sim, i/exp, i$.

4.3.2. Termination Rule

An early evolutionary algorithm generally terminates after the expiry of a fixed number of terminations. However, when the solution has already found the minimum error but not yet arrived at the designated generation, it is undoubtedly time-consuming to go on iterating. For this reason, an appropriate termination rule should be created so as to relieve the unnecessary computational burden.

The termination strategy in this study is proposed under two aspects: one is depending on maturity degree of the population proceeding in a certain generation. Another is in view of the fittest individuals after iterating a certain generation, controlling the real calculation accuracy.

Rule 1: Terminate the GA-PSO if a reduction of minimum error lower than 20% of maximum error does not arise in further generation, which is defined as

$$e^k_{\min} - e^{k+1}_{\min} \leqslant 0.2 \max_k\{e^k_{\min}\}; \tag{11}$$

where e^k_{min} represents the minimum error in k th generation. This rule can guarantee that the population should not be diversified any more, and the best individual is very close to the global solution.

Rule 2: Terminate the GA-PSO if the minimum fitness value is below a threshold e_{min}, which is given by

$$fit_{\min} \leqslant e_{\min}; \tag{12}$$

where e_{min} is the designated threshold value of fitness, and fit_{min} represents the minimum fitness value in individuals. This rule can guarantee the final solution's precision is adequately satisfied.

The flowchart of the hybrid evolutionary algorithm is introduced in Fig. 5. Firstly, the initial population is randomly generated according to structural optimization problems, and then the objective function is utilized to evaluate the status of each individual or particle in the population. Based on the evaluation results, the population is divided into two sub-populations. Within the population, 50% of the individuals with lower fitness are input to the GA-based identifier to identify the unknown parameters. Simultaneously, another 50% with higher fitness are input to the PSO. The above allocation scheme can ensure improving the convergence speed of GA, while avoiding plunging into local optimum in PSO. The process will be repeated until one solution can satisfy the requirement of the termination rule, and it should be exacted to be the final or optimal solution.

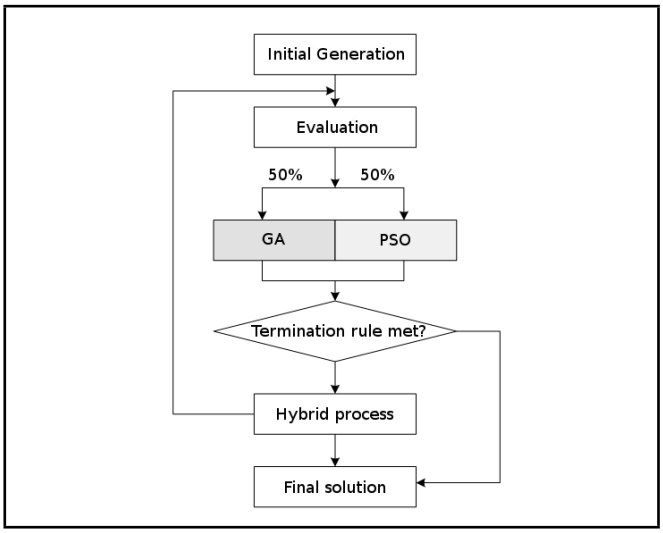

Figure 5. Flow chart of hybrid evolutionary algorithm.

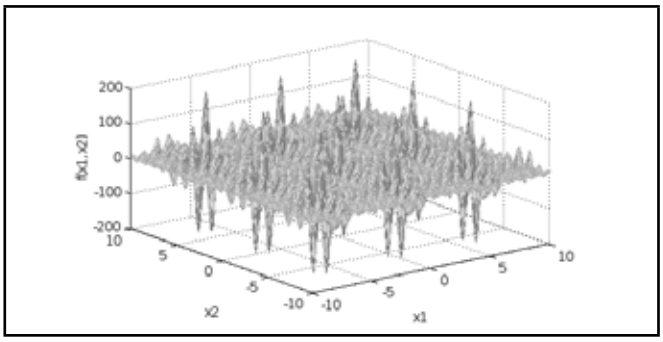

Figure 6. *Shubert* functions graph.

4.4. Validation in Test Function Problems

The performance of the hybrid evolutionary algorithm was evaluated by multi-variable, multi-model function problem that is known as the *Shubert* function. The test function is as follows:

$$\text{Optimize the minimum in } f(x_1, x_2) = \sum_{i=1}^{5} i\cos[(i+1)\cdot x_1 + i]\cdot\sum_{i=1}^{5} i\cos[(i+1)\cdot x_2 + i];$$
$$x_1, x_2 \in [-10, 10].$$

The *Shubert* function graph in Fig. 6 displays multiple peaks. If Standard GA or PSO is used, the best solution will usually search for the local minimum value of the function. Avoiding the problems of "premature" and "local optimization" is an arduous task that should be settled successfully. In order to prove the superiority of the proposed approach, we applied the Standard GA and the GA-PSO respectively to solve the minimum value of the *Shubert* function, and their efficiencies and accuracies are compared to each other.

Note that the standard GA is performed using the following algorithm settings: roulette wheel selection, crossover rate $P_c = 0.85$, mutation rate $P_m = 0.01$, and the maximum gener-

Table 2. Test data of *Shubert* function minimization.

min $f(x_1, x_2)$	Generation					
	5	10	25	30	40	50
Standard GA	-110.3478	-162.8241	-186.2324	-186.6189	-185.8875	-186.7301
GA-PSO	-183.4561	-186.7098	-186.7306	–	–	–

ation $N = 50$. Both in the standard GA and GA-PSO, the number of population/particles is a set of 80. The above-mentioned approach has been implemented by MATLAB. Simulation is processed by an Intel Core2 Duo E6300 1.86 processor with 1024M RAM, under Windows 7.

Figure 7 illustrates that the value of the fitness function experiences an approximate descending course as optimization processes both in the Standard GA and GA-PSO. It is observed in Fig. 7a that the first twelve generations finish more than 90% of the convergence in the iterative process, and the further reduction in estimation error is in the region of gentle slope. There is no more evolution after the 16th generation when the error is reaching the minimum value. Thus, it is very crucial to establish an appropriate termination rule which can get rid of redundant iterative generations in due time. When GA-PSO adopts the termination *Rule 1* and *Rule 2*, the process shows a very quickly descending tendency, only experiencing twenty-five generations, and the best solution (-186.7306) is found out. Meanwhile, by comparison between the average solution experiences with standard GA and GA-PSO, the solution range in GA-PSO is a little farther from the final solution than result in the standard GA. This is because the average solution is mainly dependent on the dispersion degree of the individuals in optimization algorithms. If the individuals were more diversified, the average solution would be more decentralized. In this sense, the generated individuals in GA-PSO are much more diversified, resulting in one global optimized solution. Thus, a more accurate solution in GA-PSO will be obtained, which is also verified in Table 2.

As illustrated in Table 2, the minimum value of the *Shubert* function by using Standard GA is -186.7301 in the 50th generation. With regard to the GA-PSO, the minimum value maintains -186.7306 in the 25th generation. Obviously, a smaller number of generations are required, and higher accuracy is obtained by the GA-PSO before termination. In view of this, we recommend the hybrid evolutionary algorithm (GA-PSO) for solving complex problems because of its high precision and efficiency.

5. IDENTIFICATION RESULT AND DISCUSSION

In order to implement numerical calculation for the Bouc-Wen model, a 4th order Runge-Kutta method is adopted to solve the differential Eq. (2) with a time step $\Delta t = 0.02$ s. Assuming that the excitation function is harmonic displacement $x = 10sin(\pi t)$ (where the unit is mm), some typical solutions of the mechanical formulation are shown in Fig. 8.

In this study, the first case that was considered original values of eight parameters $(c_0, k_0, f_0, \alpha_0, A_0, \beta_0, \gamma_0, n_0)$ are assumed to be fixed at 0.08 kN·s/mm, 0.01 kN/mm, 0 kN, 20 kN/mm, 0.05, 4 kN·s/mm$^{2.8}$, 2 kN·s/mm$^{2.8}$ and 1.8 respectively. Likewise the second case is considered that original values of parameters are assumed to be fixed at 0.1 kN·s/mm, 0.01 kN/mm, 2.0 kN, 25 kN mm, 0.05, 4 kN·s/mm$^{2.5}$, 2 kN·s/mm$^{2.5}$ and 1.5 respectively.

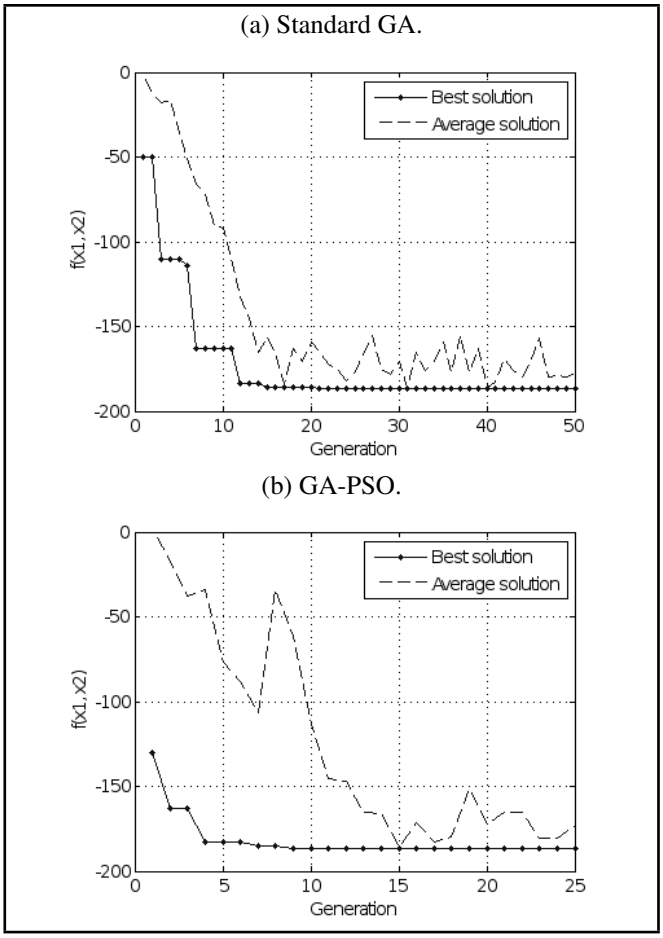

Figure 7. Iterative track of the best and average fitness values.

5.1. Noise-free Estimation

Firstly, we consider noise-free estimation, in which force data is not corrupted. In order to validate the superiority of the GA-PSO, it is compared with the Standard GA in terms of the accuracy and efficiency of the results. The Standard GA is performed using the following algorithm settings: roulette wheel selection, crossover rate $P_c = 0.85$, mutation rate $P_m = 0.01$, and the maximum generation $N = 30$.

Statistics of the estimated parameters with case 1 and case 2 are illustrated in Table 3 and Table 4, respectively. Furthermore, we also compare the accuracy and efficiency between the Standard GA and the GA-PSO in Table 5. The errors in the GA are 0.1351 kN on average, the process of which is terminated in the 30th generation. Regarding the GA-PSO, however, the average errors are less than 0.0933 kN , and its process is terminated within the 16th generation. Obviously, the GA-PSO requires a smaller number of generations but obtains results with much greater accuracy.

As shown in Fig. 9, it is found that the hysteretic loops are in very close agreement with the simulated hysteresis. Note that the original curves are plotted by solid lines, and the estimated results are plotted by a series of small circles. In Fig. 10, the errors between the original and estimated damper force values

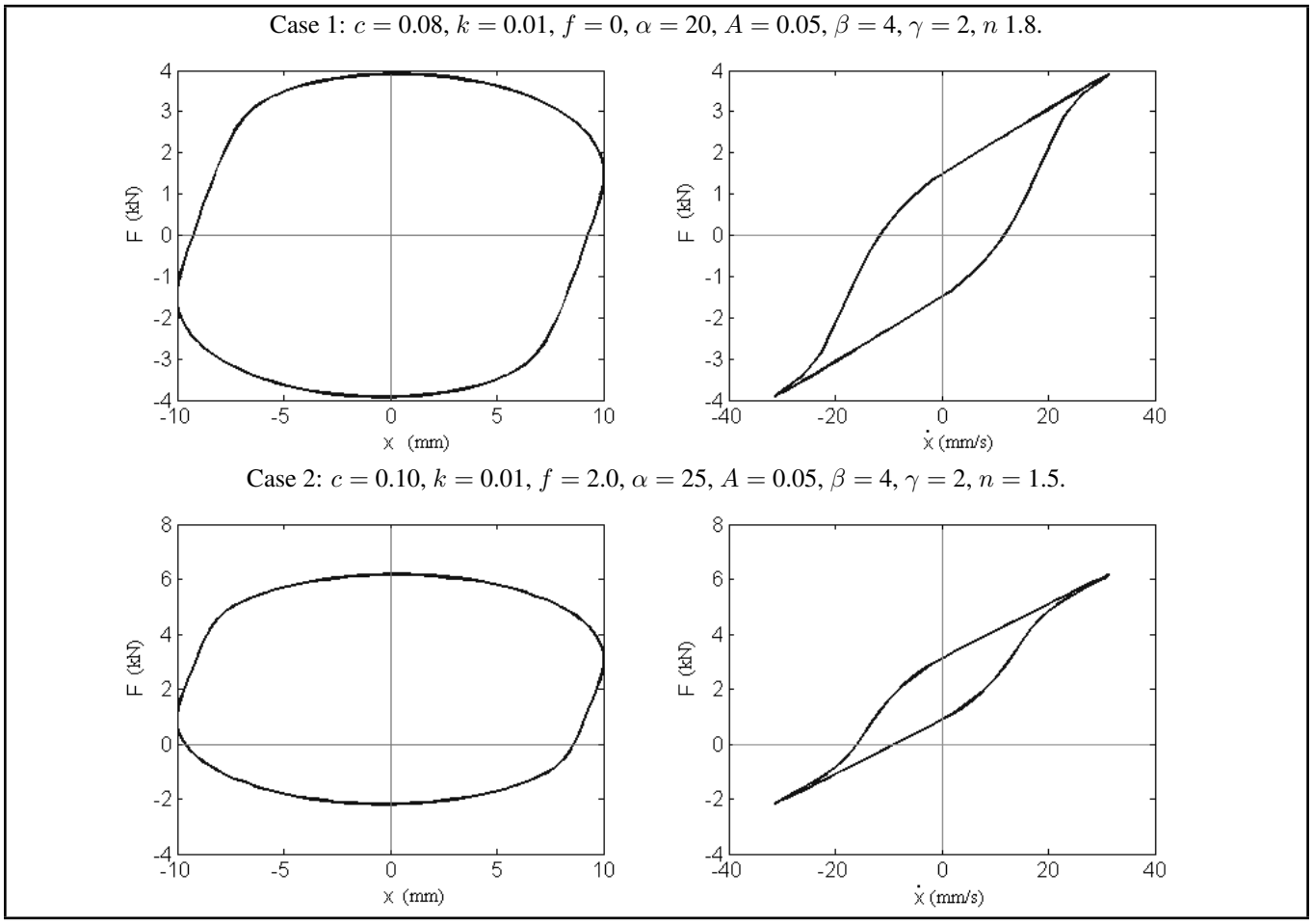

Figure 8. The hysteresis loops generated by the Bouc-Wen model.

Table 3. Comparisons of estimated parameters from the case 1 by using Standard GA and GA-PSO.

Estimated by	Original	Standard GA	GA-PSO
c (kN·s/mm)	0.08	0.0849	0.0817
k (kN/mm)	0.01	0.0157	0.0241
f (kN)	0	0.0568	0.0146
α (kN/mm)	20	15.9478	16.7831
A (dimensionless)	0.05	0.0573	0.0673
β (kN·s/mm^{n+1})	4	1.4041	3.1223
γ (kN·s/mm^{n+1})	2	2.2604	2.0178
n (dimensionless)	1.8	1.7031	1.7167
RMSE (kN)	N/A	0.1425	0.0933

Table 4. Comparisons of estimated parameters from the case 2 by using Standard GA and GA-PSO.

Estimated by	Original	Standard GA	GA-PSO
c (kN·s/mm)	0.1	0.1087	0.1018
k (kN/mm)	0.01	0.0148	0.0201
f (kN)	2	1.9717	2.0311
α (kN/mm)	25	19.9222	16.2741
A (dimensionless)	0.05	0.0416	0.0774
β (kN·s/mm^{n+1})	4	3.2460	2.7106
γ (kN·s/mm^{n+1})	2.00	2.3371	3.1919
n (dimensionless)	1.5	1.5981	1.5362
RMSE (kN)	N/A	0.1277	0.074

can also be surveyed, and maintain less than 0.2 kN everywhere.

5.2. Noise Estimation

Next, parameter estimation of the Bouc-Wen model with a set of noisy data is considered. In the real parameter estimation problem of the model, measured data are often corrupted by noise. Then uncertainty can arise from measurement instruments, system noise, low-accuracy calculation, etc. Thus, the effect of noise should be taken into account. In this paper, a series of random values are added to the original data. Assume x' is noise data, and then it can be divided two parts:

Table 5. Comparison of accuracy and efficiency by using Standard GA and GA-PSO with original data.

	Standard GA		GA-PSO	
	RMSE (kN)	Generation	RMSE (kN)	Generation
Case 1	0.1425	30	0.0933	15
Case 2	0.1277	30	0.0740	16
Average	0.1351	30	0.0836	15.5

$$x' = x + x_n \xrightarrow{Bouc-Wen} F' = F + F_n; \tag{13}$$

where x represents the component of original data, and x_n represents the component of additive noise at each particular time. Through substituting x' for x in Bouc-Wen model, a set of damper force data F' is obtained subsequently. Then the RMSE function Eq. (10) can be replaced by

$$fit = \frac{1}{n}\sqrt{\sum_{i=1}^{k}(F_{sim,i} - F'_i)^2}; \tag{14}$$

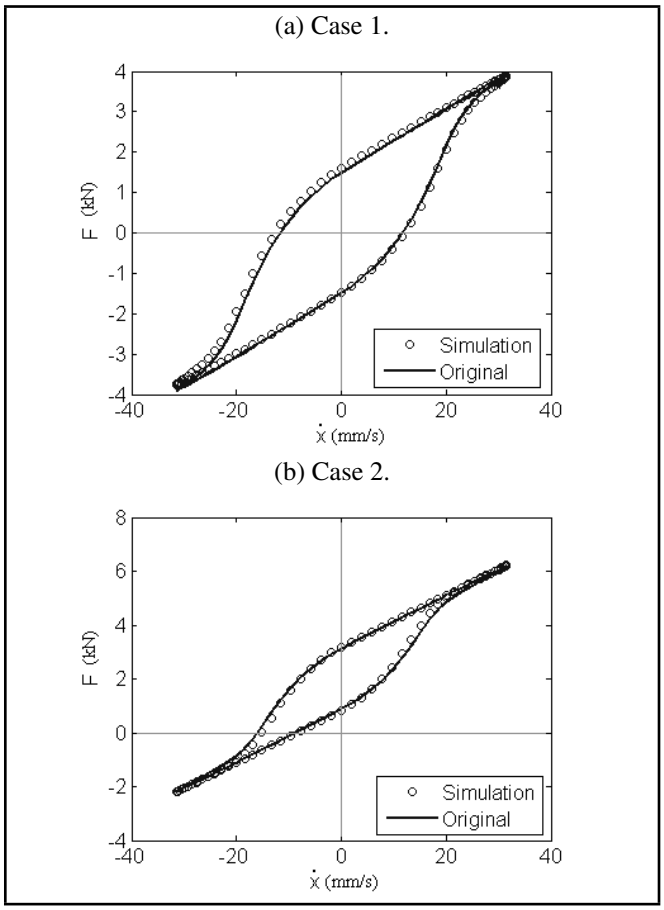

Figure 9. Parameter estimation results using the GA-PSO.

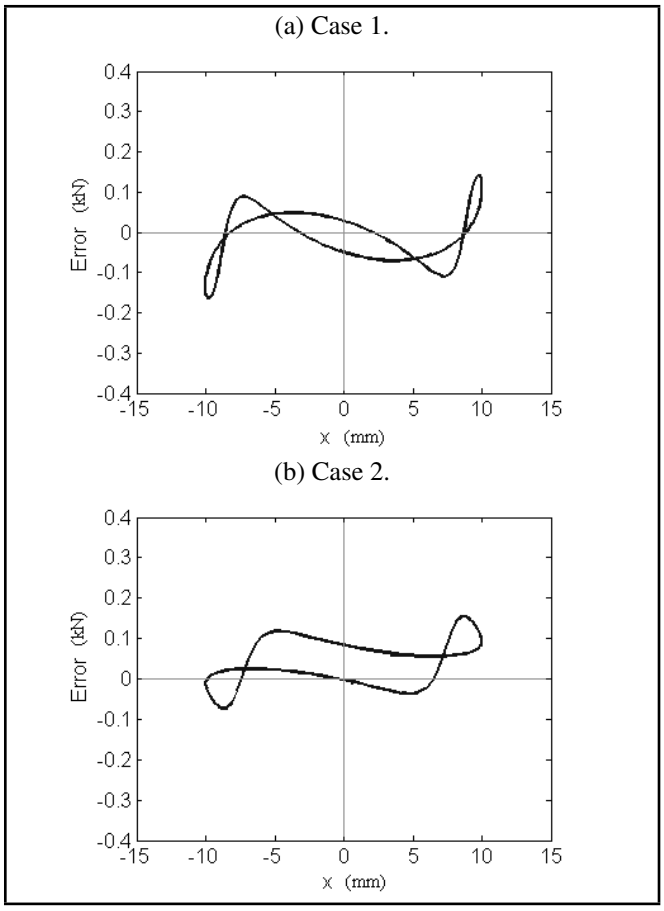

Figure 10. Errors by using GA-PSO.

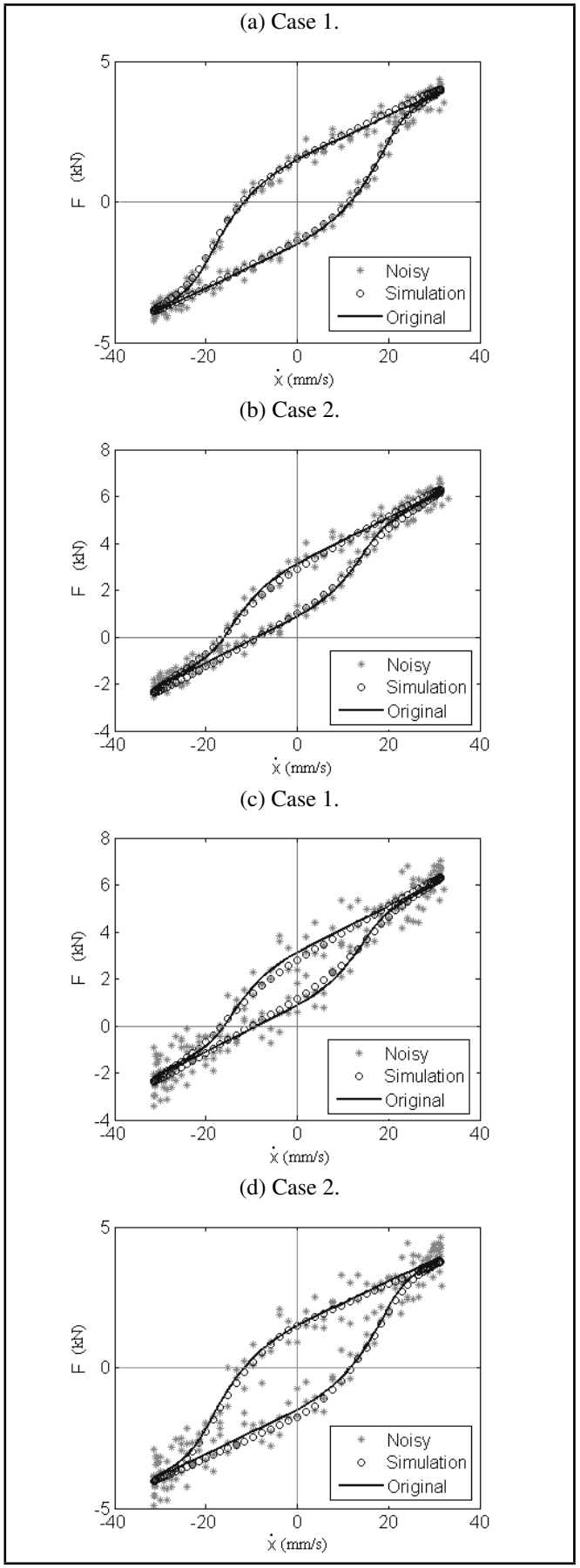

Figure 11. Parameter estimation by the GA-PSO with noisy data at (a),(b)10% and (c),(d)25% levels of NR.

In this study, the percentage noise ratio is designed to perform optimization for different level noise. The noise ration (NR) is given by

$$NR = \frac{1}{n}\sum_{i=1}^{n}(\frac{x_i - x_i'}{\bar{x}}) \times 100\%; \quad (15)$$

where n is the number of data points, each data point is indexed by subscript i, and $\bar{x}$ represents the average value of original data .

Some numerical results of hysteretic loops simulated using GA-PSO with noise data are displayed in Fig. 11, in which the estimation curves appear to remain quite close to the original one. This proves that the proposed method is effective, even if the original data are corrupted by different degrees of noise.

By collecting a large amount of examples shown in Table 6 and Table 7, most of the estimated parameter values differ from the original values, and there exist different errors under different degrees of noise. When the noise ratio becomes bigger, the error will increase. It should be noted that the errors are basically below 0.2 kN, even if the noise ratio reaches up to 40%.

5.3. Simulation of a Real MR Damper

In the experiment, the damper behavior of the MR damper is observed under 0.5 Hz, 1.0 Hz and 2.0 Hz sinusoid excitation with 10 mm amplitude displacement, and the magnetic field is varied by different currents ranging from 0 A to 3.0 A. In Figure 2, the damping curves from experimental data are not very smooth, which should be interfered by a certain degree of noises, possibly arising from measurement instruments, system noise, etc. The noise existing in hysteretic curves will impose more difficulties on construction for an effective Bouc-Wen model with accurate identified parameters. In this paper, a large amount of experimental data obtained from the MR fluid damper is utilized to verify that the proposed approach has the capability to estimate the satisfactory parameters of the Bouc-Wen model efficiently. We also compare it with Standard GA in terms of accuracy and efficiency. (Herein the Standard GA is performed using the following algorithm settings: roulette wheel selection, crossover rate $P_c = 0.85$, mutation rate $P_m = 0.01$, and the maximum generation $N = 60$.)

In the proposed method, several sets of identified parameters are figured out due to different applied current intensities, which are shown in Table 8. By using Standard GA, the average errors are 0.1254 kN, 0.1766 kN and 0.2701 kN under the frequency of 0.5 Hz, 1.0 Hz and 2.0 Hz, respectively. Regarding the GA-PSO, however, the average errors are less than 0.1012 kN, 0.1214 kN and 0.2 kN, and their processes are terminated in the 35th, 40th, and 42th generation, respectively. In GA-PSO, the solution is quite precise, where its errors are consistently below 0.2 kN . In addition, the GA-PSO represents higher computational efficiency whose iteration are around forty generations.

In the proposed method, the typical results are drawn in different cases of 0.5 Hz, 1.0 Hz and 2.0 Hz frequency with different current intensities from 0 A to 3 A. Each case has the sinusoidal displacement of 10 mm. Part of the calculation values of the estimated parameters are listed in Table 9. As exhibited in Fig. 12, it merits great attention that the nonlinear hysteresis responses are in large agreement with theexperimental data by using GA-PSO method. It is intended to testify that the results of the proposed method are very satisfactory.

Table 6. Estimated parameters from case 1 with noisy data.

NR (%)	10	20	30	40
c (kN·s/mm)	0.0791	0.0837	0.0958	0.0760
k (kN/mm)	0.0228	0.0300	0.0315	0.0015
f (kN)	0.0159	0.0224	0.0379	0.0626
α (kN/mm)	17.4237	27.5348	15.5224	28.6553
A (dimensionless)	0.0492	0.0273	0.0387	0.0412
β (kN·s/mm^{n+1})	1.0009	2.6252	4.3346	3.6241
γ (kN·s/mm^{n+1})	4.2481	2.6995	3.9699	3.8054
n (dimensionless)	1.8955	1.7282	1.9878	1.8416
RMSE (kN)	0.1237	0.1345	0.1520	0.1982

Table 7. Estimated parameters from case 2 with noisy data.

NR (%)	10	20	30	40
c (kN·s/mm)	0.0979	0.1101	0.1121	0.1105
k (kN/mm)	0.0092	0.0147	0.0180	0.0083
f (kN)	1.9020	1.9618	1.8989	2.0804
α (kN/mm)	22.0790	23.0376	15.5506	21.7743
A (dimensionless)	0.0592	0.0251	0.0375	0.0234
β (kN·s/mm^{n+1})	4.7363	2.5276	1.6250	4.9113
γ (kN·s/mm^{n+1})	2.9286	4.9258	3.1510	3.8106
n (dimensionless)	1.6124	1.6960	1.5912	1.7903
RMSE (kN)	0.1015	0.1304	0.1640	0.1892

6. CONCLUSION

This paper reports on an experimental study of the MR damper, the results of which indicate that the MR damper has the remarkably nonlinear hysteretic characteristic. Usually the Bouc-Wen model is utilized to model the hysteretic characteristic. However, the Bouc-Wen model consists of a set of multi-unknown parameters that need to be estimated simultaneously. It is a burdensome task to effectively identify the exact values of the parameters. In view of this, this paper proposes a novel hybrid evolutionary algorithm combining Genetic Algorithm with Particle Swarm Optimization (GA-PSO). The simulation results verify the GA-PSO has the ability to search for the global optimal solution with remarkable computational accuracy and efficiency. Finally, a series of preliminary data obtained from a real MR damper is used to again testify that the proposed method is capable of estimating the satisfactory parameters of the Bouc-Wen model efficiently. It makes sense to predict that the approaches presented herein can also throw light on the development and characterization of other complex hysteretic systems.

ACKNOWLEDGMENT

This research is financially supported by the project from the National Natural Science Foundation, People's Republic of China, grants No. 11172226. The supports are gratefully acknowledged.

REFERENCES

[1] Talatahari, S., Kaveh, A. and Rahbari, N. M. Parameter identification of Bouc-Wen model for MR fluid dampers using adaptive charged system search optimization, *Journal of Mechanical Science and Technology*, **26**, 2523–2534, (2012).

[2] Su, C. Y., et al. Adaptive variable structure control of a class of nonlinear systems with unknown Prandtl-Ishlinskii

(a) Cases of 2.0 Hz frequency with 1.2 A current intensity.

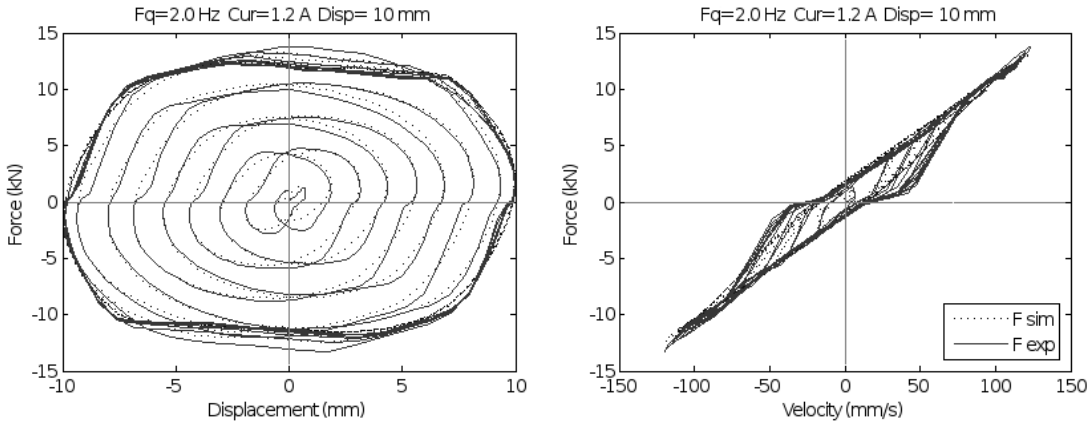

(b) Cases of 2.0 Hz frequency with 2.0 A current intensity.

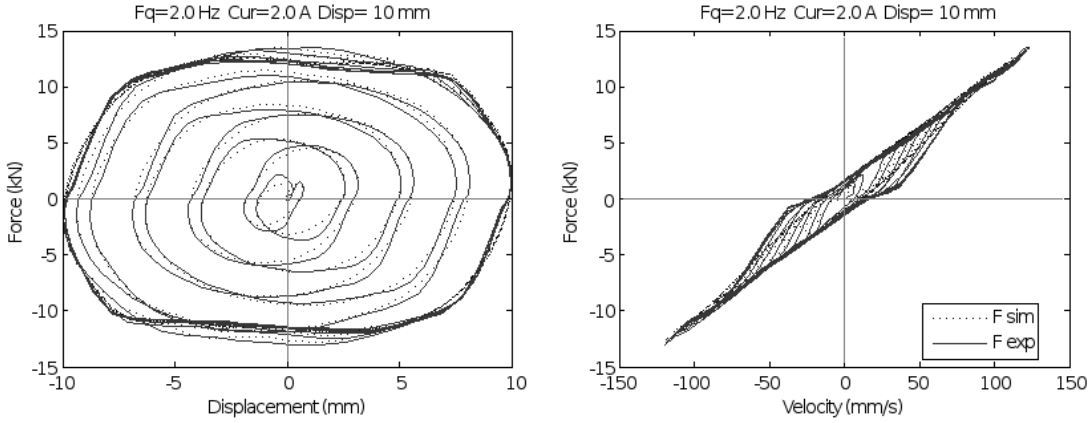

(c) Cases of 1.0 Hz frequency with 2.0 A current intensity.

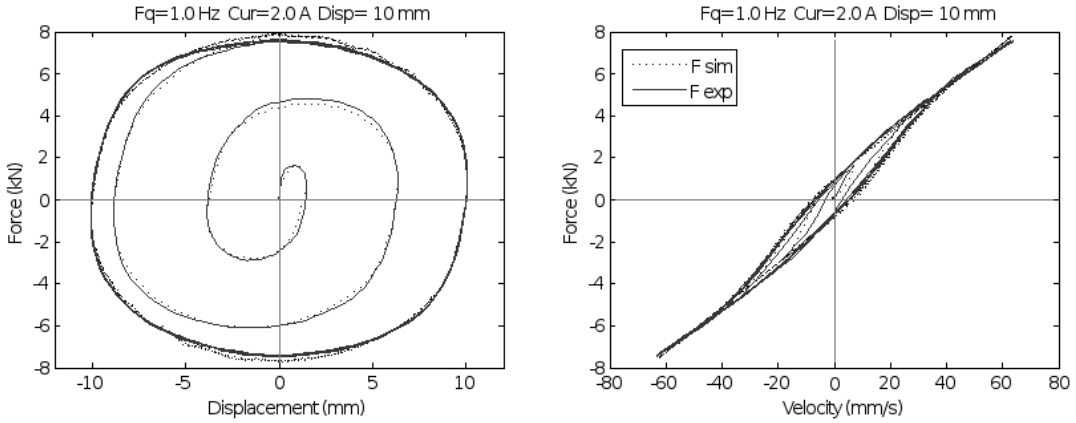

(d) Cases of 0.5 Hz frequency with 2.0 A current intensity.

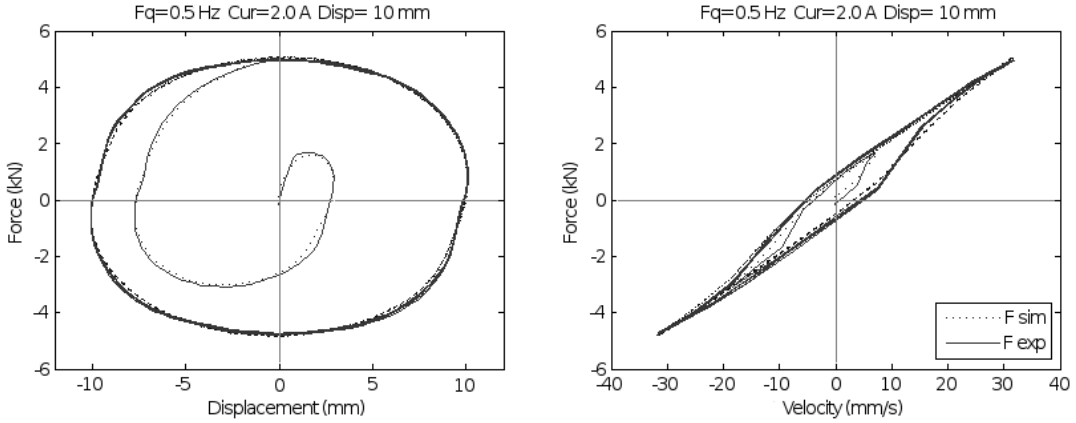

Figure 12. Comparison of experimental data and simulation result using GA-PSO.

Table 8. Comparison of accuracy and efficiency by using Standard GA and GA-PSO with experimental data.

Current	Standard GA			GA-PSO		
	RMSE (kN)/Generation			RMSE (kN)/Generation		
(A)	0.5 Hz	1.0 Hz	2.0 Hz	0.5 Hz	1.0 Hz	2.0 Hz
0.0	0.1088/60	0.1322/60	0.2182/60	0.0906/36	0.1070/39	0.1988/42
1.0	0.1345/60	0.1656/60	0.2355/60	0.1034/35	0.1252/40	0.2018/43
2.0	0.1230/60	0.1544/60	0.2858/60	0.1011/38	0.1378/41	0.1975/43
3.0	0.1220/60	0.1935/60	0.2656/60	0.0995/32	0.1416/42	0.2235/46
Average	0.1254/60	0.1766/60	0.2701/60	0.1012/35	0.1214/40	0.2000/42

Table 9. Results of estimated parameters from experimental data by GA-PSO.

Estimated parameters	0.5Hz				1.0Hz			
	0 A	1.0 A	2.0 A	3.0 A	0 A	1.0 A	2.0 A	3.0 A
c (kN·s/mm)	0.0814	0.1280	0.1379	0.1361	0.0829	0.0965	0.1077	0.1137
k (kN/mm)	0.0069	0.0053	0.0186	0.0156	0.0046	0.0097	0.0131	0.0074
f (kN)	0.0719	0.0867	0.1191	0.1099	0.1089	0.0953	0.0843	0.0855
α (kN/mm)	21.9454	22.2498	24.1578	23.5827	21.1473	22.0022	22.3648	22.6112
A (dimensionless)	0.0514	0.0437	0.0443	0.0614	0.0294	0.0512	0.0653	0.0436
β (kN·s/mm^{n+1})	1.9969	3.3321	1.9265	2.8253	4.3092	3.8721	2.1201	1.1962
γ (kN·s/mm^{n+1})	3.2880	2.1538	2.2603	1.1420	1.9211	3.5864	4.6584	4.8255
n (dimensionless)	1.3057	1.4044	1.2311	1.1510	1.3002	1.4021	1.4152	1.4440

hysteresis, *IEEE Transactions on Automatic Control*, **50**, 2069–2074, (2005).

[3] Ismail, M., Ikhouane, F. and Rodellar, J. The hysteresis Bouc-Wen model, a survey, *Archives of Computational Methods in Engineering*, **16**, 161–188, (2009).

[4] Kwok, N. M., et al. Bouc-Wen model parameter identification for a MR fluid damper using computationally efficient GA, *ISA Transactions*, **46**, 167–179, (2007).

[5] Kunnath, S. K., Mander, J. B. and Fang, L. Parameter identification for degrading and pinched hysteretic structural concrete systems, *Engineering Structures*, **19**, 224–232, (1997).

[6] Zhang, H., et al. Parameter identification of inelastic structures under dynamic loads, *Earthquake Engineering & Structural Dynamics*, **31**, 1113–1130, (2002).

[7] Ni, Y. Q., Ko, J. M. and Wong, C. W. Identification of non-linear hysteretic isolators from periodic vibration tests, *Journal of Sound and Vibration*, **217**, 737–756, (1998).

[8] Xue, X. M., et al. Semi-active control strategy using genetic algorithm for seismically excited structure combined with MR damper, *Journal of Intelligent Material Systems and Structures*, **22**, 291–302, (2011).

[9] Ye, M. and Wang, X. Parameter estimation of the Bouc–Wen hysteresis model using particle swarm optimization, *Smart Materials and Structures*, **16**, 2341, (2007).

[10] Charalampakis, A. E. and Dimou, C. K. Identification of Bouc–Wen hysteretic systems using particle swarm optimization, *Computers & Structures*, **88**, 1197–1205, (2010).

[11] Sivanandam, S. N. and Deepa, S. N. Introduction to genetic algorithms, Springer, (2007).

[12] Habib, S. J. and Al-kazemi, B. S. Comparative study between the internal behavior of GA and PSO through problem-specific distance functions, *The 2005 IEEE Congress on Evolutionary Computation*, **3**, 2190–2191, (2005).

[13] Dimian, M. and Andrei, P. Noise induced resonance phenomena in stochastically driven hysteretic systems, *Journal of Applied Physics*, **109**, 07D330–07D330, (2011).

[14] Jeong, S., et al. Development and investigation of efficient GA/PSO-hybrid algorithm applicable to real-world design optimization, *Computational Intelligence Magazine, IEEE*, **4**, 36–44, (2009).

[15] Li, Y. and Xu, Q. Adaptive sliding mode control with perturbation estimation and PID sliding surface for motion tracking of a piezo-driven micromanipulator, *IEEE Transactions on Control Systems Technology*, **18**, 798–810, (2010).

[16] Assareh, E., et al. Application of PSO (particle swarm optimization) and GA (genetic algorithm) techniques on demand estimation of oil in Iran, *Energy*, **35**, 5223–5229, (2010).

[17] Shi, X. H., et al. An improved GA and a novel PSO-GA-based hybrid algorithm, *Information Processing Letters*, **93**, 255–261, (2005).

[18] Juang, C. F. A hybrid of genetic algorithm and particle swarm optimization for recurrent network design, *IEEE Transactions on Systems, Man, and Cybernetics, Part B: Cybernetics*, **34**, 997–1006, (2004).

[19] Rudolph, G. Convergence analysis of canonical genetic algorithms, *IEEE Transactions on Neural Networks*, **5**, 96–101, (1994).

[20] Knjazew, D. OmeGA: A competent genetic algorithm for solving permutation and scheduling problems, Springer, (2002).

[21] Kennedy, J. Particle swarm optimization, *In Encyclopedia of Machine Learning*, Springer US, (2010).

Vibrations of a Rotationally Restrained Circular Plate Resting on a Concentric Rigid Ring Support

Lokavarapu Bhaskara Rao

School of Mechanical & Building Sciences, VIT University, Chennai Campus, Vandalur-Kelambakkam Road, Chennai-600127, Tamil Nadu, India

Chellapilla Kameswara Rao

Department of Mechanical Engineering, Guru Nanak Institutions Technical Campus, Ibrahimpatnam, Hyderabad -501506, A.P, India

(Received 3 September 2013; accepted 3 October 2015)

In this paper, the vibrations of a circular plate with a rotationally restrained edge that has concentric rigid ring support are studied. The influences of the rotational restraint parameter and radius of internal rigid ring support on the vibration of the plate's natural frequencies are investigated. Frequencies for the first three modes of vibration are obtained and plotted graphically. The cross-over radius and the optimum location point of internal rigid ring support are determined. The results presented in this paper are from exact analysis, and hence can serve as standard values for estimating the accuracy of results obtained from various approximate methods.

1. INTRODUCTION

In many branches of engineering—such as naval, automobile, and civil—continuous plates are extensively used. There exists a great deal of literature on the present subject area of circular plate vibrations, predominantly with free, clamped, and simply supported edges.[1–4] Leissa[5–10] has reported natural frequency results in many of his papers on continuous circular plates, and other researchers have reported results on the influence of internal rigid ring supports on the dynamic characteristics of circular plates.

Bodine[11] has premeditated the axisymmetric free vibrations of the circular plates, and Laura, et al.[12] presented useful results on the natural frequencies of axisymmetric modes of vibration. The case of the influence of rigid supports along with mode switching was studied by Bodine,[13] varying the values of the ring support radius and Poisson's ratio of the circular plate material. Ding Zhou[14] studied the free vibration of arbitrarily shaped plates with concentric ring elastic and/or rigid supports. In realistic circumstances, to fortify the load-carrying capability of the plate, occasionally internal stiffeners and/or concentric supports are used. In such cases, vibrational characteristics of the plate will vary significantly. Hence, the stiffeners' properties and concentric support should be included in the analysis of the circular plates. Many researchers studied the vibration characteristics of the circular plates with a range of boundary situation and internal intensification.[15–26] Wang[26] studied the problem of fundamental frequency of a circular plate on a ring and free boundary and presented the results for the fundamental frequency related to an anti-symmetric mode of vibration when the support radius is small. Many researchers studied the problem of vibrations of circular plates with concentric ring support, as well.[27–30]

Najafizadeh and Mirkhalaf Valashani[31] carried out the vibration analysis of circular plates that have an eccentric circular perforation and a free edge with an attached concentrated mass at any arbitrary position on the plate. The Rayleigh-Ritz variational method was applied to determine the fundamental natural frequency coefficient for the circular plates with the eccentric circular perforation and arbitrarily attached concentrated mass based on the classical plate theory (CPT). Mirkhalaf Valashani[32] utilized the Rayleigh-Ritz method to investigate the transverse vibration of clamped and simply supported circular plates with an eccentric circular perforation and attached concentrated mass. Wang[33] studied the vibration of a circular plate with an attached core and clamped, simply supported, free and sliding boundary conditions.

However, as we know, in practical industrial engineering situations, we seldom come across such ideal edge conditions. The review of research on the vibration of circular plates restrained against rotation can be found in the studies made by Laura, et al.,[34] Laura and Grossi,[35] Narita and Leissa,[36] Irie, et al.,[37] and Veera, et al.[38] It is well-established that the stipulation on an edge frequently tends to be in between the classical edge conditions (simply supported, free and clamped) and may be in contact with elastic restraints, such as rotational restraints.[39–42] However, there is no other research in the literature addressing the common boundary conditions with a rotational restrained edge at the plate's periphery.

In many practical situations such as bolted connections, the plate edge becomes something between a classical simply supported edge and a clamped edge. Often, the edge conditions can be simulated by using a rotational spring. This is exactly what is attempted in this paper. The main intention of this paper is therefore to study the effect of a rigid ring support radius along a concentric circle, and a plate with a rotationally restrained edge (shown in Fig. 1) using an exact method of solution approach. The natural frequencies of a circular plate for varying values of rotational restraint along the plate edge, and the ring support radius for a wide range of non-dimensional parameters, are presented in graphical form for use in design.

2. ANALYTICAL FORMULATION

Consider a plate of radius R, Poisson's ratio ν, density ρ, modulus of elasticity E, and thickness h. Figure 1 shows a plate which has an outer boundary rotationally restrained and simply supported (radius R), and a rigid ring support at radius bR.

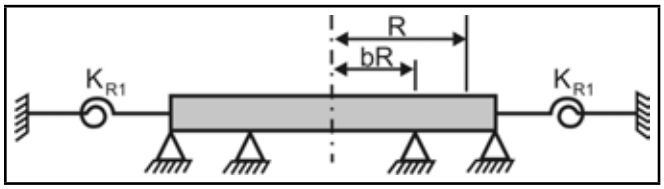

Figure 1. Rotationally restrained circular plate resting on a concentric rigid sing support.

Subscript I denotes $b \leq r \leq 1$ (outer region) and subscript II denotes $0 \leq r \leq b$ (inner region). b, 1 denotes the radius of the inner and outer regions, respectively, after normalizing every length by R. The following fourth-order differential equation[3] describes vibration of plate:

$$D\nabla^4 w + \rho h \frac{\partial^2 w}{\partial t^2} = 0. \tag{1}$$

Here, D represents the flexural rigidity of plate. The general form of the lateral displacement of the vibration of a plate can be expressed as $w = u(r)\cos(n\theta)e^{i\omega t}$, where (r, θ) are polar coordinates, w is the transverse displacement, n is the number of nodal diameters, ω is the frequency, and t is time. The function $u(r)$ is a linear combination of Bessel functions $J_n(kr)$, $Y_n(kr)$, $I_n(kr)$, $K_n(kr)$, and $k = R(\rho\omega^2/D)^{1/4}$ is the square root of the non-dimensional frequency.[3] The general solutions for regions I and II are

$$u_{\mathrm{I}}(r) = C_1 J_n(kr) + C_2 Y_n(kr) + C_3 I_n(kr) + C_4 K_n(kr); \tag{2}$$

$$u_{\mathrm{II}}(r) = C_5 J_n(kr) + C_6 I_n(kr). \tag{3}$$

Considering the rotationally restrained and simply supported edge at the outer region, the boundary conditions can be formulated as

$$M_r(r,\theta) = K_{R1}\frac{\partial w_{\mathrm{I}}(r,\theta)}{\partial r}; \tag{4}$$

$$w_{\mathrm{I}}(r,\theta) = 0. \tag{5}$$

The radial moment at the external periphery is expressed as

$$M_r(r,\theta) = -\frac{D}{R}\left[\frac{\partial^2 w_{\mathrm{I}}(r,\theta)}{\partial r^2} + \nu\left(\frac{1}{r}\frac{\partial w_{\mathrm{I}}(r,\theta)}{\partial r} + \frac{1}{r^2}\frac{\partial^2 w_{\mathrm{I}}(r,\theta)}{\partial \theta^2}\right)\right]. \tag{6}$$

From Eqs. (4) and (6) yields the following expression:

$$\left[\frac{\partial^2 w_{\mathrm{I}}(r,\theta)}{\partial r^2} + \nu\left(\frac{1}{r}\frac{\partial w_{\mathrm{I}}(r,\theta)}{\partial r} + \frac{1}{r^2}\frac{\partial^2 w_{\mathrm{I}}(r,\theta)}{\partial \theta^2}\right)\right] = -R_{11}\frac{\partial w_{\mathrm{I}}(r,\theta)}{\partial r}. \tag{7}$$

Equations (5) and (7) yield the following:

$$u_{\mathrm{I}}''(r) + \nu\left[u_{\mathrm{I}}'(r) - n^2 u_{\mathrm{I}}(r)\right] = -R_{11}u_{\mathrm{I}}'(r); \tag{8}$$

$$u_{\mathrm{I}}(r) = 0. \tag{9}$$

At the outer region (at $r = 1$), the boundary conditions are as follows:

$$u_{\mathrm{I}}''(1) + \nu\left[u_{\mathrm{I}}'(1) - n^2 u_{\mathrm{I}}(1)\right] = -R_{11}u_{\mathrm{I}}'(1); \tag{10}$$

$$u_{\mathrm{I}}(1) = 0; \tag{11}$$

where $R_{11} = \frac{K_{R1}R}{D}$ is the normalized spring constant K_{R1} of the rotational elastic spring at outer periphery.

Apart from the rotationally restrained boundary at the outer edge, the continuity requirements at concentric ring ($r = b$) are as follows:

$$u_{\mathrm{I}}(b) = 0; \tag{12}$$

$$u_{\mathrm{II}}(b) = 0; \tag{13}$$

$$u_{\mathrm{I}}'(b) = u_{\mathrm{II}}'(b); \tag{14}$$

$$u_{\mathrm{I}}''(b) = u_{\mathrm{II}}''(b). \tag{15}$$

The non-trivial solutions to Eqs. (10)–(15) are required. From Eqs. (2), (3), and (10)–(15), we obtained the subsequent equations:

$$\left[\frac{k^2}{4}P_2 + \frac{k}{2}(\nu + R_{11})P_1 - \left(\frac{k^2}{2} + \nu n^2\right)J_n(k)\right]C_1 + \left[\frac{k^2}{4}Q_2 + \frac{k}{2}(\nu + R_{11})Q_1 - \left(\frac{k^2}{2} + \nu n^2\right)Y_n(k)\right]C_2 + \left[\frac{k^2}{4}R_2 + \frac{k}{2}(\nu + R_{11})R_1 + \left(\frac{k^2}{2} - \nu n^2\right)I_n(k)\right]C_3 - \left[\frac{k^2}{4}S_2 - \frac{k}{2}(\nu + R_{11})S_1 + \left(\frac{k^2}{2} - \nu n^2\right)K_n(k)\right]C_4 = 0; \tag{16}$$

$$[J_n(k)]C_1 + [Y_n(k)]C_2 + [I_n(k)]C_3 + [K_n(k)]C_4 = 0; \tag{17}$$

$$J_n(kb)C_1 + Y_n(kb)C_2 + I_n(kb)C_3 + K_n(kb)C_4 = 0; \tag{18}$$

$$J_n(kb)C_5 + I_n(kb)C_6 = 0; \tag{19}$$

$$\left[\frac{k}{2}P_1'\right]C_1 + \left[\frac{k}{2}Q_1'\right]C_2 + \left[\frac{k}{2}R_1'\right]C_3 - \left[\frac{k}{2}S_1'\right]C_4 - \left[\frac{k}{2}P_1'\right]C_5 - \left[\frac{k}{2}R_1'\right]C_6 = 0; \tag{20}$$

$$\left[\frac{k^2}{4}P_2' - \frac{k^2}{2}J_n(kb)\right]C_1 + \left[\frac{k^2}{4}Q_2' - \frac{k^2}{2}Y_n(kb)\right]C_2 + \left[\frac{k^2}{4}R_2' + \frac{k^2}{2}I_n(kb)\right]C_3 + \left[\frac{k^2}{4}S_2' + \frac{k^2}{2}K_n(kb)\right]C_4 - \left[\frac{k^2}{4}P_2' - \frac{k^2}{2}J_n(kb)\right]C_5 - \left[\frac{k^2}{4}R_2' + \frac{k^2}{2}I_n(kb)\right]C_6 = 0; \tag{21}$$

where

$$\begin{aligned}
P_1 &= J_{n-1}(k) - J_{n+1}(k); & P_2 &= J_{n-2}(k) + J_{n+2}(k);\\
Q_1 &= Y_{n-1}(k) - Y_{n+1}(k); & Q_2 &= Y_{n-2}(k) + Y_{n+2}(k);\\
R_1 &= I_{n-1}(k) + I_{n+1}(k); & R_2 &= I_{n-2}(k) + I_{n+2}(k);\\
S_1 &= K_{n-1}(k) + K_{n+1}(k); & S_2 &= K_{n-2}(k) + K_{n+2}(k);\\
P_1' &= J_{n-1}(kb) - J_{n+1}(kb); & P_2' &= J_{n-2}(kb) + J_{n+2}(kb);\\
Q_1' &= Y_{n-1}(kb) - Y_{n+1}(kb); & Q_2' &= Y_{n-2}(kb) + Y_{n+2}(kb);\\
R_1' &= I_{n-1}(kb) + I_{n+1}(kb); & R_2' &= I_{n-2}(kb) + I_{n+2}(kb);\\
S_1' &= K_{n-1}(kb) + K_{n+1}(kb); & S_2' &= K_{n-2}(kb) + K_{n+2}(kb).
\end{aligned}$$

3. SOLUTION

For the given values of n, ν, R_{11}, and b Eqs. (16)–(21) derived above are solved to obtain an exact characteristic frequency equation by suitably eliminating the coefficients C_1, C_2, C_3, C_4, C_5, and C_6. The frequency parameter k can be

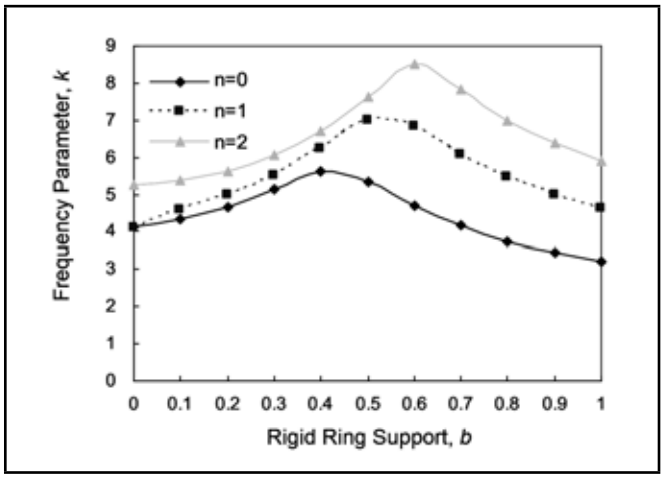

Figure 2. Frequency of a circular plate and concentric rigid ring support radius b for $R_{11} = 2.5$.

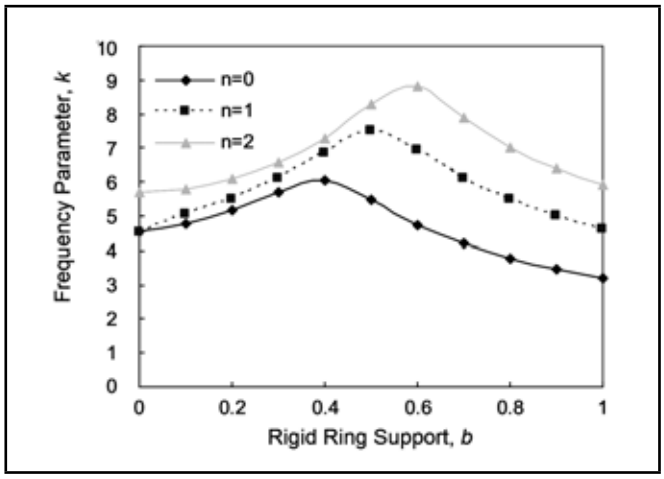

Figure 4. Fundamental frequency k of a circular plate and concentric rigid ring support radius b for $R_{11} = 20$.

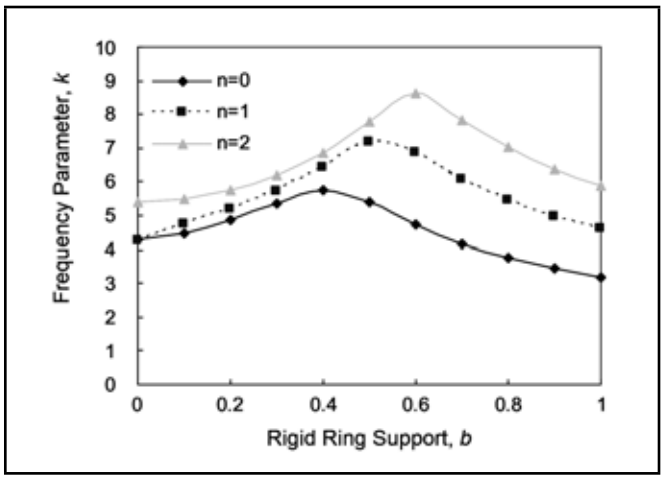

Figure 3. Fundamental frequency k of a circular plate and concentric rigid ring support radius b for $R_{11} = 5$.

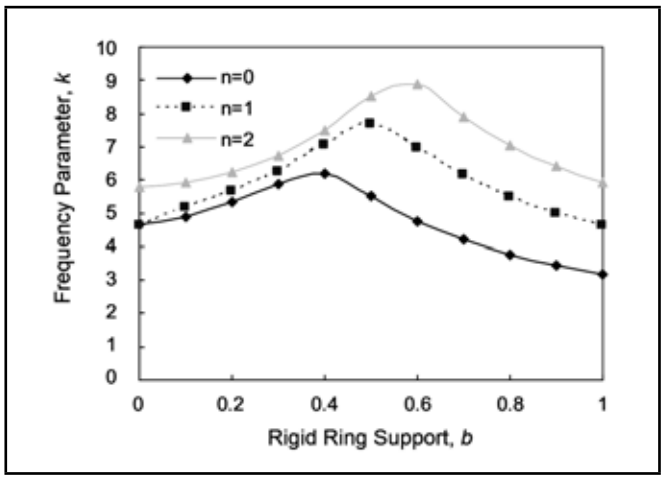

Figure 5. Fundamental frequency k of a circular plate and concentric rigid ring support radius b for $R_{11} = 50$.

determined from the characteristic equation by a simple root search method. Using Mathematica, computer software with symbolic capabilities is used to solve this problem. Poisson's ratio utilized in these studies is 0.3.

4. RESULTS AND DISCUSSION

The fundamental frequency parameters for the first three modes for diverse values of rotational restraints ($R_{11} = 2.5$, 5, 20, 50, 100, 500, 1000, and 10^{16}) are computed. Results for first three modes of vibrations are determined and presented in Figs. 2–9. As seen in Fig. 2, for a particular value of $R_{11} = 2.5$, the curve is unruffled with different segments because of mode switching. The fundamental frequency is related to asymmetric $n = 1$ mode when the concentric ring support radius b is small. Within this segment (the spotted lines in Fig. 2), the fundamental frequency reduces as the value of ring support radius b decreases. On the higher concentric rigid support radius, the fundamental frequency is related to the axisymmetric mode. Within the other segment (the continuous lines in Fig. 2), the fundamental frequency increases as b increases up to a peak point, corresponding to the maximum frequency, and thereafter decreases as b increases in value, as shown in Fig. 2.

Mode switching takes place at $b = 0.012427$, and the fundamental frequency parameter depends on the asymmetric mode when $b \leq 0.012427$ (as shown by spotted lines in Fig. 2). When the value of b goes beyond 0.012427, the axisymmetric mode leads to an accurate fundamental frequency, as shown by constant lines in Fig. 2. The optimum location is the critical radial point for the concentric rigid ring support corresponding to the maximum frequency parameter. The optimum location of concentric rigid ring support and corresponding fundamental frequencies are $b = 0.4$ and $k = 5.62304$, respectively, which are equal to the nodal radius related to the axisymmetric mode and its frequency.

Similarly, it has been observed from Figs. 3–9, for varying values of the rotational restraint ($R_{11} = 2.5$, 5, 20, 50, 100, 500, 1000, and 10^{16}) parameter, that the curve is unruffled with different segments because of the switching of vibration modes. The fundamental frequency is related to the asymmetric $n = 1$ mode when the concentric ring support radius b is small. Within this segment (the spotted lines in Figs. 3–9), the fundamental frequency reduces as the value of the ring support radius b decreases. On higher values of the concentric rigid support radius, the fundamental frequency is related to the axisymmetric mode. Within this segment (the continuous lines in Figs. 3–9), the fundamental frequency increases as b decreases up to a peak point corresponding to the maximum frequency, and thereafter decreases as b decreases in value, as shown in Figs. 3–9. The cross-over radius is the radius of the ring support where the switching of vibration mode occurs. The cross-over radius b_{cor} and the corresponding frequency parameters

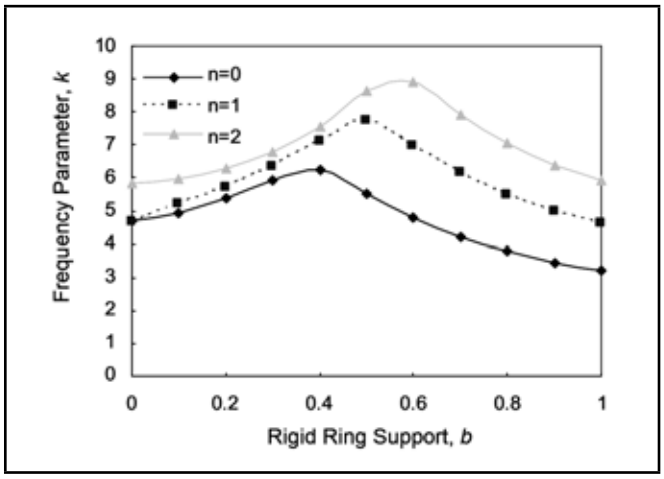

Figure 6. Fundamental frequency k of a circular plate and concentric rigid ring support radius b for $R_{11} = 100$.

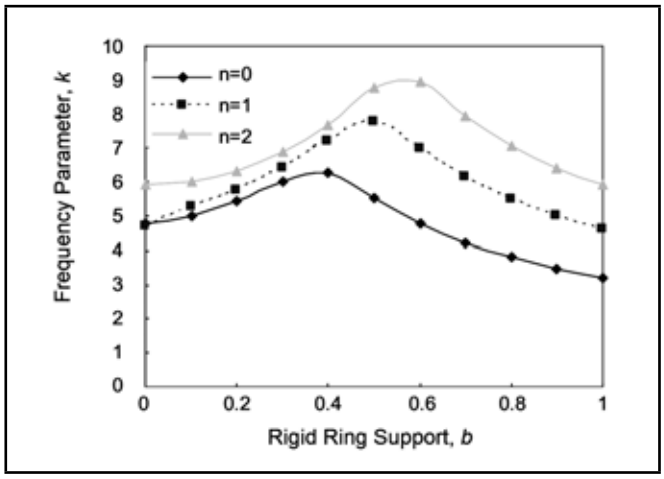

Figure 8. Fundamental frequency k of a circular plate and concentric rigid ring support radius b for $R_{11} = 1000$.

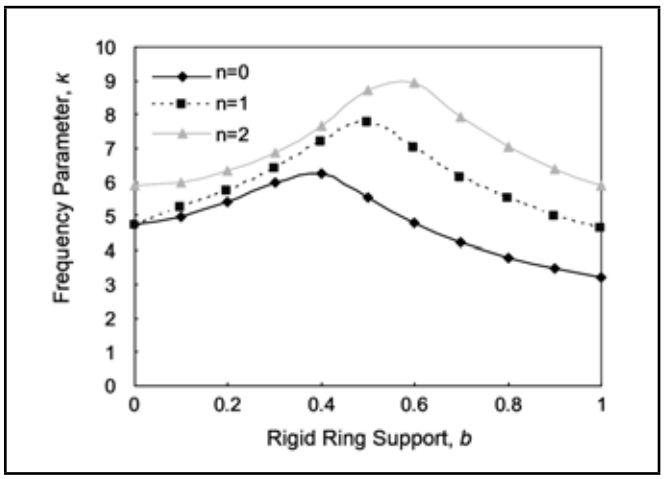

Figure 7. Fundamental frequency k of a circular plate and concentric rigid ring support radius b for $R_{11} = 500$.

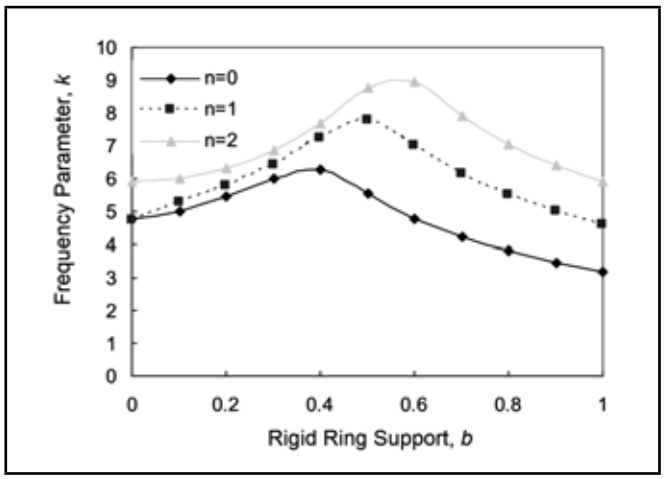

Figure 9. Fundamental frequency k of a circular plate and concentric rigid ring support radius b for $R_{11} = 10^{16}$.

k_{cor} are determined and presented in Table 1. In addition, the optimal solutions (the optimal position of concentric rigid ring support b_{opt} and subsequent fundamental frequency k_{opt}) are determined and presented in Table 2.

From the results obtained, it can be observed that the cross-over radius increases from 0.01242 to 0.017216 as the rotational restraint parameter R_{11} varies from 2.5 to 10^{16}. The optimal location is 0.4, which remains constant from $R_{11} = 2.5$ to 0.4 for $R_{11} = 10^{16}$. However, the fundamental frequency increases from 5.62304 to 6.27065 at the respective optimal locations.

In addition to the variation of the fundamental frequency parameters for the first three modes for diverse values of rotational restraints ($R_{11} = 2.5$, 5, 20, 50, 100, 500, 1000, and 10^{16}) as shown in Figs. 2–9, the percentage of variation of frequency due to the rotational restraints are computed. The percentage increment in the frequency parameter for the first three modes is presented in Table 3. It is noted that for a given radius, the percentage increment decreases for the first three modes ($n = 0$, $n = 1$, and $n = 2$) as the rotational restraint parameter R_{11} varies from 2.5 to 10^{16} in each case, i.e. for the first three modes. The percentage of variation of frequency as the rotational restraint parameter R_{11} varies from 2.5 to 10^{16} for the first three modes is shown in Fig. 10. It is noted from Fig. 10, which, for a given mode and as the rotational restraint parameter R_{11} varies from 2.5 to 10^{16}, that the percentage increment in frequency increases first and then decreases as the rigid ring radius parameter increases. Also, it is observed that there is a cross-over radius of the variation of frequency with three modes.

Results of this type are not available in the published literature. The values of the fundamental frequency for the axisymmetric mode very closely resemble those presented by Laura, et al.[12] A comparison of the results is shown in Table 4, wherein the values of the exact fundamental frequency for the plate with a free boundary (setting $R_{11} \to 0$ to the current predicament) are compared to those presented by Wang.[26] From a realistic point of view, when the rotational stiffness parameter becomes small, the edge tends to become a quasi-simply supported edge, and when it becomes larger, it tends to become very close to that of a clamped edge.

5. CONCLUSIONS

The fundamental frequencies of a rotationally restrained circular plate resting on a concentric rigid ring support have been obtained for a wide range of parametric values in this paper. It can easily be seen that the fundamental mode of frequency switches from $n = 1$ to $n = 0$ at a specific radius of the concentric ring. Mode switching is noted and computed exactly. The optimal solutions for internal concentric rigid ring support and the corresponding fundamental frequency are computed exactly, and the results are obtained from closed form solu-

Table 1. The cross-over radius, b_{cor} and the corresponding frequency parameters, k_{cor}.

R_{11}	2.5	5	20	50	100	500	1000	10^{16}
b_{cor}	0.01242	0.01436	0.01640	0.01704	0.01738	0.01713	0.01682	0.017216
k_{cor}	4.16626	4.32284	4.60973	4.71843	4.76269	4.7977	4.79848	4.80809

Table 2. Optimal locations (concentric rigid support, b_{opt} and subsequent frequency, k_{opt}).

R_{11}	2.5	5	20	50	100	500	1000	10^{16}
b_{opt}	0.4	0.4	0.4	0.4	0.4	0.4	0.4	0.4
k_{opt}	5.62304	5.77268	6.06861	6.17972	6.22338	6.26089	6.26567	6.27065

Table 3. Percentage increment of frequency for the first there modes as the rotational restraint parameter R_{11} varies from 2.5 to 10^{16}.

b	$n=0$ ($R_{11}=2.5$ to 10^{16})	$n=1$ ($R_{11}=2.5$ to 10^{16})	$n=2$ ($R_{11}=2.5$ to 10^{16})
0	15.04128004	14.74715067	11.87518234
0.1	15.5284128	14.75920692	12.14681841
0.2	16.1720786	15.21135106	12.82798834
0.3	16.35934421	15.80606952	13.74803696
0.4	11.51707973	16.13928891	14.74936342
0.5	3.341207227	11.22475509	15.10117797
0.6	1.928786856	2.289155392	5.179809962
0.7	1.531773363	1.262661622	1.178654743
0.8	1.188432836	0.988562572	0.83312529
0.9	0.706107481	0.639596197	0.580342714
1	0	0	0

Table 4. Comparison of fundamental frequency for $\nu = 0.3$, with Wang,[26] for free edge.

Ring support radius, b	Wang[26]	Present
0	0	0
0.02	1.501	1.50077
0.05	1.634	1.63422
0.1	1.789	1.78911
0.15	1.922	1.92226
0.2	2.051	2.05103

tions. Thus, the results presented in this paper are expected to serve as benchmark solutions for comparison to those from approximated methods. The exact results presented in the various graphs and tables included in this paper are also expected to be of use in various design-engineering applications.

REFERENCES

[1] Timoshenko, S. and Woinowsky-Krieger, S. *Theory of Plates and Shells*, McGraw-Hill, New York, (1959).

[2] Szilard, R. *Theory and Analysis of Plates*, Prentice-Hall, New Jersey, (1974).

[3] Leissa, A. W. *Vibration of Plates*, NASA SP-160, (1969).

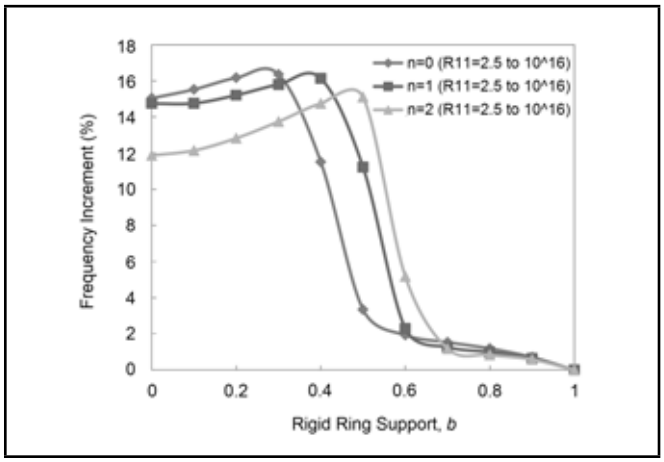

Figure 10. The percentage of variation of frequency as the rotational restraint parameter R_{11} varies from 2.5 to 10^{16} for the first three modes.

[4] Mcleod, A. J. and Bishop, R. E. D. The forced vibration of circular flat plates, *Mechanical Engineering Science Monograph*, **1**, 1–33, (1965).

[5] Leissa, A. W. Recent research in plate vibrations: classical theory, *Shock and Vibration Digest*, **9** (10), 13–24, (1977). DOI:10.1177/058310247700901005

[6] Leissa, A. W. Recent research in plate vibrations: complicating effects, *Shock and Vibration Digest*, **10** (12), 21–35, (1977). DOI:10.1177/058310247801001204

[7] Leissa, A. W. Plate vibration research, 1976–1980: classical theory, *Shock and Vibration Digest*, **13** (9), 11–22, (1981). DOI:10.1177/058310248101300905

[8] Leissa, A. W. Plate vibration research, 1976–1980: complicating effects, *Shock and Vibration Digest*, **13** (10), 17–36, (1981). DOI:10.1177/058310248101301004

[9] Leissa, A. W. Recent research in plate vibrations, 1981–1985, Part I. Classical theory, *Shock and Vibration Digest*, **19** (2), 11–18, (1987). DOI:10.1177/058310248701900204

[10] Leissa, A. W. Recent research in plate vibrations, 1981–1985, Part II. Complicating effects, *Shock and Vibration Digest*, **19** (3), 10–24, (1987). DOI:10.1177/058310248701900304

[11] Bodine, R. Y. The fundamental frequency of a thin, flat circular plate supported along a circle of arbitrary radius, *Journal of Applied Mechanics*, **26**, 666–668, (1959).

[12] Laura, P. A. A., Gutierrez, R. H., Vera, S. A. and Vega, D. A. Transverse vibrations of a circular plate with a free edge and a concentric circular support, *Journal of Sound and Vibration*, **223** (5), 842–845, (1999). DOI:10.1006/jsvi.1998.2150

[13] Bodine, R. Y. Vibration of Circular Plate supported by a concentric ring of arbitrary radius, *Journal of Acoustical Society of America*, **41**, 1551–1551, (1967).

[14] Zhou, Ding Free vibration of arbitrarily shaped plates with concentric ring elastic and/or rigid supports, *Computers & Structures*, **50** (5), 685–692, (1994). DOI:10.1016/0045-7949(94)90427-8

[15] Magrab, E. B. *Vibrations of Elastic Structural Members*, Sijthoff & Noordhoff, The Netherlands, (1979).

[16] Weisensel, G. N. Natural frequency information for circular and annular plates, *Journal of Sound and Vibration*, **133** (1), 129–134, (1989). DOI:10.1016/0022-460x(89)90987-5

[17] Azimi, S. Free vibration of circular plates with elastic or rigid interior support, *Journal of Sound and Vibration*, **120** (1), 37–52, (1988). DOI:10.1016/0022-460x(88)90333-1

[18] Lam, K. Y. and Liew, K. M. A numerical model based on orthogonal plate functions for vibration of ring supported elliptical plates, *Computational Mechanics*, **9** (2), 113–126, (1992). DOI:10.1007/bf00370066

[19] Wang, C. M. and Thevendran, V. Vibration analysis of annular plates with concentric supports using a variant of Rayleigh-Ritz method, *Journal of Sound and Vibration*, **163** (1), 137–149, (1993). DOI:10.1006/jsvi.1993.1153

[20] Liew, K. M. and Lam, K.Y. Transverse vibration of solid circular plates continuous over multiple concentric annular supports, *Transactions of ASME. Journal of Applied Mechanics*, **60** (1), 208–210, (1993). DOI:10.1115/1.2900749

[21] Liew, K. M., Xiang, Y., Wang, C. M. and Kitipornchai, S. Flexural vibration of shear deformable circular and annular plates on ring supports, *Computer Methods in Applied Mechanics and Engineering*, **110** (3–4), 301–315, (1993). DOI:10.1016/0045-7825(93)90211-f

[22] Liew, K. M., Xiang, Y., Kitipornchai, S. and Wang, C. M. Buckling and vibration of annular Mindlin plates with internal concentric ring supports subject to in-plane radial pressure, *Journal of Sound and Vibration*, **177** (5), 689–707, (1994). DOI:10.1006/jsvi.1994.1461

[23] Xiang, Y. Vibration of Circular Mindlin Plates with concentric elastic ring support, *International Journal of Mechanical Sciences*, **45** (3), 497–517, (2003). DOI:10.1016/s0020-7403(03)00059-6

[24] Wang, C. Y. and Wang, C. M. Fundamental Frequencies of Circular Plates with internal elastic ring support, *Journal of Sound and Vibration*, **263** (5), 1071–1078, (2003). DOI:10.1016/s0022-460x(03)00275-x

[25] Bhaskara Rao, L. and Kameswara Rao, C. Buckling of circular plates with an internal elastic ring support and elastically restrained guided edge against translation, *Mechanics Based Design of Structures and Machines*, **37** (1), 60–72, (2009). DOI:10.1080/15397730802706672

[26] Wang, C. Y. On the fundamental frequency of a circular plate supported on a ring, *Journal of Sound and Vibration*, **243** (5), 945–946, (2001). DOI:10.1006/jsvi.2000.3463

[27] Kunukkasseril, V. X. and Swamidas, A. S. J. Vibration of continuous circular plates, *International Journal of Solids and Structures*, **10** (6), 603–619, (1974). DOI:10.1016/0020-7683(74)90045-6

[28] Singh, A. V. and Mirza, S. Free axisymmetric vibration of a circular plate elastically supported along two concentric circles, *Journal of Sound and Vibration*, **48** (3), 425–429, (1976). DOI:10.1016/0022-460x(76)90068-7

[29] Sasaki, M. and Chonan, S. Vibration and stability of elastically supported circular plates under conservative and non-conservative loads, *Journal of Sound and Vibration*, **103** (1), 99–108, (1985). DOI:10.1016/0022-460x(85)90249-4

[30] Azimi, S. Free vibration of circular plates with elastic edge supports using the receptance method, *Journal of Sound and Vibration*, **120** (1), 19–35, (1987). DOI:10.1016/0022-460x(88)90332-x

[31] Najafizadeh, M. M. and Mirkhalaf Valashani, S. M. Vibration analysis of circular plates with an eccentric circular perforation with a free edge and attached concentrated mass at any arbitrary position, *Australian Journal of Basic and Applied Sciences*, **5** (12), 3052–3058, (2011).

[32] Mirkhalaf Valashani, S. M. Transverse vibration of clamped and simply supported circular plates with an eccentric circular perforation and attached concentrated mass, *Journal of Solid Mechanics*, **1**, 37–44, (2009).

[33] Wang, C. Y. Vibration of a circular plate with an attached core, *Journal of Sound and Vibration*, **280** (3–5), 1075–1082, (2005). DOI:10.1016/j.jsv.2004.02.029

[34] Laura, P. A. A., Paloto, J. C., and Santos, R. D. A note on the vibration and stability of a circular plate elastically restrained against rotation, *Journal of Sound and Vibration*, **41** (2), 177–180, (1975). DOI:10.1016/s0022-460x(75)80095-2

[35] Laura, P. A. A. and Grossi, R. O. Influence of Poisson's ratio on the lower natural frequencies of transverse vibration of a circular plate of linearly varying thickness and with an edge elastically restrained against rotation, *Journal of Sound and Vibration*, **60** (4), 587–590, (1978). DOI:10.1016/s0022-460x(78)80094-7

[36] Narita, Y. and Leissa, A. W. Transverse vibration of simply supported circular plates having partial elastic constraints, *Journal of Sound and Vibration*, **70** (1), 103–116, (1980). DOI:10.1016/0022-460x(80)90557-x

[37] Irie, T., Yamada, G., and Tanaka, K. Free vibration of circular plate elastically restrained along some radial segments, *Journal of Sound and Vibration*, **89** (3), 295–308, (1983). DOI:10.1016/0022-460x(83)90538-2

[38] Vera, S. A., Febbo, M., Rossit, C. A., and Dolinko, A. E. Transverse vibrations of circular annular plates with edges elastically restrained against rotation, used in acoustic underwater transducers, *Ocean Engineering*, **29** (10), 1201–1208, (2002). DOI:10.1016/s0029-8018(01)00083-x

[39] Kim, C. S. and Dickinson, S. M. The Flexural Vibration of the Isotropic and Polar Orthotropic Annular and Circular Plates with elastically restrained peripheries, *Journal of Sound and Vibration*, **143** (1), 171–179, (1990). DOI:10.1016/0022-460x(90)90576-l

[40] Wang, C. Y. and Wang, C. M. Buckling of Circular Plates with an internal ring support and elastically restrained edges, *Thin-walled Structures*, **39** (9), 821–825, (2001). DOI:10.1016/s0263-8231(01)00031-3

[41] Bhaskara Rao, L. and Kameswara Rao, C. Buckling of annular plates with elastically restrained external and internal edges, *Mechanics Based Design of Structures and Machines*, **41** (2), 222–235, (2013). DOI:10.1080/15397734.2012.717495

[42] Bambill, D. V., La Malfa, S., Rossit, C. A. and Laura, P. A. A. Analytical and experimental investigation on transverse vibrations of solid, circular and annular plates carrying a concentrated mass at an arbitrary position with marine applications, *Ocean Engineering*, **31** (2), 127–138, (2004). DOI:10.1016/s0029-8018(03)00116-1

Stability and Accuracy of Aeroacoustic Time-Reversal using the Pseudo-Characteristic Formulation

A. Mimani

School of Mechanical Engineering, The University of Adelaide, South Australia 5005, Australia

C. J. Doolan

2 School of Mechanical and Manufacturing Engineering, University of New South Wales, New South Wales 2052, Australia

P. R. Medwell

School of Mechanical Engineering, The University of Adelaide, South Australia 5005, Australia

(Received 19 September 2013; accepted 9 December 2014)

This paper investigates the stability and accuracy of the aeroacoustic Time-Reversal (TR) simulation using the Pseudo-Characteristic Formulation (PCF). To this end, the forward simulation of acoustic wave propagation in 1-D and 2-D computational domain with a uniform mean flow was implemented using the PCF of the Linearised Euler Equations (LEE). The spatial derivatives in the opposite propagating fluxes of the PCF were computed using an overall upwind-biased Finite-Difference (FD) scheme and a Runge-Kutta scheme was used for time-integration. The anechoic boundary condition (ABC) was implemented for eliminating spurious numerical reflections at the computational boundaries, thereby modelling a free-space. The stability of 1-D forward and TR (with only time-reversed acoustic pressure as the input at the boundary nodes) simulations were analysed by means of an eigenvalue decomposition, wherein it was shown that opposite upwinding directions must be considered while using the overall upwind-biased FD scheme. Furthermore, the implementation of ABC was found to be crucial for ensuring the stability of the forward simulation over a large time duration and the 2-D TR simulations. The overall central Dispersion-Relation Preserving (DRP) FD schemes were however, found to be unstable and unsuitable for TR simulation. The accuracy of both the forward and the TR simulations using the PCF was assessed by comparing the simulation results against the corresponding analytical solutions of a spatially and temporally evolving Gaussian pulse. It was shown that numerically reversing the mean flow direction during TR (using the PCF) and only the time-reversed acoustic pressure as input at the boundaries is sufficient to accurately back-propagate the waves and localise the initial emission point of the pulse in 1-D or 2-D computational domain.

1. INTRODUCTION

The acoustic Time-Reversal (TR) method, developed by Fink, et al.,[1,2] is a promising method to localise acoustic sources in time-domain and is explained by the following two-step procedure:

1. In the first step, the acoustic pressure field radiated by the source(s) is recorded by microphone line arrays (LAs) in a Time-Reversal Mirror (TRM) during experiments, or stored at the boundary nodes (virtual microphones) during forward simulations, either (a) over LAs completely enclosing the sources, or (b) over a limited angular aperture LA(s) that only partially encloses the source(s).

2. In the second step, the recorded acoustic pressure time-history is reversed in time followed by emission from "numerical sources" at the boundary nodes. The back-propagated acoustic pressure signals undergo a constructive interference to form spatio-temporal maxima[3] during TR simulations, which corresponds to the spatial location of the source(s). Method (a) which uses the enclosing LAs, can account for almost the total acoustic power radiated; therefore, back-propagation from this configuration yields the most accurate prediction of the source location, characteristics, and strength. Method (b), however, can account for only a fraction of the acoustic power radiated, thereby limiting the ability of TR to identify the location and nature of sources.[4]

Fink, et al.[2] provide an excellent review of the TR method and discuss its applications in various fields such as hydrodynamics, ultrasound medical imaging, and diagnostic and non-destructive testing. The TR method has also been used for long-range communication in deep underwater acoustics,[5] structural dynamics for health monitoring,[6] in the presence of a reflecting surface,[7] and in electromagnetic wave propagation.[8] Different methods have been presented to enhance the focal-resolution of TR, namely an active cancellation technique called the Time-Reversal Acoustic Sink (TRAS), developed by Bavu, et al.,[9] and a passive radial damping approach mimicking an acoustic sink called the Point-Time-Reversal-Sponge-Layer (PTRSL), developed by the present authors.[10] The application of the TR method in Computational Aeroacoustics (CAA) for localising sound sources in a flow field is,

however, relatively new. Deneuve, et al.[11] made use of the TR method for the first time to localise aeroacoustics sources. The forward evolution of the pressure and velocity fields was simulated by the numerical solution of the 2-D homoentropic nonlinear Euler equations using the Pseudo-Characteristic Formulation (PCF) proposed by Sesterhenn,[12] wherein the spatial derivatives in the opposite propagating fluxes were computed using an overall upwind-biased Finite-Difference (FD) scheme.[13] As the forward evolution was implemented numerically, it was possible to obtain both the pressure and particle velocity time-histories at the boundary nodes of the rectangular computational domain. Furthermore, the field variables corresponding to the final time instant (during forward simulation) were also stored at all nodes of the domain, and these data were used as an initial condition during the TR simulation. Both the time-reversed pressure and particle velocity, along with the subsonic inflow boundary conditions, were imposed on the computational boundaries during the TR simulation.

The main limitation in the TR simulation (using the PCF[12]) of Deneuve, et al.[11] is the use of time-reversed particle velocity histories at boundary nodes. This is because, in an experimental set-up, only the acoustic pressure may be measured using a microphone LA(s), while it is difficult to simultaneously measure the acoustic particle velocity history. Transducer arrays that can measure both the acoustic pressure and acoustic particle velocities (using 3-D intensity probes) are available with present technology; however, such transducers are usually very expensive. Hence, for practical considerations, measurement of only the acoustic pressure is feasible, and naturally the algorithm implementing the TR simulation using the Linearised Euler Equations[14,15] (LEE) must depend only on the time-reversed acoustic pressure history as the input for accurately localising the acoustic source(s). It is noted that the mean flow profile (about which the Euler equations are linearized) may be measured experimentally using hot-wire anemometry (or other techniques), and that the simulations using the LEE can accurately model the interaction between acoustic perturbations and the mean flow field.[3] Another limitation of the TR simulation of Deneuve, et al.[11] is use of the acoustic pressure and velocity histories stored at all the nodes during the final instant of the forward simulation as the initial condition in the TR simulation. Experimentally measuring and storing the acoustic field over the entire experiment is impossible.

The accuracy, as well as the stability analysis, of TR simulation of the LEE using only the time-reversed acoustic pressure history as the input are, therefore, necessary. Padois, et al.[3] demonstrate the accuracy of TR simulation for localising time-harmonic aeroacoustic sources using only the experimentally obtained acoustic pressure time-history measured over a microphone LA in a TRM located outside of the flow in an Anechoic Wind Tunnel (AWT). Their TR simulations, based on the numerical solution of the 2-D LEE using the 4th order Dispersion Relation Preserving (DRP) central FD schemes,[16] were able to satisfactorily estimate the monopole and dipole source locations in a shear flow field. However, their TR simulation of the LEE was not implemented using the PCF, which splits the derivative of acoustic variables into a pair of opposite propagating fluxes[12] or "pseudo-waves". This feature of the PCF makes it ideally suited for the use of upwind-biased FD schemes in comparison to the Flux-Vector Splitting (FVS) approaches.[17,18] The use of upwind-biased FD schemes is preferred over the central DRP schemes[16] because the non-zero damping (at the unresolved high-frequencies) in the former is crucial for ensuring the temporal stability of the TR simulation of the LEE, which has not been analysed in the previous works.[3,4,10,11] Indeed, the temporal stability of forward simulation of the LEE based on the PCF and using an overall (a) upwind-biased FD scheme or (b) central DRP FD scheme has also not been analysed previously,[11–13] although the stability of the overall compact FD schemes used for the forward simulation of the simple 1-D scalar wave equation is established.[19] Furthermore, although the aeroacoustic TR simulation is shown to accurately localise sound sources in flow fields,[3,4,10,11] the results have not been compared against the corresponding analytical solution, and hence are not formally validated.

This work, therefore, analyses the temporal stability and accuracy of both the forward and TR simulations of the 1-D and 2-D LEE implemented using the PCF based on (a) an overall upwind-biased FD scheme, and (b) an overall central DRP FD scheme.[16,20] The test cases consist of propagation of an acoustic pulse in both a 1-D and 2-D free-space with mean flow, modelled by the implementation of anechoic boundary condition (ABC) at (1) the terminations of a 1-D duct, and (2) the computational boundaries of a 2-D domain, respectively. The motivation of this analysis is to examine in detail the accuracy of the TR simulation using only the time-reversed acoustic pressure history as the input Dirichlet conditions[3] at the boundaries of the 2-D computational domain (involving the propagation of cylindrical wave fronts). The present work is a part of a larger study that aims to investigate the suitability of TR for experimental aeroacoustics, with a view to obtain important insights into the mechanism of flow-induced turbulent noise generation. Indeed, the authors have implemented TR simulations on experimentally-obtained acoustic pressure data sampled on two LAs of microphones to demonstrate the dipole source nature (at the Aeolian tone) of the flow-induced noise generated by a circular cylinder located in a cross-flow in the AWT of The University of Adelaide.[21] However, the TR is at an early stage in the field of aeroacoustics, and important fundamental work such as that presented here is essential to provide a strong foundation for its future applications.

The paper is organised as follows: Section 2 describes the numerical method for implementing the 1-D/2-D forward and TR simulations of the LEE based on the PCF using the overall upwind-biased FD schemes and implementation of ABC. Section 3 analyses the stability of 1-D forward and TR simulations using the PCF and two classes of overall FD schemes — (a) the upwind-biased FD scheme and (b) the central DRP FD scheme by means of an eigenvalue decomposition. Section 4 analyses the accuracy of 1-D/2-D forward and TR simulation results by comparison against the corresponding analytical solution. The important contributions of this work are then summarised in Section 5.

2. METHODOLOGY: NUMERICAL IMPLEMENTATION OF THE SIMULATIONS

In this section, the numerical implementation of the forward and TR simulations on 1-D and 2-D computational domains (in Cartesian coordinates) is described. To this end, the homogenous 2-D LEE of continuity and momentum (assuming

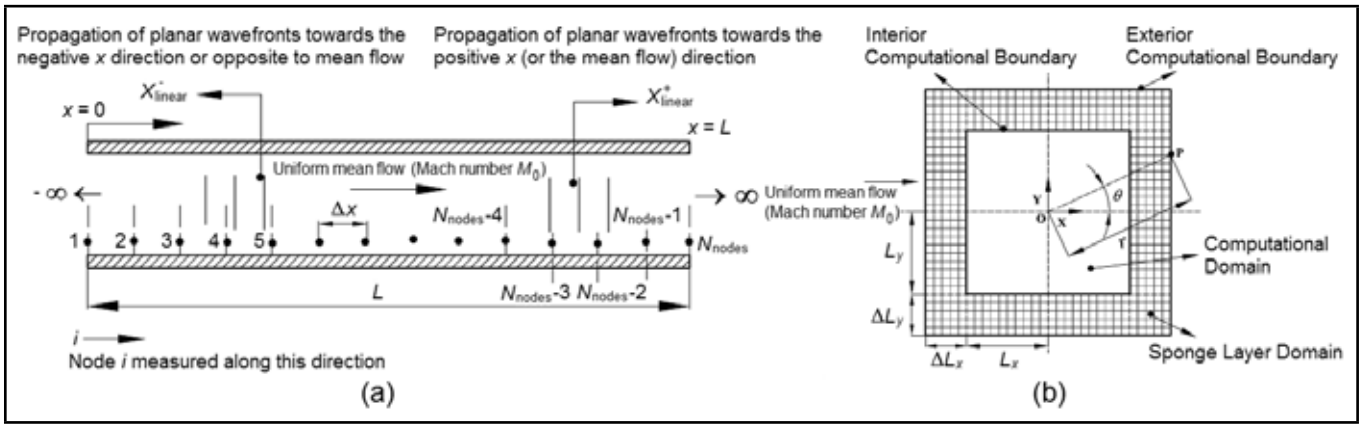

Figure 1. (a) A schematic illustrating the discretisation of a 1-D duct of finite length L (modelling a 1-D free-space) into finite parts (Δx), convention to number the nodes and fluxes ($X^{\pm}_{\text{linear}}$ propagating towards the positive and negative x directions, respectively). (b) A 2-D computational domain fully surrounded by a sponge-layer domain modelling a 2-D free space. The half-length of the computational domain and width of the sponge-layer domain are L_x and ΔL_x along the x direction, respectively, L_y and ΔL_y along the y direction, respectively. The direction of uniform mean flow is considered towards the positive x direction in parts (a) and (b).

homoentropic flow) are considered, and are shown below.[14,15]

$$\frac{\partial \tilde{\rho}}{\partial t} + U_0 \frac{\partial \tilde{\rho}}{\partial x} + \rho_0 \left(\frac{\partial \tilde{u}}{\partial x} + \frac{\partial \tilde{v}}{\partial y} \right) = 0; \tag{1a}$$

$$\rho_0 \frac{\partial \tilde{u}}{\partial t} + \rho_0 U_0 \frac{\partial \tilde{u}}{\partial x} + \frac{\partial \tilde{p}}{\partial x} = 0; \tag{1b}$$

$$\rho_0 \frac{\partial \tilde{v}}{\partial t} + \rho_0 U_0 \frac{\partial \tilde{v}}{\partial x} + \frac{\partial \tilde{p}}{\partial y} = 0; \tag{1c}$$

where $\{\tilde{p}(x,y,t), \tilde{\rho}(x,y,t), \tilde{u}(x,y,t), \tilde{v}(x,y,t)\}$ are the acoustic pressure (Pa), acoustic density (kgm^{-3}), and acoustic particle velocities (ms^{-1}) along the x and y direction, respectively, U_0 is the subsonic uniform mean flow velocity (ms^{-1}) towards the positive x direction, ρ_0 is the ambient density, taken as 1.21 kgm^{-3}, and t is the forward time (s). Furthermore, isentropic conditions are assumed, so that $c_0^2 = \tilde{p}/\tilde{\rho}$, where c_0 denotes the uniform sound speed, taken as 343.14 ms^{-1} in this work. The 1-D homogenous LEE may be obtained by neglecting the spatial variation along the y direction, i.e. ignoring Eq. (1c) and dropping the $(\partial \tilde{v}/\partial y)$ term from Eq. (1a).

2.1. Forward Simulation

2.1.1. Pseudo-Characteristic Formulation (PCF) of the Linearised Euler Equations (LEE)

The forward simulations are implemented by first recasting the homogenous 2-D LEE shown in Eqs. (1a–c) in the PCF[11–13] as

$$\frac{\partial \tilde{p}}{\partial t} = -\frac{\rho_0 c_0}{2} \left(X^{+}_{\text{linear}} + X^{-}_{\text{linear}} + Y^{+}_{\text{linear}} + Y^{-}_{\text{linear}} \right); \tag{2a}$$

$$\frac{\partial \tilde{u}}{\partial t} = -\frac{1}{2} \left(X^{+}_{\text{linear}} - X^{-}_{\text{linear}} \right); \tag{2b}$$

$$\frac{\partial \tilde{v}}{\partial t} = -\frac{1}{2} \left(Y^{+}_{\text{linear}} - Y^{-}_{\text{linear}} \right) - c_0 M_0 \frac{\partial \tilde{v}}{\partial x}; \tag{2c}$$

where

$$X^{\pm}_{\text{linear}} = \pm c_0 (1 \pm M_0) \left\{ \frac{1}{\rho_0 c_0} \frac{\partial \tilde{p}}{\partial x} \pm \frac{\partial \tilde{u}}{\partial x} \right\}; \tag{3}$$

$$Y^{\pm}_{\text{linear}} = \pm c_0 \left\{ \frac{1}{\rho_0 c_0} \frac{\partial \tilde{p}}{\partial y} \pm \frac{\partial \tilde{v}}{\partial y} \right\}; \tag{4}$$

and $M_0 = U_0/c_0$ is the Mach number of subsonic uniform mean flow. In Eqs. (2–4), X^{+}_{linear} denotes the acoustic flux propagating towards the positive x direction with an enhanced speed of $c_0(1 + M_0)$, while X^{-}_{linear} denotes the acoustic flux propagating towards the negative x direction with a reduced speed of $c_0(1 - M_0)$, respectively. Similarly, $Y^{\pm}_{\text{linear}}$ denotes fluxes propagating with a speed c_0 towards the positive and negative y directions, respectively. It is noted that the splitting of the LEE into a pair of opposing fluxes $(X^{\pm}_{\text{linear}}, Y^{\pm}_{\text{linear}})$ facilitate a straightforward implementation of the upwind-biased FD schemes and anechoic boundary condition (ABC),[11,13] which is necessary for suppressing the unresolved spurious high frequency waves, thereby stabilising the simulations. Furthermore, the $c_0 M_0 (\partial \tilde{v}/\partial x)$ term in Eq. (2c) denotes acoustic disturbances advected by the mean flow towards the positive x direction.[13]

2.1.2. Spatial and Temporal Discretization

An overall upwind-biased FD scheme is formulated for computing the spatial derivatives of the acoustic pressure and velocities in the opposing fluxes $(X^{\pm}_{\text{linear}}, Y^{\pm}_{\text{linear}})$ in Eqs. (2a–c). To this end, a 1-D computational domain along the x direction of a finite length L modelled by a duct (with only planar wave propagation) is considered in Fig. 1(a). This domain is discretized into N_{nodes} number of equally spaced nodes of mesh size $\Delta x = L/(N_{\text{nodes}} - 1)$.

The spatial derivative $(\partial \phi/\partial x)^{+}$ of the acoustic field variable ϕ ($\tilde{p}$, $\tilde{u}$ or $\tilde{v}$) in the X^{+}_{linear} flux for the entire 1-D domain is computed using the overall upwind-biased FD schemes formulated in Table 1. It is noted that the use of optimised downwind FD schemes[20,22] at the penultimate and last nodes of the boundaries, as well as the use of 3$^{\text{rd}}$ and 5$^{\text{th}}$ order upwind-biased schemes[23] near the boundary nodes, is necessary because sufficient upwind nodes do not exist near the boundary for use of the 7-point, 4$^{\text{th}}$ order optimised upwind-biased DRP FD scheme.[22]

The overall upwind-biased FD schemes used for computing the spatial derivative $(\partial \phi/\partial x)^{-}$ in the X^{-}_{linear} flux for the entire 1-D domain is similarly formulated by making use of opposite upwinding directions at a node i (with the sign of the stencil coefficients reversed). The efficiency of implementing the overall upwind-biased FD schemes is increased by recasting

Table 1. Overall upwind-biased FD Scheme for computing $(\partial\phi/\partial x)^+$ in the flux X^+_{linear}

Nodes	FD Scheme and formal order of accuracy	Stencil Coefficients
$i = N_{\text{nodes}}$	$\frac{1}{\Delta x}\sum_{k=0}^{k=6} b^{60}_{-k}\phi(N_{\text{nodes}}-k)$, 4th order (Tam[20])	$\left\{ \begin{array}{lll} b^{60}_0 = 2.1922803, & b^{60}_{-1} = -4.7486114, & b^{60}_{-2} = 5.1088519, \\ b^{60}_{-3} = -4.4615671, & b^{60}_{-4} = 2.8334987, & b^{60}_{-5} = -1.1283289, \\ b^{60}_{-6} = 0.2038764. & & \end{array} \right\}$
$i = N_{\text{nodes}}-1$	$\frac{1}{\Delta x}\sum_{k=-5}^{k=1} a^{51}_k\phi(i+k)$, 4th order (Zhuang and Chen[22])	$\left\{ \begin{array}{lll} a^{51}_{-5} = -0.0306490, & a^{51}_{-4} = 0.2022259, & a^{51}_{-3} = -0.6347280, \\ a^{51}_{-2} = 1.2962997, & a^{51}_{-1} = -2.1430548, & a^{51}_0 = 1.1088873, \\ a^{51}_1 = 0.2010190. & & \end{array} \right\}$
$5 \le i \le N_{\text{nodes}}-2$	$\frac{1}{\Delta x}\sum_{k=-4}^{k=2} a^{42}_k\phi(N_{\text{nodes}}-1+k)$, 4th order (Zhuang and Chen[22])	$\left\{ \begin{array}{lll} a^{42}_{-4} = 0.0161405, & a^{42}_{-3} = -0.1228213, & a^{42}_{-2} = 0.4553323, \\ a^{42}_{-1} = -1.2492596, & a^{42}_0 = 0.5018904, & a^{42}_1 = 0.4399322, \\ a^{42}_2 = -0.0412145. & & \end{array} \right\}$
$i = 4$	$\frac{1}{\Delta x}\sum_{k=-3}^{k=2} a^{32}_k\phi(4+k)$, 5th order (Li[23])	$\left\{ \begin{array}{lll} a^{32}_{-3} = -1/30, & a^{32}_{-2} = 1/4, & a^{32}_{-1} = -1, \\ a^{32}_0 = 1/3, & a^{32}_1 = 1/2, & a^{32}_2 = -1/20. \end{array} \right\}$
$i = 3$	$\frac{1}{\Delta x}\sum_{k=-2}^{k=1} a^{21}_k\phi(3+k)$, 3rd order (Li[23])	$\{ \; a^{21}_{-2} = 1/6, \quad a^{21}_{-1} = -1, \quad a^{21}_0 = 1/2, \quad a^{21}_1 = 1/3. \; \}$
$i = 2$	$\frac{1}{\Delta x}\sum_{k=-1}^{k=5} a^{15}_k\phi(2+k)$, 4th order (Zhuang and Chen[22])	$\left\{ \begin{array}{llll} a^{15}_{-1} = -a^{51}_1, & a^{15}_0 = -a^{51}_0, & a^{15}_1 = -a^{51}_{-1}, & a^{15}_2 = -a^{51}_{-2} \\ a^{15}_3 = -a^{51}_{-3}, & a^{15}_4 = -a^{51}_{-4}, & a^{15}_5 = -a^{51}_{-5}. & \end{array} \right\}$
$i = 1$	$\frac{1}{\Delta x}\sum_{k=0}^{k=6} b^{06}_k\phi(1+k)$, 4th order (Tam[20])	$\left\{ \begin{array}{llll} b^{06}_0 = -b^{60}_0, & b^{06}_1 = -b^{60}_{-1}, & b^{06}_2 = -b^{60}_{-2}, & b^{06}_3 = -b^{60}_{-3} \\ b^{06}_4 = -b^{60}_{-4}, & b^{06}_5 = -b^{60}_{-5}, & b^{06}_6 = -b^{60}_{-6}. & \end{array} \right\}$

them in the following matrix form:

$$\frac{\partial\{\phi\}^+}{\partial x} \approx \frac{1}{\Delta x}[\mathbf{R_1}]\{\phi\}; \tag{5a}$$

$$\frac{\partial\{\phi\}^-}{\partial x} \approx \frac{1}{\Delta x}[\mathbf{R_2}]\{\phi\}; \tag{5b}$$

where $\{\phi\} = \{\phi_1, \phi_2, \phi_3, \ldots, \phi_{N_{\text{nodes}}}\}^T$. The spatial derivatives in the fluxes $Y^{\pm}_{\text{linear}}$ are also computed using Eqs. (5a, b) while the $(\partial\tilde{v}/\partial x)$ term in Eq. (2c) is computed using Eq. (5a), as the mean flow direction is towards the positive x direction. The use of two different stencil groups at a given node (or opposite upwinding directions) ensures that the inbuilt dissipation in upwind-biased schemes damps only the unresolved high-frequency waves and does not induce spatially growing oscillations with time, which is important for temporal stability. This is explained by the following discussion:

A harmonic wave $\tilde{p}(x, t = 0) = e^{jk_0x}$ is considered as an initial disturbance where $j = \sqrt{-1}$ and k_0 is the exact wavenumber. The numerical solution of the wave propagating towards positive x direction is given by[24]

$$\tilde{p}(x,t) = e^{j(k_0x - \tilde{\omega}t)} = e^{j(k_0x - \tilde{k}c_0t)} = \underbrace{e^{j[k_0 - \mathrm{Re}(\tilde{k})]c_0t}}_{\text{dispersion}} \cdot \underbrace{e^{\mathrm{Im}(\tilde{k})c_0t}}_{\text{dissipation}} \cdot \underbrace{e^{jk_0(x-c_0t)}}_{\text{exact solution}}; \tag{6}$$

where $\tilde{\omega}$ is the numerical angular frequency and $\tilde{k} = \tilde{\omega}/c_o$ is the numerical wavenumber given by $\beta = k_0\Delta x \approx \tilde{k}\Delta x = -j\left\{\sum_{k=-N}^{k=M} a^{NM}_k e^{j(k\beta)}\right\}$, in which β is the exact non-dimensional wave number and a^{NM}_k are stencil coefficients of a $N + M + 1$ point FD stencil. Equation (6) indicates that for non-dispersive and non-dissipative frequency region given by $\{k_0 - \mathrm{Re}(\tilde{k})\} \to 0$ and $\mathrm{Im}(\tilde{k}) \to 0$, respectively, the numerical solution is an accurate approximation to the exact solution. However, for the unresolved or dispersive frequency region, i.e. $\{k_0 - \mathrm{Re}(\tilde{k})\} \neq 0$, the dissipation should be such that $\mathrm{Im}(\tilde{k}) < 0$ to ensure temporal stability of the numerical solution of the wave propagating towards the positive x direction. Similarly, for temporal stability of the numerical solution of the wave propagating towards the negative x direction, the dissipation should be such that $\mathrm{Im}(\tilde{k}) > 0$ in dispersive frequency region.

The 3rd order Total-Variation-Diminishing (TVD) Runge-Kutta scheme[25] is used for time-integration during the 1-D and 2-D forward simulations, as well as for TR simulations. The time-step Δt is computed a-priori forward simulations in accordance with the Courant–Friedrichs–Lewy (CFL) number equal to 0.2 considered to ensure accuracy of the forward/TR simulations. Equal mesh size given by $\Delta x = \Delta y = 0.005$ m is taken along the x and y directions, respectively, in the 2-D simulations. Furthermore, the same mesh size, $\Delta x = 0.005$ m, is also considered during the 1-D simulations. It is noted that amongst all the FD schemes used to formulate the overall upwind-biased FD scheme (in Table 1), the 4-point, 3rd order standard upwind-biased FD scheme[23] has the least DRP range given by $\alpha_{\text{DRP}} = \tilde{k}_{\max}\Delta x \approx 0.62$, and determines the maximum wavenumber $\tilde{k}_{\max}$ that can be accurately propagated (i.e. without significant dispersion). For the mesh sizes $(\Delta x, \Delta y)$ and c_0, the maximum wavenumber resolution band evaluates to $\tilde{k}_{\max} = [0, \alpha_{\text{DRP}}/\Delta x] = [0, 124]$ m^{-1}.

2.1.3. Implementation of the Anechoic Boundary Condition (ABC)

The ABCs are implemented at the computational boundaries to model a 1-D free-space (represented by a 1-D duct extending infinitely on both sides, as shown in Fig. 1(a)) and a 2-D free-space shown in Fig. 1(b). For the case of 1-D free-space, the ABC is implemented by setting the incoming fluxes to zero at the finite terminations of the duct,[11,13] i.e. $X^+_{\text{linear}}\big|_{x=0} = 0$ and $X^-_{\text{linear}}\big|_{x=L} = 0$, which implies that the

impedance $\tilde{p}_{i-1}/(-\tilde{u}_{i-1}) = \tilde{p}_{i=N_{\text{nodes}}}/\tilde{u}_{i=N_{\text{nodes}}} = \rho_0 c_0$, i.e. the characteristic impedance of the medium. Hence, the acoustic wave impinging on the boundaries is completely transmitted without suffering any reflection. The use of $X^{+}_{\text{linear}}\big|_{x=0} = 0$ and $X^{-}_{\text{linear}}\big|_{x=L} = 0$ boundary conditions is equivalent to the first order Clayton-Engquist-Majda (CEM) ABCs given by[26–28]

$$\left(\frac{\partial \tilde{p}}{\partial t} - c_0\left(1 - M_0\right)\frac{\partial \tilde{p}}{\partial x}\right)\Bigg|_{x=0} = 0; \quad \text{and} \tag{7}$$

$$\left(\frac{\partial \tilde{p}}{\partial t} + c_0\left(1 + M_0\right)\frac{\partial \tilde{p}}{\partial x}\right)\Bigg|_{x=L} = 0; \tag{8}$$

respectively, which is exact for the 1-D acoustic wave propagation in a mean flow.

The 2-D computational domain given by $|x| \leq L_x$, $|y| \leq L_y$ fully surrounded by a sponge-layer domain of widths ΔL_x and ΔL_y along the x and y directions, respectively, as shown in Fig. 1(b) models a 2-D free-space. At the exterior computational boundary, the first-order radiation boundary condition of Tam and Webb[16] (henceforth, referred to as Tam's ABC) is used. The Tam's ABC condition reads

$$\frac{1}{V(\theta)}\frac{\partial \tilde{p}}{\partial t} + \frac{\partial \tilde{p}}{\partial r} + \frac{\tilde{p}}{2r} = 0 \quad \Rightarrow$$
$$\frac{1}{V(\theta)}\frac{\partial \tilde{p}}{\partial t} + \cos\theta\frac{\partial \tilde{p}}{\partial x} + \sin\theta\frac{\partial \tilde{p}}{\partial y} + \frac{\tilde{p}}{2\sqrt{x^2+y^2}} = 0; \tag{9}$$

where $r = (x^2 + y^2)^{1/2}$ is the radius of the point **P** on the exterior computational boundary from the initial position of the peak of Gaussian pulse (i.e. the known source location) denoted by origin **O**, θ is the angle with respect to the x axis, and $V(\theta) = c_0\left(M_0\cos\theta + (1 - M_0^2\sin^2\theta)^{1/2}\right)$ is the convective sound speed (due to subsonic mean flow M_0), considering the directional dependence. It is noted that since the acoustic field at the exterior computational boundary comprises only the outgoing waves, the spatial derivatives ($\partial\tilde{p}/\partial x$, $\partial\tilde{p}/\partial y$) in Eq. (9) are computed in accordance with the value of θ at a particular node. This is discussed as follows:

1. $0 \leq \theta \leq \pi/2$, $\partial\tilde{p}/\partial x$ and $\partial\tilde{p}/\partial y$ are both computed using Eq. (5a);

2. $\pi/2 < \theta \leq \pi$, $\partial\tilde{p}/\partial y$ and $\partial\tilde{p}/\partial x$ are computed using Eq. (5a) and Eq. (5b), respectively;

3. $\pi < \theta \leq 3\pi/2$, $\partial\tilde{p}/\partial x$ and $\partial\tilde{p}/\partial y$ are both computed using Eq. (5b); and

4. $3\pi/2 \leq \theta < 2\pi$, $\partial\tilde{p}/\partial y$ and $\partial\tilde{p}/\partial x$ are computed using Eq. (5b) and Eq. (5a), respectively.

In order to further suppress the spurious reflections during the 2-D forward simulations, the incoming fluxes near the exterior computational boundary are damped over several nodes (N_{sponge}) of a sponge-layer domain[13] with a width of $\Delta L_x = N_{\text{sponge}}\Delta x$ and $\Delta L_y = N_{\text{sponge}}\Delta y$ along the x and y directions, respectively, fully surrounding the computational domain. The damping is implemented using the following equations:

$$Y^{\mp}_{\text{linear}}(x, \pm L_y \pm (N_{\text{sponge}} - n)\Delta y) \rightarrow \tag{10a}$$
$$Y^{\mp}_{\text{linear}}(x, \pm L_y \pm (N_{\text{sponge}} - n)\Delta y) \times G_{\text{sponge}}(n); \tag{10b}$$
$$X^{\mp}_{\text{linear}}(\pm L_x \pm (N_{\text{sponge}} - n)\Delta x, y) \rightarrow \tag{10c}$$
$$X^{\mp}_{\text{linear}}(\pm L_x \pm (N_{\text{sponge}} - n)\Delta x, y) \times G_{\text{sponge}}(n); \tag{10d}$$

where

$G_{\text{sponge}}(n = 0) = 0$ and $G_{\text{sponge}}(n) = e^{-\frac{1}{2}\left(\alpha_{\text{sponge}}\left(\frac{N_{\text{sponge}} - n}{N_{\text{sponge}} - 1}\right)\right)^2}$ for $n = [1, 2, \ldots, N_{\text{sponge}} - 1]$. Here, α_{sponge} is the damping coefficient taken equal to four in this work. It is noted that implementation of Tam's ABC (with or without the inclusion of sponge-layer domain) at boundaries of the 2-D computational domain is crucial for the temporal stability of forward simulation of a pulse propagating in a free-space over a large time duration. The condition $(\partial\tilde{v}/\partial x)\big|_{x=-L_x-\Delta L_x} = 0$ is also implemented to suppress the incoming waves at the $x = -L_x - \Delta L_x$ boundary advected by the mean flow, thereby preventing instability.

2.2. Time-Reversal (TR) Simulation

The 2-D forward simulations are implemented over a sufficiently large time-interval $t = [0, T]$ such that the pulse completely propagates out of the domain, whereby the acoustic pressure $\tilde{p}(x, y, t)$ and particle velocities $\tilde{u}(x, y, t)$, $\tilde{v}(x, y, t)$ are stored at the nodes of all four computational boundaries, i.e. at $x = \pm L_x$, $|y| \leq L_y$ and $y = \pm L_y$, $|x| \leq L_x$ after every time-step. The 2-D TR simulation is implemented by first introducing the following transformations[3,4,10,11] in Eqs. (2–4):

$$t \rightarrow T - \tilde{t}; \tag{11a}$$
$$\tilde{p}(x, y, t) \rightarrow \tilde{p}(x, y, \tilde{t}); \tag{11b}$$
$$\tilde{u}(x, y, t) \rightarrow -\tilde{u}(x, y, \tilde{t}); \tag{11c}$$
$$\tilde{v}(x, y, t) \rightarrow -\tilde{v}(x, y, \tilde{t}); \tag{11d}$$

to obtain the time-reversed 2-D LEE (in the PCF) shown as follows:[10,11]

$$\frac{\partial \tilde{p}}{\partial \tilde{t}} = -\frac{\rho_0 c_0}{2}\left\{\tilde{X}^{+}_{\text{linear}} + \tilde{X}^{-}_{\text{linear}} + \tilde{Y}^{+}_{\text{linear}} + \tilde{Y}^{-}_{\text{linear}}\right\}; \tag{12a}$$
$$\frac{\partial \tilde{u}}{\partial \tilde{t}} = -\frac{1}{2}\left(\tilde{X}^{+}_{\text{linear}} - \tilde{X}^{-}_{\text{linear}}\right); \tag{12b}$$
$$\frac{\partial \tilde{v}}{\partial \tilde{t}} = -\frac{1}{2}\left(\tilde{Y}^{+}_{\text{linear}} - \tilde{Y}^{-}_{\text{linear}}\right) - c_0(-M_0)\frac{\partial \tilde{v}}{\partial x}; \tag{12c}$$

where

$$\tilde{X}^{\pm}_{\text{linear}} = \pm c_0(1 \mp M_0)\left\{\frac{1}{\rho_0 c_0}\frac{\partial \tilde{p}}{\partial x} \pm \frac{\partial \tilde{u}}{\partial x}\right\}; \tag{13a}$$
$$\tilde{Y}^{\pm}_{\text{linear}} = \pm c_0\left\{\frac{1}{\rho_0 c_0}\frac{\partial \tilde{p}}{\partial y} \pm \frac{\partial \tilde{v}}{\partial y}\right\}; \tag{13b}$$

and $\tilde{t}$ denotes the reverse time. It is noted that the time-reversed 2-D LEE given by Eqs. (12a–c) are identical to Eqs. (2a–c), except that the direction of subsonic mean flow is reversed in $\tilde{X}^{\pm}_{\text{linear}}$ fluxes and in the $(\partial\tilde{v}/\partial x)$ term. The reversal of mean flow direction $(M_0 \rightarrow -M_0)$ during the numerical TR simulation (and not in the physical sense) is essential to ensure TR invariance.[3,4,10,11] Furthermore, the derivative $(\partial\tilde{v}/\partial x)$ in

Eq. (12c) is computed using Eq. (5b) due to reversal of the mean flow.

The 2-D TR simulation is implemented using either (a) only $\tilde{p}(x,y,\tilde{t})$, or (b) both $\tilde{p}(x,y,\tilde{t})$ and $-\tilde{u}(x,y,\tilde{t})$, $-\tilde{v}(x,y,\tilde{t})$ as input Dirichlet boundary conditions[3] (which enables the back-propagation of waves into the domain) at $x=\pm L_x$ and $y=\pm L_y$ boundaries after every reverse time-step. It is noted that the sponge-layer domain is not used during the 2-D TR simulation; rather, it is found that implementation of the CEM ABC[26–28] at all four boundaries given by

$$\left(\frac{\partial\tilde{p}}{\partial\tilde{t}} \pm c_0(1\mp M_0)\frac{\partial\tilde{p}}{\partial x}\right)\Bigg|_{x=\pm L_x} = 0; \qquad (14a,b)$$

$$\left(\frac{\partial\tilde{p}}{\partial\tilde{t}} \pm c_0\frac{\partial\tilde{p}}{\partial y}\right)\Bigg|_{y=\pm L_y} = 0; \qquad (14c,d)$$

and at the four corners of the 2-D domain, the use of special corner ABC[28] given by

$$\frac{\partial\tilde{p}}{\partial\tilde{t}} + \frac{c_0}{\sqrt{2}}(1-M_0)\frac{\partial\tilde{p}}{\partial x} + \frac{c_0}{\sqrt{2}}\frac{\partial\tilde{p}}{\partial y}\Bigg|_{x=L_x,y=L_y} = 0; \quad (15a)$$

$$\frac{\partial\tilde{p}}{\partial\tilde{t}} - \frac{c_0}{\sqrt{2}}(1+M_0)\frac{\partial\tilde{p}}{\partial x} + \frac{c_0}{\sqrt{2}}\frac{\partial\tilde{p}}{\partial y}\Bigg|_{x=-L_x,y=L_y} = 0; \quad (15b)$$

$$\frac{\partial\tilde{p}}{\partial\tilde{t}} - \frac{c_0}{\sqrt{2}}(1+M_0)\frac{\partial\tilde{p}}{\partial x} - \frac{c_0}{\sqrt{2}}\frac{\partial\tilde{p}}{\partial y}\Bigg|_{x=-L_x,y=-L_y} = 0; \quad (15c)$$

$$\frac{\partial\tilde{p}}{\partial\tilde{t}} + \frac{c_0}{\sqrt{2}}(1-M_0)\frac{\partial\tilde{p}}{\partial x} - \frac{c_0}{\sqrt{2}}\frac{\partial\tilde{p}}{\partial y}\Bigg|_{x=L_x,y=-L_y} = 0; \quad (15d)$$

is necessary for the temporal stability of 2-D TR simulations.[4,10] In comparison to Tam's ABC, the CEM ABC and the special corner ABC are relatively less accurate in modelling non-reflective boundaries. Nonetheless, it is implemented at the computational boundaries because unlike the forward simulation, the radial distance r of a boundary node from the source location during TR simulation is not known; rather, the robustness of TR algorithm (in a 2-D free-space) must be demonstrated through accurate localization of the source(s) with implementation of approximate ABCs that does not depend on an a-priori estimate of the source location. It is noted that in Eqs. (14a), (15a), and (15d), the spatial derivative $\partial\tilde{p}/\partial x$ at nodes on the $x=L_x$ boundary is computed using Eq. (5a), while $\partial\tilde{p}/\partial x$ at nodes on the $x=-L_x$ boundary in Eqs. (14b), (15b), and (15c) is computed using Eq. (5b). Furthermore, in Eqs. (14c), (15a), and (15b), the spatial derivative $\partial\tilde{p}/\partial y$ at nodes on the $y=L_y$ boundary is computed using Eq. (5a), while $\partial\tilde{p}/\partial y$ at nodes on the $y=-L_y$ boundary in Eqs. (14d), (15c), and (15d) is computed using Eq. (5b). In addition, the incoming normal acoustic fluxes (of the PCF[12] of the 2-D LEE) are also set to zero at the computational boundaries, i.e. $\tilde{X}^{\pm}_{\text{linear}}\big|_{x=\mp L_x} = \tilde{Y}^{\pm}_{\text{linear}}\big|_{y=\mp L_y} = 0$ to reinforce the ABCs during TR simulation.[4,10] The boundary condition $(\partial\tilde{v}/\partial x)\big|_{x=L_x} = 0$ is implemented for the stability of 2-D TR simulation. The 1-D TR simulation is implemented by ignoring Eq. (12c) and the $\tilde{Y}^{\pm}_{\text{linear}}$ fluxes in Eq. (12a) and solving the resultant time-reversed 1-D LEE (in the PCF) with only the time-reversed acoustic pressure as the input Dirichlet condition at the boundary nodes. However, it is found that the use of ABC at the boundary nodes is not necessary for stability of 1-D TR simulation.

3. STABILITY ANALYSIS OF THE 1-D FORWARD AND TR SIMULATIONS: EIGENVALUE DECOMPOSITION

The temporal stability of the forward and TR simulations in the 1-D infinite duct with mean flow using the overall upwind-biased FD scheme and the PCF is evaluated using eigenvalue decomposition. The objective of this analysis is to establish the stability associated with the implementation of the correct upwinding directions in the antagonistic fluxes of the PCF and the appropriate boundary conditions using a 1-D test case.

3.1. Forward Simulation

An eigenvalue problem for an acoustic pulse propagating in the 1-D duct with a mean flow is formulated. To this end, the $[\mathbf{R_1}]$ and $[\mathbf{R_2}]$ matrices are used for computing the spatial derivatives of $\{\tilde{p}\}$ and $\{\tilde{u}\}$ in the $\tilde{X}^{\pm}_{\text{linear}}$ fluxes, respectively, in the PCF of the 1-D LEE. Rearranging the resultant equations in terms of the linear combination of $\{\tilde{p}\}$ and $\{\rho_0 c_0\tilde{u}\}$ yields the following set of semi-discretised ordinary differential equations:

$$\frac{d\{\tilde{p}\}}{dt} = -\frac{c_0}{2(\Delta x)}\Bigg\{\Big[(1+M_0)[\mathbf{R_1}] + (M_0-1)[\mathbf{R_2}]\Big]\{\tilde{p}\} + \Big[(1+M_0)[\mathbf{R_1}] - (M_0-1)[\mathbf{R_2}]\Big]\{\rho_0 c_0\tilde{u}\}\Bigg\}; \quad (16a)$$

$$\frac{d\{\rho_0 c_0\tilde{u}\}}{dt} = -\frac{c_0}{2(\Delta x)}\Bigg\{\Big[(1+M_0)[\mathbf{R_1}] + (1-M_0)[\mathbf{R_2}]\Big]\{\tilde{p}\} + \Big[(1+M_0)[\mathbf{R_1}] - (1-M_0)[\mathbf{R_2}]\Big]\{\rho_0 c_0\tilde{u}\}\Bigg\}. \quad (16b)$$

By substituting $\{\tilde{p}\} = \{\hat{p}\}e^{\omega t}$ and $\{\rho_0 c_0\tilde{u}\} = \{\rho_0 c_0\hat{u}\}e^{\omega t}$ in Eqs. (16a, b) and subsequent algebraic manipulations, the following eigenvalue problem is obtained:

$$[\mathbf{A}]\Big\{\{\hat{p}\}_{N_{\text{nodes}}} \;\; \{\rho_0 c_0\hat{u}\}_{N_{\text{nodes}}}\Big\}^T = \lambda\Big\{\{\hat{p}\}_{N_{\text{nodes}}} \;\; \{\rho_0 c_0\hat{u}\}_{N_{\text{nodes}}}\Big\}^T; \quad (17a)$$

where ω represents the dimensional eigenvalues (complex, in general), $\{\hat{p}\}$ and $\{\rho_0 c_0\hat{u}\}$ denote the corresponding eigenvectors, the matrix $[\mathbf{A}]$ is given by

$$[\mathbf{A}]_{2N_{\text{nodes}}\times 2N_{\text{nodes}}} = -\frac{1}{2}\times \begin{bmatrix}(1+M_0)[\mathbf{R_1}]+(M_0-1)[\mathbf{R_2}] & (1+M_0)[\mathbf{R_1}]-(M_0-1)[\mathbf{R_2}]\\ (1+M_0)[\mathbf{R_1}]+(1-M_0)[\mathbf{R_2}] & (1+M_0)[\mathbf{R_1}]-(1-M_0)[\mathbf{R_2}]\end{bmatrix}; \quad (17b)$$

and $\lambda = (\omega\Delta x)/c_0$ denotes the corresponding non-dimensional eigenvalues of the $[\mathbf{A}]$ matrix. The solution of Eqs. (16a, b) is now obtained in terms of the matrix exponential as[29]

$$\Big\{\tilde{p}(t) \;\; \rho_0 c_0\tilde{u}(t)\Big\}^T = e^{[\mathbf{A}]\frac{c_0 t}{\Delta x}}\Big\{\tilde{p}(t=0) \;\; \rho_0 c_0\tilde{u}(t=0)\Big\}^T; \quad (17c)$$

whereby it becomes evident that the stability of the overall FD scheme depends on the whether the $\mathrm{Re}(\lambda)$ is positive or negative. It is noted that Eqs. (16a, b) are cast in a semi-discrete form because only the spatial derivatives of the acoustic variables are approximated by overall FD schemes, and

time-integration is not considered at this stage. Thus, by assuming modes of the form $\{\tilde{\phi}\} = \{\hat{\phi}\}e^{\omega t}$, discretisation errors due to numerical time-integration are avoided. Therefore, in the eigenvalue problem for the forward simulation given by Eqs. (17a, b), a perfect time-integration is considered[19] and the stability of only spatial discretisation is analysed. Similar conclusions also hold for the eigenvalue analysis of the 1-D TR simulation. Furthermore, it is noted that no boundary conditions are specified in Eq. (17a). However, in order to analyse the temporal stability of the forward simulation of a pulse propagating in the 1-D infinite duct, it is necessary to implement the ABCs by setting $X^{+}_{\text{linear}}\big|_{x=0} = 0$ and $X^{-}_{\text{linear}}\big|_{x=L} = 0$ in Eqs. (17a, b), thereby leading to

$$[\mathbf{A}_{\text{anechoic}}]\Big\{\{\hat{p}\}_{N_{\text{nodes}}} \;\; \{\rho_0 c_0 \hat{u}\}_{N_{\text{nodes}}}\Big\}^T = \lambda\Big\{\{\hat{p}\}_{N_{\text{nodes}}} \;\; \{\rho_0 c_0 \hat{u}\}_{N_{\text{nodes}}}\Big\}^T; \qquad (18)$$

where $[\mathbf{A}_{\text{anechoic}}]$ is defined by Eq. (19), which is the eigenvalue problem incorporating the ABC at both boundaries of the finite 1-D duct.

Figure 2(a) presents the eigenvalue loci of the eigenvalue problem posed in Eq. (18) using the overall upwind-biased FD schemes for $X^{\pm}_{\text{linear}}$ fluxes that are used to simulate the test case 1 with $N_{\text{nodes}} = 1500$ for $M_0 = 0$ and $M_0 = 0.30$. It is evident from Fig. 2(a) that the eigenvalue loci of Eq. (18) consists of closed loop(s) located on the negative side of the real-axis ($\text{Re}(\lambda)$ axis), indicating that opposite upwinding directions in the $X^{\pm}_{\text{linear}}$ fluxes of the PCF (by means of $[\mathbf{R_1}]$ and $[\mathbf{R_2}]$ matrices, respectively) are necessary for temporal stability. Furthermore, the implementation of the ABC at the first and last node of the computational domain (unlike Lu and Sagaut,[13] wherein the ABC was implemented at the first and the last five nodes of the 2-D domain) entirely shifts the eigenvalue loci to the negative side of the $\text{Re}(\lambda)$ axis. Indeed, none of the eigenvalues have positive real parts (regardless of their magnitude), and in order to justify this claim, an exaggerated view of the eigenvalue loci near the imaginary axis in Fig. 2(b) is presented. The lone eigenvalue in each of the loci shown in Fig. 2(b) located 'almost' at the origin has a negative real part of the order of 10^{-7}, thereby implying rather slow decay, but most importantly, a stable solution. Therefore, the implementation of ABC prevents the occurrence of eigenvalues with small positive real parts (of the order of 10^{-3}), which are liable to induce instabilities over large duration (or at later instants) of the forward simulation.[30]

The effect of a subsonic mean flow on the eigenvalue locus of the overall upwind-biased FD scheme is also illustrated in Fig. 2, wherein the mean flow is shown to 'bifurcate' the locus horizontally so that there exists two different loci on the negative side of the $\text{Re}(\lambda)$ axis of the λ plane. One of the eigenvalue locus corresponding to the wave propagation 'along' the direction of superimposed mean flow is shifted farther towards the negative side of the $\text{Re}(\lambda)$ axis, thereby implying an enhanced stability, whereas the eigenvalue locus corresponding to the wave propagation 'against' the direction of mean flow is shifted towards the imaginary-axis ($\text{Im}(\lambda)$ axis). However, for subsonic mean flow, this locus is still entirely situated on the negative side of the $\text{Re}(\lambda)$ axis, thereby allaying any concerns on the stability issue. These two loci converge or coalesce into a single locus that is oriented vertically near the $\text{Im}(\lambda)$ axis. The effect of the number of nodes N_{nodes} on the eigenvalue locus of the overall upwind-biased FD scheme was also studied for the case of zero mean flow (results not shown here). It was observed that with an increase in N_{nodes} the eigenvalue envelope expands further towards the negative side of the real axis, thereby indicating enhanced stability. However, these envelopes do not converge; rather, they expand monotonically as N_{nodes} is increased, thereby indicating that there does not exist a set of discrete natural frequencies for a finite length duct with ABC on both the sides which essentially models a system extending infinitely in both the directions.[31]

Another stability analysis (shown in Fig. 3) was performed for $M_0 = 0$ using an overall central FD scheme formulated as: (1) the 7-point, 4$^{\text{th}}$ order accurate central DRP FD scheme of Tam,[16] which are used at the interior nodes $4 \le i \le N_{\text{nodes}} - 3$, and (2) the 7-point optimised backward or downwind FD schemes,[20] which are used at the nodes $i = 1, 2, 3$ and $i = N_{\text{nodes}} - 2, N_{\text{nodes}} - 1, N_{\text{nodes}}$. (In this case, $[\mathbf{R_1}] = [\mathbf{R_2}] = [\mathbf{R_0}]$, thus the spatial derivatives in $\tilde{X}^{\pm}_{\text{linear}}$ is computed using the $[\mathbf{R_0}]$ matrix.)

It is observed from Fig. 3, that this overall central DRP FD schemes encounter a mild instability problem associated with the implementation of ABC at the first and last node only. This is because instability starts creeping into the solution (due to the eventual growth in the exponential solution due to very small real parts of the eigenvalues) after the pulse has completely propagated outside the domain. To circumvent this problem, the ABC was implemented at two or more nodes on each side of the boundary, wherein it is observed that in the last three cases presented in Fig. 3, the eigenvalue loci increasingly shifts entirely towards the negative side of the $\text{Re}(\lambda)$ axis of the λ plane, thereby stabilising the 1-D forward simulation using the overall central DRP FD scheme.

3.2. TR Simulation

The temporal stability of the 1-D TR simulation is investigated by first deriving the semi-discretised form of the 1-D LEE for implementing the TR simulation. To this end, the mean flow direction is reversed ($M_0 \to -M_0$) in Eqs. (16a, b), whereby the following matrix form is obtained:

$$\frac{d}{d\tilde{t}}\begin{Bmatrix}\{\tilde{p}\}\\ \{\rho_0 c_0 \tilde{u}\}\end{Bmatrix} = \frac{c_0}{\Delta x}[\mathbf{A_0}]\begin{Bmatrix}\{\tilde{p}\}\\ \{\rho_0 c_0 \tilde{u}\}\end{Bmatrix}; \qquad (20a)$$

where

$$[\mathbf{A_0}]_{2N_{\text{nodes}}\times 2N_{\text{nodes}}} = -\frac{1}{2}\times \begin{bmatrix}(1-M_0)[\mathbf{R_1}]-(1+M_0)[\mathbf{R_2}] & (1-M_0)[\mathbf{R_1}]+(1+M_0)[\mathbf{R_2}]\\ (1-M_0)[\mathbf{R_1}]+(1+M_0)[\mathbf{R_2}] & (1-M_0)[\mathbf{R_1}]-(1+M_0)[\mathbf{R_2}]\end{bmatrix}; \qquad (20b)$$

Equation (20a) presents the homogeneous ordinary differential matrix form of the time-reversed 1-D LEE for the temporal solution of the spatially discretized acoustic pressure and velocity fields. (The forward time t in Eqs. (16a, b) is simply replaced with the reverse time $\tilde{t}$ in Eq. (20a).) The time-history of the acoustic pressure $\tilde{p}(i = 1, \tilde{t})$ and $\tilde{p}(i = N_{\text{nodes}}, \tilde{t})$ at the boundary nodes are, however, known a-priori for $\tilde{t} = [0, T]$ at discrete time-instants from the 1-D forward simulations.

$$[\mathbf{A}_{\text{anechoic}}]_{2N_{\text{nodes}}\times 2N_{\text{nodes}}} =$$

$$-\frac{1}{2}\left[\begin{array}{c|c} (M_0-1)\left[R_2^{1,1} \;\; \ldots \;\; R_2^{1,N_{\text{nodes}}}\right]_{1\times N_{\text{nodes}}} & (1-M_0)\left[R_2^{1,1} \;\; \ldots \;\; R_2^{1,N_{\text{nodes}}}\right]_{1\times N_{\text{nodes}}} \\ \left[\begin{array}{ccc} A^{2,1} & \ldots & A^{2,N_{\text{nodes}}} \\ \vdots & \ddots & \vdots \\ A^{N_{\text{nodes}}-1,1} & \ldots & A^{N_{\text{nodes}}-1,N_{\text{nodes}}} \end{array}\right]_{(N_{\text{nodes}}-2)\times N_{\text{nodes}}} & \left[\begin{array}{ccc} A^{2,N_{\text{nodes}}+1} & \ldots & A^{2,2N_{\text{nodes}}} \\ \vdots & \ddots & \vdots \\ A^{N_{\text{nodes}}-1,N_{\text{nodes}}+1} & \ldots & A^{N_{\text{nodes}}-1,2N_{\text{nodes}}} \end{array}\right]_{(N_{\text{nodes}}-2)\times N_{\text{nodes}}} \\ (1+M_0)\left[R_1^{N_{\text{nodes}},1} \;\; \ldots \;\; R_1^{N_{\text{nodes}},N_{\text{nodes}}}\right]_{1\times N_{\text{nodes}}} & (1+M_0)\left[R_1^{N_{\text{nodes}},1} \;\; \ldots \;\; R_1^{N_{\text{nodes}},N_{\text{nodes}}}\right]_{1\times N_{\text{nodes}}} \\ \hline (1-M_0)\left[R_2^{1,1} \;\; \ldots \;\; R_2^{1,N_{\text{nodes}}}\right]_{1\times N_{\text{nodes}}} & (M_0-1)\left[R_2^{1,1} \;\; \ldots \;\; R_2^{1,N_{\text{nodes}}}\right]_{1\times N_{\text{nodes}}} \\ \left[\begin{array}{ccc} A^{N_{\text{nodes}}+2,1} & \ldots & A^{N_{\text{nodes}}+2,N_{\text{nodes}}} \\ \vdots & \ddots & \vdots \\ A^{2N_{\text{nodes}}-1,1} & \ldots & A^{2N_{\text{nodes}}-1,N_{\text{nodes}}} \end{array}\right]_{(N_{\text{nodes}}-2)\times N_{\text{nodes}}} & \left[\begin{array}{ccc} A^{N_{\text{nodes}}+2,N_{\text{nodes}}+1} & \ldots & A^{N_{\text{nodes}}+2,2N_{\text{nodes}}} \\ \vdots & \ddots & \vdots \\ A^{2N_{\text{nodes}}-1,N_{\text{nodes}}+1} & \ldots & A^{2N_{\text{nodes}}-1,2N_{\text{nodes}}} \end{array}\right]_{(N_{\text{nodes}}-2)\times N_{\text{nodes}}} \\ (1+M_0)\left[R_1^{N_{\text{nodes}},1} \;\; \ldots \;\; R_1^{N_{\text{nodes}},N_{\text{nodes}}}\right]_{1\times N_{\text{nodes}}} & (1+M_0)\left[R_1^{N_{\text{nodes}},1} \;\; \ldots \;\; R_1^{N_{\text{nodes}},N_{\text{nodes}}}\right]_{1\times N_{\text{nodes}}} \end{array}\right]; \tag{19}$$

Therefore, for the analysis of the temporal stability of TR simulations, the rows $i = 1$ and $i = N_{\text{nodes}}$ of the $[\mathbf{A_0}]$ matrix (corresponding to the semi-discretised continuity equation at boundary nodes) are discarded, while the corresponding columns $i = 1$ and $i = N_{\text{nodes}}$ are rearranged in the $[\mathbf{B}_{\text{TR}}]$ matrix shown as follows:

$$\frac{d\{\mathbf{\Psi}\}}{d\tilde{t}} = \frac{c_0}{\Delta x}[\mathbf{A}_{\text{TR}}]\{\mathbf{\Psi}\} + \frac{c_0}{\Delta x}[\mathbf{B}_{\text{TR}}]\begin{Bmatrix}\tilde{p}_1 \\ \tilde{p}_{N_{\text{nodes}}}\end{Bmatrix}_{2\times 1}; \tag{21a}$$

where

$$\{\mathbf{\Psi}\}_{(2N_{\text{nodes}}-2)\times 1} = \left\{\tilde{p}_2(\tilde{t})\ldots\tilde{p}_{N_{\text{nodes}}-1}(\tilde{t}) \;\; \rho_0 c_0\tilde{u}_1(\tilde{t})\ldots\rho_0 c_0\tilde{u}_{N_{\text{nodes}}}(\tilde{t})\right\}^T; \tag{21b}$$

$[\mathbf{A}_{\text{TR}}]$ is given by Eq. (21c), and

$$[\mathbf{B}_{\text{TR}}]_{(2N_{\text{nodes}}-2)\times 2} = \begin{bmatrix} A_0^{2,1} & A_0^{2,N_{\text{nodes}}} \\ \vdots & \vdots \\ A_0^{N_{\text{nodes}}-1,1} & A_0^{N_{\text{nodes}}-1,N_{\text{nodes}}} \\ A_0^{N_{\text{nodes}}+1,1} & A_0^{N_{\text{nodes}}+1,N_{\text{nodes}}} \\ \vdots & \vdots \\ A_0^{2N_{\text{nodes}},1} & A_0^{2N_{\text{nodes}},N_{\text{nodes}}} \end{bmatrix}. \tag{21d}$$

It is noted that Eq. (21a) is an inhomogeneous matrix differential equation. The inhomogeneity in Eq. (21a) is ascribed to the presence of the non-zero acoustic pressure vector $\{\tilde{p}_1 \;\; \tilde{p}_{N_{\text{nodes}}}\}^T$. This vector acts as a numerical source during each time-step of TR simulations and initiates and sustains a back-propagation of acoustic pulses in the computational domain during $\tilde{t} = [0, T]$ which eventually coalesces at $\tilde{t} = T$. It is also noted that solving the time-reversed 1-D LEE in the inhomogeneous form is equivalent to the numerical time-integration of Eq. (20a) immediately followed by the enforcement of time-reversed acoustic pressure $\tilde{p}(i = 1, \tilde{t})$ and $\tilde{p}(i = N_{\text{nodes}}, \tilde{t})$ at the boundary nodes. The stability of implementation of the 1-D TR simulation using the PCF and the overall upwind-biased FD scheme can now be assessed using the exact temporal solution of Eq. (21a) expressed as

$$\left\{\tilde{p}_2\ldots\tilde{p}_{N_{\text{nodes}}-1} \;\; \rho_0 c_0\tilde{u}_1\ldots\rho_0 c_0\tilde{u}_{N_{\text{nodes}}}\right\}^T = \frac{c_0}{\Delta x}e^{[\mathbf{A}_{\text{TR}}]\frac{c_0\tilde{t}}{\Delta x}}\left\{\int_{\tau=0}^{\tau=\tilde{t}} e^{-[\mathbf{A}_{\text{TR}}]\frac{c_0\tau}{\Delta x}}[\mathbf{B}_{\text{TR}}]\begin{Bmatrix}\tilde{p}_1(\tau) \\ \tilde{p}_{N_{\text{nodes}}}(\tau)\end{Bmatrix}d\tau\right\}. \tag{22}$$

Equation (22) is a formal representation of the exact temporal solution; however, the TR simulation is not implemented using this formal solution. This is because the exact function expressing the variation of the vector $\{\tilde{p}_1(\tau) \;\; \tilde{p}_{N_{\text{nodes}}}(\tau)\}^T$ with time τ is not known a-priori, rather $\tilde{p}(i = 1, \tilde{t})$ and $\tilde{p}(i = N_{\text{nodes}}, \tilde{t})$ time-histories are known at only discrete values of $\tilde{t}$. Nonetheless, Eq. (22) can be used for a stability analysis of the TR method by examining the eigenvalues of the $[\mathbf{A}_{\text{TR}}]$ matrix. The TR simulations are stable if all the eigenvalues of the $[\mathbf{A}_{\text{TR}}]$ matrix have negative or zero real parts (provided that the parameters of the $[\mathbf{B}_{\text{TR}}]$ matrix and the inhomogeneous vector $\{\tilde{p}_1(\tau) \;\; \tilde{p}_{N_{\text{nodes}}}(\tau)\}^T$ are finite). It is for this reason that the inhomogeneous part of Eq. (21a) is disregarded in formulating the eigenvalue problem. On substituting $\{\mathbf{\Psi}\}^T = \{\hat{\mathbf{\Psi}}\}^T e^{\omega\tilde{t}}$ in Eq. (21a) and subsequent algebraic manipulations, the following eigenvalue problem is posed:

$$[\mathbf{A}_{\text{TR}}]\{\hat{\mathbf{\Psi}}\}^T = \lambda\{\hat{\mathbf{\Psi}}\}^T; \tag{23a}$$

$$\{\hat{\mathbf{\Psi}}\}^T = \left\{\tilde{p}_2\ldots\tilde{p}_{N_{\text{nodes}}-1} \;\; \rho_0 c_0\tilde{u}_1\ldots\rho_0 c_0\tilde{u}_{N_{\text{nodes}}}\right\}^T; \tag{23b}$$

where λ denotes the non-dimensional eigenvalues of the $[\mathbf{A}_{\text{TR}}]$ matrix.

Figure 4 presents the eigenvalue loci of the $[\mathbf{A}_{\text{TR}}]$ matrix for $N_{\text{nodes}} = 1500$. It is observed from Fig. 4(a) that the eigenvalue loci for $M_0 = 0$ and $M_0 = 0.30$ consists of a closed loop mostly located on the negative side of the $\text{Re}(\lambda)$ axis, thereby demonstrating the stability and robustness of the 1-D TR simulations by considering two different upwinding directions (to compute the spatial derivatives in opposing fluxes $\tilde{X}^{\pm}_{\text{linear}}$) while using the overall upwind-biased FD schemes formulated here. Figure 4(b) depicts an exaggerated view of the

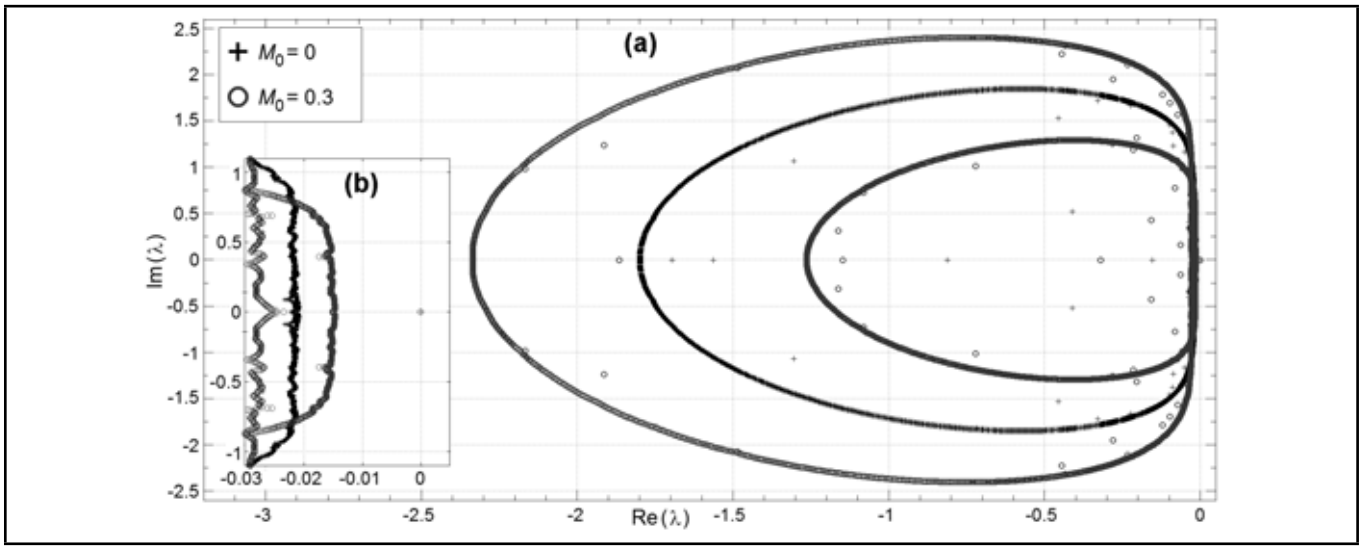

Figure 2. Eigenvalue loci of the overall upwind-biased FD scheme obtained from Eq. (18): Illustration of the stability with implementation of the ABC and the bifurcating effect of a mean flow.

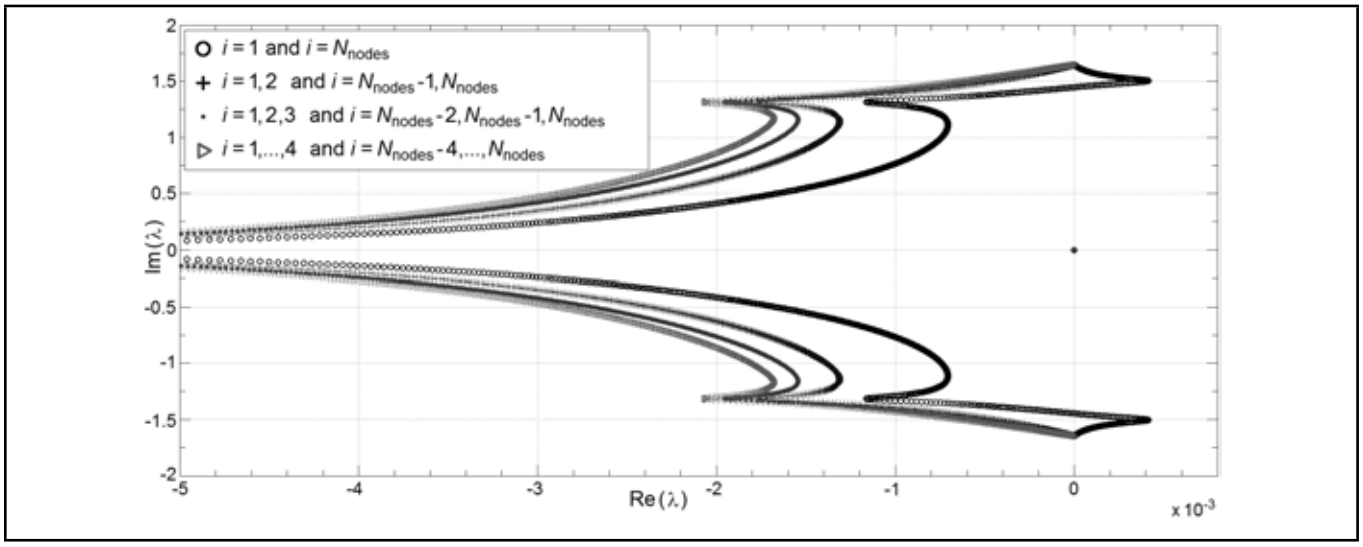

Figure 3. Stabilising effect of enforcing ABC on the first two (or more) and the last two (or more) nodes of the computational domain on the eigenvalue loci of the overall central DRP FD scheme.

eigenvalue loci near the imaginary axis. It is observed that the enlarged eigenvalue loci for $M_0 = 0$ and $M_0 = 0.30$ have very small positive real parts whose magnitudes are of the order of 10^{-5} or even smaller. This suggests a mild instability problem in the strict sense, which might be a concern only over a large duration of TR simulation. Indeed, it is observed that these mild instabilities do not affect the accuracy and robustness of TR (shown in subsections 4.1.2 and 4.2.2) in predicting the initial location of the pulse.

The eigenvalue loci of the $[\mathbf{A}_{\mathrm{TR}}]$ matrix using the overall central DRP FD schemes[16,20] are presented in Fig. 5(a) for $N_{\mathrm{nodes}} = 1500$. Two different mean flow values given by $M_0 = 0$ and $M_0 = 0.30$ are also considered for evaluating the stability of overall central DRP FD schemes.[16,20]

It is observed from Figs. 5(a, b) that for both the stationary medium as well as for the moving medium, the eigenvalue loci resemble a straight line aligned vertically along the imaginary axis. Some of the eigenvalues have large positive real parts (of the order of 10^{-1}) which signify the rapid growth of instabilities during the TR simulations. An enlarged view of the eigenvalue loci is depicted in Fig. 5(b), wherein it is observed that the eigenvalues are clustered along the imaginary axis. The magnitudes of the real part of these eigenvalues are of the order 10^{-4} (an order of magnitude greater than the unstable eigenvalues shown in Fig. 4(b)). Therefore, based on these features of the eigenvalue loci shown in Fig. 5, it may be concluded that the overall central FD schemes have eigenvalues with relatively larger positive real parts, and thus are more prone to instabilities. To conclude, the overall central DRP FD scheme (without the Artificial Selective Damping[32] (ASD)) is thus unsuitable for simulation of Euler equations for TR application. It may however be mentioned that inclusion of the extraneous ASD terms in the LEE while using the overall central DRP FD scheme stabilizes the 1-D TR simulation. This is because the eigenvalue loci would shift entirely to the negative side of the $\mathrm{Re}(\lambda)$ axis of the λ plane (so that none of the eigenvalues have a positive real part), and its shape would resemble the eigenvalue loci of the overall upwind-biased FD scheme shown in Fig. 4. Indeed, similar conclusions also hold for the effect of ASD on the 1-D forward simulation using the overall central DRP FD scheme. It is important to note that the damping in the ASD stencil is directly proportional to the in-

$$[\mathbf{A}_{\text{TR}}]_{(2N_{\text{nodes}}-2)\times(2N_{\text{nodes}}-2)} = \begin{bmatrix} \begin{bmatrix} A_0^{2,2} & \dots & A_0^{2,N_{\text{nodes}}-1} \\ \vdots & \ddots & \vdots \\ A_0^{N_{\text{nodes}}-1,2} & \dots & A_0^{N_{\text{nodes}}-1,N_{\text{nodes}}-1} \end{bmatrix}_{(N_{\text{nodes}}-2)\times(N_{\text{nodes}}-2)} & \begin{bmatrix} A_0^{2,N_{\text{nodes}}+1} & \dots & A_0^{2,2N_{\text{nodes}}} \\ \vdots & \ddots & \vdots \\ A_0^{N_{\text{nodes}}-1,N_{\text{nodes}}+1} & \dots & A_0^{N_{\text{nodes}}-1,2N_{\text{nodes}}} \end{bmatrix}_{(N_{\text{nodes}}-2)\times N_{\text{nodes}}} \\ \begin{bmatrix} A_0^{N_{\text{nodes}}+1,2} & \dots & A_0^{N_{\text{nodes}}+1,N_{\text{nodes}}-1} \\ \vdots & \ddots & \vdots \\ A_0^{2N_{\text{nodes}},2} & \dots & A_0^{2N_{\text{nodes}},N_{\text{nodes}}-1} \end{bmatrix}_{N_{\text{nodes}}\times(N_{\text{nodes}}-2)} & \begin{bmatrix} A_0^{N_{\text{nodes}}+1,N_{\text{nodes}}+1} & \dots & A_0^{N_{\text{nodes}}+1,2N_{\text{nodes}}} \\ \vdots & \ddots & \vdots \\ A_0^{2N_{\text{nodes}},N_{\text{nodes}}+1} & \dots & A_0^{2N_{\text{nodes}},2N_{\text{nodes}}} \end{bmatrix}_{N_{\text{nodes}}\times N_{\text{nodes}}} \end{bmatrix}; \tag{21c}$$

verse mesh Reynolds number (R_Δ^{-1}), and therefore in practice, R_Δ^{-1} is chosen in a rather ad-hoc manner (and is specific to a particular CAA problem) such that the ASD does not induce any inaccuracy due to over-damping.[32] It is noted that the foregoing remarks on the stability of 1-D simulations also hold for overall upwind-biased or central FD schemes formulated using other available FD schemes such as the wavenumber extended schemes of Li,[23] optimised scheme of Lockard,[33] and the 15-point central DRP FD scheme of Tam.[34]

4. RESULTS AND DISCUSSION: ACCURACY ANALYSIS OF THE SIMULATIONS

The accuracy of the 1-D and 2-D forward simulation and the TR simulation (implemented using only the time-reversed acoustic pressure as input at the boundary nodes) is analysed by comparison with the corresponding analytical solution of the acoustic pressure field due to the propagation of an acoustic pulse in a mean flow field involving planar wave fronts in the 1-D duct and cylindrical wave fronts in the 2-D free-space.

4.1. Test Case 1: Propagation of a Gaussian Pulse in an Infinite 1-D Duct with Mean Flow

The initial acoustic pressure field $\phi(x)$ is taken as a Gaussian function. Therefore, $\tilde{p}(x, t=0) = \phi(x) = \varepsilon e^{-\alpha(x-x_0)^2}$ where ε is the initial amplitude of the pulse, x_0 denotes the initial location of the peak of the Gaussian pulse in the 1-D domain given by $0 \le x \le 1$, and α pertains to the sharpness of the pulse and decides the maximum wavenumber content computed by the Fourier transform $\frac{1}{\sqrt{2\pi}} \int\limits_{x=-\infty}^{x=\infty} e^{-\alpha x^2} e^{-jk_0 x} dx = \left(e^{-\frac{k_0^2}{4\alpha}} / \sqrt{2\alpha} \right)$. In the ensuing simulation results, $\varepsilon = 0.1$ Pa and $\alpha = 100$ m^{-2}, and therefore the maximum wavenumber content k_0 of the 1-D Gaussian pulse is less than 40 m^{-1}, thereby indicating that the spatial discretisation and the overall upwind-biased FD scheme warrants an accurate acoustic wave propagation. Furthermore, $x_0 = 0.5$ m and $M_0 = 0.3$ are considered; hence, $\Delta t_1 = 2.2418 \times 10^{-6}$ s based on the CFL number equal to 0.2.

4.1.1. Forward Simulation

Figures 6(a–d) compare the spatio-temporal evolution of the acoustic pressure field predicted by the 1-D forward simulation against the corresponding analytical solution of the propagation of a Gaussian pulse in an infinite 1-D duct with mean flow (given by Eq. (24)) at time-instants (a) $t = 0$ (Initial condition), (b) $t = 200\Delta t_1$, (c) $t = 400\Delta t_1$, and (d) $t = 700\Delta t_1$, respectively.

$$\tilde{p}_{\text{analytical}}(x,t) = \frac{1}{2} \times \left\{ \overbrace{\phi(x-(1+M_0)c_0 t)}^{\text{Pulse propagating along the positive } x \text{ direction}} + \underbrace{\phi(x+(1+M_0)c_0 t)}_{\text{Pulse propagating along the negative } x \text{ direction}} \right\}. \tag{24}$$

An excellent agreement is observed from Fig. 6(a–d) between the forward simulation and the analytical solution at all time-instants, thereby establishing the accuracy of 1-D forward simulations. It is observed that the initial Gaussian pulse starts decaying and splitting into two Gaussian pulses of equal amplitude but propagating in opposite directions with unequal speeds (due to convective effect of mean flow). The pulse propagating towards the positive x direction propagates at an enhanced speed $c_0(1+M_0) = 1.3c_0$ and leaves the domain earlier than the pulse that propagates towards negative x direction at the reduced speed $c_0(1-M_0) = 0.7c_0$.

The forward simulations were carried out for a large time-interval $t = [0, T_1 = 3000\Delta t_1]$ during which the pulse completely propagates out of the domain and the acoustic pressure and particle velocities are vanishingly small (less than machine precision) beyond this interval.

In order to formally assess the accuracy, a L_1 norm error between the $\tilde{p}(x,t)$ and $\rho_0 c_0 \tilde{u}(x,t)$ fields predicted by the forward simulations and the corresponding 1-D analytical solutions is defined as

$$L_1^p(t) = \frac{1}{L} \int\limits_{x=0}^{x=L=1} \left| \tilde{p}_{\text{analytical}}(x,t) - \tilde{p}(x,t) \right| dx; \tag{25a}$$

$$L_1^u(t) = \frac{1}{L} \int\limits_{x=0}^{x=L=1} \rho_0 c_0 \left| \tilde{u}_{\text{analytical}}(x,\tilde{t}) - \tilde{u}(x,t) \right| dx; \tag{25b}$$

and has been evaluated at every time-step of the forward simulations. It is observed from Fig. 7(a) that for the initial time duration of forward simulation $t = [0, 1500\Delta t]$, the $L_1^p(t)$ and $L_1^u(t)$ norm errors are equal and of the order 10^{-7} for the overall upwind-biased scheme, whereas the $\tilde{p}(x,t)$ and $\rho_0 c_0 \tilde{u}(x,t)$ fields are of the order 10^{-2} (maximum value over the domain $0 \le x \le 1$) during this interval, thereby formally validating the 1-D forward simulation using the PCF and overall upwind-biased FD schemes.

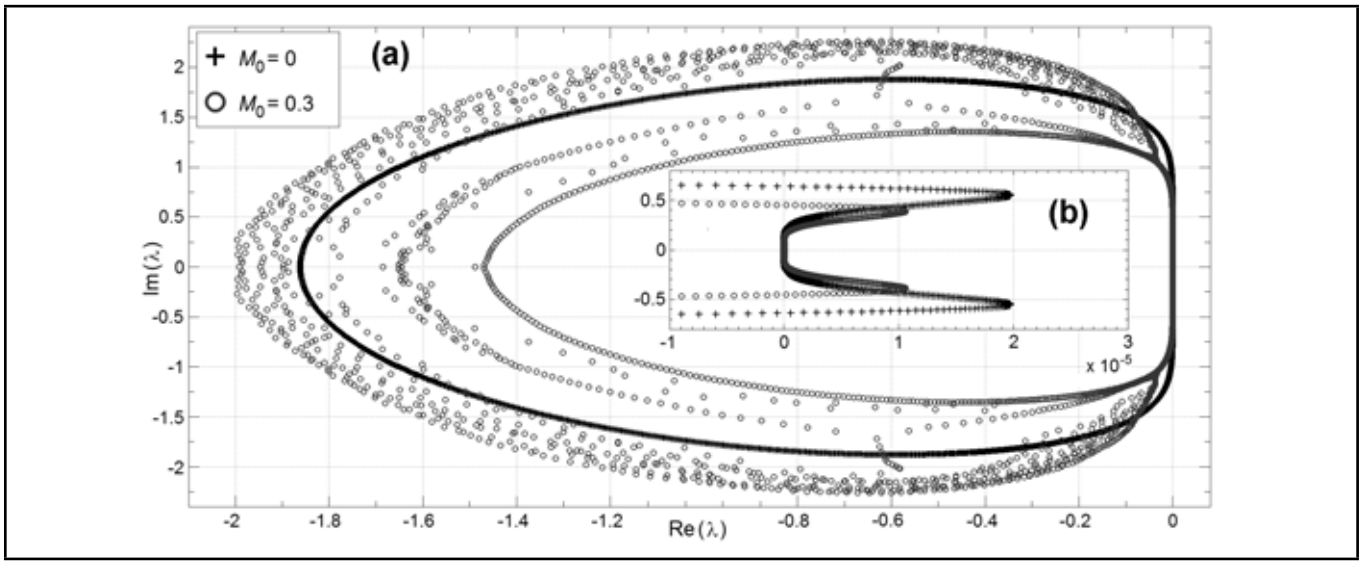

Figure 4. Eigenvalue loci of the $[\mathbf{A}_{\text{TR}}]$ matrix shown in Eq. (21c) for $N_{\text{nodes}} = 1500$ based on the overall upwind-biased FD scheme: Illustration of stability and the bifurcating effect of a mean flow M_0.

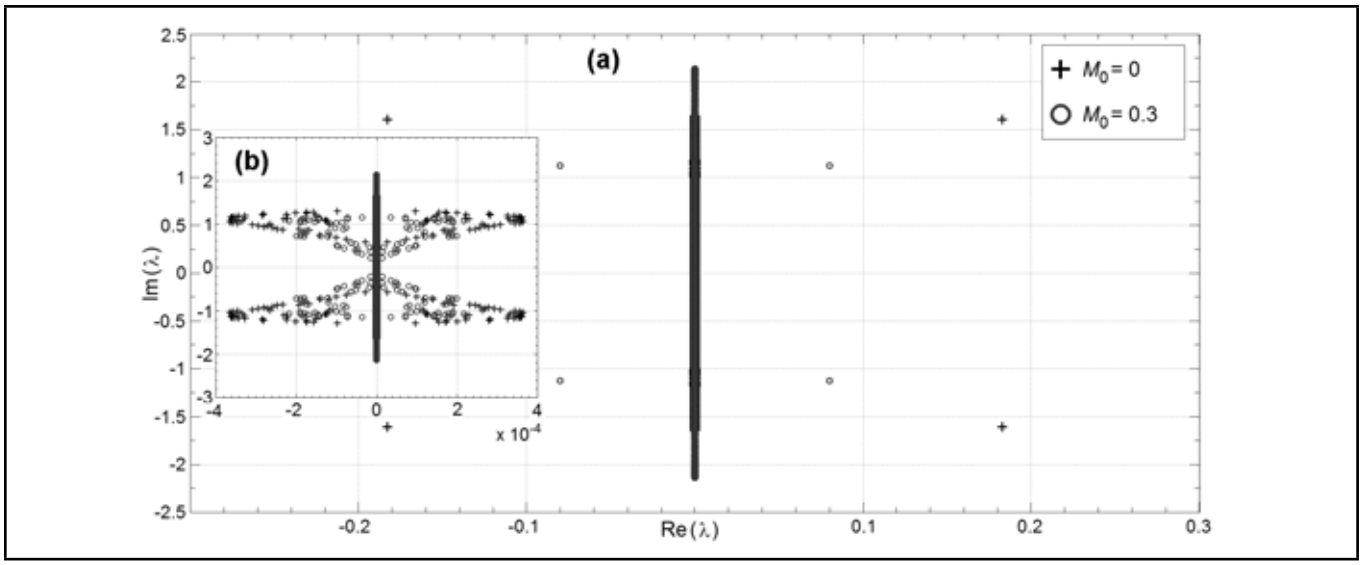

Figure 5. Eigenvalue loci of the $[\mathbf{A}_{\text{TR}}]$ matrix shown in Eq. (21c) for $N_{\text{nodes}} = 1500$ based on the overall central DRP FD schemes: Illustration of instability during the TR simulation due to a few eigenvalues with large positive real parts.

The 1-D forward simulations were also implemented using the overall central DRP FD schemes[16,20] (discussed in Section 3) wherein a numerically stable and accurate solution was obtained. Indeed, the $L_1^p(t)$ and $L_1^u(t)$ norm errors in this case were almost identical to that of the overall upwind-biased FD schemes due to the similar resolution characteristics (DRP property) of the 4$^{\text{th}}$ order, the 7-point central DRP FD stencil[16] and the 4$^{\text{th}}$ order, and the 7-point optimised upwind-biased FD stencil.[22] However, it was observed that the relative execution time of the forward simulations per time-step using the overall central DRP FD scheme is approximately half that taken by the overall upwind-biased FD schemes.

4.1.2. TR Simulation

Figures 6(d–a) show the $\tilde{p}(x,\tilde{t})$ field predicted by the 1-D TR simulation using only the time-reversed acoustic pressure as input at the boundary nodes ($i = 1, N_{\text{nodes}}$) at discrete time-instants (d) $\tilde{t} = 2300\Delta t_1$, (c) $\tilde{t} = 2600\Delta t_1$, (b) $\tilde{t} = 2800\Delta t_1$, and (a) $\tilde{t} = T_1 = 3000\Delta t_1$ (the final time-instant of the TR simulation), respectively. It is noted that during the 1-D TR simulation, the ABCs have not been implemented at the finite termination of the duct. The $\tilde{p}(x,\tilde{t})$ field obtained by the 1-D TR simulation is found to be in excellent agreement with the $\tilde{p}(x,t)$ field predicted by the forward simulation, and also with the time-reversed analytical solution (obtained by replacing t with $T - \tilde{t}$ in Eq. (24)) at the corresponding time-instants. It is observed that two Gaussian pulses of equal amplitude back propagate into the computational domain at unequal speeds (the pulse propagating from the $x = 0$ and the $x = L$ boundary propagate at a speed of $0.7c_0$ and $1.3c_0$, respectively), undergo constructive interference, and eventually coalesce at $\tilde{t} = T_1$ to form a single amplified Gaussian pulse at the same spatial location ($x = x_0$) and amplitude as the initial Gaussian pulse (at $t = 0$ during the forward simulation), thereby revealing the correct source location and amplitude. For formally assessing the accuracy, a L_1 norm error between the $\tilde{p}(x,\tilde{t})$ and $\rho_0 c_0 \tilde{u}(x,\tilde{t})$ fields predicted by the 1-D TR simulation and the corresponding time-reversed analytical solutions has also been evaluated at every time-step of the TR simulation. The $L_1^p(\tilde{t})$ and $L_1^u(\tilde{t})$ versus $\tilde{t}$ graphs are presented in Fig. 7(b). It

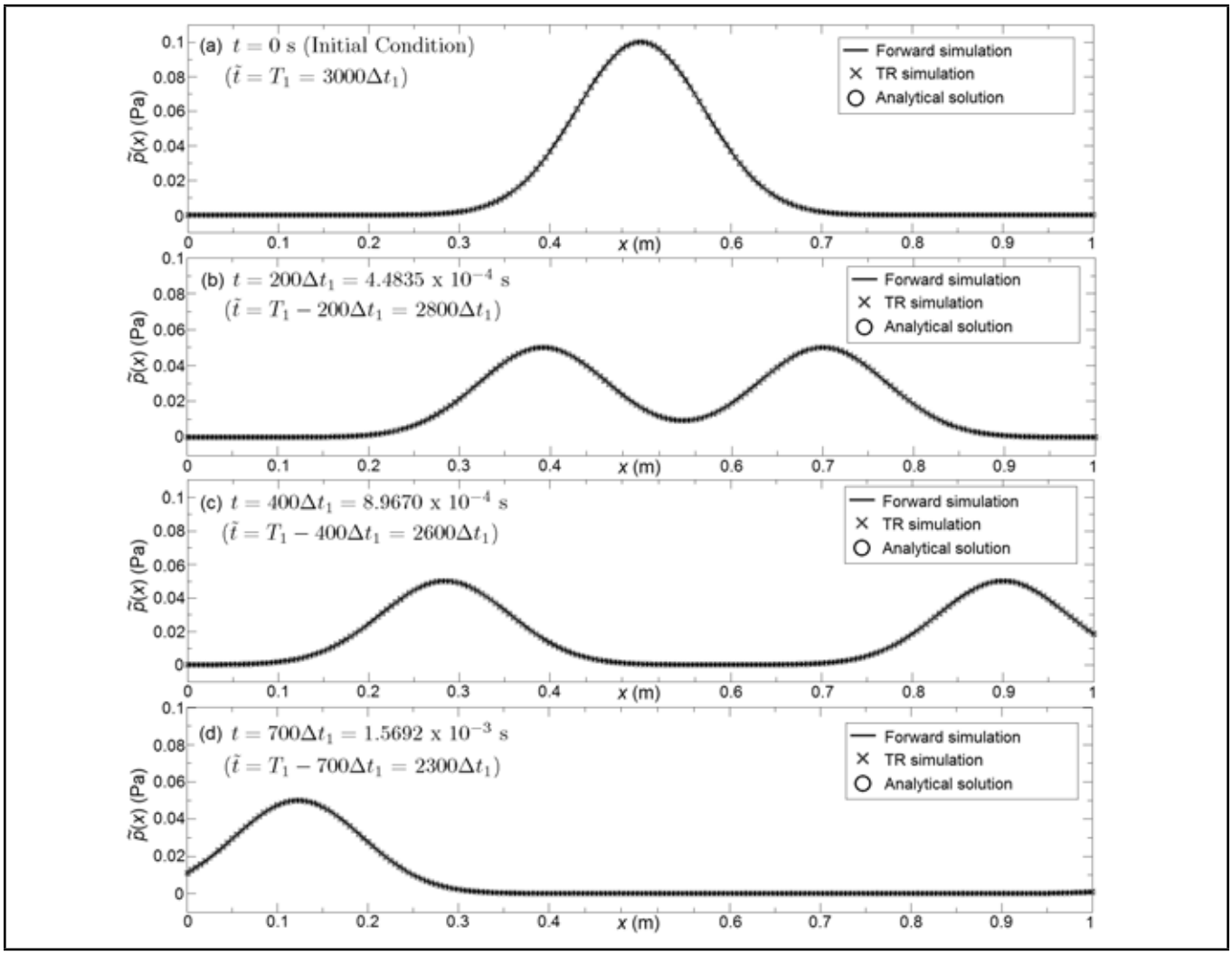

Figure 6. The acoustic pressure field $\tilde{p}(x,t)$ computed using the forward simulation of a Gaussian pulse propagating in a 1-D infinite duct (shown in Fig. 1(a)) with mean flow $M_0 = 0.3$ towards the positive x direction at time-instants $t =$ (a) 0, (b) $200\Delta t_1$, (c) $400\Delta t_1$, and (d) $700\Delta t_1$, and comparison with the analytical solution (given by Eq. (24)). The time-reversed acoustic pressure field $\tilde{p}(x,\tilde{t})$ obtained during the TR simulation using only the time-reversed acoustic pressure as input at the boundary nodes at the reverse time-instants $\tilde{t} =$ (a) $2300\Delta t_1$, (b) $2600\Delta t_1$, (c) $2800\Delta t_1$, and (d) $T_1 = 3000\Delta t_1$ demonstrates one-to-one correspondence with the forward simulation and the analytical solution.

is noted that analysing the L_1 norm errors is meaningful only over the time interval $\tilde{t} = [1500\Delta t, 3000\Delta t]$ corresponding to arrival of the acoustic pulses at the computational boundaries until the coalescing of the two pulses to form a single amplified acoustic pressure pulse at time $\tilde{t} = T_1$. The order of magnitude of L_1 norm errors is approximately 10^{-5} over the interval $\tilde{t} = [2000\Delta t, 3000\Delta t]$, whereas the order of magnitudes of $\tilde{p}(x,\tilde{t})$ and $\rho_0 c_0 \tilde{u}(x,\tilde{t})$ over the same time interval is approximately 10^{-2}, while the peak of the Gaussian pulse in $\tilde{p}(x = L/2, \tilde{t} = T_1)$ is of the order 10^{-1}. This confirms the accuracy of TR simulations using only the time-reversed acoustic pressure as input at the boundary nodes for the 1-D test case.

4.2. Test Case 2: Propagation of a Gaussian Pulse in a 2-D Free-space with Uniform Mean Flow

The initial acoustic pressure field $\phi(x,y)$ is taken as a 2-D Gaussian pulse given by $\tilde{p}(x,y,t=0) = \phi(x,y) = \varepsilon e^{-\alpha\{(x-x_0)^2+(y-y_0)^2\}}$, where $\alpha = 100$ m^{-2}, $\varepsilon = 0.1$ Pa and $x_0 = y_0 = 0$ denotes its peak in the 2-D domain $|x| \leq (L_x + \Delta L_x)$, $|y| \leq (L_y + \Delta L_y)$, where $L_x = L_y = 0.5$ m, while $N_{\text{sponge}} = 30$, therefore, $\Delta L_x = \Delta L_y = 30 \times 0.005$ m $= 0.15$ m. The maximum wavenumber content in the 2-D Gaussian pulse is determined by computing the Hankel transform of order zero[35] of the function $f(r) = e^{-\alpha r^2}$ and is given by $e^{-\frac{k_0^2}{4\alpha}}/(2\alpha)$. For the values of α considered, the maximum wavenumber content k_0 is less than 55 m^{-1}, thereby ensuring an accurate propagation of the pulse with the mesh-size considered here.

4.2.1. Forward Simulation

Figures 8(a–d) depict the spatio-temporal evolution of the Gaussian pulse in a 2-D free space (over the domain $|x| \leq 0.65$ m, $|y| \leq 0.65$ m) with a uniform mean flow $M_0 = 0.3$ considered along the positive x direction obtained by the forward simulation at time-instants (a) $t = 0$ (Initial condition), (b) $t = 300\Delta t_2$, (c) $t = 600\Delta t_2$, and (d) $t = 1000\Delta t_2$, where $\Delta t_2 = 2.2418 \times 10^{-6}$ s.

It is noted that the domain shown in Figs. 8(a–d) also includes the sponge-layer domain which is necessary to damp the incoming spurious reflections at the exterior computational boundaries. Furthermore, in Figs. 8(a–d), the direction of the uniform mean flow along the positive x direction is indicated

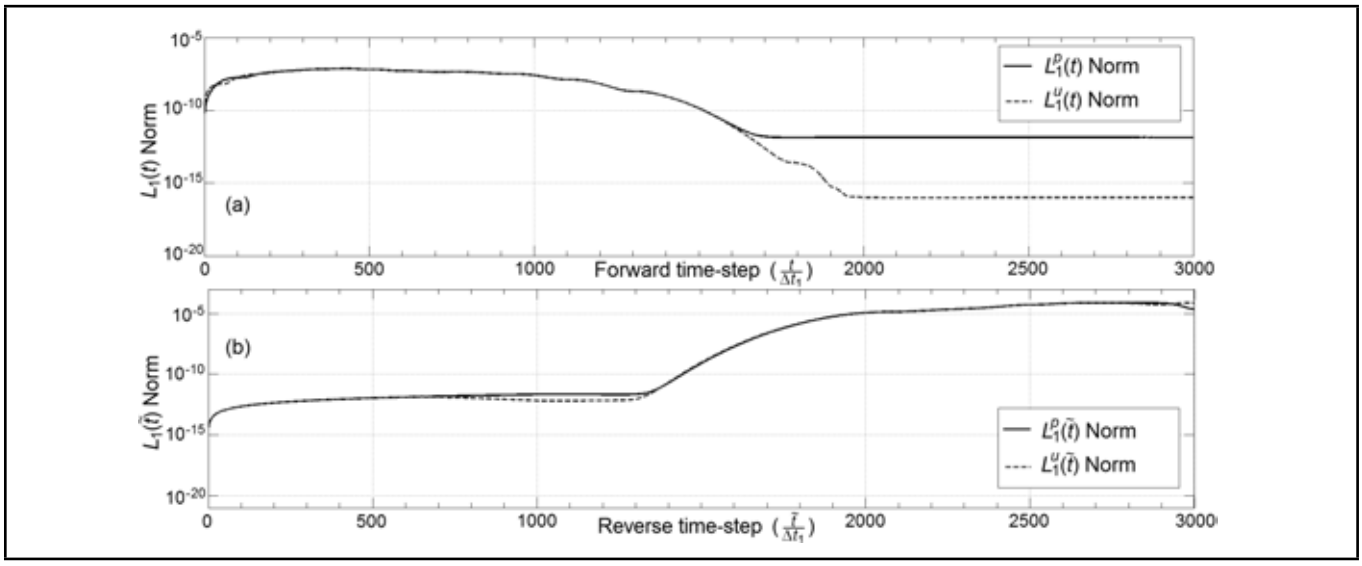

Figure 7. Temporal variation of (a) the $L_1(t)$ error norms in the 1-D forward simulation and (b) the $L_1(t)$ error norms in the 1-D TR simulation: Quantification of the accuracy of the simulations using the PCF of the LEE and the overall upwind-biased FD scheme.

by an arrow, the colorbar depicts the magnitude of acoustic pressure in Pa (Nm^{-2}), and the known location of the peak of the Gaussian pulse in Fig. 8(a) is indicated by a circle **O**. The same symbol and unit conventions are also followed for the remaining 2-D simulations. Figures 8(a–d) demonstrate that the 2-D Gaussian pulse collapses and the cylindrical wave fronts expand radially such that the center of pulse is convected with a speed $c_0 M_0$ towards positive x direction due to mean flow.

The accuracy of the 2-D forward simulation results (shown in Figs. 8(a–d)) is assessed by comparison against the corresponding analytical solution of the acoustic pressure field due to the spatio-temporally evolving Gaussian pulse in a 2-D free-space given by[16]

$$\tilde{p}(x,y,t) = \frac{\varepsilon}{2\alpha} \int_{\xi=0}^{\xi=\xi_0\to\infty} \xi e^{-\frac{\xi^2}{4\alpha}} \cos(c_0\xi t) J_0(\xi\eta)\, d\xi; \quad (26)$$

where $J_0(\cdot)$ is the ordinary Bessel function of zero order and $\eta = \{(x - c_0 M_0 t)^2 + y^2\}^{1/2}$. Figures 9(a–d) depict the comparison of the acoustic pressure field $\tilde{p}(x, y = 0, t)$ along the x axis $t = [0, 300\Delta t_2, 600\Delta t_2, 1000\Delta t_2]$, respectively, obtained using forward simulation and the analytical solution, wherein an excellent agreement is observed between the two approaches, especially during the initial time-instants. At $t = 1000\Delta t_2$, the forward simulation results exhibit a small deviation from the analytical solution as may be observed from Fig. 9(d). It is however noted that the $\tilde{p}(x, y = 0)$ field predicted by the forward simulation and the corresponding analytical solution are both of the order 10^{-3}, while the discrepancy between the two approaches (due to small wave reflections that back propagate into the computational domain despite the use of Tam's ABC at the $x = 0.65$ m boundary and the use of sponge-layer near nodes of this boundary) is of the order of 10^{-4}. This indicates that a reasonable estimate of the $\tilde{p}(x, y, t)$ field may be obtained by means of forward simulations based on the PCF of 2-D LEE, overall upwind-biased FD schemes, and the implementation of ABC. Indeed, the forward simulations were carried out for $t = [0, 5000\Delta t_2]$ during which the Gaussian pulse completely propagates out of the 2-D domain, and the acoustic pressure and particle velocity fields tend to zero.

The $\tilde{p}(x, y, t)$ field obtained using the overall central DRP FD scheme[16,20] based on the PCF and implementation of ABC was found to be similar to that shown in Figs. 8(a–d), (the results are not shown for brevity), thereby demonstrating the stability and accuracy of the 2-D forward simulations using the overall central DRP FD scheme.

4.2.2. TR Simulation

Time-reversed Acoustic Pressure as Input

Figures 10(a–d) show the $\tilde{p}(x, y, \tilde{t})$ field predicted by the 2-D TR simulations (over the domain $|x| \leq 0.5$ m, $|y| \leq 0.5$ m,) using only the time-reversed acoustic pressure history as input at all four computational boundaries, i.e. $x = \pm 0.5$ m and $y = \pm 0.5$ m at (a) $\tilde{t} = 4000\Delta t_2$, (b) $\tilde{t} = 4400\Delta t_2$, (c) $\tilde{t} = 4700\Delta t_2$, and (d) $\tilde{t} = T_2 = 5000\Delta t_2$ (the final time-instant of TR simulation). The 'reversed' direction of mean flow is indicated by an arrow in Figs. 10(a–d), while the predicted location of the peak of the Gaussian pulse in Fig. 10(d) is indicated by a cross **X**. (These same symbolic conventions are also followed for the remaining results.) It is noted that the use of time-reversed acoustic pressure Dirichlet boundary conditions as input at the four computational boundaries results in the generation of both the incoming acoustic wave fronts (that propagates into the domain, converges and eventually coalesces to form the initial Gaussian pulse) and the outgoing waves that tend to propagate outside the computational domain. In order to prevent the spurious numerical reflections at the boundaries due to the outgoing waves from back-propagation into the domain and thereby inducing instability, the CEM ABC and the special corner ABCs were implemented at the boundaries,[4,10,21] crucial for stabilising the 2-D TR simulations. Furthermore, $\partial\tilde{v}/\partial x|_{x=L_x} = 0$ condition was also implemented to prevent instability due to incoming disturbances advected by 'reversed' mean flow.

Figure 10(d) indicates that the predicted location of the peak of the Gaussian pulse is co-incident with the known peak location. Indeed, a comparison of $\tilde{p}(x, y, \tilde{t})$ field in Figs. 10(a–d) with the corresponding $\tilde{p}(x, y, t)$ field shown in Figs. 8(d–

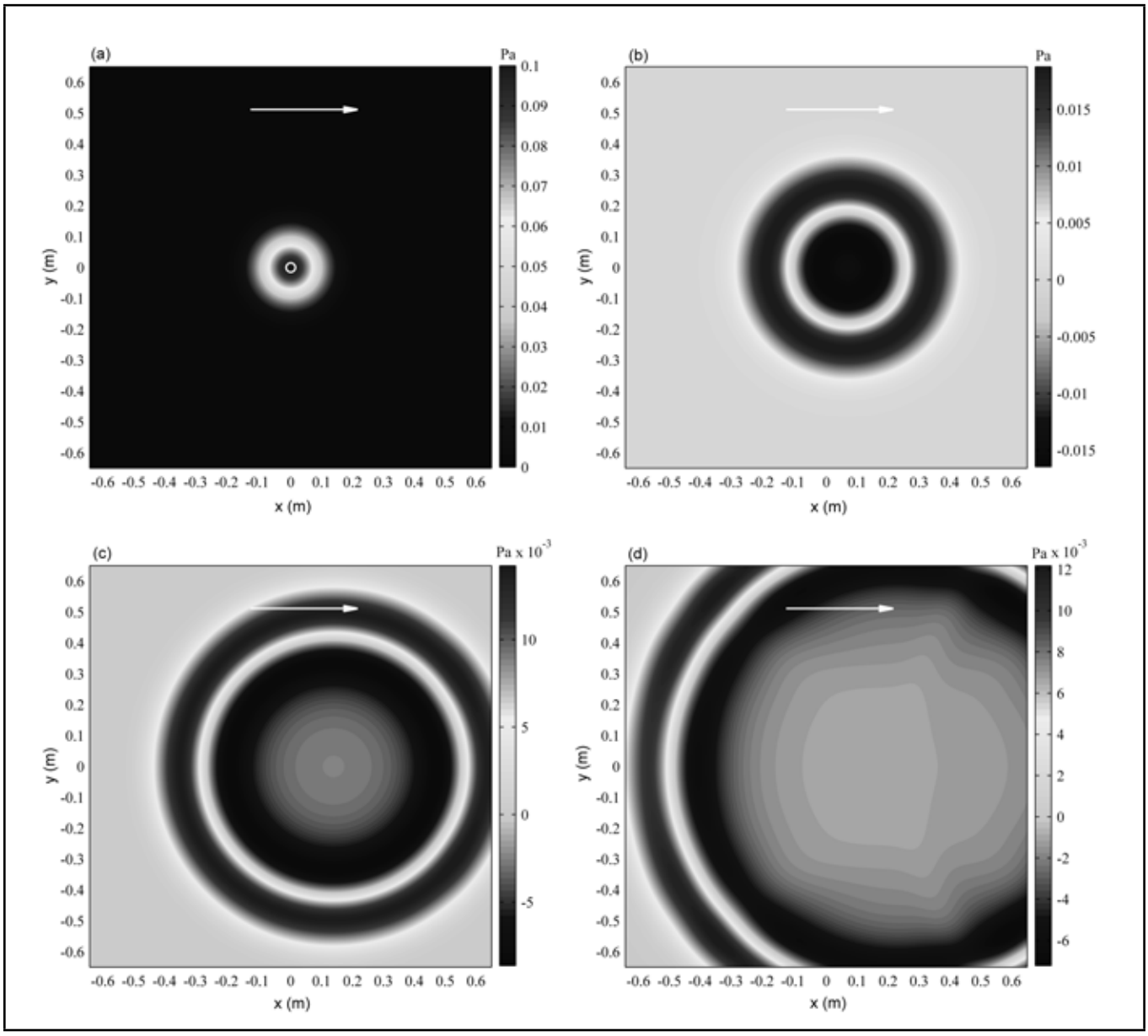

Figure 8. The forward simulation of acoustic pressure field $\tilde{p}(x, y, t)$ due to a Gaussian pulse propagating in a 2-D free-space with uniform mean flow $M_0 = 0.3$ towards the positive x direction at $t =$ (a) 0, (b) $300\Delta t_2$, (c) $600\Delta t_2$, and (d) $1000\Delta t_2$. It is noted that different colorbar scales are used in parts (a–d).

a), respectively, demonstrates an accurate back- propagation of cylindrical acoustic waves from the boundaries during 2-D TR simulations using only the time-reversed acoustic pressure as input. A similar conclusion may also be drawn on comparing the time-reversed $\tilde{p}(x, y = 0, \tilde{t})$ field with the forward $\tilde{p}(x, y = 0, t)$ field shown in Fig. 9.

Time-reversed Acoustic Pressure and Particle Velocities as Input: A Comparison

The $\tilde{p}(x, y, \tilde{t})$ field obtained by the 2-D TR simulations using both the time-reversed acoustic pressure and acoustic particle velocities as input (shown in Figs. 11(a–d)) is compared to that obtained using only the time-reversed acoustic pressure as input (shown in Figs. 10(a–d)) at the corresponding reverse time-instants.

It is observed that the $\tilde{p}(x, y, \tilde{t})$ fields obtained in Figs. 10(a–d) and 11(a–d) are similar. In particular, Figs. 10(d) and 11(d) predicting the initial location of peak of the Gaussian pulse are identical. Similar conclusions may also be made from Figs. 9(a–d). This demonstrates that measuring the acoustic particle velocity histories at the computational boundaries is unnecessary and the use of only the time-reversed acoustic pressure as input is sufficient for an accurate localization of sound sources in flows by means of 2-D TR simulations.

It is also observed by means of numerical experiments that the use of an overall central DRP FD scheme[16,20] for 2-D TR simulations using (a) only the time-reversed acoustic pressure as input, or (b) both the time-reversed acoustic pressure and acoustic particle velocities as input is unsuitable due to instability problems (despite implementing the ABC at the boundary nodes). This temporal instability is attributed to the identically zero damping in the central FD schemes. Hence, the unresolved spurious numerical waves generated at the computational boundaries due to implementation of Dirichlet boundary conditions[3] cannot be suppressed and thus propagate in the domain leading to instability.

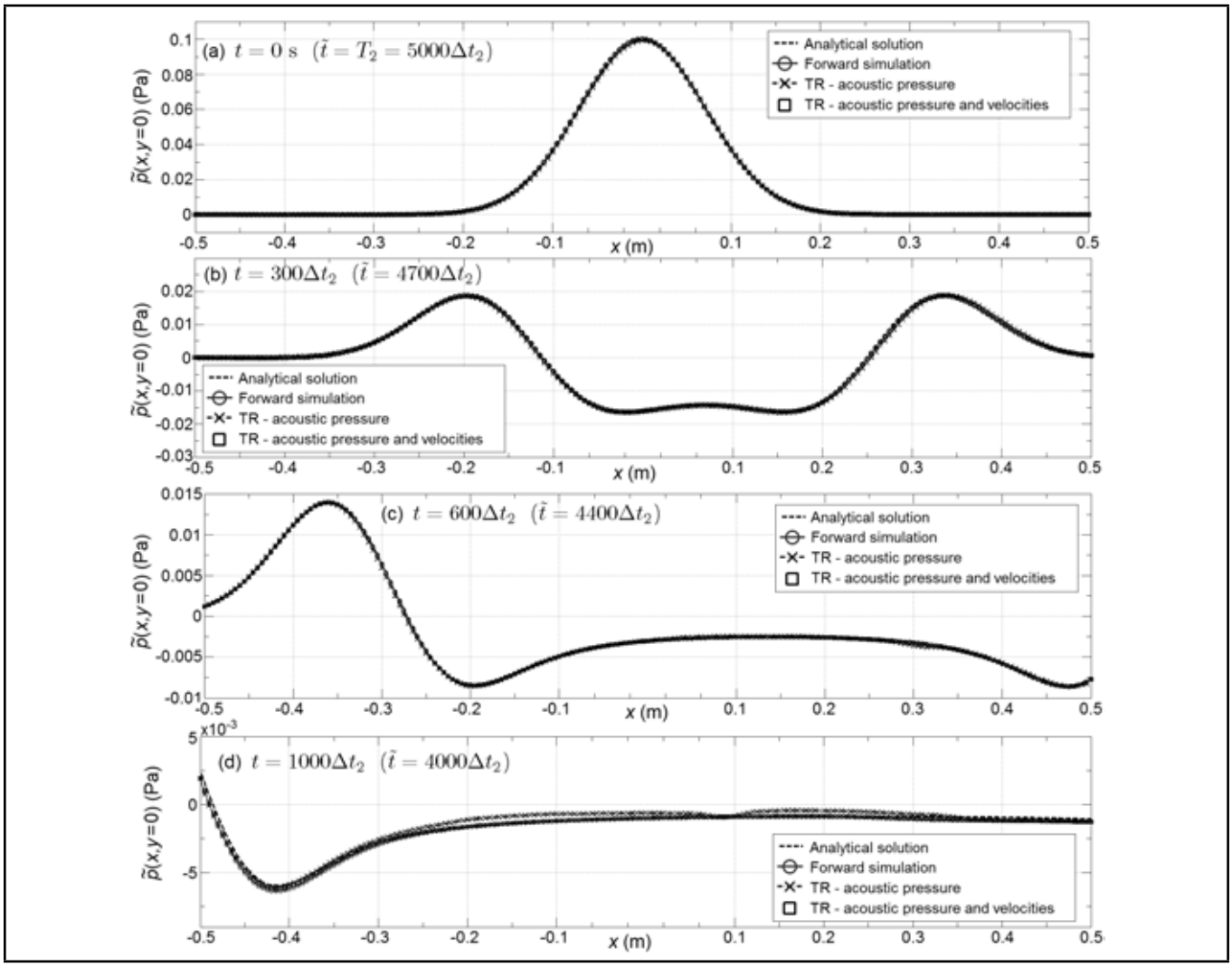

Figure 9. Spatio-temporal evolution of the acoustic pressure field along the x axis, i.e., $\tilde{p}(x, y = 0)$: Comparison of the analytical solution with results of the forward simulation, the TR simulation with only time-reversed acoustic pressure as input and TR simulation with both, the time-reversed acoustic pressure and particle velocity as input at the computational boundaries.

5. CONCLUSIONS

The temporal stability and accuracy of the forward and TR simulations of the Linearised Euler Equations (LEE) based on the Pseudo-Characteristic Formulation (PCF) and using two different classes of overall Finite-Difference (FD) schemes, (a) upwind-biased schemes and (b) central DRP schemes, have been analysed. The important contributions of this investigation are:

1. The stability of the 1-D forward and TR simulations using the overall upwind-biased FD scheme has been established by means of a matrix eigenvalue decomposition, wherein it is shown that two opposite upwinding directions must be considered for computing the spatial derivatives in the opposing fluxes of the PCF. The implementation of ABC is necessary to ensure stability of both, the 1-D and 2-D forward simulation of a pulse propagating in a free-space (with mean flow) over an arbitrarily large time duration. The stability of 1-D TR simulation using only time-reversed acoustic pressure as input is due to the use of upwind-biased schemes near the boundary and interior nodes, and the use of optimised downwind schemes at and near the boundary nodes having DRP property over a large range of wave numbers. Unlike the 1-D TR simulation, the ABC must be implemented for ensuring the stability of the 2-D TR simulation using overall upwind-biased schemes.

2. The stability of the forward simulation using the overall central DRP FD schemes[16,20] in the PCF is also ensured by implementation of the ABC, wherein the execution time-step of the central DRP FD scheme is found to be almost half that of the overall upwind-biased FD scheme. However, for the 1-D TR simulations, some of the eigenvalues of overall central DRP FD schemes[16,20] (without ASD[32]) are shown to have significantly large positive real parts, which implies the manifestation of instabilities towards the final time-instants. In fact, for the 2-D TR simulations, these instabilities manifest during the initial time-instants. Therefore, it may be concluded that the overall central DRP FD schemes are unsuitable for the TR simulation.

3. It is demonstrated that the use of both the time-reversed acoustic pressure and acoustic particle velocity histories as input during TR simulation is unnecessary. Rather, use of (a) only the time-reversed acoustic pressure his-

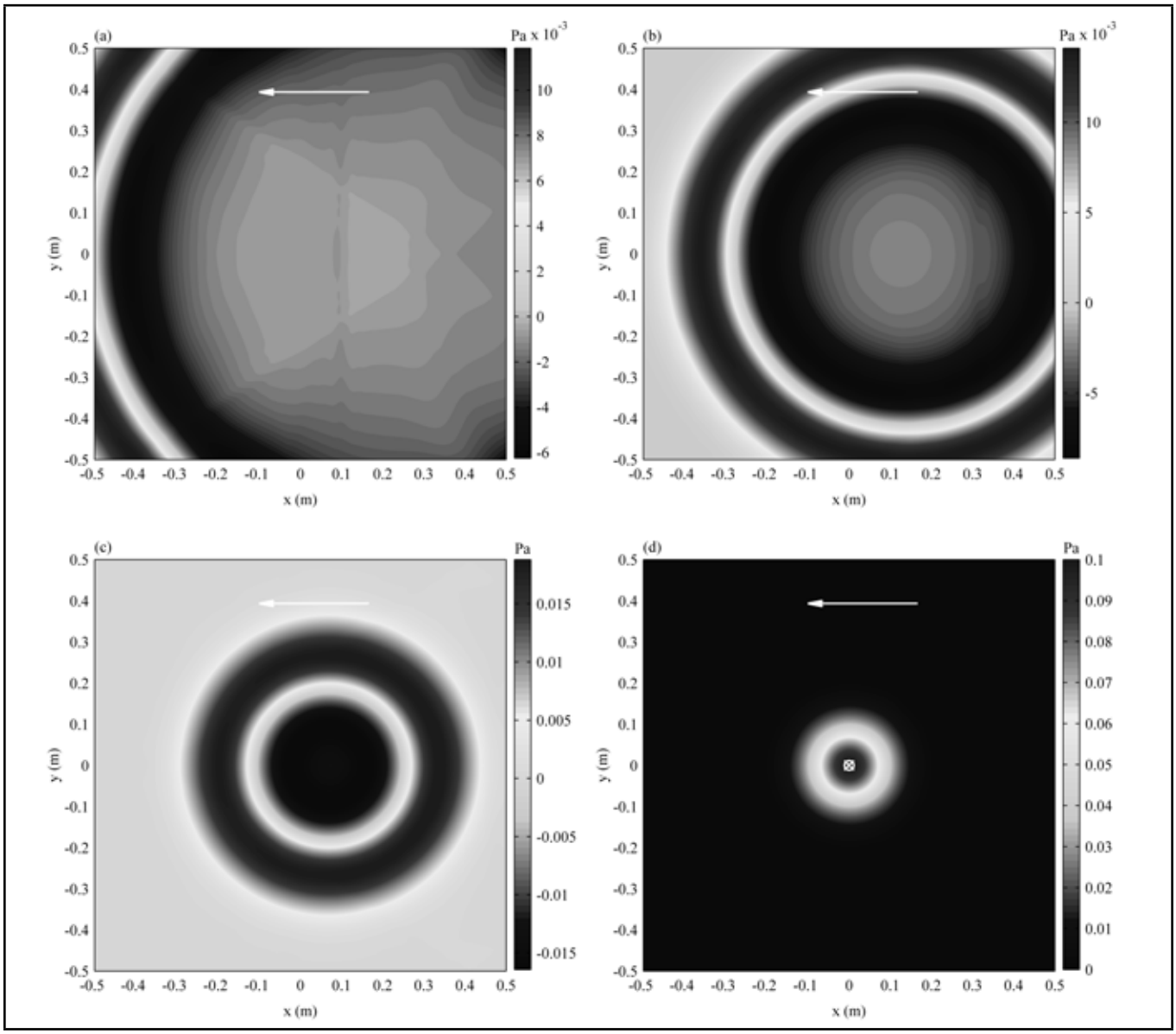

Figure 10. The acoustic pressure field $\tilde{p}(x, y, \tilde{t})$ due to back-propagation of a Gaussian pulse in a 2-D free-space obtained by means of the TR simulation using only the time-reversed acoustic pressure as input Dirichlet conditions at the nodes on the computational boundaries at reverse time-instants $\tilde{t}$ = (a) $4000\Delta t_2$, (b) $4400\Delta t_2$, (c) $4700\Delta t_2$, and (d) $T_2 = 5000\Delta t_2$. (The direction of uniform mean flow is reversed.)

tory as input at computational boundaries, and (b) the numerically reversed mean flow profile (which is known, a-priori during the forward simulation[4,7,10,36] or experimentally measured using hot-wire anemometry[3]) is sufficient to warrant an accurate back-propagation of waves and thereby localise the sound source(s) in flow fields using the TR method.

4. The accuracy of the forward and TR simulation (using the overall upwind-biased FD schemes and PCF) is established by comparing the 1-D/2-D simulation results of the propagation of a Gaussian pulse in a free-space to the corresponding analytical solution. The physical significance of the accuracy analysis of TR simulation, in particular, is that for acoustic pressure and velocity fields at every forward time-instant t, there exists corresponding time-reversed acoustic pressure and velocity fields at reverse time $\tilde{t} = T - t$, thus, analytically validating the aeroacoustic TR simulation for the first time using simple test cases of back-propagation of a pulse in a free-space.

ACKNOWLEDGEMENTS

This work was supported by the Australian Research Council (ARC) under grant DP 120102134 'Resolving the mechanics of turbulent noise production'.

REFERENCES

[1] Fink, M. Time reversal of ultrasonic fields, I. Basic principles, *IEEE Transactions on Ultrasonics, Ferroelectrics, and Frequency Control*, **39** (5), 555–556, (1992).

[2] Fink, M., Cassereau, D., Derode, A., Prada, C., Roux, P., Tanter, M., Thomas, J. L., and Wu, F. Time-reversed acoustics, *Report on Progress in Physics*, **63** (12), 1933–1995, (2000).

[3] Padois, T., Prax, C., Valeau, V., and Marx, D. Experimental localization of an acoustic sound source in a wind-tunnel flow by using a numerical time-reversal technique, *Journal*

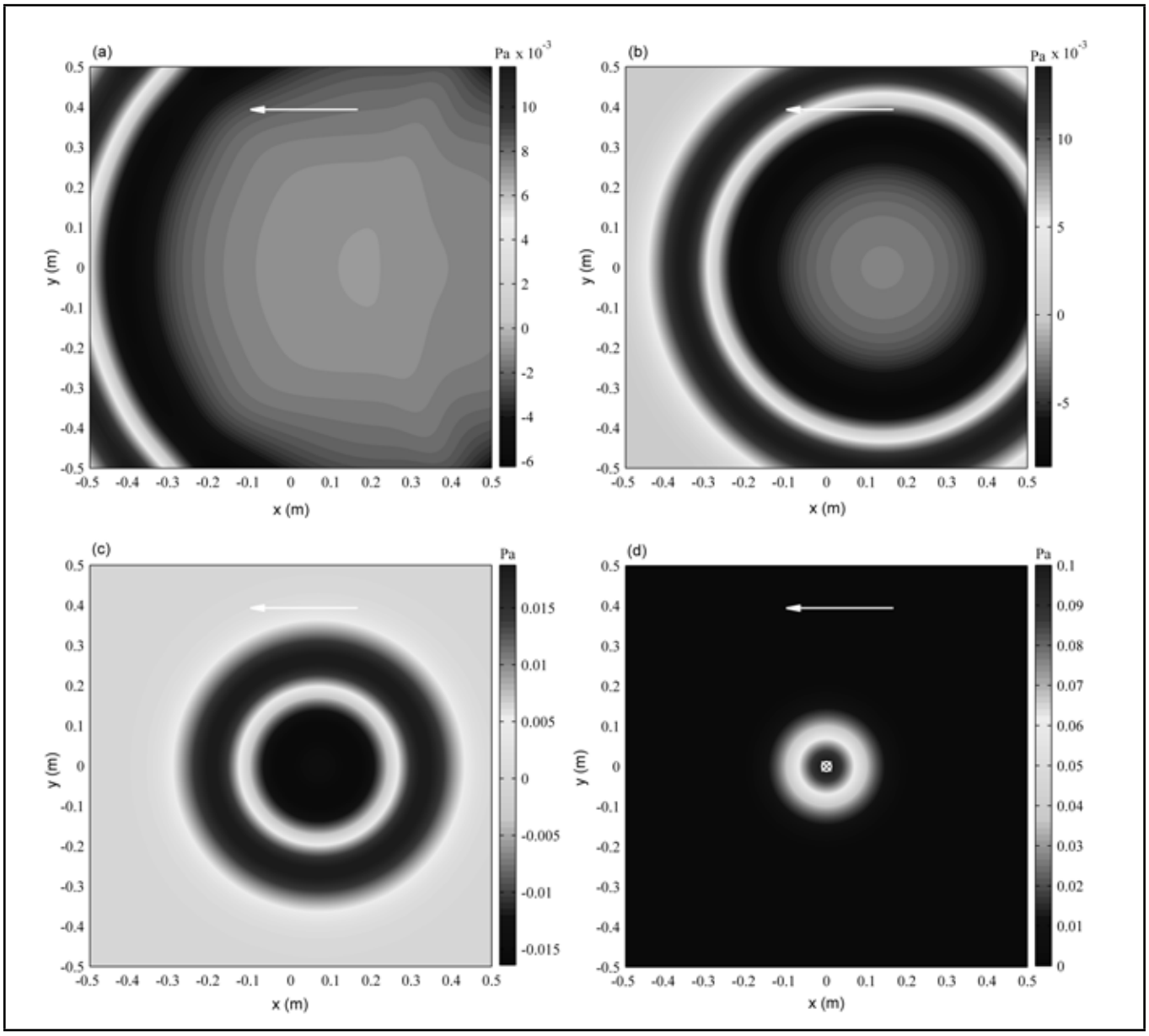

Figure 11. The acoustic pressure field $\tilde{p}(x, y, \tilde{t})$ due to back-propagation of a Gaussian pulse in a 2-D free-space obtained by means of the TR simulation using both, the time-reversed acoustic pressure and velocities as input Dirichlet conditions at the nodes on the computational boundaries at reverse time-instants $\tilde{t} =$ (a) $4000\Delta t_2$, (b) $4400\Delta t_2$, (c) $4700\Delta t_2$, and (d) $T_2 = 5000\Delta t_2$. (The direction of uniform mean flow is reversed.)

of the Acoustical Society of America, **132** (4), 2397–2407, (2012).

[4] Mimani. A., Doolan, C. J., and Medwell, P. R. Multiple line arrays for the characterization of aeroacoustic sources using a time-reversal method, *Journal of the Acoustical Society of America*, **134** (4), EL327–EL333, (2013).

[5] Shimura, T., Watanabe, Y., Ochi, H., and Song, H. C. Long-range time reversal communication in deep water: Experimental results, *Journal of the Acoustical Society of America*, **132** (1), EL49–EL53, (2012).

[6] Park, H. W., Sohn, H., Law, K. H., and Farrar, C. R., Time reversal active sensing for health monitoring of a composite plate, *Journal of Sound and Vibration*, **302** (1–2), 50–66, (2007).

[7] Mimani. A., Doolan, C. J., and Medwell, P. R. Aeroacoustic time-reversal in the presence of a reflecting surface, Paper No. 96, *Proc. 43rd International Congress on Noise Control Engineering InterNoise 2014*, Melbourne, Australia, (2014).

[8] Lerosey, G., Rosny, J. D., Tourin, A., Derode, A., Montaldo. G., and Fink, M. Time reversal of electromagnetic waves, *Physical Review Letters*, **92** (19), 193904, (2004).

[9] Bavu, E., Besnainou, C., Gibiat, V., Rosny, J. D., and Fink, M. Subwavelength sound focusing using a time-reversal acoustic sink, *Acta Acustica United with Acustica*, **93** (5), 706–715, (2007).

[10] Mimani. A., Doolan, C. J., and Medwell, P. R. Enhancing the focal-resolution of aeroacoustic time-reversal using a point sponge-layer damping technique, *Journal of the Acoustical Society of America*, **136** (3), EL199–EL205, (2014).

[11] Deneuve, A., Druault, P., Marchiano, R., and Sagaut, P. A

coupled time-reversal/complex differentiation method for aeroacoustic sensitivity analysis: towards a source detection procedure, *Journal of Fluid Mechanics*, **642**, 181–212, (2010).

[12] Sesterhenn, J. A characteristic-type formulation of the Navier-Stokes equations for high order upwind schemes, *Computers and Fluids*, **30** (1), 37–67, (2001).

[13] Lu, S.-Y. and Sagaut, P. Pseudo-characteristic formulation and dynamic boundary conditions for computational aeroacoustics, *International Journal of Numerical Methods in Fluids*, **53** (2), 201–227, (2007).

[14] Bailly, C. and Juve, D. Numerical solution of acoustic wave propagation problems using linearized Euler equations, *AIAA Journal*, **38** (1), 22–29, (2000).

[15] Zhang, R., Qin, G., and Zhu, C. Spectral element method for acoustic propagation problems based on linearized Euler equations, *Journal of Computational Acoustics*, **17** (4), 383–402, (2009).

[16] Tam, C. K. W. and Webb, J. C., Dispersion-relation-preserving finite-difference schemes for computational acoustics, *Journal of Computational Physics*, **107** (2), 262–281, (1993).

[17] Toro, E. F. *Riemann Solvers and Numerical Methods for Fluid Dynamics*, Springer-Verlag, Berlin, (1999), 2nd Edition, 265–291.

[18] Sesterhenn, J., Muller, B., and Thomann, H., Flux-Vector Splitting for compressible low mach number flow, *Computers and Fluids*, **22** (4), 441–451, (1993).

[19] Lele, S. K. Compact finite difference schemes with spectral-like resolution, *Journal of Computational Physics*, **103** (1), 16–42, (1992).

[20] Tam, C. K. W. Computational aeroacoustics: issues and methods, *AIAA Journal*, **33** (10), 1788–1796, (1995).

[21] Mimani, A. and Moreau, D. J. and Prime, Z. and Doolan, C. J., Enhanced focal-resolution of dipole sources using aeroacoustic time-reversal in a wind-tunnel, Mechanical Systems and Signal Processing. (2015), DOI: 10.1016/j.ymssp.2015.09.037.

[22] Zhuang, M. and Chen, R. F. Applications of high-order optimised upwind schemes for computational aeroacoustics, *AIAA Journal*, **40** (3), 443–449, (2002).

[23] Li, Y. Wavenumber-extended high-order upwind-biased finite-difference schemes for convective scalar transport, *Journal of Computational Physics*, **133** (2), 235–255, (1997).

[24] Berland, J., Bogey, C., Marsden, O., and Bailly, C., High-order, low dispersive and low dissipative explicit schemes for multiple-scale and boundary problems, *Journal of Computational Physics*, **224** (2), 637–662, (2007).

[25] Gottlieb, S. and Shu, C.-W. Total variation diminishing Runge-Kutta schemes, *Mathematics of Computation*, **67** (221), 73–85, (1998).

[26] Clayton, R. and Engquist, B. Absorbing boundary conditions for acoustic and elastic wave equations, *Bulletin of the Seismological Society of America*, **67** (6), 1529–1540, (1977).

[27] Engquist, B. and Majda, A. Absorbing boundary conditions for the numerical simulation of waves, *Mathematics of Computation*, **31** (139), 629–651, (1977).

[28] Engquist, B. and Majda, A. Radiation boundary conditions for acoustic and elastic wave calculations, *Communications in Pure and Applied Mathematics*, **32** (3), 313–357, (1979).

[29] Strang, G. *Linear algebra and its applications*, Thomson Brooks/Cole, (2005), 3rd Edition, 275–286.

[30] Shukla, R. K., Tatineni, M., and Zhong, X. Very high-order compact finite difference schemes on non-uniform grids for incompressible Navier Stokes equations, *Journal of Computational Physics*, **224** (2), 1064–1094, (2007).

[31] Marburg, S. Normal modes in external acoustics. Part I: Investigation of the one-dimensional duct problem, *Acta Acustica United with Acustica*, **91** (6), 1063–1078, (2005).

[32] Tam, C. K. W, Webb, J. C., and Dong, Z. A study of the short wave components in computational acoustics, *Journal of Computational Acoustics*, **1** (1), 1–30, (1993).

[33] Lockard, D. P., Brentner, K. S., and Atkins, H. L. High-accuracy algorithms for computational aeroacoustics, *AIAA Journal*, **33** (2), 246–251, (1995).

[34] Tam, C. K. W. *Computational aeroacoustics: A wave number approach*, Cambridge University Press, New York, (2012), 30–36.

[35] Myint-U, T. and Debnath, L. *Linear partial differential equations for scientists and engineers*, Birkhäuser Boston, (2007), 4th Edition, 488–495, 691–694.

[36] Mimani, A., Prime, Z., Doolan, C. J., and Medwell, P. R. A sponge-layer damping technique for aeroacoustic time-reversal, *Journal of Sound and Vibration* **342**(1), 124–151, (2015).

Ball Bearing Fault Diagnosis Using Supervised and Unsupervised Machine Learning Methods

V. Vakharia, V. K. Gupta and P. K. Kankar

Mechanical Engineering Discipline, PDPM Indian Institute of Information Technology, Design and Manufacturing Jabalpur, Jabalpur-482005, India

(Received 29 September 2013; accepted 9 June 2014)

This paper deals with the approach of using multiscale permutation entropy as a tool for feature selection for fault diagnosis in ball bearings. The coefficients obtained from the wavelet transformation of the vibration signals of the bearings are used for the calculation of statistical parameters. Based on the minimum multiscale permutation entropy criteria, the best scale is selected and statistical parameters such as crest factor, form factor, and permutation entropy are calculated. Finally, the faults are classified by considering the statistical parameters and permutation entropy as features in supervised and unsupervised machine learning methods, such as a support vector machine and self-organizing maps, respectively. Results revealed that the multiscale permutation entropy-based feature extraction techniques provide higher classification accuracy in comparison to the other methodologies that have been proposed in previous published works. The methodology proposed in this paper also gives good results for unsupervised learning methods, i.e. self-organizing maps.

NOMENCLATURE

C	penalty constant
m	embedding dimension
M	total number of samples
N	length of data
s	scale
t_1	time
z	time series
Y_j^s	coarse-grain time series
w	weight
ξ_i	slack variable
π	permutation pattern
τ	time delay

1. INTRODUCTION

Techniques designed to monitor the conditions of rolling element bearings receive considerable attention from researchers across the globe. Faults in the bearings are the major source of the breakdown of machinery. When a defect in the surface of one bearing strikes the surface of another, impulsive force is generated. This effect has been exploited by several vibration analysis methods, as well as various signal processing techniques.[1] Incipient fault diagnosis in rolling element bearings is essential for production efficiency and plant safety. Fault diagnosis depends mainly on the feature extraction techniques, because the signals carry dynamic information about the state of the machinery. The patterns of vibration signals, due to defects in various rotating parts, exhibit specific features. That is to say, faults can be identified by looking at pattern abnormalities in plant machinery and rotating parts. Signal processing techniques such as time domain, frequency domain, and combined time frequency domain (such as wavelet transformation) have been investigated by various researchers.[2–5] Due to variations in friction, loading conditions, interaction of various rotating elements, and clearance and nonlinear stiffness of the bearings,[6,7] the vibration signals generated by machinery are often characterized by nonlinearity. Thus, nonlinear parameter estimation techniques have been widely used by many researchers.[8–12] Numerous methods such as the correlation dimension[13] and the Lyapunov exponent[14] have been developed recently to detect nonlinearity. Entropy estimation is an important parameter for measuring system complexity. Analysis of the vibration signals generated from rotating machinery, using complexity measure such as approximate entropy[15] and multiscale entropy,[16] was used for the bearing fault diagnosis. Permutation entropy was introduced by Bandt and Pompe,[18] and is a new nonlinear parameter estimation tool that was efficiently used for the fault diagnosis.[17] By comparing neighbouring values, the complexity of a time series can be extracted using permutation entropy. Shannon entropy is useful for the estimation of the complexity of a time series based on a single scale, while multiscale permutation entropy is useful for calculating the complexity of a time series after comparing neighbouring values and entropy over multiple scales. Bandt and Pompe[18] presented permutation entropy, as a parameter of average entropy, to describe the complexity of a time series. It should also be noted that feature vectors consisting of multiscale permutation entropy provide better information about physical phenomena such as the occurrence of faults in the rotor bearing system.[19] The use of permutation entropy for chatter detection in the turning process,[20] known as electroencephalography (EEG) signal analysis,[21] has been used for chaotic time series. Signals obtained from complex mechanical systems that have several components are usually complicated. Approximate entropy and permutation entropy are based on a single scale, and are therefore inefficient in diagnosing the signals correctly. Multiscale permutation entropy was proposed by Costa, et al.,[22] and this concept was utilized by Wu, et al.[23] and Vakharia, et al.,[24] for bearing fault diagnosis and classification.

In this paper, raw vibration signals are used, and the concept of permutation entropy is utilized for the selection of scale. Wavelet coefficients are calculated by considering coiflet as

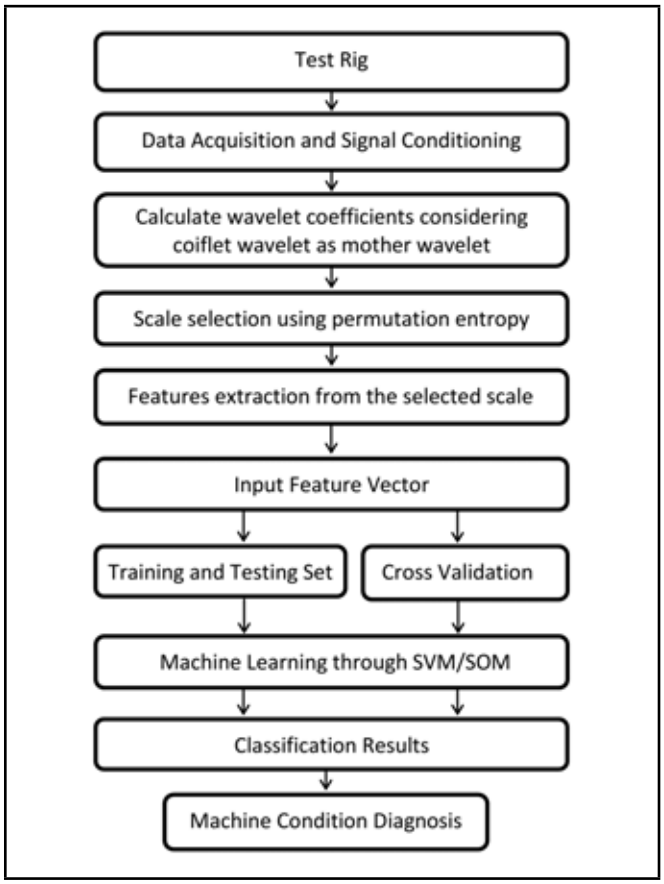

Figure 1. Proposed fault diagnosis strategy.

mother wavelet, and a scale giving the least permutation entropy is selected for the calculation of statistical parameters. A feature vector includes these statistical parameters: speed, loading condition, and permutation entropy. A feature vector is fed as the input for fault classification using a support vector machine (SVM) and self-organizing maps (SOM). Results revealed that the proposed feature extraction method gives improved results compared to the conventional feature extraction methods. The complete methodology for fault diagnosis is shown in Fig. 1.

2. PERMUTATION ENTROPY

Signals obtained from complex machinery parts using EEG show that stock markets are very complex in nature. Initially, entropy was used for quantifying the predictability of a time series on a single scale. It does not give insight between regularity and complexity. Costa, et al.[22] have developed multiscale entropy for the analysis of physiologic time series, in which initial sample entropy is calculated and, based on the concept of multiscale, various entropies can be calculated.

Permutation entropy was introduced as a computational efficient method for extracting the information from compound systems. For a given time series,

$$Z(t) = (Z_1, Z_2, Z_3, \ldots, Z_n); \tag{1}$$

at each time t_1, a vector composed of the m^{th} subsequent values is constructed as:[25]

$$t_1 \rightarrow (Z_{t_1}, Z_{t_1+1}, \ldots, Z_{t_1+(m-2)}, Z_{t_1+(m-1)}); \tag{2}$$

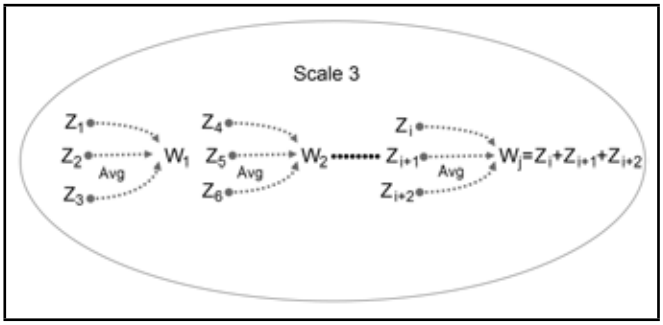

Figure 2. Coarse grain procedure.

where m is called embedding dimension and tells how much information is present in a vector. Further, by considering time delay of τ, Eq. (2) can be rewritten as

$$t_1 \rightarrow (Z_{t_1}, Z_{t_1+\tau}, \ldots, Z_{t_1+\tau(m-2)}, Z_{t_1+\tau(m-1)}). \tag{3}$$

For a given embedding dimension, there will be $m!$ possible permutation π of order m. Permutation entropy employs the concept of Shannon entropy by analysing the relative frequency of patterns generated from a time series. The permutation entropy is defined as:

$$\text{PE} = -\sum_{i=1}^{m!} \pi_i \ln \pi_i. \tag{4}$$

Permutation entropy depends mainly on the selection of embedding dimension m and time delay τ. Bandt and Pompe[18] suggested in their study that value of embedding dimension m should be $3 \leq m \leq 7$ and time delay $\tau = 1$.

Normalized permutation entropy is given by

$$\text{NPE} = \frac{\text{PE}}{\ln m!}; \tag{5}$$

where $\ln m!$ denotes maximum PE value.

2.1. Multiscale Permutation Entropy

The concept of multiscale entropy has been proposed by Costa, et al.[22] For a given time series and 3 scales, the data points are averaged by selecting non-overlapping windows of increasing length to form multiple coarse-grained time series as shown in Fig. 2.

For the scale factor s, the elements of coarse-grained time series are evaluated by

$$Y_j^s = \frac{1}{s} \sum_{i=(j-1)s+1}^{js} z_i, \qquad 1 \leq j \leq \frac{N}{s}; \tag{6}$$

where N denotes the length of the data. For scale 1, the coarse-grained time series is simply the original time series.

3. MACHINE LEARNING TECHNIQUES

Machine learning is a type of artificial intelligence technique used essentially for classification and regression. An important task of machine learning is classification where algorithms are constructed between different data based on their specific patterns. Algorithms can be broadly categorized into supervised and unsupervised algorithms.

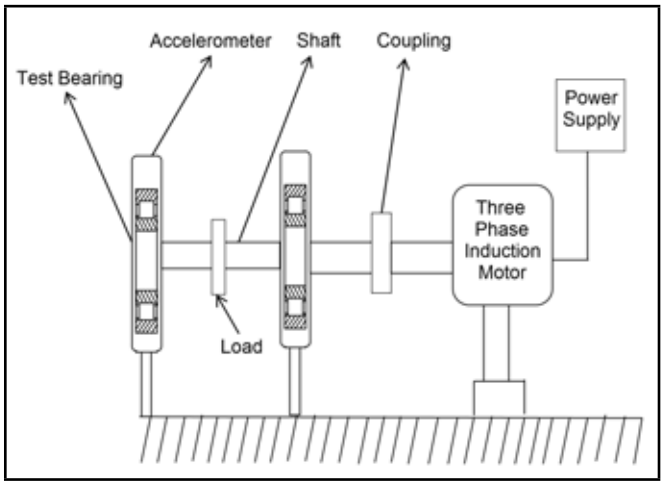

Figure 3. Schematic diagram of rotor bearing system.

3.1. Supervised Learning

In supervised learning, a label is associated with each feature of training data. Training data consists of input and desired result. The task of an algorithm is to search for patterns and develop mathematical models. Based on their prediction accuracy, models are evaluated. Naive Bayes, artificial neural networks, and support vector machines are some examples of supervised learning methods.

The support vector machine (SVM) is a statistical learning method based on the principle of structural risk minimization and was introduced by Vapnik.[26] SVM is a supervised learning algorithm in which a learning machine has allotted some set of features to a class of labels.

For linearly separable data, a hyperplane is constructed which separates hyperspace to achieve maximum separation between the classes known as the margin. The nearest data points that are used to define the margin are known as support vectors.

The optimal hyperplane separating the data can be obtained as a solution to the following optimization problem:
Minimize

$$\frac{1}{2}||w||^2 + C\sum_{i=1}^{M}\xi_i \tag{7}$$

subject to

$$y_i\left(w'x_i + b\right) \geq 1 - \xi_i, \quad \xi_i \geq 0, \quad i = 1, 2, \ldots, M. \tag{8}$$

3.2. Unsupervised Learning

An unsupervised learning model is not provided with correct results during training. The task is to identify hidden patterns in unlabelled data. It can also be used for clustering the input data in to classes based on their statistical property. Self-organizing maps, K means, and blind signal separation are among the techniques which come under unsupervised learning.

A self-organizing map (SOM) is a type of neural network model commonly used for unsupervised classification.[27] In self-organizing maps, "self-organizing" means that no supervision is required. The models learn on their own through unsupervised competitive learning, while the "map" is used to map their weights according to the given input data.

Table 1. Parameters of bearing 6205 (SKF).

Parameter	Value
Outer race diameter	52 mm
Inner race diameter	25 mm
Ball diameter	7.94 mm
Ball number	10
Contact angle	0°

In the initial stage, all node weights are initialized and a vector is randomly chosen from the set of training data and forwarded to network. Every node in the network is then used to calculate which weights are similar to the input vector. Nodes which are within the boundary of the best-matching unit are adjusted to make them like the input vector. Finally, the location of the most similar node is arranged in such a way that a topographic map is generated. The locations of the most similar nodes indicate statistical features contained in the input patterns.

4. EXPERIMENTAL SETUP AND DATA ACQUISITION

In the present study, an experimental test rig has been used, and vibration responses for healthy bearings and bearings with faults are obtained. A schematic diagram of a rotor bearing system is shown in Fig. 3. Table 1 shows the dimensions of the ball bearing used for this study. The vibration signals from the rig are taken after some hours of initial running.

The signals are measured at rotor speeds 1000, 1500, and 2000 rpm, and in all five classes with no loader, one loader, and two loader conditions, respectively. The following five bearing conditions are considered for the study:

1. Bearing with no defect (BND);
2. Bearing with spall on inner race (SI);
3. Bearing with spall on outer race (SO);
4. Bearing with spall on ball (SB);
5. Combined defects (CD).

The combined defects represent bearing conditions which have a spall on the inner race, the outer race, and ball together.

5. FEATURE EXTRACTION

Statistical analysis of vibration signals gives different primary and secondary parameters.

The continuous wavelet coefficients (CWC) of all signals were calculated at the 7^{th} level of decomposition (2^7 scales). A scale giving the least permutation entropy was selected, and the statistical features of CWC corresponding to that scale were calculated for both horizontal and vertical directions. The selected embedded dimension m and the time delay τ of multiscale permutation entropy are 5 and 1, respectively.

The following features were selected for both horizontal and vertical conditions:

a. Permutation entropy, defined by Eq. (4).

b. Form factor, defined as the ratio of the RMS value and the average value of the signal.

Table 2. Sample input feature values for SOM/SVM.

Horizontal response			Vertical Response					
Permutation entropy	Crest factor	Form factor	Permutation entropy	Crest factor	Form factor	Loader	Speed	Class
0.6188	-0.9115	-1.0971	0.7100	0.8356	1.1968	0	1000	CD
0.5665	0.8123	1.2311	0.6356	-8.004	-1.2494	0	1500	CD
0.5823	-0.8453	-1.1831	0.7711	0.8259	1.2108	0	2000	CD
0.5169	-0.8519	-1.1738	0.5155	0.4019	2.4881	1	1000	SB
0.6154	0.4970	2.0121	0.8217	-0.6378	-1.5679	1	1500	SB
0.7166	-0.6240	-1.6025	0.7974	0.3539	2.8259	1	2000	SB
0.4255	0.8674	1.1528	0.4568	0.7593	1.3170	2	1000	SO
0.4120	0.8849	1.1301	0.7877	0.1105	9.0499	2	1500	SO
0.4939	-0.9028	-1.1076	0.8260	-0.5253	-1.9037	2	2000	SO
0.6045	0.8888	1.1251	0.5695	0.3862	2.5891	0	1000	BND
0.5901	0.2458	4.0691	0.5652	0.7917	1.2631	0	1500	BND
0.5666	-0.8682	-1.1518	0.6888	0.9204	1.0865	0	2000	BND
0.5093	0.7406	1.3503	0.7466	-0.7828	-1.2775	2	1000	SI
0.5712	-0.8311	-1.2032	0.5927	0.1317	7.5934	1	1500	SI
0.5241	0.4286	2.3334	0.5087	-0.6191	-1.6153	1	2000	SI

c. Crest factor, defined as the ratio of the peak value of the signal to its RMS value.

These features were extracted from the vibration signals and were fed as an input to machine learning techniques such as SOM and SVM for the classification of faults.

6. RESULTS AND DISCUSSION

Testing and cross validation of feature sets have been carried out using SOM and SVM as classifiers.[28] These features consist of permutation entropy, form factor, and crest factor, each for horizontal and vertical responses, and the number of loaders and rotor speed are also considered as the features for testing and cross-validation purposes. A sample input feature values are shown in Table 2.

The effects of bearing defects like ball defect, combined defect, outer race defect and inner race defect on multiscale permutation entropy are shown in Fig. 4. For the cases considered, it was found that for the vertical response, multiscale permutation entropy is higher as compared to the horizontal response.

With no loader and 1500 rpm, maximum multiscale permutation entropy is 0.7625 for ball defects under vertical response conditions, and minimum multiscale permutation entropy is 0.4015 for outer race defects under horizontal response conditions, as shown in Fig. 4(a). It can be interpreted that ball defects under no-loader conditions and 1500 rpm exhibit more disorder when compared to other classes, and outer race defects contain less disorder.

From Fig. 4(b), it is observed that the maximum multiscale permutation entropy, 0.8368, is for ball defects under vertical response conditions, and the minimum value of 0.521 for inner race defects is under horizontal response conditions. It can be interpreted that when speed is increased, disorder increased in ball defects and decreased in inner race defects. When the load is increased and the speed is 1500 rpm, the maximum multiscale permutation entropy is 0.836 for ball defects, the vertical response conditions and minimum multiscale permutation entropy is 0.3028 for combined defects, and the horizontal response conditions are shown in Fig. 4(c). With one loader and 2000 rpm, the maximum multiscale permutation entropy is 0.7974 for ball defects, the vertical response conditions and minimum multiscale permutation entropy is 0.5087 for inner race defects, and vertical response conditions are shown in Fig. 4(d). Thus, it is concluded that ball defects are severe as compared to other defects considered in the present study for all load conditions and speeds.

A total of 75 instances are considered which consist of 6, 16, 18, 17, and 18 cases of BND, SI, SO, SB, and CD, respectively. For coiflet wavelets, a scale is selected based on minimum multiscale permutation entropy. Testing and cross-validation results are shown in Tables 3 and 4 for SOM and SVM, respectively. Cross validation is a technique to evaluate the performance of classifiers. Therefore, 10-fold cross validation, which is the standard method of testing classifiers, was carried out.

From Table 3, for testing purpose 6/6, 16/16, 12/18, 17/17, and 18/18 cases were predicted correctly for BND, SI, SO, SB, and CD, respectively. Similarly, for cross-validation purposes, 4/6, 12/16, 11/18, 17/17, and 18/18 cases were predicted correctly. We infer that for SB and CD, SOM has correctly predicted 17/17 and 18/18 cases each for both testing and cross validation. It is also clear that for SO, the prediction accuracy rate is comparatively lower compared to other classes. It can be concluded that for SO, about 22% (4/18) of the data matches with CD, and about 16% (3/18) of the data matches with SI, which suggests that while performing cross validation, SOM is unable to distinguish between these fault classes efficiently. A possible reason for spalls on the outer race is that the vibration data collected contains more noisy data compared to other faults. Similarly, for SI about 12% (2/16) of the data matches with SO, and 12% (2/16) of the data matches with SB. Another possible reason for not correctly identifying these defects during cross validation may be due to over fitting; i.e. the optimization of the parameters for the SOM classifier is not done properly.

Table 4 shows the prediction accuracy when SVM is used as a classifier. For testing purposes, 6/6, 16/16, 18/18, 17/17, and 18/18 cases are predicted correctly for BND, SI, SO, SB, and CD, respectively. For cross validation, 6/6, 14/16, 14/18, 16/17, and 18/18 cases are predicted correctly for BND, SI, SO, SB, and CD, respectively. Thus, it is clear that the prediction accuracy of BND and CD is 100% for both testing and cross validation when SVM is used as a classifier. SI and SO are comparatively less accurately predicted. For SO, about 10% (2/18) of the data falls under CD. This means that 10% of the data of SO matches with the CD class. Similarly, 10% (2/18) of the data matches with the SI class during cross validation, which is an indication that SO contains more noisy data compared to other classes. Similarly, for SI about 13% (2/16)

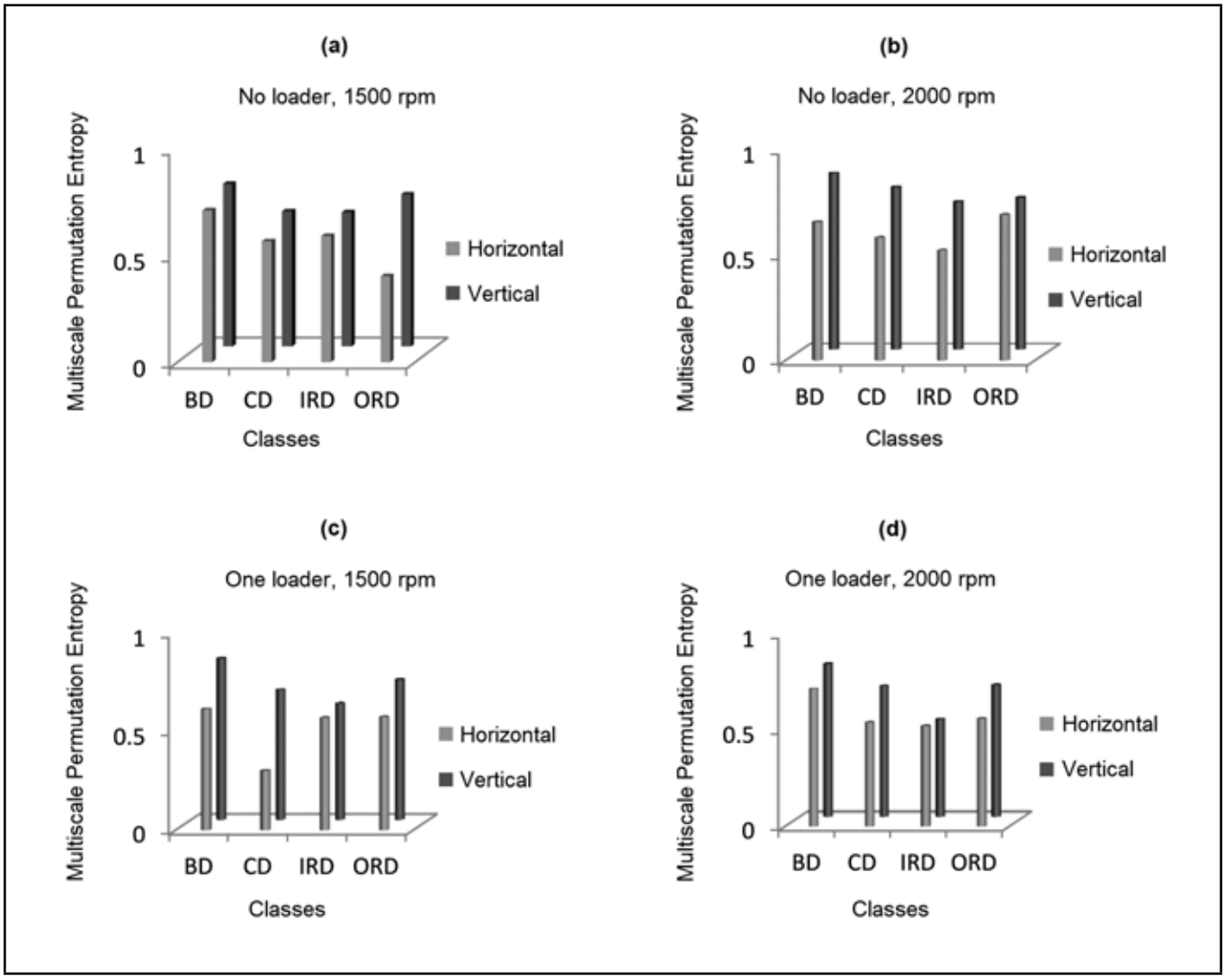

Figure 4. Multiscale permutation entropy with load condition and speed.

Table 3. Confusion matrix for SOM.

Using Test Set						Using 10 fold cross validation					
BND	SI	SO	SB	CD	Classified as	BND	SI	SO	SB	CD	Classified as
6	0	0	0	0	BND	4	0	1	0	1	BND
0	16	0	0	0	SI	0	12	2	2	0	SI
0	2	12	0	4	SO	0	3	11	0	4	SO
0	0	0	17	0	SB	0	0	0	17	0	SB
0	0	0	0	18	CD	0	0	0	0	18	CD

Table 4. Confusion matrix for SVM.

Using Test Set						Using 10 fold cross validation					
BND	SI	SO	SB	CD	Classified as	BND	SI	SO	SB	CD	Classified as
6	0	0	0	0	BND	6	0	6	0	6	BND
0	16	0	0	0	SI	0	14	0	2	0	SI
0	0	18	0	0	SO	0	2	14	0	2	SO
0	0	0	17	0	SB	0	0	0	16	1	SB
0	0	0	0	18	CD	0	0	0	0	18	CD

Table 5. Classification accuracy.

Parameters	SOM		SVM	
	Test set	10 fold cross validation	Test set	10 fold cross validation
Correctly classified instances	69 (92%)	63 (84%)	75 (100%)	68 (90.667%)
Incorrectly classified instances	6 (8%)	12 (16%)	0 (0%)	7 (9.33%)
Kappa statistic	0.8977	0.8161	1	0.8806
Total number of instances	75	75	75	75

Table 6. A comparative study between the presented work and published literature.

References	Machine Learning Method used	Faults considered	Efficiency of classification (%)	Techniques used for vibration analysis	Remarks
Kankar, et al.[29]	SOM, ANN, SVM	Spall in inner race, outer race, rolling element, and combined component fault, healthy bearing	70.66, 89.33, 90.66 by SOM, ANN, and SVM, respectively (cross validation)	Meyer, coiflet5, symlet2, gaussian, complex morlet, and shannon wavelet	Wavelets are compared
Kankar, et al.[30]	ANN, SVM	Spall in inner race, outer race, rolling element, and combined component fault, healthy bearing	71, 74 by ANN and SVM, respectively (test set)	NA	Time series data used
Seker, et al.[31]	NA	Fault at ball, inner race, outer race	71.33	Daubechies 15 and 20	Time series data used
Abbasion, et al.[32]	SVM	Bearing looseness, defects in rolling elements and bearing raceways	100 by SVM	Meyer wavelet	Wavelet denoising
Wu, et al.[23]	SVM	Fault at ball, inner race, outer race, and normal bearing	97–100 by SVM (training)	NA	Time series data used
Proposed work	SOM, SVM	Inner race, outer race, ball, combined fault, and bearing with no defect	92, 100 (test set) and 84, 91 (cross validation) by SOM and SVM, respectively	coiflet2	Best scale is selected using Permutation Entropy criterion

of the data matches exactly with SB, which also indicates that the classifier is not able to distinguish between them during cross validation.

Table 5 depicts the overall classification accuracy for both the test set and the 10-fold cross validation set using two classifiers. It can be observed that, for SOM, 69/75 test instances were classified correctly, which gives a 92% classification accuracy rate, and for 10-fold cross validation, 63/75 test instances were classified correctly, giving an 84% classification accuracy rate. Similarly, for SVM, 75/75 test instances were classified correctly, giving a 100% classification accuracy rate, and for 10-fold cross validation, 68/75 test instances were classified correctly, giving a 90.66% classification accuracy rate, as shown in Table 5.

The kappa statistic is used for assessing the degree to which two or more classes that are testing the same data match when it comes to assigning the data to classes. For complete matching, the corresponding value of the kappa statistic is 1, and for totally incomplete matching, its value is 0. For SVM, using a testing set, the ideal value of 1 is achieved for the kappa statistic. It is clear from the above mentioned results that the classification accuracy of SVM is much better compared to SOM, and is reported by Kankar, et al. in their study.[29] SOM is a type of unsupervised learning method in which the objective is to identify hidden structures in unlabelled data. Since the inputs given are unlabelled, it becomes difficult for the learning algorithm to train itself to correctly identify that particular feature belonging to a specific class. This makes it quite difficult to correctly predict the given feature set, and thus the classification accuracy is lower. On the other hand, the classification accuracy of SVM is high because of its good generalization capability. For demonstrating the effectiveness of the proposed methodology, a comparative study between the present work and some published literature is shown in Table 6. The proposed work is compared in terms of the machine learning method used, faults considered on the bearings, classification efficiency, and the vibration analysis technique.

7. CONCLUSIONS

In the present study, a methodology is proposed for comparing supervised and unsupervised learning methods for fault diagnosis of bearings. Raw vibration signals of various fault categories are used and the concept of permutation entropy is applied for the best scale selection of wavelet coefficients. Features based on the best scale are extracted for both horizontal and vertical response conditions. In total, 8 features have been considered, including permutation entropy, form factor, and crest factor for both horizontal responses and vertical responses, along with the number of loaders and shaft rotation. The classification results of SOM and SVM are compared, and the results show that SVM is able to give much better results due to its better generalization capability. It is observed that severe vibration is observed for ball defects. The prediction accuracy rate of both learning algorithms is lower for outer race defects and higher for combined defects. It can be concluded that the proposed methodology based on scale selection using multiscale permutation entropy along with supervised and unsupervised machine learning techniques has potential for application to the development of real-time fault diagnosis systems.

REFERENCES

[1] Tandon, N. and Choudhury, A. A review of vibration and acoustic measurement methods for the detection of defects in rolling element bearings, *Tribology International*, **32**, 469–480, (1999).

[2] Bonnardot, F., Randall, R. B., and Antoni, J. Enhanced unsupervised noise cancellation using angular resampling for planetary bearing fault diagnosis, *International Journal of Acoustics and Vibration*, **9** (2), 51–60, (2004).

[3] Harsha, S. P., Nataraj, C., Kankar, P. K. The effect of ball waviness on nonlinear vibration associated with rolling element bearings, *International Journal of Acoustics and Vibration*, **11** (2), 56–66, (2006).

[4] Sharma Aditya, Amarnath M., and Kankar P. K. Feature extraction and fault severity classification in ball bearings, *Journal of Vibration and Control*, (2014). DOI: 10.1177/1077546314528021

[5] Wang, J., Cui, L., Wang, H., and Chen, P. Improved complexity based on time-frequency analysis in bearing quanti-

tative diagnosis, *Advances in Mechanical Engineering*, **11**, (2013). DOI: 10.1155/2013/258506

[6] Kankar, P. K., Sharma S. C., and Harsha, S. P. Vibration based performance prediction of ball bearings caused by localized defects, *Nonlinear Dynamics*, **69** (3), 847–875, (2012).

[7] Harsha, S. P. and Kankar, P. K. Nonlinear dynamic analysis of a complex rotor bearing system, *International Journal of Acoustics and Vibration*, **10** (1), 33–39, (2005).

[8] Pincus, M. Approximate entropy as a complexity measure, *Chaos*, **5** (1), 110–117, (1995).

[9] Signorini, M. G., Magenes, G., Cerutti, S., and Arduini, D. Linear and nonlinear parameters for the analysis of fetal heart rate signal from cariotocographic recordings, *IEEE Transactions on Biomedical Engineering*, **50** (3), 365–374, (2003).

[10] Li, X., Cui, S., and Voss, L. J. Using permutation entropy to measure the electroencephalographic effects of sevoflurane, *Anesthesiology*, **109**, 448–456, (2008).

[11] Li, X., Ouyang, G., and Richards, D. A. Predictability analysis of absence seizures with permutation entropy, *Epilepsy Research*, **77**, 70–74, (2007).

[12] Quiroga, R. Q., Arnhold, J., Lehnertz, K., and Grassberger, P. Kulback-Leibler and renormalized entropies: Applications to electroencephalograms of epilepsy patients, *Physical Review E*, **62**, 8380–8386, (2000).

[13] Rolo-Naranjo, A. and Otero, M. E. M. A method for the correlation dimension estimation for on-line condition monitoring of large rotating machinery, *Mechanical Systems and Signal Processing*, **19**, 939–954 (2005).

[14] Ding, R. Q. and Li, J. P. Nonlinear finite-time lyapunov exponent and predictability, *Physics Letter A*, **364**, 396–400, (2007).

[15] Yan, R. and Gao, R. X. Approximate entropy as a diagnostic tool for machine health monitoring, *Mechanical Systems and Signal Processing*, **21**, 824–839, (2007).

[16] Zhang, L., Xiong, G., Liu, H., Zou, H., and Guo, W. Bearing fault diagnosis using multi-scale entropy and adaptive neuro-fuzzy inference, *Expert Systems and Applications*, **37**, 6077–6085, (2010).

[17] Yan, R., Liu, Y., and Gao, R. X. Permutation entropy: A nonlinear statistical measure for status characterization of rotary machines, *Mechanical Systems and Signal Processing*, **29**, 474–484, (2011).

[18] Bandt, C. and Pompe, B. Permutation entropy: A natural complexity measure for time series, *Physical Review Letters*, **88**, 174102, (2002).

[19] Tiwari, R, Gupta,V. K., and Kankar, P. K. Bearing fault diagnosis based on multi-scale permutation entropy and adaptive neuro fuzzy classifier, *Journal of Vibration and Control*, (2013). DOI: 10.1177/1077546313490778

[20] Nair, U., Krishna, B. M., Namboothiri,V. N. N., and Nampoori, V. P. N. Permutation entropy based real-time chatter detection using audio signal in turning process, *International Journal of Advanced Manufacturing Technology*, **46**, 61–68, (2010).

[21] Bruzzo, A. A., Gesierich, B., Santi, M., Tassinari, C. A., Birbaumer, N., and Rubboli, G. Permutation entropy to detect vigilance changes and preictal states from scalp EEG in epileptic patients: A priminary study, *Neuro Science*, **29**, 3–9, (2008).

[22] Costa, M., Goldberger, A. L., and Peng, C. K. Multiscale entropy analysis of complex physiological time series, *Physical Review Letters*, **89**, 068102–1–4, (2002).

[23] Wu, S. D., Wu, P. H., Wu, C. W., Ding, J. J., and Wang, C. C. Bearing fault diagnosis based on multiscale permutation entropy and support vector machine, *Entropy*, **14**, 1343–1356, (2012).

[24] Vakharia,V., Gupta,V. K., and Kankar, P. K. A Multiscale entropy based approach to select wavelet for fault diagnosis of ball bearings, *Journal of Vibration and Control*, (2014). DOI: 10.1177/1077546314520830

[25] Zanin, M., Zunino, L., Rosso, O. A., and Papo, D. Permutation entropy and its main biomedical and econophysics applications: A review, *Entropy*, **14**, 1553–1577, (2012).

[26] Vapnik, V. N., *Statistical learning theory*, John Wiley and Sons, (1998).

[27] Haykin, S. *Neural Networks: A comprehensive foundation*, Pearson Prentice Hall Publications, Ontario, Canada, (2005).

[28] Hall, M., Frank, E., Holmes, G., Pfahringer, B., Reutemann, P., and Witten, I. H. The WEKA data mining software: An update, *SIGKDD Explorations*, **11** (1), (2009).

[29] Kankar, P. K., Sharma, S. C., and Harsha, S. P. Fault diagnosis of ball bearings using continous wavelet transform, *Applied Soft Computing*, **11**, 2300–2312, (2011).

[30] Kankar, P. K., Sharma, S. C., and Harsha, S.P. Fault diagnosis of ball bearings using machine learning methods, *Expert Systems with Applications*, **38**, 1876–1886, (2011).

[31] Seker, S. and Ayaz, E. Feature extraction related to bearing damage in electric motors by wavelet analysis, *Journal of Franklin Institute*, **340** (2), 125–134, (2003).

[32] Abbasion, S., Rafsanjani, A., Farshidianfar, A., and Iranic, N. Rolling element bearings multi-fault classification based on the wavelet denoising and support vector machine. *Mechanical Systems and Signal Processing*, **21**, 2933–2945, (2007).

Free Vibration of the Damping Beam Using Co-simulation Method Based on the MFT

D. Q. Wang, C. J. Wu and R. C. Yang

School of Mechanical Engineering, Xi'an Jiaotong University, Xi'an, Shanxi, China

(Received 6 October 2013; accepted 12 May 2014)

The particle damping technique has been in development for several decades, and has been used successfully in many fields. However, it is difficult to predict its damping characteristics due to complex collisions and friction mechanisms, as well as high non-linear damping characteristics in dense particles. The focus of these current main achievements is centralized on the equivalent single degree of freedom (SDOF) system under free and forced vibration. In this paper, a brand new co-simulation approach for the continuum structure system based on the multiphase flow theory (MFT) of gas solid is developed by the COMSOL Multiphysics live link for MATLAB. A simple continuum structure system, (*i.e.*, the cantilever particle damped beam) is made as an experiment. It is further shown that the damping capacity of a cantilever beam depends not only on the exerted location of the particle damper, but also the quantity of the filling. An experimental verification is performed, and an acceptable accordance is achieved between the theoretical results and the experimental data. It can be shown that the theoretical work in this paper is valid. The co-simulation method simplifies the complicated modelling problem, and offers the possibility to analyse the vibro-acoustic response prediction for complicated particle-damping composite structures.

1. INTRODUCTION

Granular particle damping, which is derived from the impact damping, is a promising technique of providing damping with granular particles placed in an enclosure attached to or embedded in the holes drilled in the vibrating structure.[1,2] This emerging technology can perform well even in extreme temperatures (either low or high) and harsh chemical environments where traditional passive damping methods, such as the widely used viscous and viscoelastic dampers, are ineffective in particular applications. Particle damping technology has drawn the attention of many researchers in engineering and academic fields, and has been well researched for several decades, with a large volume of books and papers published on the subject. With the development of the particle damping technology in many fields, coherent computer simulation technology is also being developed. The simulation method is very convenient in investigating the effect of the system parameters on the characteristic of the particle damping without extensive trial-and-error testing. However, the popular simulation approaches in the published studies were more often focused on the single degree of freedom (SDOF) system or the equivalent SDOF under the free and forced vibration. It is noted that these current methods have been stretched beyond their normal capacity for the simulation of the continuum damping structure system. Consequently, it is desirable to develop a new simulation technology to predict the characteristics of particle damping. Even to this day, the simulation methods to evaluate the damping characteristic of the continuum structure systems, such as the plate and shell with the particle damper, are rare in recent research. The principal challenges are that their performances are highly nonlinear. There has also been some considerable research in the area of particle damping, and some analytical models have been developed on heuristic evaluations of particle damping.

The Discrete Element Method (DEM) simulation has been extensively developed over the years to evaluate the dissipative properties of granular materials. The DEM simulation can capture the complex interactions of the dissipation mechanisms in a particle damper. However, the DEM simulation suffers from a complicated dynamic model, and it is highly time-consuming, which make it difficult to perform parametric analysis when the number of granules is large. It is very regrettable that the application field is only limited to the SDOF system, and therefore is not competent for the vibration analysis of the complicated continuity system with particle damper. Saeki[3] used this method and investigated the damping behaviour of a horizontally vibrating system in which the gravity is not as important as in a vertically vibrating system. Mao and coworkers[4] studied the characterization of particle damping in transient vibrations.

Friend *et al.*[5] developed a lumped mass approach, also referred to as the numerical algorithm, where the particles inside the cavity are assumed to form a lumped mass without consideration of collision and friction effects between particles. The particle damper is attached to the free end of a cantilevered aluminium beam,and the system is reduced to an equivalent SDOF system. The effects of acceleration amplitude and clearance inside the enclosure were studied, and the damping was found to be highly nonlinear, *i.e.*, amplitude dependent. Such an approach is also applicable to investigate the damping performance of the multiple degree-of-freedom (MDOF) system to multi-body vibrating structure.[6]

Liu, *et al.*[7] used an equivalent viscous damping model to represent the nonlinearity, which was extracted from experimental results. However, their studies were limited to the

use of a single mass to simulate all particles, and the relative motions between the particles were neglected. Papalou and Masri[8,9] developed a simple model to predict the performance of a particle damper. This model was empirically derived from experiments on a SDOF system.

Our previous work (Wu, *et al.*[10]) originally introduced the multiphase flow theory (MFT) of gas solid to evaluate the characteristics of granular particle damping. It is convenient to investigate the performance of particle damping in terms of the effective viscosity. The numerical and experimental studies showed that the particles are helpful to add damping for attenuating the vibration responses of the host structures. Fang and Tang[11] further utilized this theory to carry out detailed studies under various forced excitation levels, packing ratios and enclosure dimensions, and the different energy dissipation mechanisms were also quantitatively analysed. Wu, *et al.* further improved the analytical model based our proceeding work,[10] where the expression of equivalent viscous damping for inter-particle friction was introduced instead of the expression of Coulomb friction damping based on the Hertz contact theory discussed in work by Wu, Liao, and Wang.[10] Two typical examples[12,13] - the free vibration of a cantilever particle-damping beam (equivalent SDOF system) and the harmonic forced vibration of a SDOF system with particle damping were used to verify this improved model.

However, the above research achievements were all limited on the SDOF system. If the continuum structure system is subjected to the particle damper, it is obvious that this analysis can be very complicated. In the real engineering field, the structure can not reasonably be approximated as a SDOF system, since the complex external loading and the damper impacting are likely to excite more than just the fundamental mode of vibration. The primary objective of this paper is to develop a new simulation method with low time-consuming for the complex continuous structure with particle damper based on MFT. In the next section, for the sake of brevity, here a simple particle-damping beam is considered as an attempt.

2. BASIC THEORY

As mentioned by Fan and Zhu,[14] granular particles enclosed in a cavity of a vibrating structure can be considered as a multiphase flow of gas solid with low Reynolds number where the particle concentration is high (*i.e.* the flow is dense). For inelastic particles and a simple shear flow such as a laminar flow, the effective viscosity due to inter-particle collisions can be derived from the kinetic theory of dense multiphase flow as follows:

$$\mu_c = \frac{6}{5}(1+\mathrm{e}_p)\sqrt{\frac{\Theta}{\pi}}{\alpha_p}^2 g_p \rho_p d_p; \tag{1}$$

where μ_c is the effective viscosity due to inter-particle collisions, e_p is the restitution coefficient of the particle, and α_p is the packing ratio defined as the volume of particles to the total volume of the cavity. ρ_p and d_p denote the density and the mean diameter of particles respectively, Θ is the fluctuation-specific kinetic energy, and g_p is the radial distribution function.

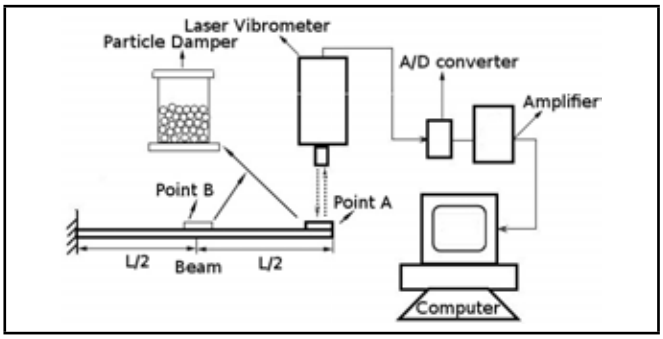

Figure 1. A schematic of a cantilever particle-damping beam and its experimental setup.

Schaeffer[15] conducted a linear analysis of granular flow equations that included frictional stress terms. The equivalent shear viscosity corresponding to friction force between particles can be expressed as follows:[15]

$$\mu_f = \frac{p_p \sin\phi}{2\sqrt{I_{2D}}}.; \tag{2}$$

where ϕ is the angle of internal friction, I_{2D} is the second invariant of the deviatoric stress tensor. p_p is the solids pressure, which is composed of a kinetic term and a second tem due to particle collision.

Considering that the friction model and collision model have the same form of expression, the complete damping effect between the particles can be uniformly expressed as follows:

$$\mu_p = \mu_c + \mu_f. \tag{3}$$

Furthermore, one can find the equivalent viscous damping coefficient due to the inter-particle collisions and friction as shown below (the derivation process of the formulas and the description of parameters can be found in our previous work[12,13]):

$$c_{eq} = c_1|\dot{x}|^{1/2} + c_2|\dot{x}| - c_3|\dot{x}|^{2/3} + c_1|\dot{x}| + c_1|\dot{x}|^2 - c_1|\dot{x}|^3. \tag{4}$$

Equation (4) shows that the particle damping can be equivalent to the viscous damping, including the inter-particle collisions and friction effects based on the multiphase flow theory (MFT) of gas solid.

As shown in Fig. 1, a granular particle damper is attached to the free end of the beam. The kind of beam can be idealized as a Bernoulli-Euler beam with end mass. Considering the intrinsic structure damping and particle damping, the free vibration equation of the continuous particles damping beam system can be written by the matrix form as

$$\mathbf{M}\ddot{\mathbf{x}} + \mathbf{C}\dot{\mathbf{x}} + \mathbf{K}\mathbf{x} = \mathbf{F} + f; \tag{5}$$

where $\mathbf{M}$ is the system mass matrix, $\mathbf{C}$ is the system damping matrix, $\mathbf{K}$ is the system stiffness matrix, and $\mathbf{F}$ is the excite force. The viscous damping force $f = -c_{eq}\dot{x}$, c_{eq} is derived from the Eq. (4), and $|\dot{x}|$ is the amplitude of vibration velocity on the beam where the particle damper is placed. The Eq. (4) includes the velocity coupling that is found to be highly nonlinear.

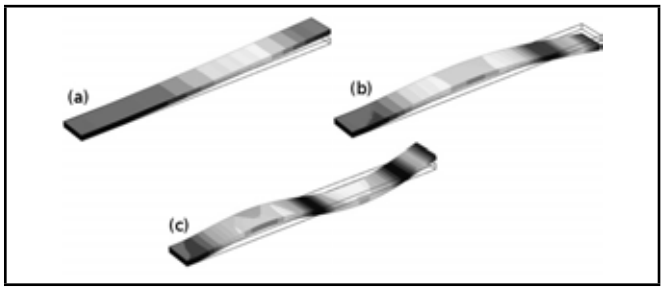

Figure 2. Three first computed bending mode shape of the clamped-free beam: (a) first mode shape, $f_1 = 58.98$ Hz; (b) second mode shape, $f_2 = 369.74$ Hz; (c) third mode shape, $f_3 = 1035.5$ Hz.

It is noted that the effect of the particle damper can be equivalent to a viscous force and a lump mass which includes the mass of the enclosure and the total mass of the particles filled. Such an idea is novel, which leads to a breakthrough that the continuous particle damping structure may be analysed by the commercial software COMSOL Multiphysics live link for MATLAB, using the finite element method (FEM). This step is a key in this article; it becomes an implementation detail process using FEM to analyse a continuous particle damping beam based on MFT of gas solid.

The co-simulation is made by the COMSOL Multiphysics live link for MATLAB by self-programming. Live link provides an interface between COMSOL and MATLAB based on the COMSOL client/server architecture. A COMSOL thin client is running inside MATLAB, and has access to the COMSOL API through the MATLAB Java interface.

On the other hand, the result accuracy of a computer simulation depends on the computational parameters used in the simulation, especially the system parameter Rayleigh damping matrix $\mathbf{C}$. The objective of the next section is to gain the damping parameter $\mathbf{C}$.

3. THE SIMULATION PARAMETERS DETERMINATION

A schematic of the test set-up is shown in Fig. 1. A cantilever beam is chosen as the test specimen to evaluate particle damping performance, in part, because it is an infinite DOF system, as opposed to the SDOF system studied in the literature. The dimensions of the beam are: Young's modulus 66 GPa, density 2828 kg/m^3, length 0.38 m, width 0.02 m, and height 0.006 m. To determine the characteristics of the undamped beam, experimental measurements are taken and FEA of the beam is performed using COMSOL. Results from experimental impact testing of the structure indicate that the first three fundamental modes of the structure are 58.99 Hz, 373.27 Hz, and 1041.5 Hz. FEA indicates that this first three fundamental mode are 58.98 Hz, 369.74 Hz and 1035.5 Hz. These values differ slightly from the experimentally determined data, in which the relative errors of FEA values to the experiment values are respectively 0.017%, 0.95%, and 0.58%. The deformed shapes of these modes predicted by the COMSOL are shown in Fig. 2.

In order to quantify the structural damping, it is more appropriate to define specific damping capacity as

$$\delta = \frac{\Delta T}{T}; \tag{6}$$

where ΔT is the kinetic energy converted into heat during one cycle of vibration, and T is the maximum kinetic energy during the cycle. If we define a cycle to be the duration between two successive maxima of the structural mass velocity curve $v(t)$, then T is maximum at the start of the cycle and given by

$$T = \frac{1}{2} M V^2. \tag{7}$$

The energy dissipated during the i cycle is calculated as $\Delta T_i = T_i - T_{i+1}$, or

$$\Delta T_i = \frac{1}{2} M \left({V_i}^2 - V_{i+1}^2 \right). \tag{8}$$

Therefore, the energy dissipation of the particle damping is expressed by the specific damping capacity as

$$\delta_i = \frac{V_i^2 - V_{i+1}^2}{V_i^2}. \tag{9}$$

The specific damping capacity applies to linear or nonlinear damping in either transient or steady-state vibrations. In particular, when ξ is small, $\xi \approx \delta / 4\pi$ ($\xi < 0.01$). In this study, the value of δ can be found from the experimental data corresponding to the beam without particles (*i.e.* $\alpha_{mp} = 0\%$). At time $t = 0$, the beam is given a tip displacement of $U_0 = 1.5$ mm, released from rest, and allowed to decay freely; the beam vibrates in its fundamental mode. An LK-G3001V Keyence laser vibrometer is used to measure the displacement of the beam. Using the well-known Doppler Effect and the principle of heterodyne interferometry, the displacement is measured by frequency demodulation to an extremely high resolution of 0.1 μm. The displacement amplitude ranges are set from -5 mm to 5 mm. The sampling interval is 250 μs. The value of δ is shown in Table 1. Thus, in the subsequent numerical studies, the value of δ_0 is selected as the mean value for any of four sequenced cycles (*i.e.* $\delta_0 = 0.026477$).

To find the values for the Rayleigh damping, we can use the relationship between the damping ratio and the Rayleigh damping parameters. It is often easier to interpret the critical damping ratios, which are given by

$$\xi = \frac{1}{2} \left(\frac{\alpha_{dM}}{2\pi f} + \beta_{dK} 2\pi f \right); \tag{10}$$

where α_{dM} and β_{dK} are the mass and stiffness damping parameters, respectively; f corresponds to any resonant frequency.

Note that Eq. (10) holds separately for each vibration mode in the system at its resonant frequency. In the frequency domain, it uses frequency-dependent values of α_{dM} and β_{dK}. For example, setting $\alpha_{dM} = 0$ produces an equivalent viscous damping model at the resonant frequency

$$\xi = \beta_{dK} \pi f. \tag{11}$$

Table 1. Specific damping capacity.

Items	1	2	3	4	Mean values
Specific damping capacity	0.023668	0.029749	0.030198	0.022292	0.026477

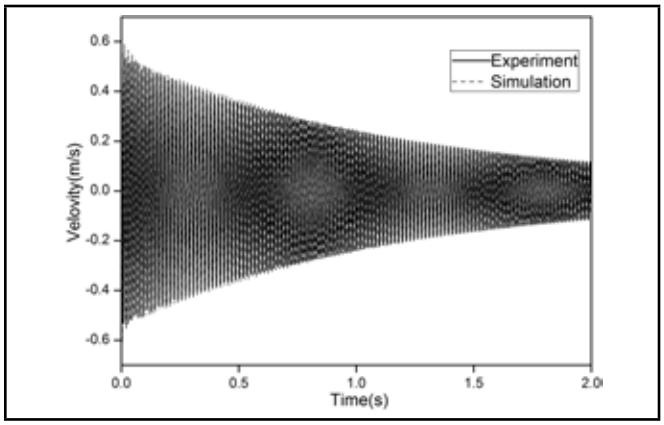

Figure 3. Evolution of the waveforms of velocities in the time domain under free vibration without particles.

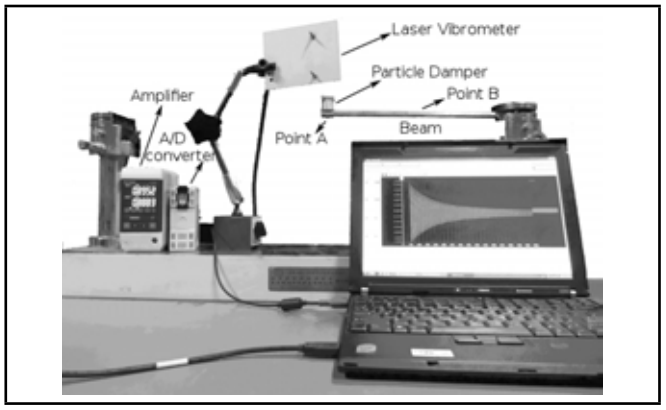

Figure 4. A figure of the experimental apparatus used.

Thus,

$$\beta_{dK} = \frac{\xi}{\pi f} = \frac{\delta/4\pi}{\pi f} = \frac{\delta_0}{4\pi^2 f}. \tag{12}$$

Assuming that the structure has a constant damping ratio, the first fundamental mode of the structure is at a frequency of 58.98 Hz. Solving the system of equations above will give the result $\beta_{dK} = 1.14\times10^{-5}$.

Figure 3 shows the velocity responses comparison between the simulation by COMSOL and the experimental measurement of the beam without particles. It is noted that the simulation results in COMSOL differ slightly from the experimental results. That is to say, the actual intrinsic structural damping in the experimental is not exactly the Rayleigh damping considered in the COMSOL model.

To verify the theoretical model developed in this study, an experiment for a cantilever beam with a particle damper is set up and shown in Fig. 4. The specifications for the experiment are the same as those specifications used in the simulation for the purpose of comparison. The transient velocity responses are measured. At time $t = 0$, the beam is given an initial tip displacement, released from rest, and allowed to decay freely, and the beam vibrates in its fundamental mode. A laser vibrometer LK-G3001V Keyence is used to measure the velocity responses of the particle damper block.

4. FREE VIBRATION OF A CANTILEVER PARTICLE-DAMPING BEAM

In this section, the transient response of a continuum cantilever particle-damping beam is analysed. The initial value of the tip displacement of the beam is 1.5 mm. The mass of the damper with no particles is 14.52 grams, and its interior dimensions are: diameter = 16 mm, and height = 20 mm. The particle is made of iron powder whose density is 6800 kg/m^3, and the mean diameter of particles is 0.3 mm. The restitution coefficient of the particles is 0.6 on the basis of testing. The kinetic friction coefficients between the individual particles and between the particles and the wall of the cavity are 0.3 and 0.2, respectively, from experimental results. In addition, the kinematic viscosity and density of air are 1.51×10^{-5} m^2/s and 1.21 kg/m^3, respectively.

As documented by Wu, Liao, and Wang,[10] the experimental set-up to carry out the free vibrations consists of imposing an initial displacement at the beam tip and allowing it to decay freely. The beam decays freely with known initial displacement and velocity. The mass packing ratio α_{mp}, which is defined as the actual packing mass of particles to the maximum permissive packing mass of particles in a cavity, is also introduced to describe the packing condition of the damper.

The process is organized in two parts. The first part consists of studying the vibratory behaviour of the system under free vibration. The velocity of the whole cantilever beam and enclosure is measured for two cases. In the first case, the mass packing ratio is the same, but the position is different where the particle damper is placed (point A or point B) (Fig. 1). In the second measurement, the mass packing ratio is different, and the particle damper location is the same. In the second part of the process, the fast Fourier transformation of the system velocities obtained in the same experimental conditions are shown for both a system without particles and a system with a particle damper.

To determine the characteristics of the damped system with the particle damper, both experimental testing and FEA are performed. The transient velocity responses are measured. To bring the influence of the mass packing ratio α_{mp} and the location where the particle damper is exerted on the evolution of specific damping capacity, some measurements are performed for the continuous cantilever beam with the enclosure containing the particles.

Figures 5a and 5b show the results of the free vibrations at the free end of the beam when the particle damper is placed in a different position on the beam (see Fig. 1, and the point A or point B), the mass packing ratio is kept for the same values. It is shown that the vibrations of the beam with particles decay much faster when the particle damper is placed on the point A, compared to the case in which the particle damper is placed on the point B.

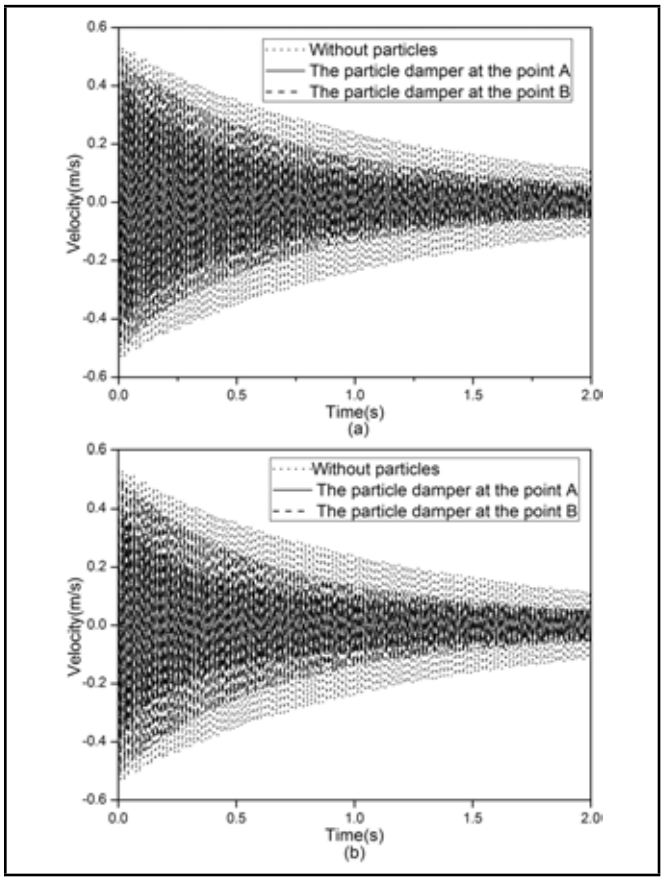

Figure 5. Velocity response at the free end of the beam, when the particle damper is placed on the different position: (a) $\alpha_{mp} = 10\%$; (b) $\alpha_{mp} = 40\%$.

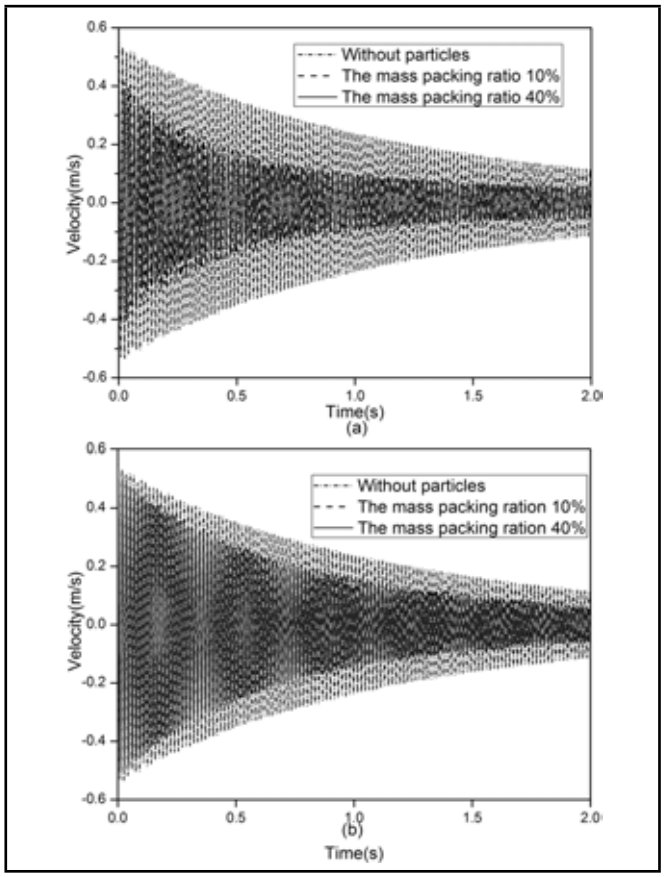

Figure 6. Velocity response at the free end of the beam, when the particle damper is placed on the same position: (a) The particle damper on point A; (b) The particle damper on point B.

Figures 6a and 6b show velocity response at the free end of the beam, when the particle damper is placed on the same point, the mass packing ratio is kept for the different values. It is shown that the vibrations of the beam with particles decay much faster (with increasing mass packing ratio α_{mp}) compared to the case without particles.

Figures 5 and 6 present a comparison of typical decay curves for the two cases described above. The effects of a particle damper on the velocity amplitude are seen in the differences between the two curves. Clearly, a particle damper causes a significant decrease in the velocities amplitude within the first few cycles.

Figures 7 and 8 show the comparisons of the velocity responses of the beam between the simulation results and the experiments. The simulation results show reasonably accurate estimates of the response of the transient vibration. It is noted that the theoretical results differ slightly from the experimental results. That is to say, the actual intrinsic structural damping in the experiment is not exactly the viscous damping considered in the theoretical model.

In Figs. 9 and 10, the fast Fourier transformation of the system velocities obtained in the same experimental conditions are shown for both a system without the particles and for a system with a particle damper. For the first case, when the particle damper is placed in a different position on the beam, the mass packing ratio α_{mp} is kept for the same values, and the fast Fourier transformation in Figs. 5a and b are corresponding to the experimental data in Figs. 9a and b. For the mass packing ratio $\alpha_{mp} = 10\%$, three spectral peaks could be clearly identified at $\approx$ 59.5 Hz (without particles), 57.5 Hz (the particle damper on point B) and 46 Hz (the particle damper on point A) in Fig. 5a.The presence of particle collisions reduces the spectral amplitude of these peaks significantly about 12.05% and 33.45% compared to the case without particles, respectively. For the mass packing ratio $\alpha_{mp} = 40\%$, there are three spectral peaks, respectively: z at $\approx$ 59.5 Hz, (without particles), 56.5 Hz (the particle damper on point B), and 43 Hz (the particle damper on point A) in Fig. 5b.The corresponding spectral amplitude peaks decrease about 30.43% and 58.35% compared to the case without particles.

For the second case, when the particle damper is placed on the same point, but the mass packing ratio is kept for the different values, the fast Fourier transformations of the system velocities in Figs. 6 a and b are correspond to the experimental data in the Figs. 10 a and b. For the particle damper is localized on point B, three spectral peaks appear at $\approx$ 59.5 Hz (without particles), 57.5 Hz (the mass packing ratio $\alpha_{mp} = 10\%$) and 56.5 Hz (the mass packing ratio $\alpha_{mp} = 40\%$). The corresponding spectral amplitude peaks are lowered about 12.05% and 30.43% compared to the case without particles, respectively. For the particle damper is exerted on point A, three spectral peaks are got at $\approx$ 59.5 Hz (without particles), 46 Hz (the mass packing ratio $\alpha_{mp} = 10\%$) and 43 Hz (the mass packing ratio $\alpha_{mp} = 40\%$). The peaks of the corresponding spectral amplitude are respectively dropped about 33.45% and 58.35% compared to the case without particles.

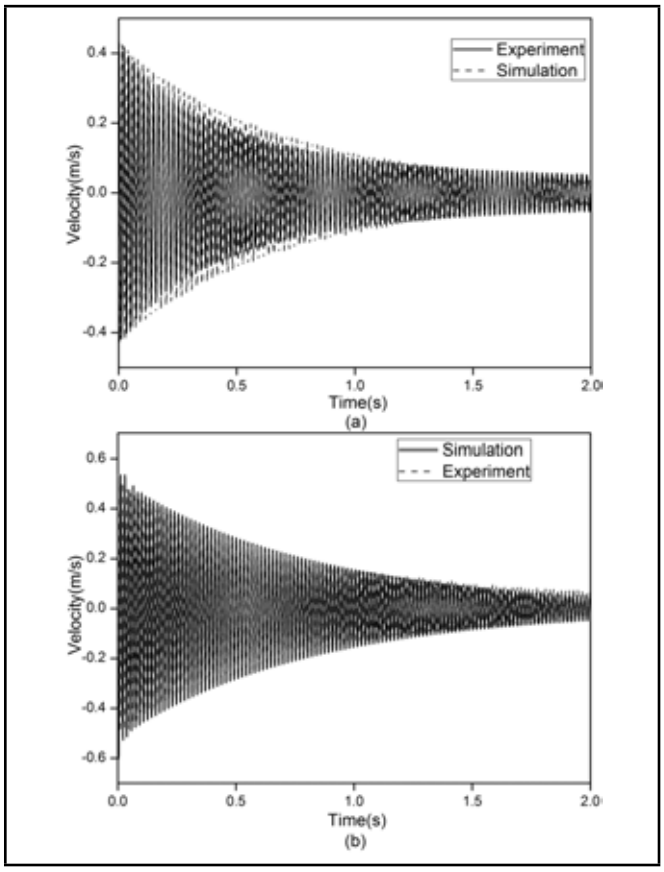

Figure 7. Evolution of the waveforms of velocities in the time domain under free vibration $\alpha_{mp} = 10\%$ (a) the particle damper is placed on point A; (b) the particle damper is placed on point B.

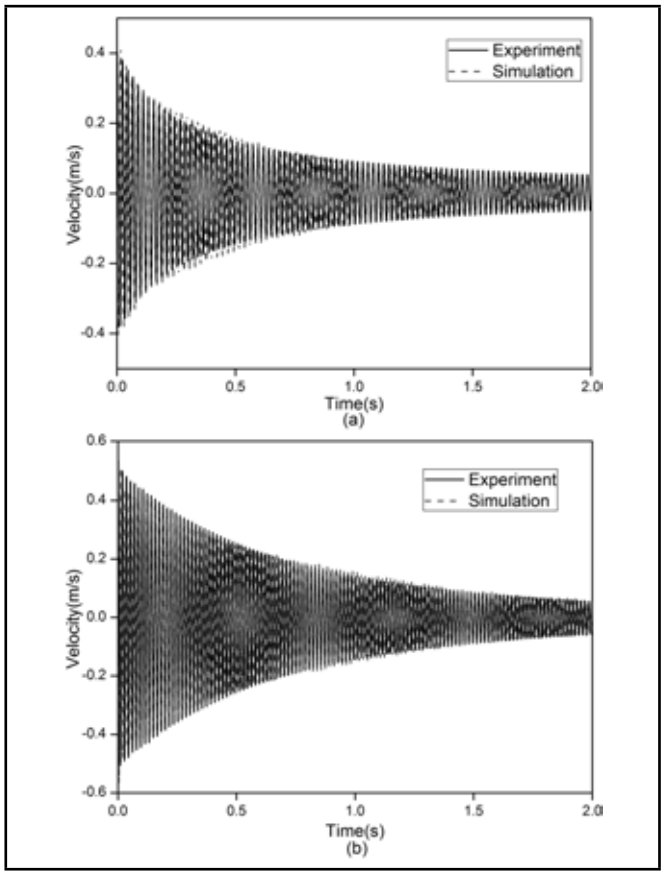

Figure 8. Evolution of the waveforms of velocities in the time domain under free vibration $\alpha_{mp} = 40\%$ (a) the particle damper is placed on point A; (a) the particle damper is placed on point B.

These results prove that total particle mass and the particle damper arrangement appear to have a fairly significant effect on damping for the cantilever beam. Increasing the mass tends to increase damping. And the particle damper which is attached to the structure in a region of high vibration levels can significantly reduce the vibration of the host structures. As might be expected, changes in the total particle mass can lead to a fairly significant shift in the frequency of peak response.

5. CONCLUDING REMARKS

In this article, the specific damping capacity of a cantilever continuous particle damping beam is experimentally studied and simulated. The effect of particle impacts on the vibratory behaviour of the structure is illustrated. A comparison of typical decay velocities in a waveform of the system is conducted without particles and with particles dampers. It is proved that, with a particle damper, a very high value of specific damping capacity can be achieved, compared to intrinsic material damping of the structure. Numerical results show that total particle mass appears to have a fairly significant effect on damping for the cantilever particle damping beam. Increasing the filling mass of the particles tends to increase damping. When the particle damper is exerted on different positions of the beam, the damping properties can present an obvious change. The ideal damping effect can be achieved by putting the particle damper in a position on the structure with high-level vibration.

It is encouraging to note that the novel simulation approach based on MFT of gas solid can accurately and reasonably predict the characteristics of particle damping. The co-simulation of COMSOL Multiphysics with MATLAB will broaden our horizons in the design and application for particle dampers. This method provides an effective instruction to the implementation of particle damping in practice, and offers the possibility to analyse the more complex particle-damping system with lower computational cost than DEM, and it can lay a theoretical foundation for the vibration and acoustic radiation response prediction problem for particle damping composite structures.

ACKNOWLEDGMENTS

The work described in this paper was supported by NSFC (Natural Science Foundation of China) P̃roject No.51075316 and Program for Changjiang Scholars and Innovative Research Team in University (PCSIRT).

REFERENCES

[1] Chen, T., et al. Dissipation mechanisms of non-obstructive particle damping using discrete element method, *Proc. SPIE 4331, Smart Structures and Materials 2001: Damping and Isolation*, Newport Beach, CA, (2001).

[2] Fricke, J. R. Lodengraf damping: An advanced vibration damping technology, *SV Sound and Vibration*, **34** (7), 22–27, (2000).

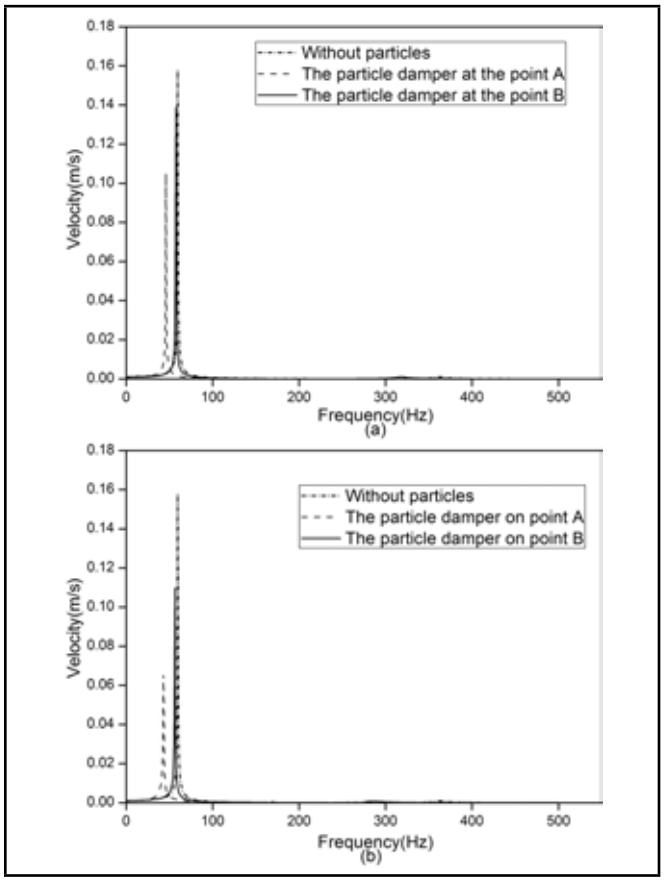

Figure 9. Spectrum of velocities of the system under free vibration, the particle damper is placed on the different position: (a) $\alpha_{mp} = 10\%$; (b) $\alpha_{mp} = 40\%$.

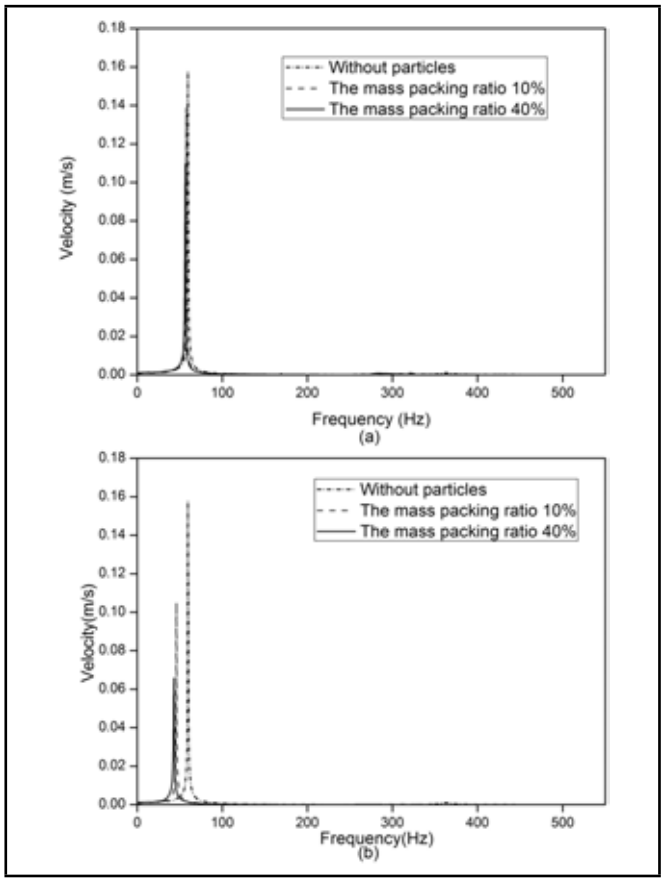

Figure 10. Spectrum of velocities of the system under free vibration, the particle damper is placed on the same position: (a) the particle damper is placed on point B; (b) the particle damper is placed on point A.

[3] Saeki, M. Analytical study of multi-particle damping, *Journal of Sound and Vibration*, **281** (3), 1133–1144, (2005).

[4] Mao, K., et al. Simulation and characterization of particle damping in transient vibrations, *Journal of Vibration and Acoustics*, **126** (2), 202–211, (2004).

[5] Marhadi, K. S. and Kinra, V. K. Particle impact damping: effect of mass ratio, material, and shape, *Journal of Sound and Vibration*, **283** (1), 433–448, (2005).

[6] Isao, Y., Yoshito, T., and So, N. Y. Particle damping with granular materials for multi-body system, *ICSV 15 Internation Congress on Sound and Vibration*, Daejeon, Korea, (2008).

[7] Liu, W., Tomlinson, G. R., and Rongong, J. A. The dynamic characterisation of disk geometry particle dampers, *Journal of Sound and Vibration*, **280** (3), 849–861, (2005).

[8] Papalou, A. and Masri, S. F. An experimental investigation of particle dampers under harmonic excitation, *Journal of Vibration and Control*, **4** (4), 361–379, (1998).

[9] Papalou, A. and Masri, S. F. Performance of particle dampers under random excitation, *Journal of Vibration and Acoustics*, **118** (4), 614–621, (1996).

[10] Wu, C. J., Liao, W. H., and Wang, M. Y. Modelling of granular particle damping using multiphase flow theory of gas-particle, *Journal of Vibration and Acoustics*, **126** (2), 196–201, (2004).

[11] Fang, X. and Tang, J. Granular damping in forced vibration: Qualitative and quantitative analyses, *Journal of Vibration and Acoustics–Transactions of the ASME*, **128** (4), 489–500, (2006).

[12] Wu, C. J., Yang, R. C., and Wang, D. Q. Prediction on vibration response of a cantilever particle-damping beam based on two-phase flow theory of gas-particle, *Chinese Journal of Mechanical Engineering*, **49** (10), 53–61, (2013).

[13] Wu, C. J., Yang, R. C., and Wang, D. Q. An improved modelling of granular particle damping using multiphase flow theory of gas-particle, *ICSV 20th International Congress on Sound & Vibration*, Bangkok, Thailand, (2013).

[14] Fan, L. S. and Zhu, C. *Principles of Gas-Solid Flows*. Cambridge University Press, Cambridge, UK, (1998).

[15] Schaeffer, D. G. Instability in the evolution equations describing incompressible granular flow, *Journal of Differential Equations*, **66** (1) 19–50, (1987).

Study of Secondary Field Waves at Scattering of Nonlinearly Interacting Acoustic Waves by an Elongated Spheroid

Iftikhar B. Abbasov

Taganrog Technological Institute of the Southern Federal University, Nekrasovskyi 44, Taganrog, 347928, Russia

(Received 25 October 2013; revised 1 April 2008; accepted 6 October 2014)

The study and three-dimensional simulation of the field of the second harmonic wave at the scattering of nonlinearly interacting acoustic waves by an elongated spheroid are carried out in this work. The problem is presented in the elongated spheroidal coordinate system, and the foci of the spheroid coincide with foci of the spheroidal coordinate system. The description of the occurring wave processes is presented on the basis of the obtained relation for acoustic pressure of the second harmonic wave. The scattering diagrams for the acoustic pressure field of the second harmonic wave are presented, and three-dimensional models of a scattering diagram are created.

1. INTRODUCTION

The problem of acoustic waves scattering by elongated spheroids was formulated for the first time about half a century ago.[1–3] Some of this research considered the problem of the sound scattering by an elongated spheroid with different boundary conditions.[1] Other research considered the problem of the sound scattering by a rigid spheroid in the long-wave approximation.[2] And other work is devoted to the problem of sound waves scattering by an elongated spheroid.[3] The angular characteristics of the acoustic waves scattering by a soft and rigid elongated spheroid were presented.

The process of the plane acoustic waves scattering by thin, acoustically rigid and resilient bodies of revolution was considered in some of the research used in this study.[4,5] In other works, the problem of the plane acoustic wave scattering by spheroidal shells was investigated.[6,7] These works study the surface waves directly on scatterers, and the frequency dependence of the backscattering amplitude in the far field is presented. With the exception of the works on the linear scattering by spheroids, there are several papers devoted to nonlinear acoustic spectroscopy. Some studies used here consider the problem of nonlinear acoustic diagnostics of defects in materials and structures.[8] Other research presented here is devoted to solving the problem of the nonlinear acoustic spectroscopy of defects in geomaterials.[9]

However, the problem of interacting nonlinear acoustic waves scattered by an elongated spheroid has not been examined elsewhere. This problem becomes essential when an acoustic parametric antenna is used for remote diagnostics of a water medium, as well as in the medical tomography field.

In the present work, the study and simulation of the secondary field of the second harmonic wave is carried out. The study of the secondary field of the difference-frequency wave for nonlinearly interacting plane acoustic waves scattered by a rigid elongated spheroid was also performed.[10] However, the scattering process for the high-frequency second harmonic wave has a purely geometrical character ($k_{2\omega}h_0 \gg 1$). But the difference-frequency wave covers the Rayleigh- ($k_{-}h_0 \ll 1$) and resonance- ($k_{-}h_0 \approx 1$) scattering regions. A multi-frequency analysis will lead to an increase in informativeness of the scattered signal.

2. STATEMENT OF PROBLEM

The problem of wave diffraction by elongated bodies is often described in ellipsoidal coordinates. These coordinates are used in the study of radiation and the scattering of acoustic waves by ellipsoids, or cigar-shaped bodies, and when studying the diffraction by circular apertures.[11]

The elongated spheroidal coordinate system, ξ, η, and φ, is used for the study of diffraction by cigar-shaped bodies . The foci of the spheroid coincide with foci of the spheroidal coordinate system. The spheroid is formed by rotating the ellipse ξ_0 around its major axis, which coincides with the x-axis in the Cartesian coordinate system. The geometry of the problem is presented in Fig. 1. The $\xi = const$ spheroids and $\eta = const$ two-sheeted hyperboloids are the coordinate surfaces in this case.

Elongated spheroidal coordinates are related to Cartesian coordinates by the following equations:[12]

$$x = h_0\xi\eta, \qquad y = h_0\sqrt{(\xi^2-1)(1-\eta^2)}\cos\varphi,$$
$$z = h_0\sqrt{(\xi^2-1)(1-\eta^2)}\sin\varphi;$$

where $h_0 = d/2$ and d is the interfocal distance. Spheroidal coordinates ξ, η, and φ vary within the limits $1 \le \xi < \infty$; $-1 \le \eta \le 1$; and $0 \le \varphi \le 2\pi$.

The perfect elongated spheroid is placed into a homogeneous medium. The spheroid's surface is characterized by the radial coordinate ξ_0. In our case, the spheroid is supposed to be acoustically rigid. Consequently, the Neumann boundary

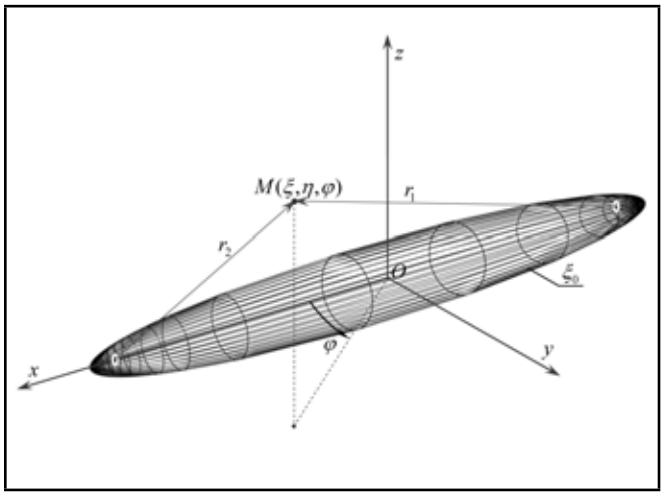

Figure 1. Geometry of the problem.

condition is satisfied at the surface. We assume that interacting high-frequency plane acoustic waves of the unit pressure amplitude fall onto the spheroid at an arbitrary polar angle θ_0 ($\theta_0 = \arccos\eta_0$) and an azimuthal angle φ_0 in the spheroidal coordinate system:[11]

$$p_{ni} = \exp\left[-i(k_n r_0\cos\theta_0 - \omega_n t)\right] = -2\exp(i\omega_n t)\sum_{m=0}^{\infty}\sum_{l\geq m}^{\infty} i^{-l}\overline{S_{ml}}(k_n h_0,\eta_0)\overline{S_{ml}}(k_n h_0,\eta)\cdot R_{ml}^{(1)}(k_n h_0,\xi)\cos m(\varphi-\varphi_0); \quad (1)$$

where k_n is the wavenumber; $n = 1, 2$ according to the waves with frequencies ω_1 and ω_2; r_0 is the radius-vector of the polar coordinate system; $\overline{S_{ml}}(k_n h_0,\eta)$ is the normalized angular first-order function; and $R_{ml}^{(1)}(k_n h_0,\xi)$ is the radial spheroidal first-order function.

After the plane wave scattering by the spheroid, the scattered spheroidal wave with pressure[3] will propagate in the environment

$$p_{ns}(\xi,\eta,\varphi) = 2\exp(i\omega_n t)\sum_{m=0}^{\infty}\sum_{l\geq m}^{\infty} A_{ml}(k_n h_0,\xi_0)\cdot \overline{S_{ml}}(k_n h_0,\eta)R_{ml}^{(3)}(k_n h_0,\xi)\cos m\varphi; \quad (2)$$

where $A_{ml}(k_n h_0,\xi_0)$ is the coefficient dependent on boundary conditions on the spheroid surface, and $R_{ml}^{(3)}(k_n h_0,\xi)$ is the radial spheroidal third-order function.

When the scattered spheroidal wave occurs, the total acoustic pressure of the primary field around the spheroid will be

$$p^{(1)} = p_{ni} + p_{ns} = \left[\sum_{m=0}^{\infty}\sum_{l\geq m}^{\infty} B_{ml}(k_n h_0)\exp\left[i(\omega_n t - l\pi/2)\right] + \sum_{m=0}^{\infty}\sum_{l\geq m}^{\infty} D_{ml}(k_n h_0)\exp\left[i(\omega_n t - m\varphi)\right]\right] + (c.c.); \quad (3)$$

where

$$B_{ml}(k_n h_0) = 2\overline{S_{ml}}(k_n h_0,\eta_0)\overline{S_{ml}}(k_n h_0,\eta)R_{ml}^{(1)}(k_n h_0,\xi)\cdot\cos m(\varphi-\varphi_0),$$

$$D_{ml}(k_n h_0) = 2A_{ml}(k_n h_0,\xi_0)\overline{S_{ml}}(k_n h_0,\eta)R_{ml}^{(3)}(k_n h_0,\xi)\cdot\cos m\varphi,$$

and $(c.c.)$ is the complex-conjugate part.

When solving problems of nonlinear interaction, it is necessary to take into account the reality of sound pressure; therefore, Eq. (3) is presented with the complex-conjugated part.

The nonlinear wave processes around the spheroid can be described by the inhomogeneous wave equation[13]

$$\Delta p^{(2)} - \frac{1}{c_0^2}\frac{\partial^2 p^{(2)}}{\partial t^2} = -Q = -\frac{\varepsilon}{c_0^4\rho_0}\frac{\partial^2 p^{(1)}}{\partial t^2}; \quad (4)$$

where Q is the volume density of the sources of secondary waves, c_0 is the sound velocity in the medium, ε is the quadratic nonlinearity parameter, ρ_0 is the density of the unperturbed medium, and $p^{(1)}$ and $p^{(2)}$ are the total acoustic pressures of the primary and secondary fields.

The wave in Eq. (4) is solved by the method of successive approximations. In the first approximation, the solution is represented by Eq. (3) for the total acoustic pressure of the primary field $p^{(1)}$. To find the solution in the second approximation, $p^{(2)}$, the right side of Eq. (4) should feature four frequency components: second harmonics of the incident waves, $2\omega_1$, $2\omega_2$, and the combination frequency waves, $\omega_1 + \omega_2$, $\omega_2 - \omega_1 = \Omega$.

The equation for the volume density of secondary waves sources $Q_{2\omega}$ at the second harmonic $2\omega_1$ is

$$Q_{2\omega} = \frac{8\varepsilon\omega_1^2}{c_0^4\rho_0}\left[\sum_{m=0}^{\infty}\sum_{l\geq m}^{\infty} B_{ml}^2(k_1 h_0)\cos(2\omega_1 t - l\pi) + \sum_{m=0}^{\infty}\sum_{l\geq m}^{\infty} 2B_{ml}(k_1 h_0)D_{ml}(k_1 h_0)\cos(2\omega_1 t - l\pi/2 - m\varphi) + \sum_{m=0}^{\infty}\sum_{l\geq m}^{\infty} D_{ml}^2(k_1 h_0)\cos(2\omega_1 t - 2m\varphi)\right]. \quad (5)$$

3. SOLUTION OF NONLINEAR WAVE EQUATION FOR THE SECOND HARMONIC WAVE

To solve the inhomogeneous wave shown in Eq. (4) with the right-hand side given by Eq. (6) in the second approximation, we seek the solution in the complex form

$$p_{2\omega}^{(2)} = \frac{1}{2}P_{2\omega}^{(2)}\exp\left(i(2\omega_1 t + \delta)\right) + (c.c.). \quad (6)$$

The inhomogeneous Helmholtz equation is obtained by supplanting Eq. (6) into the inhomogeneous wave Eq. (4):

$$\Delta P_{2\omega}^{(2)} + k_{2\omega}^2 P_{2\omega}^{(2)} = -q_{2\omega}(\xi,\eta,\varphi); \quad (7)$$

where $k_{2\omega}^2 = 2k_1$ is the wavenumber of the second harmonic $2\omega_1$, and $q_{2\omega}(\xi,\eta,\varphi)$ is the function of the sources of secondary waves

$$q_{2\omega}(\xi,\eta,\varphi) = \frac{8\varepsilon\omega_1^2}{c_0^4\rho_0}\Bigg[\sum_{m=0}^{\infty}\sum_{l\geq m}^{\infty} B_{ml}^2(k_1h_0)\exp\big(i(2\omega_1 t - l\pi)\big) + \sum_{m=0}^{\infty}\sum_{l\geq m}^{\infty} 2B_{ml}(k_1h_0)D_{ml}(k_1h_0)\exp\big(i(2\omega_1 t - l\pi/2 - m\varphi)\big) + \sum_{m=0}^{\infty}\sum_{l\geq m}^{\infty} D_{ml}^2(k_1h_0)\exp\big(i(2\omega_1 t - 2m\varphi)\big)\Bigg].$$

The solution to the inhomogeneous Helmholtz equation in Eq. (7) takes the form of a volume integral of the product of the Green's function with the secondary wave sources density[13, 14]

$$P_{2\omega}^{(2)}(\xi,\eta,\varphi) = \int_V q_{2\omega}(\xi',\eta',\varphi')G(r_1)h_{\xi'}h_{\eta'}h_{\varphi'}\,d\xi'd\eta'd\varphi'; \tag{8}$$

where $G(r_1)$ is the Green function, r_1 is the distance between the current point of the volume $M'(\xi',\eta',\varphi')$ and the observation point $M(\xi,\eta,\varphi)$, and $h_{\xi'}$, $h_{\eta'}$, $h_{\varphi'}$ are the scale factors (coefficients of Lame).[15]

The Green's function in the far zone $r' \ll r$ is determined by the asymptotic equation

$$G(r_1) \approx \exp\Big[-ik_{2\omega}\Big(h_0\xi - h_0\xi'\eta\eta' - h_0\xi'\sqrt{(1-\eta^2)(1-\eta'^2)}\times\cos(\varphi-\varphi')\Big)\Big]\Big/h_0\xi. \tag{9}$$

The integration in Eq. (8) is performed over the volume V occupied by the second wave sources and bounded in the spheroidal coordinates by relations $\xi_0 \leq \xi' \leq \xi_S$, $-1 \leq \eta' \leq 1$, $0 \leq \varphi' \leq 2\pi$.

This volume represents a spheroidal layer of the medium, stretching from the spheroidal scatterer surface to the boundary of the nonlinear interaction area. A spheroidal surface with the coordinate ξ_S is the boundary of this area. The coordinate ξ_S is defined by the length of the nonlinear interaction area (attenuation area) of the initial high-frequency waves. The length of this area is inversely proportional to the coefficient of viscous sound absorption at the corresponding pumping frequency. The scattered waves' interaction can be neglected due to attenuation beyond this area. For the interacting incident waves, the boundary introduction is equivalent to placing the absorption filter at the boundary.

As a result of the final integration over coordinates φ' and η' when taking into account the equation for the sources of secondary waves, Eq. (8) takes the form[16]

$$P_{2\omega}^{(2)}(\xi,\eta,\varphi) = P_{2\omega\mathrm{I}}^{(2)}(\xi,\eta,\varphi) + P_{2\omega\mathrm{II}}^{(2)}(\xi,\eta,\varphi) + P_{2\omega\mathrm{III}}^{(2)}(\xi,\eta,\varphi) = C_{2\omega}\frac{1}{k_{2\omega}h_0\eta}\Bigg[\int_{\xi_0}^{\xi_S} T\xi'\sin(k_{2\omega}h_0\xi'\eta)d\xi' - \int_{\xi_0}^{\xi_S} T\frac{\sin(k_{2\omega}h_0\xi'\eta)}{\xi'}d\xi'\Bigg]; \tag{10}$$

where

$$C_{2\omega} = \frac{32\pi h_0^3\varepsilon\omega_1^2\exp(-ik_{2\omega}h_0\xi)}{c_0^4\rho_0\xi},$$

$$T = \Bigg[\sum_{m=0}^{\infty}\sum_{l\geq m}^{\infty} B_{ml}^2(k_1h_0)\exp(-il\pi) + \sum_{m=0}^{\infty}\sum_{l\geq m}^{\infty} 2B_{ml}(k_1h_0)D_{ml}(k_1h_0)\exp\big(-i(l\pi/2+m\varphi)\big) + \sum_{m=0}^{\infty}\sum_{l\geq m}^{\infty} D_{ml}^2(k_1h_0)\exp(-2im\varphi)\Bigg],$$

(and from here on, the time factor $\exp(i2\omega_1 t)$ is omitted).

In contrast with the different frequency wave in Eq. (10), the total acoustic pressure of the second harmonic wave $P_{2\omega}^{(2)}(\xi,\eta,\varphi)$ consists of three spatial components. Therefore, the contribution of the separate components in the total field will increase.

The first component, $P_{2\omega\mathrm{I}}^{(2)}(\xi,\eta,\varphi)$, corresponds with the part of the total acoustic pressure of the second harmonic wave, which is formed in the spheroidal layer of the nonlinear interaction area by the incident high-frequency plane wave ω_1. The second component, $P_{2\omega\mathrm{II}}^{(2)}(\xi,\eta,\varphi)$, describes the interaction of the incident plane wave with the scattered spheroidal wave of frequency ω_1. The third component, $P_{2\omega\mathrm{III}}^{(2)}(\xi,\eta,\varphi)$, characterizes the self-interaction of the scattered spheroidal wave of frequency ω_1. It should also be noted that these components characterize the nonlinear interaction of incident and scattered waves with different spatial configurations of the wave fronts.

After the final integration over the coordinate ξ', the equation for the first component $P_{2\omega\mathrm{I}}^{(2)}(\xi,\eta,\varphi)$ takes the following form:

$$P_{2\omega\mathrm{I}}^{(2)}(\xi,\eta,\varphi) = P_{2\omega\mathrm{I}1}^{(2)} + P_{2\omega\mathrm{I}2}^{(2)} + P_{2\omega\mathrm{I}3}^{(2)} + P_{2\omega\mathrm{I}4}^{(2)}; \tag{11}$$

where

$$P_{2\omega\mathrm{I}1,2\omega\mathrm{I}2}^{(2)} = \pm\frac{C_{2\omega}}{2k_{2\omega}^2h_0^2\eta(\eta_0\mp\eta)}\cdot \Big[\xi_S\exp\big[-ik_{2\omega}h_0(\eta_0\mp\eta)\xi_S\big] - \xi_0\exp\big[-ik_{2\omega}h_0(\eta_0\mp\eta)\xi_0\big]\Big],$$

$$P_{2\omega\mathrm{I}3,2\omega\mathrm{I}4}^{(2)} = \mp\frac{C_{2\omega}}{2i(k_{2\omega}h_0\eta)}\cdot \Big[-\mathrm{Ei}\big[-ik_{2\omega}h_0(\eta_0\mp\eta)\xi_S\big] + \mathrm{Ei}\big[-ik_{2\omega}h_0(\eta_0\mp\eta)\xi_0\big]\Big],$$

and $\mathrm{Ei}(ax) = \int \frac{\exp(ax)}{x}$ is the integral exponential function.[17,18]

Analysing what was obtained in Eq. (11) for the first component, $P^{(2)}_{2\omega\mathrm{I}}(\xi,\eta,\varphi)$, of the total acoustic pressure of the second harmonic wave, one can note that the scattering diagram of this component is determined by the behaviour of the function $1/(\eta_0 \pm \eta)$. This function depends on the coordinate η_0, i.e. on the angle of incidence θ_0 of the high-frequency plane waves in the polar coordinate system.

Now consider the second component of Eq. (10), $P^{(2)}_{2\omega\mathrm{II}}(\xi,\eta,\varphi)$, for the total acoustic pressure of the second harmonic wave, which characterizes the nonlinear interaction of the incident plane wave with the scattered spheroidal wave. After the final integration, the equation for the second component of the total acoustic pressure of the second harmonic wave takes the form

$$P^{(2)}_{2\omega\mathrm{II}}(\xi,\eta,\varphi) = P^{(2)}_{2\omega\mathrm{II}1} + P^{(2)}_{2\omega\mathrm{II}2} + P^{(2)}_{2\omega\mathrm{II}3} + P^{(2)}_{2\omega\mathrm{II}4}; \quad (12)$$

where

$$P^{(2)}_{2\omega\mathrm{II}1,2\omega\mathrm{II}2} = \mp \frac{iC_{2\omega}A(k_1k_0)}{2k_1k_{2\omega}h_0^2\eta\sqrt{(1-\eta_0)(1-\eta)}} \cdot \left[\frac{\exp(-iu_{2\omega}\xi_S) - \exp(-iu_{2\omega}\xi_0)}{u_{2\omega}}\right],$$

$$P^{(2)}_{2\omega\mathrm{II}3,2\omega\mathrm{II}4} = \pm \frac{C_{2\omega}A(k_1k_0)}{2k_1k_{2\omega}h_0^2\eta\sqrt{(1-\eta_0)(1-\eta)}} \cdot \left[\frac{\exp(-iu_{2\omega}\xi_S)}{\xi_S} - \frac{\exp(iu_{2\omega}\xi_0)}{\xi_0} - iu_{2\omega}\left[\mathrm{Ei}(-iu_{2\omega}\xi_S) - \mathrm{Ei}(-iu_{2\omega}\xi_0)\right]\right],$$

and $u_{2\omega} = (k_1h_0\eta - k_1h_0 \mp k_{2\omega}h_0\eta)$.

An analysis of Eq. (12) shows that the scattering diagrams of the second component $P^{(2)}_{2\omega\mathrm{II}}(\xi,\eta,\varphi)$ are determined mainly by the function $1/\eta\sqrt{(1-\eta_0)(1-\eta)}$, where the dependence on the incident angle θ_0 (that is η_0) is not very pronounced.

Now, we consider the third component of Eq. (10), $P^{(2)}_{2\omega\mathrm{III}}(\xi,\eta,\varphi)$, for the total acoustic pressure of the second harmonic wave, characterizing the nonlinear self-interaction of the scattered spheroidal wave frequency ω_1. After the final integration, the equation for the third component of the total acoustic pressure of the second harmonic wave takes the form

$$P^{(2)}_{2\omega\mathrm{III}}(\xi,\eta,\varphi) = P^{(2)}_{2\omega\mathrm{III}1} + P^{(2)}_{2\omega\mathrm{III}2} + P^{(2)}_{2\omega\mathrm{III}3} + P^{(2)}_{2\omega\mathrm{III}4}; \quad (13)$$

where

$$P^{(2)}_{2\omega\mathrm{III}1,2\omega\mathrm{III}2} = \mp \frac{C_{2\omega}A^2(k_1k_0)}{2ik_{2\omega}h_0^3k_1^2\eta(1-\eta_0)(1-\eta)} \cdot \left[-u_{3\omega}\left[\mathrm{Ei}(-iu_{3\omega}\xi_S) - \mathrm{Ei}(-iu_{3\omega}\xi_0)\right]\right],$$

$$P^{(2)}_{2\omega\mathrm{III}3,2\omega\mathrm{III}4} = \mp \frac{C_{2\omega}A^2(k_1k_0)}{4ik_{2\omega}h_0^3k_1^2\eta(1-\eta_0)(1-\eta)} \cdot \left[iu_{3\omega}\left(\frac{\exp(-iu_{3\omega}\xi_S)}{\xi_S} - \frac{\exp(iu_{3\omega}\xi_0)}{\xi_0}\right) + u_{3\omega}^2\left[\mathrm{Ei}(-iu_{3\omega}\xi_S) - \mathrm{Ei}(-iu_{3\omega}\xi_0)\right]\right],$$

and $u_{3\omega} = (k_{2\omega}h_0 \mp k_{2\omega}h_0\eta)$.

The scattering diagrams type is defined mainly by the function $1/\eta(1-\eta_0)(1-\eta)$ of Eq. (13).

4. DRAWING OF SCATTERING DIAGRAMS

To reveal the features of the acoustic field of the second harmonic wave, we consider the scattering diagrams for separate spatial components. The diagrams of the second harmonic wave components $P^{(2)}_{2\omega}(\xi,\eta,\varphi)$ scattered by a rigid elongated spheroid $\xi_0 = 1.005$ are presented in Fig. 2 (relation axis 1:10, $h_0 = 0.01$ m, distance from focal points $r_1 = 0.01$ m, $r_2 = 0.0101$ m) at: $\xi = 7$, angle of incidence shown an arrow $\theta_0 = 30^\mathrm{o}$, $f_2 = 1000$ kHz, $f_1 = 976$ kHz ($k_{1,2}h_0 \approx 40$), $2f_1 = 1952$ kHz, $k_{2\omega}h_0 = 82$, ($k_-h_0 = 1$). The initial parameter values of the second harmonic wave are connected to values for the difference-frequency wave.[10]

The scattering diagram for the first component $P^{(2)}_{2\omega\mathrm{I}}(\xi,\eta,\varphi)$ has maxima in the direction of the angle of incidence and in the symmetrical (with respect to the z-axis) direction (30^o and 150^o). The diagrams of other components have major maxima in the reverse and lateral directions (0^o and $\pm 90^\mathrm{o}$) and do not show dependence on the angle of incidence.

The scattering diagrams for the second harmonic wave $P^{(2)}_{2\omega}(\xi,\eta,\varphi)$ on a rigid elongated spheroid $\xi_0 = 1.005$ ($h_0 = 0.01$ m) for different radial distance values ξ are presented in Fig. 3 (the size of the re-radiating volume) at: $\theta_0 = 30^\mathrm{o}$, $f_2 = 1000$ kHz, $f_1 = 976$ kHz, ($k_{1,2}h_0 \approx 40$), $2f_1 = 1952$ kHz, $k_{2\omega}h_0 = 82$ ($k_-h_0 = 1$), $\xi = 3; 7; 15$.

The scattering diagrams for different wave dimensions of the spheroid and for different sizes of the interaction area were calculated. As a result, it was found that increasing the wave dimension of the spheroidal scatterer leads to minor changes in the maxima levels (in contrast with the difference-frequency wave). An increase in the size of the interaction area around the elongated spheroidal scatterer (coordinates ξ) leads to narrowing of these maxima.

In Fig. 4 are presented the scattering diagrams of the second harmonic wave $P^{(2)}_{2\omega}(\xi,\eta,\varphi)$ by a rigid elongated spheroid $\xi_0 = 1.005$ ($h_0 = 0.01$ m) for the different incidence angle values of the initial pumping waves $\theta_0 = 0^\mathrm{o}; 60^\mathrm{o}; 90^\mathrm{o}$ ($f_2 = 1000$ kHz, $f_1 = 976$ kHz, ($k_{1,2}h_0 \approx 40$), $2f_1 = 1952$ kHz, $k_{2\omega}h_0 = 82$ ($k_-h_0 = 1$), $\xi = 7$).

The scattering diagrams of the second harmonic wave $P^{(2)}_{2\omega}(\xi,\eta,\varphi)$ for the different incidence angle values $\theta_0 = 0^\mathrm{o}; 60^\mathrm{o}; 90^\mathrm{o}$ reproduce the features of the scattering diagrams of the difference-frequency wave $P^{(2)}_{-}(\xi,\eta,\varphi)$.

The scattering diagram of the second harmonic wave retains the general regularity in directions to the maxima. However, unlike the difference-frequency wave, the diagram does not undergo significant changes for different values of the spheroid's wave dimensions in accordance with the maxima, and it has more sharpened maxima. These features are associated with the geometric character of the scattering process.

Figures 5 and 6 show spatial models of the scattering diagrams of the second harmonic wave $P^{(2)}_{2\omega}(\xi,\eta,\varphi)$ by a rigid

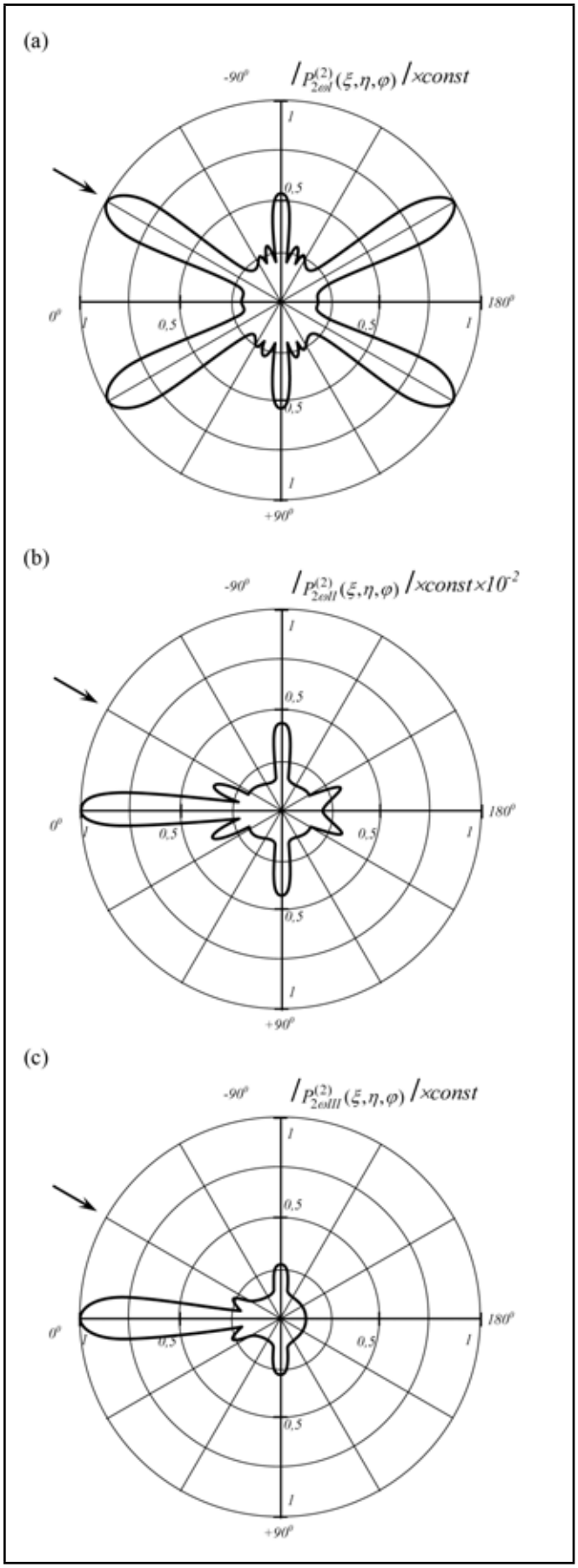

Figure 2. Scattering diagrams for the second harmonic wave $P^{(2)}_{2\omega}(\xi,\eta,\varphi)$ components on a rigid elongated spheroid $\xi_0 = 1.005$ for: $\xi = 7$, $\theta_0 = 30^{\circ}$, $f_2 = 1000$ kHz, $f_1 = 976$ kHz, $2f_1 = 1952$ kHz, $k_{2\omega}h_0 = 82$ ($k_- h_0 = 1$).

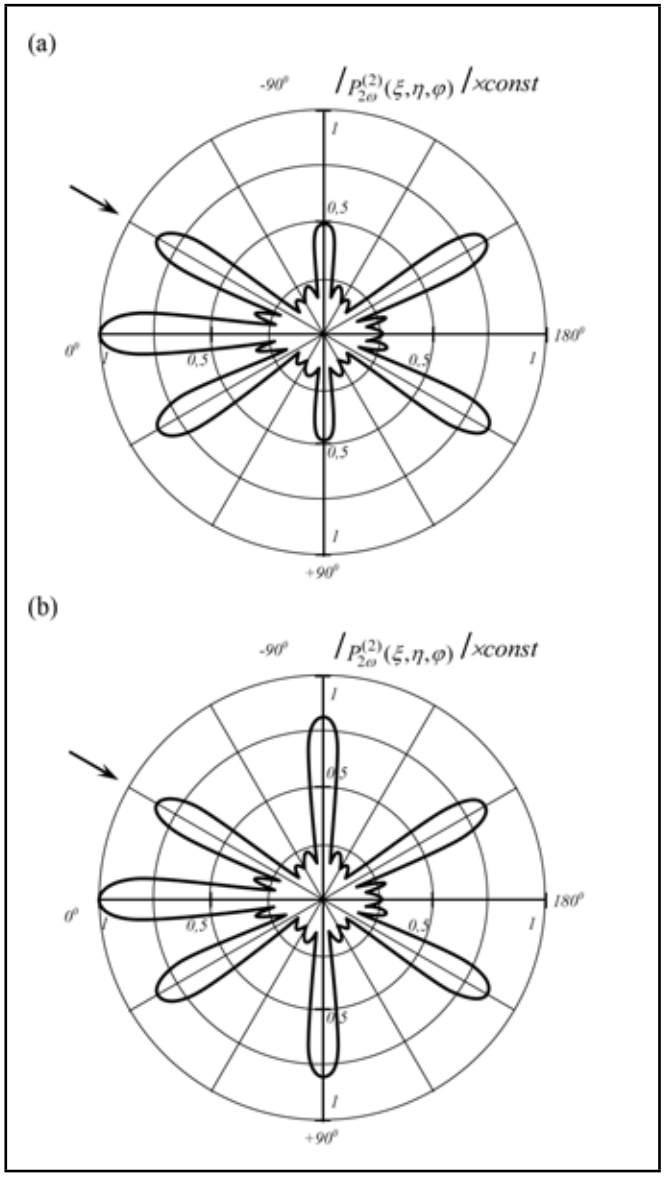

Figure 3. Scattering diagrams of the second harmonic wave $P^{(2)}_{2\omega}(\xi,\eta,\varphi)$ on a rigid elongated spheroid $\xi_0 = 1.005$ for different ξ values for: $f_2 = 1000$ kHz, $f_1 = 976$ kHz, $2f_1 = 1952$ kHz, $k_{2\omega}h_0 = 82$, $\theta_0 = 30^{\circ}$, $\xi = 3; 7; 15$.

elongated spheroid $\xi_0 = 1.005$ for the angle of incidence $\theta_0 = 0^{\circ}; 30^{\circ}$. These diagrams provide a visual representation of the spatial distribution of the scattered pressure field.

5. DISCUSSION AND COMPARISON OF RESULTS

Further, it should be noted that the acoustic pressure of the second harmonic wave was calculated in the far field of the spheroidal scatterer, in the Fraunhofer zone. Therefore, the scattering field can be considered to be formed since the observation point $M(\xi,\eta,\varphi)$ was located at the radial distance $\xi = 7$ and 15. This distance exceeds 3 to 5 times the quasi-diffraction zone length.

The scattering diagrams are shown in the plane xOz. The polar angle θ varies in the range from 0° to $\pm 180^{\circ}$ since the diagrams are axisymmetric with respect to the x-axis. The value

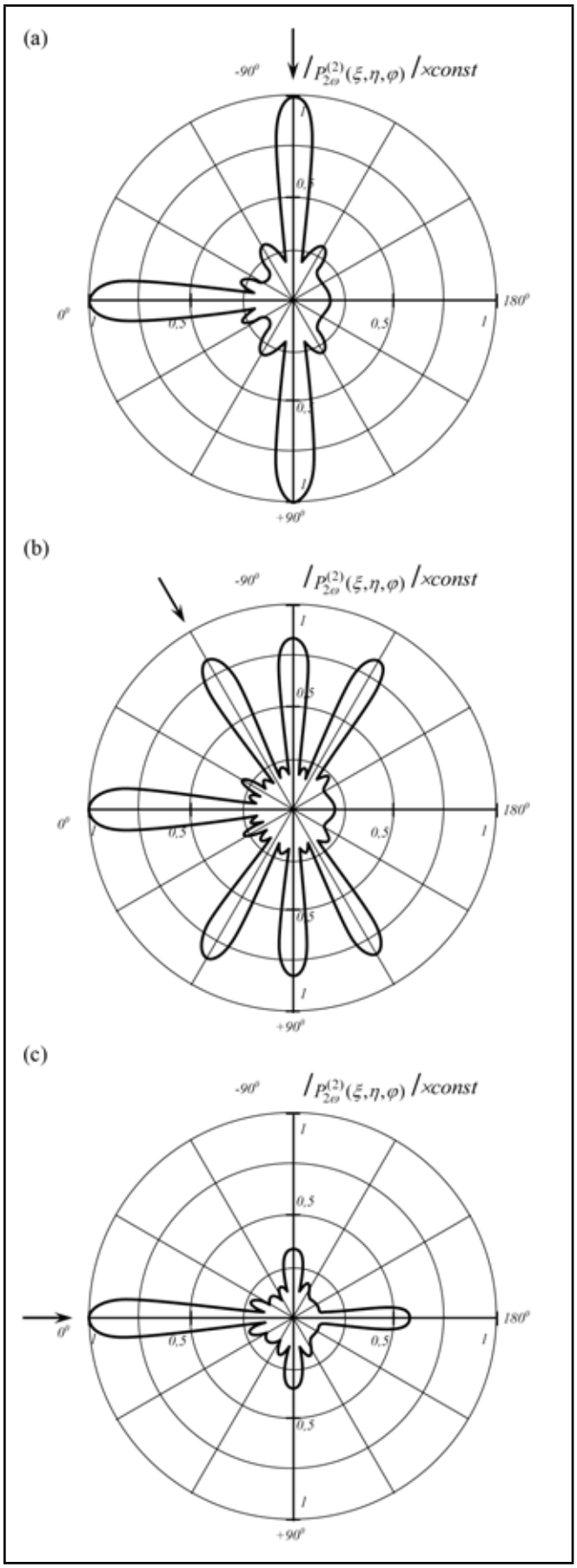

Figure 4. Scattering diagrams of the second harmonic wave $P_{2\omega}^{(2)}(\xi,\eta,\varphi)$ on a rigid elongated spheroid $\xi_0 = 1.005$ for angles of incidence $\theta_0 = 0^{\rm o}; 60^{\rm o}; 90^{\rm o}$ for: $f_2 = 1000$ kHz, $f_1 = 976$ kHz, $2f_1 = 1952$ kHz, $k_{2\omega}h_0 = 82$ ($k_-h_0 = 1$), $\xi = 7$.

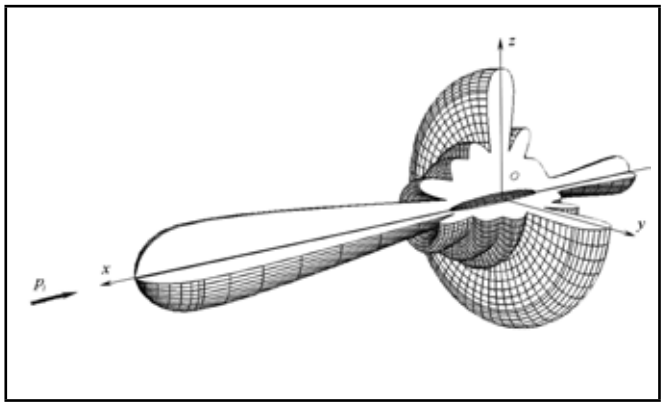

Figure 5. Three-dimensional wireframe model of scattering diagram of the second harmonic wave $P_{2\omega}^{(2)}(\xi,\eta,\varphi)$ on a rigid elongated spheroid $\xi_0 = 1.005$ at the angle of incidence $\theta_0 = 0^{\rm o}$ ($k_{2\omega}h_0 = 82$, $\xi = 7$).

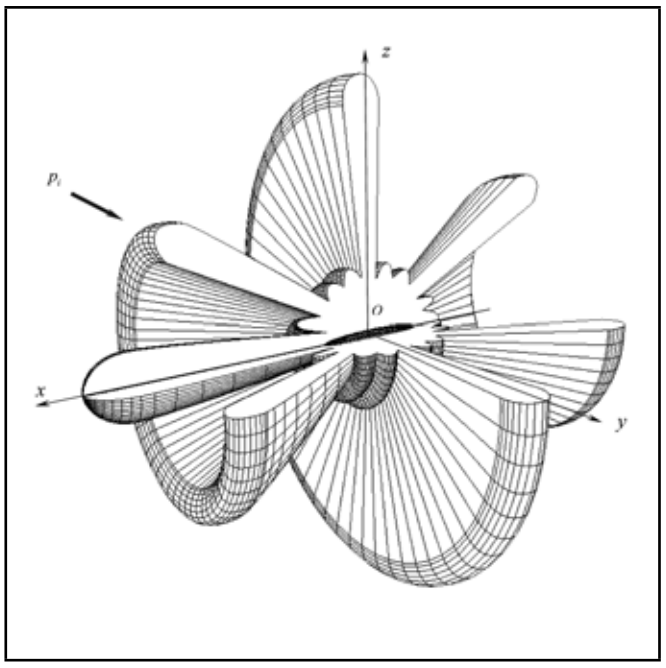

Figure 6. Three-dimensional wireframe model of scattering diagram of the second harmonic wave $P_{2\omega}^{(2)}(\xi,\eta,\varphi)$ on a rigid elongated spheroid $\xi_0 = 1.005$ at the angle of incidence $\theta_0 = 30^{\rm o}$ ($k_{2\omega}h_0 = 74$, $\xi = 3$).

of the angle $\theta = 0^{\rm o}$ corresponds to the axis x position, and the value $\theta = 90^{\rm o}$ corresponds to the z-axis. The arrow shows the direction of the initial plane waves' incidence.

For clarity, the figures show the acoustic pressure $P_{2\omega}^{(2)}(\xi,\eta,\varphi)$ dependence not on the angle of the hyperbola's asymptote η, but on more convenient polar angle $\theta = \arccos\eta$ in spherical coordinates. This representation is conventionally employed for the scattering diagrams in spheroidal coordinates.[2,3,19]

In order to check the correctness of the obtained diagrams of scattering by an elongated spheroid, we should compare them with the results of other studies. It should be also noted that the problem in the nonlinear formulation was not previously investigated, neither theoretically nor experimentally. Within the framework of our consideration, in the case of primary high-frequency waves, the scattering by a spheroid is linear. The secondary field is generated by the secondary wave sources lo-

cated in the volume around the spheroid. In the linear case, they are located on the spheroid's surface. In general, it can be emphasized that the obtained scattering diagrams are in good agreement with diagrams in the works cited in this paper.[3,5,20]

In the far field, the spheroidal coordinates are transformed into the spherical ones $P_+^{(2)}(\xi,\eta,\varphi) \to P_+^{(2)}(r,\theta,\varphi)$. The diagrams of scattering by an elongated spheroid in the far field are in good agreement with the author's study results on scattering by a sphere.[21,22] However, unlike the case of a sphere, where the scattered field does not depend on the angle of incidence θ, the lobes in the directions of incidence and reflection of the initial plane waves appear in the case of a spheroid.

REFERENCES

[1] Cpence, R. and Ganger, S. The scattering of sound from a prolate spheroid, *Journal of the Acoustical Society of America*, **23** (6), 701–706, (1951). DOI:10.1121/1.1906827

[2] Burke, J. E. Long-wavelength scattering by hard spheroids, *Journal of the Acoustical Society of America*, **39** (5), 826–831, (1966). DOI:10.1121/1.1909959

[3] Kleshchev, A. A. and Sheiba, L. S. Scattering of a sound wave by ideal prolate spheroids, *Soviet Physic Acoustic*, **16** (2), 219–222, (1970).

[4] Fedoryuk, M. V. Scattering of sound wave from thin acoustically rigid revolve body, *Soviet Physic Acoustic*, **27** (4), 605–609, (1981).

[5] Boiko, A. I. Scattering of plane sound wave from thin revolve body, *Soviet Physic Acoustic*, **29** (3), 189–191, (1983).

[6] Werby, M. F. and Green, L. H. Correspondence between acoustical scattering from spherical and end-on incidence spherical shells, *Journal of the Acoustical Society of America*, **81** (2), 783–787, (1987). DOI:10.1121/1.394796

[7] Veksler, N. D., Dubus, B., and Lavie, A. Acoustic wave scattering by an ellipsoidal shell, *Acoustical Physics*, **45** (1), 46–51, (1999).

[8] Guyer, R. A. and Johnson, P. A. Nonlinear mesoscopic elasticity evidence for a new class of materials, *Physics Today*, **52** (4), 30–36, (1999). DOI:10.1063/1.882648

[9] Lebedev, A. V., Ostrovskii, L. A., and Sutin, A. M. Nonlinear acoustic spectroscopy of local defects in geomaterials, *Acoustical Physics*, **51** (1), S88–S101, (2005).

[10] Abbasov, I. B. Study of the scattering of nonlinearly interacting plane acoustic waves by an elongated spheroid, *Journal of Sound and Vibration*, **309** (1–2), 52–62, (2008). DOI:10.1016/j.jsv.2007.03.060

[11] Skudrzyk, E. *The Foundations of Acoustics*, Vol. 2, Springer, New York, (1971).

[12] Tikhonov, A. N. and Samarskyi, A. A. *The Equations of Mathematical Physics*, Nauka, Moscow, (1966).

[13] Novikov, B. K., Rudenko, O. V., and Timoshenko, V. I. *Nonlinear Underwater Acoustic*, Acoustical Society of America, New York, (1987).

[14] Lyamshev, L. M. and Sakov, P. V. Nonlinear scattering of sound from an pulsted sphere, *Soviet Physics Acoustics*, **38** (1), 50–54, (1992).

[15] Korn, H. and Korn, T. *Mathematical Handbook for Scientists and Engineers*, McGraw-Hill, (1961).

[16] Abbasov, I. B. *Scattering nonlinear interacting acoustic waves: sphere, the cylinder and a spheroid*, Fizmatlit, Moscow, (2007).

[17] Abramovitz, M. and Stegun, I. *Handbook of Special Functions with Formulas, Graphs, and Mathematical Tables*, Dover, New York, (1971).

[18] Prudnikov, A. P., Brychkov, Yu. A., and Marichhev, O. I. *Integrals and series*, Nauka, Moscow, (1983).

[19] Chertock, G. Sound radiation from circular pistons of elliptical profile, *Journal of the Acoustical Society of America*, **33** (7), 871–8876, (1961). DOI:10.1121/1.1908831

[20] Kleshchev, A. A. and Rostovtsev, D. M. Scattering of sound from elastically and liquidly ellipsoidal revolve shell, *Soviet Physic Acoustic*, **32** (5), 432–433, (1986).

[21] Abbasov, I. B. and Zagrai, N. P. Sphere scattering of nonlinear interacting acoustic waves, *Fluid Dynamics*, **30** (2), 158–165, (1995).

[22] Abbasov, I. B. and Zagrai, N. P. The investigation of the second field of the summarized frequency originated from scattering of nonlinearly interacting sound waves at a rigid sphere, *Journal of Sound and Vibration*, **216** (1), 194–197, (1998). DOI:10.1006/jsvi.1998.1638

Chen Long-Xiang received his PhD in 2009 from the Department of Engineering Mechanics, Shanghai Jiaotong University, Shanghai, China, where he is currently a lecturer. His current research interests focus on structural dynamics and control and delayed system dynamics and control.

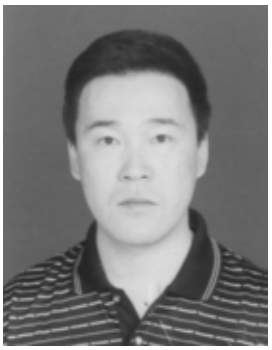

Cai Guo-Ping is currently a professor in the Department of Engineering Mechanics, Shanghai Jiaotong University, Shanghai, China. He received the PhD in Engineering Mechanics from Xian Jiaotong University, Xian, China, in 2000. His current research interests focus on structural dynamics and control, delayed system dynamics and control, and coupled system dynamics and control.

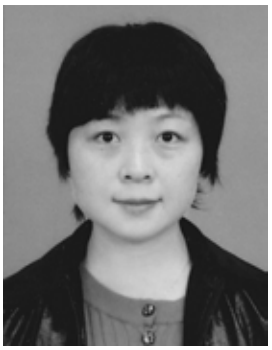

Xiaomin Xue is a lecturer in the Civil Engineering Department at Xian Jiaotong University, Xi'an, Shaanxi, China, where she received her PhD in 2011 and MS in 2007. Her research interests lie within the broad areas of structural vibration control and smart material structures. She is currently working on an electric-mechanical hysteretic model of smart material systems with various applications in system identification, structural health monitoring, and the control and simulation of structural response under various vibration loadings, such as earthquakes and wind.

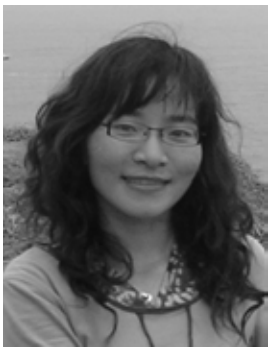

Xiaohong Wu is an associate professor in the School of Aerospace at Xian Jiaotong University, Xi'an, Shaanxi, China, where she received her PhD in engineering mechanics in 2004. She received her MS in metal plastic working from Xian University of Architecture and technology in 1996. Her current research interests are in the fields of mechanic behavior analysis of smart materials and structures. She is currently working on modelling the nonlinear and hysteretic behaviors of smart material systems, as well as the dynamic response analysis of structures under various periodic and vibration loadings.

Qing Sun is a professor in the Civil Engineering Department at Xian Jiaotong University in Xi'an, Shaanxi, China, where he received his PhD in engineering mechanics in 2003. He received his MS in structural engineering in 1997 from Xian University of Architecture and technology. His research interests include structural vibration control, smart materials and structures, stability of steel structures, aseismatic performance of steel-reinforced concrete structures, and limited capacity of FRP composite material structures. He is currently working on the theory and experiment of structural vibration active control using the MFC actuator, and his former study included theoretical and experimental research on structural control with time-delay of seismic excited buildings. He is currently a member of the Chinese Society of the Theoretical and Applied Mechanics and of the China Civil Engineering Society.

About the Authors

Ling Zhang is a professor in the State Key Laboratory for Strength and Vibration of Mechanical Structures School of Aerospace at Xian Jiaotong University in Xi'an, Shaanxi, China. He received his PhD in engineering mechanics from Northwestern Polytechnical University and his MS in structural engineering from Xian University of Architecture and technology. He is currently a member of the Chinese society of Vibration Engineering and of the Basic Mechanics Teaching Guidance Committee of the Chinese Ministry of Education, and he is the eExecutive director of the Shaanxi Provincial Institute of Mmechanics. MHe was a recipient of the National Excellent Teaching Achievement Award and of a special government allowance.

Lokavarapu Bhaskara Rao is an associate professor in the School of Mechanical and Building Sciences at Vellore Institute of Technology University, Chennai Campus, India. He graduated with a degree in mechanical engineering from Bapatla Engineering College in 1993 and obtained his master of technology degree in machine design engineering in 1996 from the National Institute of Technology, Durgapur, India. He obtained his PhD in 2008 from Osmania University, Hyderabad, India. He has worked at various engineering colleges such as Syed Hashim College of Science & Technology, CMR College of Engineering & Technology, DRK Institute of Science & Technology, and Gokaraju Rangaraju Institute of Engineering & Technology located in Hyderabad, India in various capacities such as assistant professor, associate professor, professor, and head of the department. His research interests include stability and vibrations of mechanical systems, such as FGM and nano-circular plates, beams, Graphene sheets, and CNTs.

Chellapilla Kameswara Rao is a professor in the Department of Mechanical Engineering, Nalla Narasimha Reddy Group of Institutions, Korremulla, Hyderabad. Previously, he worked as the dean of the Department of Mechanical Engineering at Guru Nanak Institute of Technology, Integrated Campus, and as both the dean and head of the Department of Mechanical Engineering at TKR College of Engineering College, Hyderabad. He graduated with a degree in Mechanical Engineering from Anantapur Government Engineering College in 1968 and obtained master of technology in machine design in 1971 and PhD in 1976 from Andhra University, Waltair. He taught there from 1972 to 1977 and later worked in BHEL, Research & Development Division, in various capacities for 26 years. He worked at the University of Ottawa, Canada from 1986 to 1988 as a visiting professor. He was the head of intellectual property management in Bharat Heavy Electricals Limited from 1999 to 2003 and has three Indian patents granted in the area of diverter damper related to combined cycle power plants. After retiring from his position as the senior deputy general manager in 2003, he worked as HOD, PG head, and principal at various engineering colleges in Hyderabad. From February 2006 to June 2008, he worked as a manager in client relations at SciTech Patent Art Services Private Limited and managed patent related analytics projects in mechanical and electrical engineering.

Akhilesh Mimani received his PhD from the Department of Mechanical Engineering, Indian Institute of Science, Bangalore, India, in 2012. His doctorate work was focused in the field of muffler acoustics and specifically on designing silencers based on a 3-D analytical approach to obtain a broadband acoustic attenuation performance for minimising vehicle engine noise. He has published over 20 research papers in peer-reviewed international journals and conference proceedings. He is currently a post-doctoral researcher with the Flow and Noise Group, School of Mechanical Engineering, The University of Adelaide, Australia, where he works on developing high-performance computational aeroacoustics (CAA) algorithms and aeroacoustic time-reversal (TR) source localization techniques to analyze flow-induced noise generation mechanisms.

Con Doolan is an associate professor and leads the Flow and Noise Group (FNG) at the University of New South Wales, Sydney, whose focus is on understanding and controlling flow-induced noise in application areas like jets, wind turbines, aircraft, and submarines. He obtained his PhD in Aerospace Engineering from the University of Queensland and completed a postdoctoral position at the University of Glasgow, a research scientist position at the Defence Science and Technology Organisation (DSTO), and an academic post at The University of Adelaide. He has combined his interests of unsteady compressible fluid dynamics and acoustics to study fundamental and applied research problems in aeroacoustics.

Paul Medwell is a senior lecturer in the School of Mechanical Engineering at The University of Adelaide, Australia. He completed both his PhD and postdoctoral position at the same institute. He is now involved in a range of research areas based on developing the fundamental understanding of reacting and non-reacting flows. His combustion and laser-diagnostic background enables him to contribute to research programmes in jet aeroacoustics, as well as humanitarian technology, sports, engineering, and solar-thermal energy systems.

Vinay Vakharia is currently a PhD student in the Mechanical Engineering Discipline at PDPM Indian Institute of Information Technology, Design and Manufacturing Jabalpur, India. He received his masters degree in CAD/CAM from Vellore Institute of Technology, Vellore, India, in 2007. His research interests include vibration, fault diagnosis, design, and manufacturing.

Vijay Kumar Gupta is currently a professor at PDPM IIITDM Jabalpur. He received his PhD in smart structures from the Indian Institute of Technology Bombay. He received the "ISAMPE K. Suryanarayan Rao Memorial Senior student award for R&D in smart technology" in 2003. His research interests include mechanical vibrations, smart structures, mechatronics, robotics, and finite element analysis.

P. K. Kankar obtained his PhD from the Mechanical and Industrial Engineering Department at the Indian Institute of Technology Roorkee, India. He received his masters degree from Malviya Regional Engineering College, Jaipur, India (which is now Malviya National Institute of Technology) in 2000. He has published more than 50 research papers in refereed international journals and conference proceedings. His research interests include vibration, fault diagnosis, design, and analysis of nonlinear dynamical systems.

About the Authors

Dongqiang Wang completed his Master's degree on mechanical design, manufacturing, and automation in 2006. He attends the Institute of Vibration and Noise Control, School of Mechanical Engineering of Xian Jiaotong University (XJTU), Xian City, China, where he began his work in September 2012 as a doctoral candidate. His research fields include structural-acoustic interaction, modal analysis and dynamic optimization design, acoustic prediction, passive vibration and noise control, and particle damping technique. At present, he has authored and co-authored more than five journal and conference papers, has declared one national invention patent, and has co-finished one State Natural Sciences Foundation (NSFC).

ChengJun Wu is a professor in the Institute of Vibration and Noise Control, School of Mechanical Engineering of Xian Jiaotong University (XJTU), Xian City, China, where he completed his PhD on sound and structural interaction in 1999. He was a Research Associate in the Department of Automation & Computer-Aided Engineering at The Chinese University of Hong Kong from July 2001 to January 2002, and a visiting professor in the School of Mechanical Engineering of The University of Western Australia in 2011. His research fields include structural-acoustic interaction, modal analysis and dynamic optimization design, acoustic prediction and CFD simulation, passive vibration and noise control, and particle damping & visco-elastic damping technique, etc. He is also a member of the Mechanical Dynamics Society of China. Professor Wu has authored and co-authored more than 30 journal and conference papers, and finished nearly 30 research projects for the mechanical industry in China. He was honored as the New Century Excellent Talents in the University of China in 2006 and was awarded the 2nd Prize of Natural Science and 2nd Prize of Science & Technology Advance of State Education Ministry of China in 2004 and 1995, respectively.

Ruichao Yang completed his bachelors degree on mechanical design, manufacturing and automation at Northwestern Polytechnical University (NWPU) in 2011. He is currently a masters student in the Institute of Vibration and Noise control, School of Mechanical Engineering of Xian Jiaotong University (XJTU), Xian City, China. His main research fields include modal analysis, passive vibration and noise control, and the prediction of vibration responses for granular particle damping structures. At present, Mr. Yang has authored and co-authored more than five journal and conference papers, has declared one national invention patent, and has co-finished one State Natural Sciences Foundation (NSFC).

Iftikhar B. Abbasov received his diploma from the Taganrog State University of Radio Engineering in 1988, where he focused on microelectronics and electronic engineering and directed operations in the Institute of Space researches (Baku, Azerbaijan). He was the head of the laboratories in the Department of Electrohydroaccoustic and Ultrasonic Engineering from 1989 until 1993. Afterward, he studied as a post-graduate from 1993 until 1996. In 1996, he was awarded a grant from TRTU's Scientific Society and Soros Fund. He defended his dissertation in 1997, gaining his PhD in physic-mathematical sciences. He has been an associate professor in the Department of Engineering Graphics and Computer Design at Taganrog Technological Institute since 1998. He received a grant from the American Fund of Civil Researches and Development in 2000. He is now the head of the Department of Engineering Graphics and Computer Design of Taganrog Technological Institute of Southern Federal University, Taganrog, Russia. His research interests include simulation wave phenomena in fluid dynamics and computer modeling in industrial design. He is the author of seven books and textbooks and of 64 publications in refereed journals.